

LOW MASS STARS AND BROWN DWARFS IN OPEN CLUSTERS

A thesis submitted
for the degree of
Doctor of Philosophy

by
David J. Pinfield

Astronomy Group
Department of Physics and Astronomy
University of Leicester

February 1998

UMI Number: U531269

All rights reserved

INFORMATION TO ALL USERS

The quality of this reproduction is dependent upon the quality of the copy submitted.

In the unlikely event that the author did not send a complete manuscript and there are missing pages, these will be noted. Also, if material had to be removed, a note will indicate the deletion.



UMI U531269

Published by ProQuest LLC 2013. Copyright in the Dissertation held by the Author.
Microform Edition © ProQuest LLC.

All rights reserved. This work is protected against
unauthorized copying under Title 17, United States Code.



ProQuest LLC
789 East Eisenhower Parkway
P.O. Box 1346
Ann Arbor, MI 48106-1346

Abstract

David J. Pinfield

Low Mass Stars and Brown Dwarfs in Open Clusters

This thesis describes several open cluster searches for very low mass stars (VLM) and brown dwarfs (BD) ($M/M_{\odot} < 0.08$).

With recent developments in charged coupled devices, it has become possible to survey open clusters to well into the BD regime. The principal aim of this work is to employ these new instruments to conduct such open cluster surveys, to investigate the properties of VLM and BD populations.

The thesis begins with a short introduction, which describes the fundamental properties of brown dwarfs, relates research in this field to other areas of astronomy, and summarises the project aims and thesis structure. The second chapter gives a review of the current theoretical and observational status of the field, and the third chapter describes the principles and methods used to carry out the photometry presented in this thesis.

The results are presented in chapters (4), (5), (6) and (7). An RIZ survey of Praesepe produces a sample of 26 candidate VLM and BDs. K band photometric follow up of 11 of these highlights one as a binary system that almost certainly contains at least one brown dwarf. K photometry is still needed for the remaining 15. The RIZ survey also finds a possible steepening of Praesepe's mass function into the BD regime. The Praesepe infrared sequence compares very well with the latest non gray model predictions, and the binary fraction in Praesepe is found to be essentially the same as for The Pleiades.

A catalogue of Pleiades stars is used to model the cluster. King profiles are plotted for 4 mass bins and these profiles suggest that the cluster is relaxed. Virial analysis is then used to show that the cluster contains not more than $131M_{\odot}$ of dark matter (BDs) to add to the observed mass of $735M_{\odot}$.

Further deep surveys in The Pleiades, Praesepe and the Hyades result in 88 new Pleiades BD candidates, 141 Praesepe VLM candidates and 33 Hyades BD candidates. These new candidate lists, as well as finder charts are given in the appendices.

Chapter (8) summarises the results of the thesis, and discusses future work.

Acknowledgments

I would like to acknowledge the excellent supervision I have received during the course of this work from Richard Jameson. Richard has always been happy to explain things that I didn't understand, and has corrected my written work (and spelling !) very rapidly. I have also enjoyed our shared appreciation of alcohol, which has livened up my conference visits. I would also like to thank Simon Hodgkin for useful help and advice in my first year particularly.

I am very grateful to my parents, who have always encouraged and helped me with my pursuits.

While at Leicester I have enjoyed much time in the local pubs, in particular The Old Horse (my second home). I am indebted in particular to Graham Wynn, Steve Sembay and Paul Foulsham, for accompanying me to this establishment on no small number of occasions. Thanks also to Luciano and Martin, for the pasta and the point.

Many thanks also to Norma Corby and Ray McErlean.

I have also enjoyed the company of my other fellow Underpassians, as well as others from or connected to the university: Thanks to Matt, Richard W, Maruschka, Gillian, Ben, Jezza, Helen, Pete & Debs, Brendan & Barbs, Meoff, Geoff, John & Lisa, Gordon, Adam, Chris, James, Ewa, Rudolph, Gareth, Paul, Tim, Kevin and Richard T.

I also acknowledge Starlink and PPARC for facilities and my funding.

Contents

Abstract	ii
Acknowledgments	iii
1 Introduction	1
1.1 The Stellar limit	1
1.2 Missing mass	2
1.3 Theoretical test beds	2
1.4 Project aims	2
1.5 Thesis structure	3
2 A Review of the Theory and Observations	5
2.1 Introduction	5
2.2 Formation	5
2.3 Structural Modelling	6
2.3.1 The boundary conditions	7
2.3.2 Opacities	8
2.3.3 Convection	8
2.3.4 Evolution	9
2.3.5 Model results	9
2.4 Conversions to the observational plane	12
2.4.1 Recent T_{eff} scales and bolometric corrections	13
2.4.2 Comparisons	15
2.5 Luminosity and Mass Functions	18
2.5.1 In the field	20

2.5.2	In Open Clusters	20
2.6	Searching for Brown Dwarfs	22
2.6.1	Brown Dwarfs in binaries	22
2.6.2	Free Floating Brown Dwarfs	25
2.7	Conclusions	30
3	Photometry	31
3.1	Introduction	31
3.2	The Photometric scale	31
3.3	Magnitudes	32
3.4	Photometric calibration	33
3.5	Measuring fluxes	35
3.5.1	Optical Charged Coupled Devices	35
3.5.2	Infrared imaging cameras	36
3.5.3	Image reduction	37
3.5.4	Detection of sources	38
3.5.5	Aperture photometry	38
3.5.6	Errors	39
3.5.7	Aperture corrections	40
3.6	Filter Systems	42
3.6.1	Red – near infrared filters	42
3.6.2	Infrared filters	44
3.7	Conclusions	44
4	Praesepe: RIZ survey	46
4.1	Introduction	46
4.2	Praesepe: Observational review	47
4.3	Filters	48
4.4	The survey	50
4.4.1	Observations	50
4.4.2	Image reduction and photometry	52
4.4.3	Shape analysis	54

4.5	Photometric results	56
4.5.1	The photometric catalogue	56
4.5.2	The Praesepe sequence	57
4.5.3	Colour magnitude diagrams	58
4.5.4	Summary	60
4.6	Luminosity and Mass functions	61
4.6.1	The mass luminosity relation	61
4.6.2	Correction factors	61
4.6.3	The mass function	63
4.7	Discussion	64
4.8	White dwarfs	67
4.9	Conclusions	69
5	Praesepe: Infrared photometry	70
5.1	Introduction	70
5.2	Observations	71
5.2.1	The HSHJ Proper motion members	71
5.2.2	Photometry of RIZpr candidates	72
5.3	Cluster Membership	72
5.3.1	I K selection	74
5.3.2	J H K selection	74
5.4	Binaries	77
5.5	Object masses - Brown Dwarfs	79
5.6	Conclusions	83
6	The mass of the Pleiades	85
6.1	Introduction	86
6.2	The dynamics of star clusters	86
6.3	Cluster observations	88
6.4	The density distribution	88
6.4.1	Surface density	88
6.4.2	Space density	89

6.4.3	The tidal radius	90
6.5	The observed mass of the Pleiades	91
6.5.1	The Pleiades catalogue	91
6.5.2	Stellar masses	91
6.5.3	Binaries	93
6.5.4	The cluster centre	94
6.5.5	Cluster flattening	96
6.5.6	The Pleiades distribution	98
6.5.7	Deprojection	101
6.5.8	Pleiades time scales	102
6.6	The dynamical mass of the Pleiades	102
6.6.1	The Virial Theorem	102
6.7	Discussion	107
6.8	Conclusions	109
7	Burrell Schmidt surveys: Pleiades Praesepe & the Hyades	111
7.1	Introduction	111
7.2	The survey	112
7.3	Image reduction and photometry	114
7.4	Photometric results	115
7.5	Luminosity and Mass functions	120
7.6	Discussion	121
7.7	Conclusions	124
8	Conclusions and Future Work	126
8.1	Chapter (4) - RIZ Praesepe survey	126
8.2	Chapter (5) - Infrared photometry	127
8.3	Chapter (6) - The Mass of the Pleiades	129
8.4	Chapter (7) - The Burrell Schmidt surveys	130
8.5	Closing remarks and the future	132
A	Praesepe photometry	134
A.1	R I Z Praesepe VLM and BD candidates	135

A.2	U B V Praesepe white dwarf candidates	136
A.3	HSHJ star photometry	138
A.4	I Z Kitt Peak Praesepe candidates	141
B	Praesepe finder charts	146
B.1	R I Z Praesepe candidates	146
B.2	I Z Kitt Peak Praesepe candidates	149
C	Pleiades photometry	160
C.1	Kitt Peak candidate Pleiades brown dwarfs	161
D	Pleiades finder charts	165
D.1	I Z Kitt Peak Pleiades BD candidates	165
E	Hyades photometry	173
E.1	Kitt Peak candidate Hyades brown dwarfs	174
F	Hyades finder charts	176
F.1	I Z Kitt Peak Hyades BD candidates	176
G	Publication reprints	180
	References	195

List of Figures

2.1	BD evolution, from Nelson, Rappaport & Joss (1986).	10
2.2	Sets of model isochrones (100 Myrs) varying convection, opacities, metallicity and gray/non gray atmospheres.	11
2.3	Water vapour opacity verses wavelength for various temperatures. . .	14
2.4	R-I and I-K T_{eff} scales.	16
2.5	I band bolometric correction against T_{eff} and I-K.	17
2.6	Optical and infrared images of Gl229b.	23
2.7	The near infrared spectrum of Gl229b.	24
3.1	An example of an air mass curve.	34
3.2	An example of an aperture correction.	41
3.3	Filter pass bands for Cousins, RGO and KP filters.	43
3.4	Atmospheric transmission against wavelength.	45
4.1	CCD and Filter pass bands plotted with the spectrum of VB 10. . . .	49
4.2	Two colour diagram for calibration of Z photometry.	53
4.3	Shape analysis plot for RIZ survey objects.	55
4.4	The I verses R-I, and I verses I-Z colour magnitude diagrams for the RIZ survey.	59
4.5	Mass luminosity relation in Praesepe (0.9 Gyrs).	62
4.6	The Luminosity function for Praesepe.	65
4.7	The Mass function for Praesepe.	66
4.8	The U-B verses B-V two colour diagram for the Praesepe white dwarfs.	68
5.1	The (I_c , R_c-I_c) colour magnitude diagram of the HSHJ stars.	73

5.2	The (I, I-K) colour magnitude diagram of the HSHJ stars indicating non members.	75
5.3	The (J-H, H-K) two colour diagram of 54 HSHJ stars.	76
5.4	The (I, I-K) colour magnitude diagram of the HSHJ stars showing the binary line.	78
5.5	The (I, I-K) colour magnitude diagram for the RIZpr members, showing mass divisions.	80
5.6	The (I, I-K) colour magnitude diagram showing the tracks of a VLM and a BD as BD binary companions are added.	80
6.1	The Pleiades.	85
6.2	Strip counts profiles for the centre of the Pleiades.	95
6.3	Strip count profiles in galactic coordinates for higher and lower mass Pleiades stars.	97
6.4	Surface density and total star count profiles for the four mass bins making up the Pleiades.	100
6.5	Spatial density and mass profiles for the four mass bins making up the Pleiades.	101
6.6	$\langle \sigma^2 \rangle^{1/2}$ against $1/\sqrt{m}$ for the four mass bins making up the Pleiades.	104
6.7	The distribution of the largest possible unseen Pleiades brown dwarf population.	108
7.1	I, I-Z colour magnitude diagram of 5 square degrees of the Pleiades. .	116
7.2	I, I-Z colour magnitude diagram of 5 square degrees of Praesepe. . . .	118
7.3	I, I-Z colour magnitude diagram of 2 square degrees of the Hyades. .	119
7.4	The mass function of the Pleiades.	122
7.5	The mass function of Praesepe.	123
B.1	RIZpr finder charts 1-15	147
B.2	16-26	148
B.3	IZpr finder charts 1-15	150
B.4	16-30	151
B.5	31-45	152

B.6	46-60	153
B.7	61-75	154
B.8	76-90	155
B.9	91-105	156
B.10	106-120	157
B.11	121-135	158
B.12	136-141	159
D.1	IZpl finder charts 1-15	166
D.2	16-30	167
D.3	31-45	168
D.4	46-60	169
D.5	61-75	170
D.6	76-90	171
D.7	91-96	172
F.1	IZh finder charts 1-15	177
F.2	16-30	178
F.3	31-33	179

List of Tables

2.1	BD dark matter fraction with α	21
2.2	Brown dwarfs in the Pleiades	30
4.1	Praesepe parameters.	47
4.2	Survey Criteria.	52
4.3	Praesepe luminosity and mass function results	64
5.1	The masses of the RIZpr Praesepe members.	82
6.1	Pleiades Catalogue Sources	92
6.2	Mass bins for the Pleiades	98
6.3	Pleiades King fit results	99
6.4	Virial analysis results for the Pleiades	106
7.1	The Kitt Peak survey.	113
7.2	Cluster mass functions.	121

Chapter 1

Introduction

1.1 The Stellar limit

I will chose to define Very low mass stars (here after VLM) as stars with a mass less than $0.3M_{\odot}$, which is approximately the mass where the onset of complete interior convection occurs. These objects are known to numerically dominate the solar neighbourhood. As one progresses to lower and lower mass, there will eventually be a mass limit where the onset of degeneracy prevents the core ever reaching a high enough temperature to burn hydrogen to helium by nuclear fusion. This limit is referred to as the “stellar limit”. The value of the stellar limit depends on composition of the star, but is generally assumed to be near to $0.08M_{\odot}$. Above this limit one can have main sequence stars, but below it, there exist faint cool objects which shine only as a result of cooling. The possible existence of these objects was first discussed by Kumar (1963). The currently accepted nomenclature is that these objects are “Brown Dwarfs” (here after BDs). This name was first suggested by Tarter (1975), and out of a collection of other suggestions (see the review of Tarter (1986)) is the one that has been generally adopted. Planets are excluded from the definition of a BD by requiring that BDs form in the same way as stars, from the collapse of a gas cloud.

Reviews of the subject include Liebert & Probst (1987) and Stevenson (1991), while Allard *et al.* (1997) describes the current state of interior and atmosphere modelling of VLM and BDs.

1.2 Missing mass

It is well known from the rotation velocities of gas in our own Milky Way as well as in other spiral galaxies, that there exists a substantial amount of unseen dark matter in galaxies. For a review of the observed stellar luminosity function, see Bessell & Stringfellow (1993). This dark matter could be partly due to BDs, and the technique of gravitational micro-lensing has recently turned up some interesting results. Alcock (1993) and Aubourg (1993) found several possible detections in the halo, and the (EROS and MACHO)¹, groups have detected a substantial population of low mass objects in the halo, as well as a surprisingly large number of lensing events in the disk, some of which indicate lenses with planetary masses (Bennett 1997).

1.3 Theoretical test beds

Modern theoretical work on star formation makes various predictions concerning the possible existence of BDs, and the relative size of BD populations. Different formation scenarios make different predictions, and observations of actual BD populations would place constraints on which models are in general most applicable to the major regions of star formation (see Section 2.2).

Observations of any identified BDs can be compared to the predicted observational properties of interior and atmospheric models to help improve our understanding of the physics of degenerate bodies and the complexities of energy transport through the relatively low temperature BD atmospheres (see Section 2.3).

1.4 Project aims

In order to determine what form the true population of VLM and BDs takes, one really needs to search for free-floating objects, because to all intents and purposes this removes the problem of differentiating between large planets in orbit around a

¹EROS: Earth Resources Observation Systems, MACHO: MAssive Compact Halo Objects collaboration

primary, and BDs that have either been captured, or formed as a binary in their own right.

It is the aim of this work to try to further understand the nature of these objects, and the approaches taken to do this are summarised below.

- Continue the search for VLM and BDs in a variety of open clusters, as well as the Pleiades, using optical charged coupled devices that can go deeper than photographic plates, and thus hope to discover lower mass objects than was previously attainable.
- Carry out follow up infrared photometry on low mass members in open clusters other than the Pleiades, in an effort to understand the form of the lower main sequence in open clusters in general.
- Attempt to understand more about the structure and dynamical processes involved in open clusters by modelling the distribution of stars in the most heavily observed open cluster (the Pleiades), and use the results of this work to identify any indications of a large population of undiscovered BDs in this cluster.

1.5 Thesis structure

In chapter 2 I review the major theoretical work that has been carried out on VLM and BDs to date, and describe methods for converting the predictions of this theory to observable quantities, as well as reviewing the results of other BD searches. Chapter 3 then goes on to describe the basics of photometry, the instruments used, and the methods of data reduction, including techniques specifically suited to the search for faint sources. Chapter 4 then describes the results of a red and near infrared photometric search for BDs in the Praesepe open cluster, which turned up a collection of BD candidates, as well as producing a mass function that extends below the stellar limit. Chapter 5 then continues the study of Praesepe, with the results of infrared photometric follow up of a sample of proper motion members of the cluster, as well as a number of the fainter Praesepe candidate members from

the previous chapter. Many of these objects appear to be Praesepe members, and a binary sequence is seen. Chapter 6 describes the methods used in and the results of, the modelling of the Pleiades cluster. Chapter 7 then presents the results of a second deep photometric survey covering 5 square degrees in both the Pleiades and Praesepe open clusters, as well as 2 square degrees in the Hyades. A large number of BD candidates are presented. Finally, Chapter 8 discusses the overall conclusions of the work, and talks about future follow up work resulting from this thesis.

Chapter 2

A Review of the Theory and Observations

2.1 Introduction

This chapter will review the current theoretical work concerning VLM and BDs. To begin with, I will discuss current ideas on formation, and its relevance to stellar and BD populations. Next, I will describe the latest computer models used to predict the VLM and BD structure, as well as methods to transform these properties onto the observation plane. Finally, I will talk about recent observations concerning luminosity and mass functions, as well as searches for BDs.

2.2 Formation

Giant molecular clouds ($10^5 \leq M_{\text{cloud}}/M_{\odot} \leq 3 \times 10^6$, $R_{\text{cloud}} \sim 10\text{pc}$) are the principal sites of active star formation in our galaxy (Soloman, Sanders & Scoville 1979). Spatially resolved CO observations show that these clouds have sub-structure, and are composed of “clumps” ($10^3 \leq M_{\text{clump}}/M_{\odot} \leq 10^4$, $2 \leq R_{\text{clump}} \leq 5\text{pc}$, clump densities $n_{\text{H}_2} \sim 300\text{cm}^{-3}$, $T_{\text{clump}} \sim 10\text{K}$), from RowanRobinson (1979)). The formation of stars and BDs begins with the collapse and fragmentation of such clump cores. The mass of the resulting objects then comes from equation (2.1),

$$M \sim \dot{M} t_{\text{infall}} \tag{2.1}$$

where \dot{M} is the mass in-fall rate, and t_{infall} is the time over which in-fall takes place. Scenarios of clump collapse can essentially be split into two groups; “inside out” and “outside in” models.

For “inside out” models, the clump cores are thought to collapse after the loss of magnetic field support by ambipolar diffusion. \dot{M} is a function of the distribution of initial conditions, and t_{infall} is limited by the switching on of powerful stellar winds and outflows, preventing further infall. Adams & Fatuzzo (1996) take such an approach, and develop a semiempirical mass formula, which is a transform between the initial conditions, and the final masses of the stars and BDs formed. They conclude that BDs should be rare, because they can only form in regions with very low values of \dot{M} , where sufficiently small outflowing winds could halt the inflow early enough to produce $M/M_{\odot} < 0.08$.

“Outside in” collapse is initiated by the compression of the clump cores by shock waves from Supernovae. Such shock induced collapse can produce high initial mass accretion rates that decline rapidly to much lower values, thus producing a sufficiently small value of t_{infall} to create BDs easily. Boss (1995) calculates a minimum mass of $0.01M_{\odot}$ from such a formation mechanism.

2.3 Structural Modelling

Calculating the subsequent evolution of VLM and BDs requires numerical modelling of their interiors. This is done by integrating the basic equations of stellar structure. The equations comprise;

- The **hydrostatic equilibrium equation** relating pressure to radius.
- The **mass conservation equation**.
- The **energy equation** relating luminosity to radius, taking into consideration all forms of energy generation (D and Li burning, the p-p chain/CNO cycle for VLM, as well as gravitational energy generation).

- The **energy transport equations** relating temperature to radius, using the appropriate form of energy transport (convection for VLM and BDs) and opacities.

In order to calculate the luminosity, T_{eff} and radius for an object of a given mass, initial composition and age, the Henyey method is generally used (Henyey *et al.* 1959). In Brief, Henyey’s method involves choosing M_r (the mass inside a given shell) as the independent variable, and calculating pressure(M_r), temperature(M_r), luminosity(M_r), composition(M_r) and radius(M_r). A new independent variable ($\zeta(M_r)$) is then introduced such that small changes in M_r near the surface (where the pressure and temperature change rapidly) correspond to large changes in $\zeta(M_r)$. This facilitates the ability to replace the differential equations by difference equations, and thus solve a system of linear equations for the stellar parameters at all depth points in the star, using both the central and the surface boundary conditions simultaneously. As the VLM and BDs evolve, these parameters change, and by calculating the changes over sufficiently small time steps, the time independent model can be evolved.

2.3.1 The boundary conditions

The surface boundary conditions in the majority of models are calculated assuming that the atmospheres are in radiative equilibrium, using the Eddington approximation ($T^4(\tau) = \frac{3}{4}T_{\text{eff}}^4(\tau + \frac{2}{3})$), or some other $T(\tau)$ relation. However, for VLM and BDs the convection zone actually penetrates deeply into the optically thin outer most layers ($\tau \ll 1$) (Burrows *et al.* 1993), since these regions cover the temperature range $T_{\text{eff}} < 4000\text{K}$, which corresponds to H_2 dissociation and grain formation ($T_{\text{eff}} < 1700\text{K}$), producing a consequent decrease in the adiabatic temperature gradient (Baraffe *et al.* 1995). Therefore, such $T(\tau)$ relations are no longer valid, as the presence of convection has direct consequences on the atmospheric temperature stratification. A way to model such atmospheres is to solve the radiative transfer equations coupled with a model of convection. The boundary conditions for the interior Henyey integration are taken at about $\tau = 100$, and for a fixed mass and composition, there is only one atmosphere “temperature – density” profile (with a

given T_{eff} and g) which matches the interior profile (at $\tau = 100$). This determines the complete stellar model for this mass and composition, and is a method that has recently been implemented by Baraffe *et al.* (1995), Chabrier, Baraffe & Plez (1996) and Chabrier & Baraffe (1997).

2.3.2 Opacities

The use of accurate opacities is a very important ingredient when calculating the correct absorption coefficients. Near the surface of VLM and BDs the presence of molecules with millions of lines make the opacities very complicated. Prior to 1991, in general, the Los Alamos tables were used in conjunction with the low temperature opacities of Cox & Tabor (1976). Improvements came with Alexander, Augason & Johnson (1989) and Kurucz (1975) who included some molecules and grains as well as an updated treatment of water vapour. However, the opacity tables are still by no means complete as Allard *et al.* (1997) explain, and need to include better treatment particularly of TiO, H₂O and CH₄ (methane) molecules, as well as the presence of grains (their size distributions and growth time scales). Opacities can be treated as gray or non gray (wavelength independent/dependent respectively). Most models assume gray atmospheres, using a mean opacity for all wavelengths. However, molecular opacities have a steep dependence on wavelength, making the use of gray models inappropriate. The recent models that couple the inner structure with atmosphere models (mentioned in the previous section) employ non gray opacities, producing not only T_{eff} and L , but also magnitudes and colours, obtained directly from the synthetic spectra constructed from the model atmospheres.

2.3.3 Convection

Current descriptions of mixing length theory (MLT) are incomplete. Canuto & Mazzitelli (1991 and 1992, CM here after) attempted to improve on the theory by taking the full spectrum of convective turbulent eddies into account, however neither compressibility (the presence of sound waves), or inhomogeneities were included.

2.3.4 Evolution

Figure (2.1) shows the evolution of luminosity, T_{eff} , T_c and radius for VLM and BDs from $0.10 - 0.01M_{\odot}$, (taken from Nelson, Rappaport & Joss (1986)). The models begin at an age of 1 Myr. Prior to this, the objects had been contracting under gravity, and moving down their Hayashi tracks. They then arrive on the “deuterium main sequence”, and burn the small amount of deuterium in their cores. This period lasts for anywhere between $\sim 3\text{Myrs} - \sim 10\text{Myrs}$ ($0.10 - 0.01M_{\odot}$ respectively). This internal energy source supports the star against collapse temporarily, and maintains constant luminosity and radius.

Once the supply of deuterium is burnt the objects contract again, their central densities and temperatures (T_c) increasing. At an age of approximately 0.5 Gyrs, the $0.10M_{\odot}$ VLM attains a sufficiently high T_c to burn Hydrogen via p-p chain reactions ($T_{\text{min}}(\text{Hburning})$ in Figure (2.1)). These VLM are thus able to reach hydrostatic equilibrium, and maintain constant luminosity, T_{eff} and radius during their main sequence lifetime.

However, for objects with $M \leq 0.08M_{\odot}$ (the BDs), electron degeneracy plays an important role. As the density in the core rises, the electron fermi energy becomes greater than their average thermal energy ($3/2 kT$), producing a degenerate electron gas. Internal pressure is then supplied by these degenerate electrons, and the BDs once again stabilise. The BDs then radiate thermally at approximately constant radius, cooling down and thus becoming fainter. It is worth noting that degeneracy switches on sooner for the lowest mass BDs (due to their lower T_c), and therefore after $\sim 1\text{Gyr}$ the lowest mass BDs are the largest. However, all BDs older than 100 Myrs have radii within $\sim 25\%$ of that of Jupiter.

2.3.5 Model results

In order to summarise current structural models, Figure (2.2) shows several sets of isochrones, all of which are for an age of 100 Myrs.

The first shows how new ideas in convection change the predictions of MLT (D’Antona & Mazzitelli 1994). The CM isochrone is a little hotter than that of MLT, but the difference is very small, and essentially negligible in the BD range.

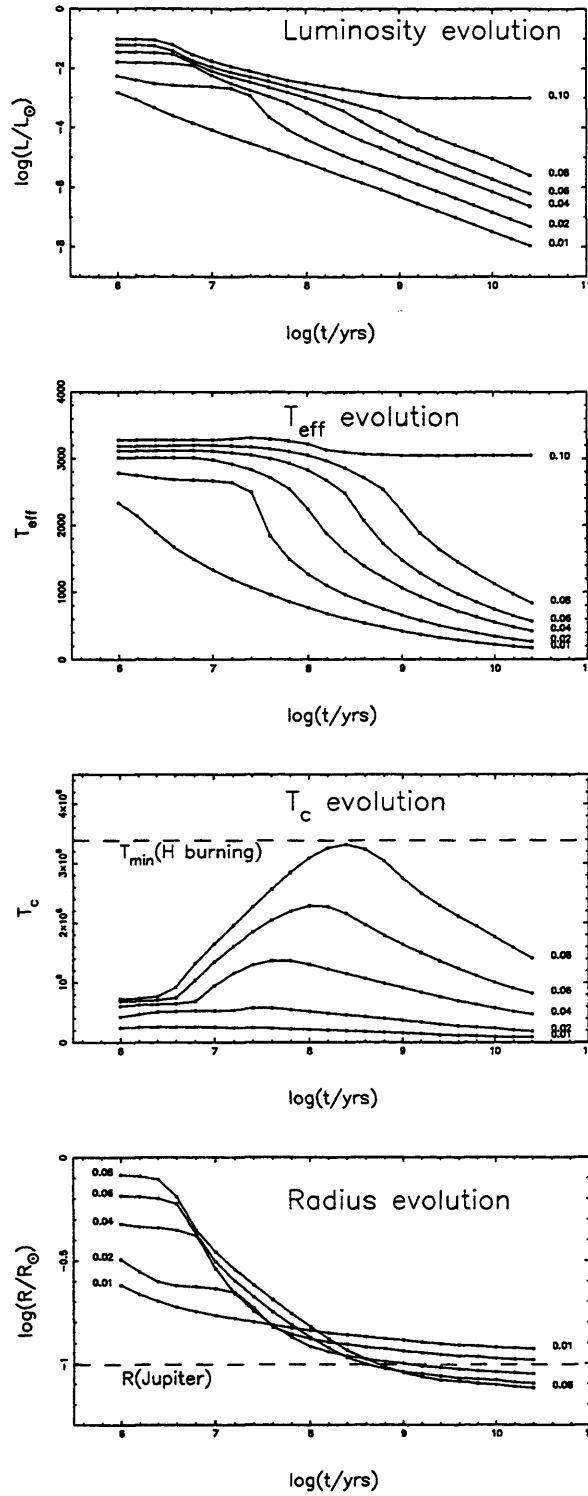


Figure 2.1: The evolution of Brown Dwarf luminosity, effective temperatures, central temperatures and radii, as a function of time. (Nelson, Rappaport & Joss 1986).

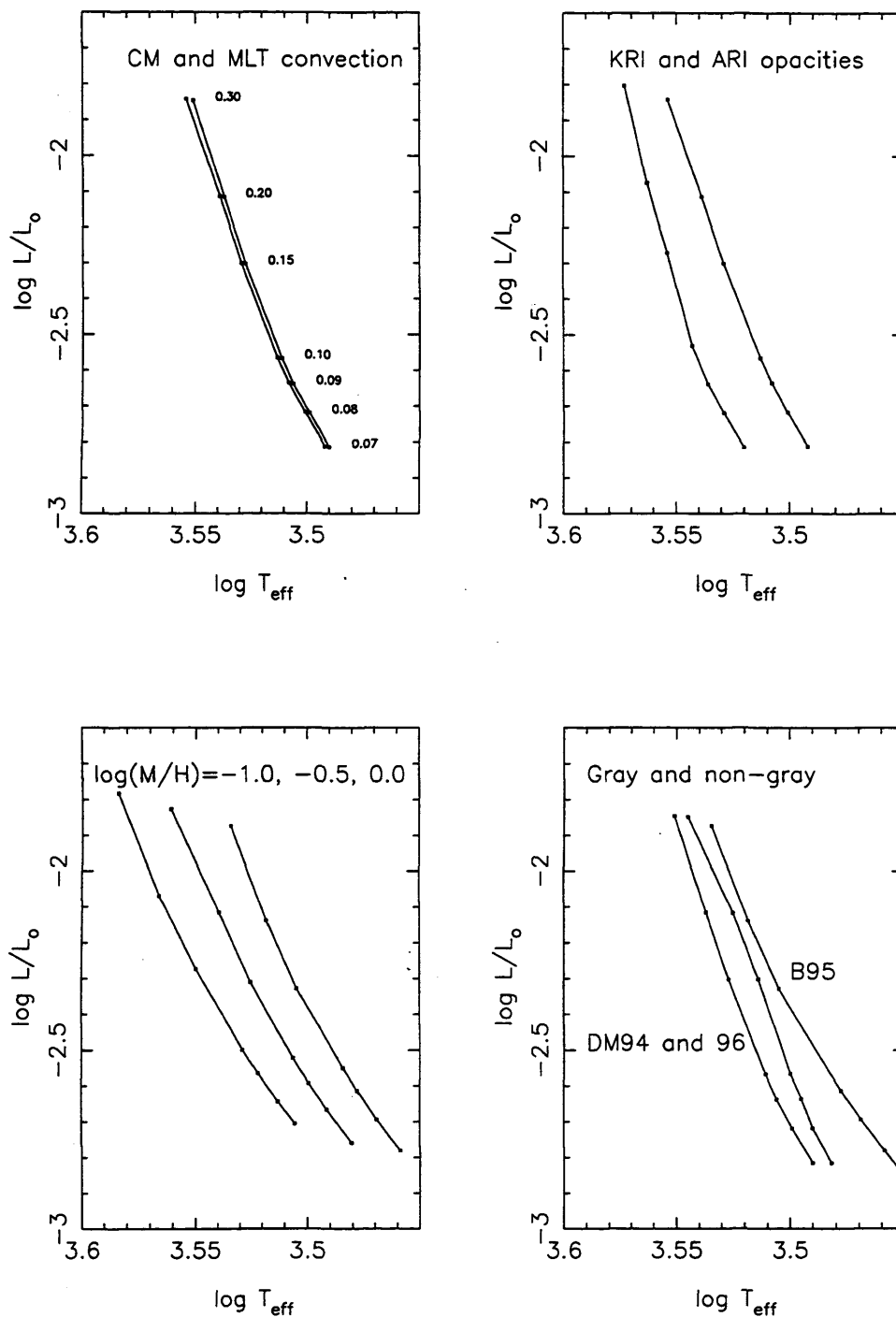


Figure 2.2: Sets of model isochrones for an age of 100 Myrs. The first plot shows the effects of different treatments of convection. The second shows how different opacity tables effect the isochrones. The third plot shows isochrones for different metallicity, and the final plot shows isochrones from models that assume gray and non gray atmospheres.

The second plot shows two isochrones from D'Antona & Mazzitelli (1994), but using different opacity tables. Both isochrones employ Rogers and Iglesias (RI) opacities for $T \geq 6000\text{K}$, but with Kurucz and Alexander opacities being used for lower temperatures, labeled KRI and ARI respectively. KRI opacities are on average somewhat larger than ARI, and there is considerable spread between the two isochrones.

Next, I have plotted a set of isochrones to demonstrate the effect of metallicity. The coolest isochrone is for solar metallicity, with isochrones of $\log(\frac{M}{H})$ of -0.5 and -1.0 (Baraffe priv. com) moving to hotter T_{eff} and brighter luminosity, as the fraction of heavier elements decreases.

The final plot comprises two gray-model isochrones from D'Antona & Mazzitelli (1994) and D'Antona 96 (priv. com), and the latest non-gray model isochrone of Chabrier, Baraffe & Plez (1996)(CBP96). It is clear that the most important difference between the two sets of isochrones is that the gray atmosphere models are hotter than the non-gray model, and particularly for $\log T_{\text{eff}} < 3.58$. Kroupa & Tout (1997) note this, and conclude that although both non-gray and gray models agree well with observed luminosities, only the non-gray isochrones agree well with T_{eff} as well.

To summarise, it is clear that the use of non-gray atmospheres is an improvement on gray atmosphere models. However theoretical spectra still differ somewhat with observed spectra, due to an incomplete treatment of opacities. For a review of the current model atmospheres see Allard *et al.* (1997).

2.4 Conversions to the observational plane

When using gray atmosphere models, the observable properties calculated are T_{eff} and luminosity. In order to convert these properties to photometric magnitudes and colours, T_{eff} scales and bolometric corrections are required. Such conversions are calculated by deriving T_{eff} and luminosities (by various means) for stars with observed colours and magnitudes. I shall summarise a collection of five of the most recent attempts, as well as showing the purely synthetic results from the non-gray atmosphere models used by CBP96. These five are, Bessell (1991)(B91), Berriman,

Reid & Leggett (1992)(BRL92), Kirkpatrick *et al.* (1993)(KKRLAW93), Jones *et al.* (1994)(JLJM94) and Leggett *et al.* (1996)(LABDH96).

2.4.1 Recent T_{eff} scales and bolometric corrections

The T_{eff} values of Bessell (1991) were derived by fitting black body distributions to broad band fluxes. Bolometric magnitudes were derived using photometric (B - L') data to define an energy curve, integrating under the curve, adding a Rayleigh-Jeans correction term ($\text{Flux} \propto T_{\text{eff}} \lambda^{-4}$) beyond 3.8 microns, and defining a bolometric zero point from the sun ($M_{\text{bol}}=4.75$, $L_{\odot} = 3.86 \times 10^{33} \text{ ergs s}^{-1}$).

Berriman, Reid & Leggett (1992) match the flux under a black body anchored at K(2.2 microns) to the total bolometric observed flux, which is integrated under both spectroscopic and photometric (U - M) data. This method assumes that the flux at K is black body (i.e. continuum) flux.

Kirkpatrick *et al.* (1993) used the theoretical atmosphere models of Allard (1990) to obtain T_{eff} from spectroscopic fits of M dwarfs. In the red (0.7 - 0.9 microns) region, spectral fits were made for the TiO and VO absorption features, while in the infrared (1.08 - 1.35 microns) region the pseudo-continuum and the H₂O feature at 1.35 microns were fit. The bolometric magnitudes calculated here were based on a linear interpolation of the results of Bessell (1991).

Jones *et al.* (1994) uses the strength of the H₂O absorption bands beyond 1.34 microns for M dwarfs of known distance, cooler than 3500K. Allard's models (Allard 1990) show that H₂O opacity dominates over its nearest rival (H⁻) between 1 and 2.5 microns, and therefore in this range, the total opacity will be well represented by H₂O alone. The oscillatory nature of the water vapour opacity is shown in Figure (2.3), for temperatures ranging from 1500K-3000K. In this temperature range, a number of wavelengths can be chosen with the same opacity. Therefore, at these wavelengths, radiation from an H₂O opacity dominated spectral region will be coming from the same depth in the star, and can thus be fit with a black body. The procedure followed by Jones *et al.* (1994) is outlined below.

- An initial estimate of temperature (T) is made (say 2500K), and a set of wavelengths with equal opacity for this temperature are selected.

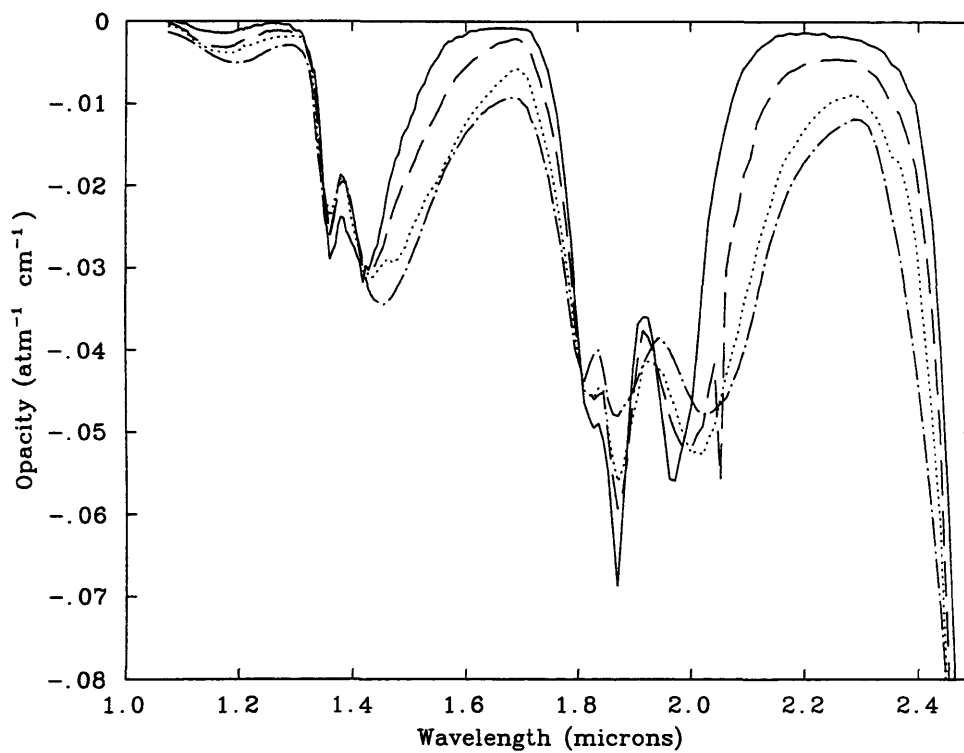


Figure 2.3: Laboratory data for water vapour opacity against wavelength (from Ludwig (1971)) for 1500K, 2000K, 2500K and 3000K (solid, dashed, dotted and dot-dashed lines respectively).

- A new value of T is obtained from a black body fit at these wavelengths. A new set of equal opacity wavelengths is then selected appropriate to this new T . This procedure is iterated until the value of T converges.
- The final value of T will be the temperature at the depth of the emitting region (corresponding to the points of equal opacity). Since the depth of this region is insignificant compared to the radius of the star, the angular diameter of the star $\frac{R}{d}$ can be calculated using equation (2.2), where f_λ is the flux at one of the constant opacity wavelengths, and F_λ is the Planck function.

$$f_\lambda = \left\{ \frac{R}{d} \right\}^2 F_\lambda(T) \quad (2.2)$$

- The bolometric flux (F_{bol}) is then calculated using available photometry and spectroscopy (with synthetic spectra used to fill in the gap long of 2.5 microns)
- T_{eff} can then be found from the bolometric flux and the angular diameter using equation (2.3).

$$\sigma T_{eff}^4 = \left\{ \frac{d}{R} \right\}^2 F_{bol} \quad (2.3)$$

M_{bol} can simply be found using the known distance to the star and F_{bol} .

Leggett *et al.* (1996) use a more up to date atmosphere model (Allard & Hauschildt 1995) than Kirkpatrick *et al.* (1993) to obtain T_{eff} s. This model contains many more important opacity sources, and resulted in discrepancies between observed and synthetic spectra of only about 10% - a distinct improvement on Kirkpatrick's fits. Bolometric fluxes were found using photometry (B - I) and infrared spectra, and M_{bol} was then obtained from the known distances of the stars.

2.4.2 Comparisons

Figure (2.4) shows the five R-I and I-K T_{eff} scales just discussed, as well as the I-K T_{eff} scale resulting from the non-gray atmosphere models employed by CBP96. The results all agree fairly well at the hotter end of the scale. However, the results of KKRLAW93 and B91 are somewhat hotter than the others below 3000K in both R-I and I-K. This is presumably because B91 assumed black body distributions, which are inappropriate for the spectra of these late M dwarfs, and KKRLAW93

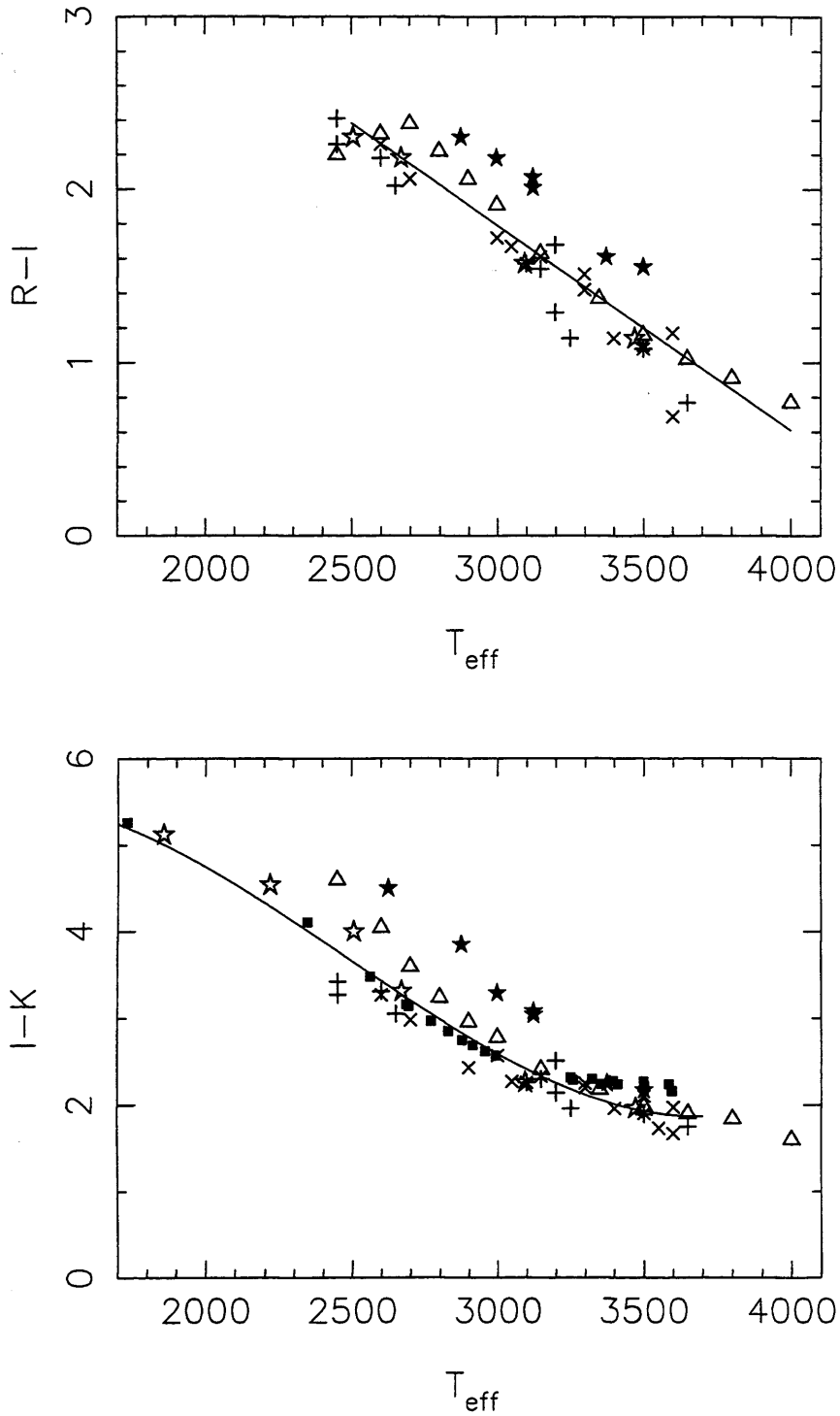


Figure 2.4: R-I and I-K T_{eff} scales from B91(triangles), BRL92(plus signs), KKR-LAW93(filled stars), JLJM94(open stars), LABDH96(crosses) and CBP96(squares).

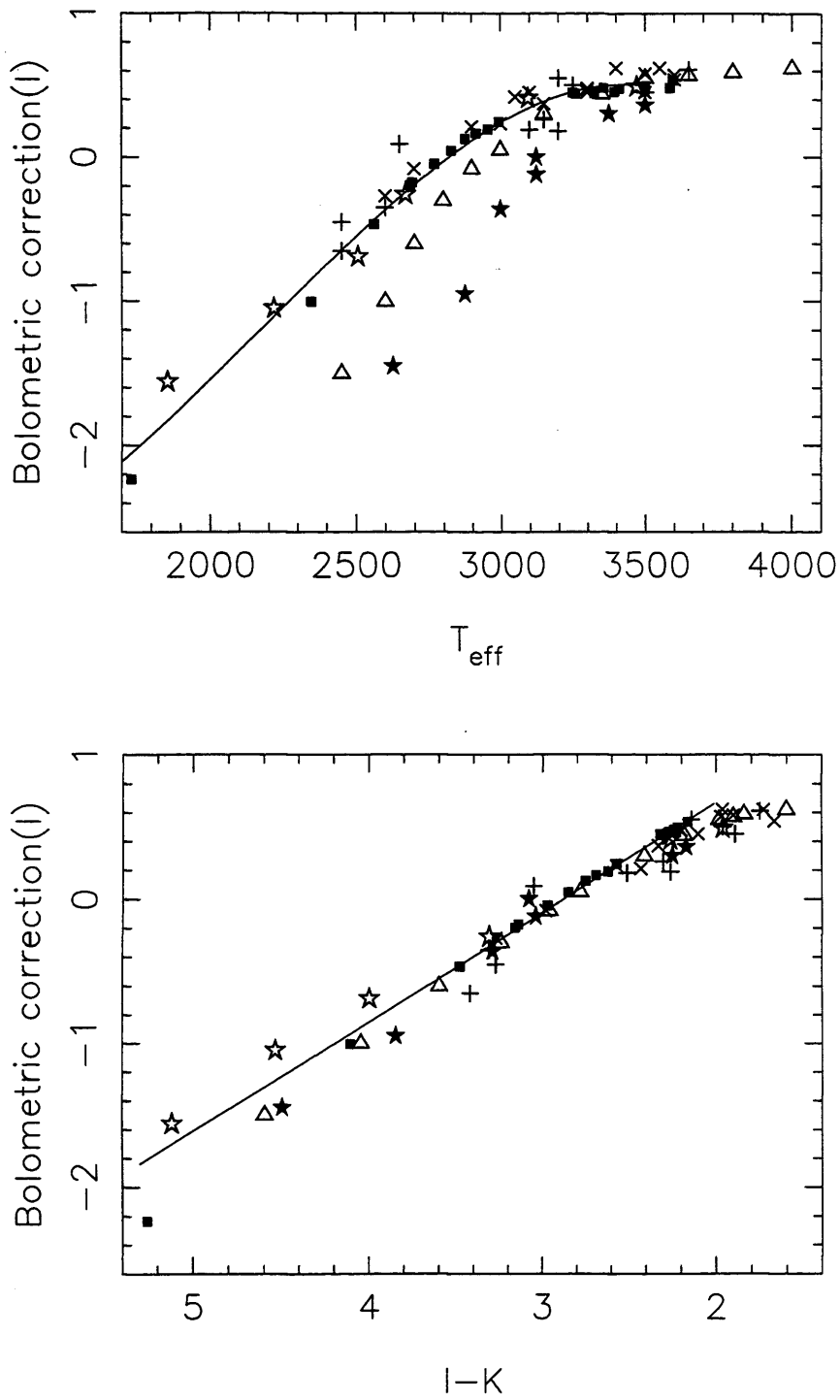


Figure 2.5: I band bolometric correction against T_{eff} and $I-K$. symbols are as in Figure (2.4).

was using a relatively basic atmosphere model, that had been greatly improved upon by the time LABDH96 calculated there values, which are in reasonably good agreement with BRL92, JLJM94 and CBP96. Only CBP96 and JLJM94 extend below $\sim 2500K$, but the agreement between them is encouraging. I have therefore calculated a best-fit polynomial for each of the T_{eff} scales, using the results of BRL, JLJM94, LABDH96 and CBP96. The polynomials are over-plotted in Figure (2.4), and given in equations (2.4) and (2.5).

$$(R - I) = (-1.183 \times 10^{-3})T_{\text{eff}} + 5.34 \quad (2.4)$$

for $(2500K \leq T_{\text{eff}} \leq 4000K)$

$$(I - K) = (5.2273 \times 10^{-10})T_{\text{eff}}^3 - (3.8873 \times 10^{-6})T_{\text{eff}}^2 + (7.3493 \times 10^{-3})T_{\text{eff}} + 1.415 \quad (2.5)$$

for $(1700K \leq T_{\text{eff}} \leq 3700K)$

Figure (2.5) shows the same authors' I band bolometric corrections against T_{eff} and (I-K). Once again, B91 and KKRLAW93 fall to the hotter side of the others when plotted against T_{eff} , however all the authors seem to be in reasonable agreement when plotted against I-K. Since I-K is an observed quantity, it is clear that the agreement is genuine, and that inconsistencies only arise when T_{eff} (a derived quantity) is introduced. Thus, polynomial fits for the I band bolometric corrections as a function of T_{eff} were found, using BRL, JLJM94, LABDH96 and CBP96, and using all the data for the I-K function. The polynomials are once again over-plotted in the figures, and are given in equations (2.6) and (2.7).

$$BC_I = (-4.284 \times 10^{-10})T_{\text{eff}}^3 + (2.797 \times 10^{-6})T_{\text{eff}}^2 - (4.06 \times 10^{-3})T_{\text{eff}} - 1.19 \quad (2.6)$$

for $(1700K \leq T_{\text{eff}} \leq 3500K)$

$$BC_I = (-0.759)(I - K) + 2.18 \quad (2.7)$$

for $(2.0 \leq I - K \leq 5.3)$

2.5 Luminosity and Mass Functions

The luminosity function (LF) of a stellar population is defined as the number of stars per unit magnitude interval. It is often expressed as the number of stars per

unit M_v per cubic parsec. For cool VLM and BDs, it is better to use M_R , M_I , or even M_{bol} . It should also be noted that the volume of 1 parsec cubed is used for field luminosity functions. When looking at open clusters however, one would need to use the entire cluster as the volume, and thus produce a cluster LF. This often involves calculating a LF for the centre of the cluster (where it is observed, using proper motion and photometry), and employing a correction term (see later) so as to represent the whole cluster.

The mass function (MF) of a stellar population is defined as the number of stars per unit mass interval. The MF can be determined from the LF and a mass-luminosity relation, as shown in equation (2.8),

$$N(m) = LF_\lambda \frac{dM_\lambda}{dm} \quad (2.8)$$

where $N(m)$ is the MF, and $\frac{dM_\lambda}{dm}$ is the derivative of the mass-luminosity relation. The MF is usually talked about in terms of a power law. There are two power laws that are commonly used. These are shown in equation (2.9).

$$\begin{aligned} N &= k_1 m^{-\alpha_1} \\ \frac{dN}{dm} &= k_2 m^{-\alpha_2} \\ (\alpha_2 &= \alpha_1 + 1) \end{aligned} \quad (2.9)$$

If $\alpha_1 = 1$ ($\alpha_2 = 2$) then lower and higher mass stars contribute equally to the overall mass ($N(m)m = \text{constant}$). For $\alpha_1 > 1$ the lower mass stars begin to dominate. When one plots N in $\log N \log m$ space a line of gradient $(d \log N / d \log m) = -\alpha_1$ is produced. This is a convenient way to represent the mass function, and therefore from now on, I shall drop the subscript, but will be implicitly referring to α_1 .

For lower mass stars, the stellar structure changes significantly, as stars become fully convective, and hydrogen associates to H_2 in the outer layers (Kroupa & Tout 1997). Points of inflection in the mass-luminosity relation exist because of the effects of H^- , H_2 and of other molecules on the opacity and the equation of state, and the results of the first two of these are a flattening and a maxima in the LF at $M_v = 7$ and $M_v = 12$ respectively (Kroupa, Tout & Gilmore 1990).

2.5.1 In the field

There are a number of important considerations when constructing field LFs. Firstly, intrinsically brighter stars can be seen at greater distances in a flux limited sample. Since the LF is a number density, the relative volumes for each class of star must be accounted for. A more subtle effect is known as the “Malmquist bias”, which is caused by stars scattering into and out of any magnitude range because of photometric errors. This scatter becomes significant near the flux limit of the sample, and a correction must be made for all magnitudes. Other considerations include a vertical density gradient (in the galactic disk) and the fraction of un-resolved binaries, which increases with distance. There have been numerous attempts to measure the MF in the field. For ($0.4 \leq M/M_{\odot} \leq 10$), Salpeter (1955) found a power law relation for the MF of $\alpha = 2.35$. Field LFs extending to lower masses have been produced by Reid (1987) and Hawkins & Bessell (1988), while Laughlin & Bodenheimer (1993), Kirkpatrick *et al.* (1994) and Mera, Chabrier & Baraffe (1996) calculate MFs down to near the stellar limit.

2.5.2 In Open Clusters

LFs and MFs can be constructed for open clusters also, and assuming no evolutionary loss of cluster stars, should be as significant as those of the field. The construction of such LFs encounters less problems than for field LFs. The cluster stars are essentially all at the same distance, so there is no need to correct for the volume effects, the disk density gradient will not affect the cluster stars, and the binary problem (although still there) will be the same for all stars.

In Praesepe, Jones & Cudworth (1983) obtained proper motions as deep as $m_v = 17$ and calculated an LF assuming an exponential cluster distribution. Mermilliod *et al.* (1990) followed up proper motion members of Artjikhina (1966), and presented an uncorrected LF for the central square degree of the cluster. Jones & Stauffer (1991) obtained proper motions down to $m_v = 18$, once again calculating his LF assuming an exponential cluster distribution. Hambly *et al.* (1995b) obtained proper motions down to $m_I = 17.5$, and followed the method of Jones & Stauffer (1991) to obtain an LF. He then calculated an MF and found it to be rising with $\alpha = 1.3$

down to about $0.1M_{\odot}$. Also, Williams, Rieke & Stauffer (1995) covered 290 square arc-minutes down to $m_v = 23$ (\sim the BD limit) and found a similar MF to the field.

In the Pleiades, Hambly, Hawkins & Jameson (1991) calculated the LF down to $m_I = 17.5$, with no correction for the cluster extent, and calculated an MF that was consistent with the field MF. Stauffer *et al.* (1991) constructed an LF down to $m_v = 18$, by assuming distributions for the new stars similar to those defined by previously identified members. Also, Simons & Becklin (1992) suggest that the MF has $\alpha = 2.8$ in to the BD range, using I and K photometry down to $I \sim 20$.

The earliest deep survey of the Hyades cluster was carried out by Leggett & Hawkins (1988). This was followed by Leggett, Harris & Dahn (1994), who updated this work with new V and I photometry, incorporating the proper motion surveys of Reid (1992 and 1993) and Bryja *et al.* (1992 and 1994). She found the expected peak at $M_v = 12$, and a value of α in the range $0 - 1$ for the low mass stars.

In summary, the field MF has an α of 2.35 from $10 - 0.4M_{\odot}$, which changes to 1.5 for $0.4 - 0.1M_{\odot}$. Cluster MFs from $0.4 - 0.1M_{\odot}$ have been found to be consistent with, or close to that of the field. The value of α in the BD range has important ramifications for dark matter. In a recent review talk, Hambly (1997) gives Table (2.1), indicating the fraction of matter in the form of BDs for different values of α .

α	Fraction of BD matter
0.5	1%
1.5	12%
2.5	48%
3.5	99%

Table 2.1: BD dark matter fraction with α

2.6 Searching for Brown Dwarfs

2.6.1 Brown Dwarfs in binaries

I shall start by describing the recent exciting discovery of Gl229b (Nakajima *et al.* 1995), which is the first bona fide BD discovered outside the Pleiades, and potentially the lowest mass BD yet discovered. The method employed was to use both optical and infrared corona-graphic imaging (blocking out light from the primary using a cryogenically cooled occulting disk) of a sample of about 200 stars with either small space motion or active coronae, both of which indicate youth. The optical and infrared images obtained are shown in Figure (2.6), where the R-band, I-band, Z-band and K_s -band images are top left, top right, bottom left and bottom right respectively. The triangular support for the cooled occulting disk can be seen in the K_s -band image. Gl229b has been followed up spectroscopically in the infrared, by Oppenheimer *et al.* (1995) and Geballe *et al.* (1996). Allard *et al.* (1996) fits her non-gray models to Gl229b, calculating upper limits of 1000K for the T_{eff} and $0.065M_{\odot}$ for the mass (for the unlikely age of 10Gyrs), with a more likely solution being between 0.04 - $0.055M_{\odot}$. The infrared spectrum of Gl229b is shown in Figure (2.7), and shows very strong methane absorption. In fact most of the flux is concentrated in three large peaks, one at about 1 micron, and the other two in the J and H bands (1.2 and 1.6 microns respectively). It is apparent that these spectral signatures could be employed both spectroscopically and photometrically (with the correct choice of filters) in future searches for such low T_{eff} BDs.

Spectroscopic radial velocity surveys are proving very productive also. The search for “Extra Solar Planets” has turned up many very interesting objects using extremely high doppler-resolution ($\sim 3\text{ms}^{-1}$) long term searches (with the use of an iodine absorption cell providing a multitude of calibration lines). Some of the objects found are of Jupiter mass, while others are several times more massive, and may be BDs (Butler & Marcy (1996) finds that “47 Ursa Majoris b” has $M \leq 4.8M_J$, and Marcy & Butler (1996) calculates $M \leq 15M_J$ for “70 Virginis b”).

Several searches have been carried out using infrared imaging of field stars, where

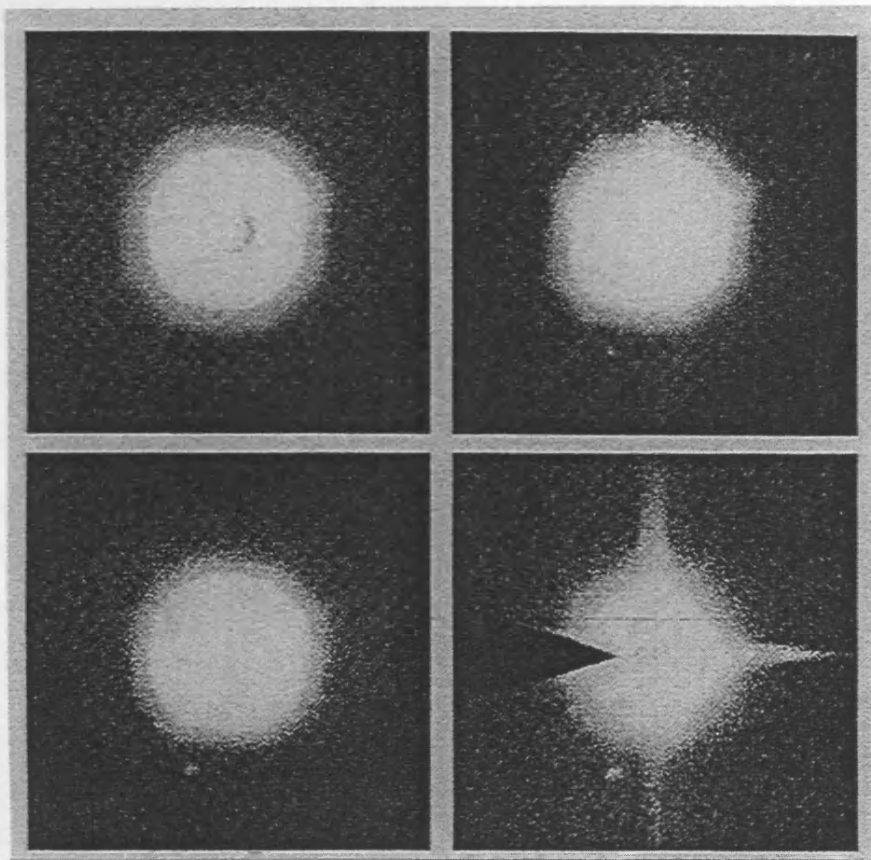


Figure 2.6: Optical and infrared images of Gl229b. Top left; R-band image; top right, I-band image; bottom left, Z-band image; bottom right, K_s -band image. Gl229b is 7.6 arc-seconds from the primary. The triangular support to the occulting disk can be seen in the K_s -band image.

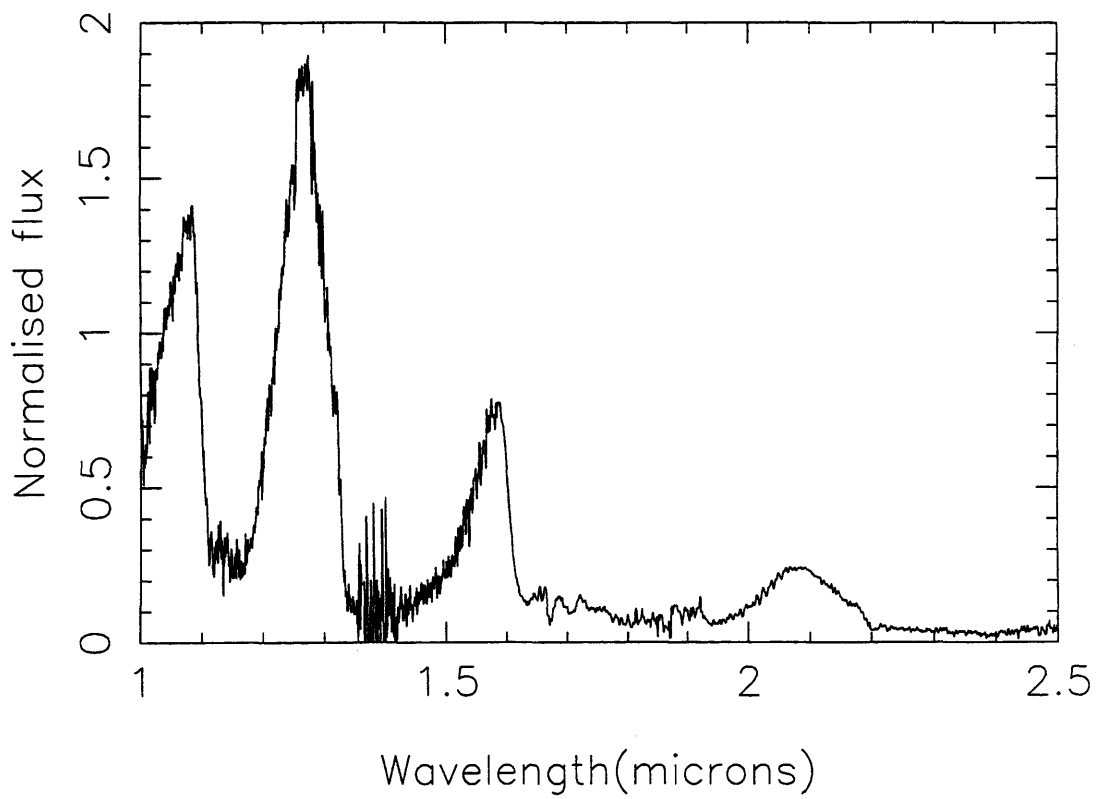


Figure 2.7: The near infrared spectrum of Gl229b from Geballe *et al.* (1996). The dominant source of opacity is methane.

any BD companions would be brightest (Jameson, Sherrington & Giles (1983), Skrutskie, Forrest & Shure (1989), and Rieke & Rieke (1990)), however no BDs were found. Using white dwarfs as the target primaries was first tried (unsuccessfully) by Probst & Liebert (1983), who realised that the lower infrared (J, H and K) flux from a white dwarf (hotter, but considerably smaller than main sequence stars) would improve the chances of success. Zuckerman & Becklin (1988) and Zuckerman & Becklin (1992) continued this search, and found two objects. Initially the object G29-38 was thought to have an unresolved BD companion, however this looked less credible as 10 micron observations by Graham *et al.* (1990a and 1990b) showed an excess more suggestive of a dust shell. The second object found was a resolved companion (120AU from the primary) to the white dwarf GD165. GD165b was observed spectroscopically by Kirkpatrick, Henry & Liebert (1993) in the red-infrared and by Jones *et al.* (1994) in the infrared (who calculates $T_{\text{eff}} = 1860 \pm 160\text{K}$ and $L = 8.6 \times 10^{-5}L_{\odot}$). The spectrum of GD165b was unlike that of M dwarfs in the visible, possibly containing new previously unidentified molecules, but followed the M dwarf sequence quite well in the infrared. It is possible that spill over light from the white dwarf interferes in the visible (Kirkpatrick 1997). The cooling age of GD165 is 600Myrs, which gives a mass for GD165b of 0.058 - 0.078 M_{\odot} (from its luminosity). This is then, potentially a BD.

Previous searches using astrometric techniques or speckle interferometry had been unsuccessful, with all the potential BDs being refuted. Marcy, Basri & Graham (1994) reviews these results, and concludes that they have no bona fide BDs. However future plans described by Paresce (1997) indicate that there may be considerable improvement in this area in the near future.

2.6.2 Free Floating Brown Dwarfs

The Lithium test

Verification of a BD requires a demonstration that hydrogen burning does not occur in an object's core. Lithium is a relatively fragile element, and burns at $2.5 \times 10^6\text{K}$ (to 2 He), which is lower than the ignition temperature of hydrogen. Therefore, the retention of Lithium in a fully convective star that has had time to become well mixed

(a few Myrs) will indicate a lack of hydrogen burning, and hence the BD status of an object (Rebolo, Martin & Magazzu 1992). Lithium can be detected by locating the resonance line at 6708\AA (which is strictly speaking, a very close doublet). Lithium should always be present for BDs with $M/M_{\odot} < 0.065$, but is also expected in young more massive BDs, such as those in the Pleiades. The lithium test is an important tool and has been used on a number of free floating Pleiades BD candidates, which will be mentioned presently.

Brown Dwarfs in the field

Searching for BDs in the field has its draw backs. The ages of field objects cannot be determined directly, and have to be inferred from their space motions (high = old), rotation rates and surface activity (high = young). This is an important point, because as was seen earlier the properties of BDs evolve considerably with time. In short, what you may think is a relatively young BD could be nothing more than an older main sequence M dwarf. The most promising BD candidates are the following; Jones, Miller & Glazebrook (1994) found several candidates at J, H and K. They estimated a mass for one of them of $0.071\text{-}0.079M_{\odot}$ assuming an intermediate age, but this object was later shown to be a distant compact galaxy (Becklin, Macintosh & Zuckerman 1995). Hawkins (1994) found many red candidates by digitally stacking ~ 60 Schmidt plates. Thackrah, Jones & Hawkins (1997) reported the first field BD candidate to have lithium detected in it, and inferred a T_{eff} of 2800K and a mass of $0.065 \pm 0.025M_{\odot}$.

Two projects are currently in progress that should find many more cool VLM and BDs in the field.

DENIS, the Deep Near Infrared Survey of the Southern Sky commenced in late 1993 and was a 4 year project. It is based at The European Southern Observatory 1m telescope on La Silla (Chile), and surveys the entire southern sky in the I, J and K' bands. The sensitivity limits will be 18.0, 16.0 and 14.5 magnitudes respectively, with an angular resolution of 1 arcsecond in I, and 3.0 arcseconds in J and K' (Epchtein 1994).

2MASS, the Two Micron All Sky Survey commenced in early 1997, and is also a 4

year project. It is based at Mt. Hopkins (Arizona U.S.A.) and Cerro Tololo (Chile), and uses 1.3m telescopes constructed specifically for the program. It plans to survey the entire sky in the J, H and K_s bands. The sensitivity limits will be 15.8, 15.1, and 14.3 magnitudes respectively, producing a point source catalogue with positions accurate to <0.5 arcseconds, an extended source catalogue, and an image database of co-added survey FITS images with 1 arcsecond pixels (Skrutskie *et al.* 1995).

One recently reported 2MASS discovery is the coolest isolated M Dwarf found to date (Kirkpatrick, Beichman & Skrutskie 1997).

Brown Dwarfs in open clusters

Knowledge of the age of a stellar (and of course any non-stellar) cluster population is vital when trying to determine the mass of potential BDs. In this respect, searching for BDs in open clusters has several advantages over searching in the field, because:

- The composition of cluster stars can be determined, and should be the same irrespective of mass.
- The distance to the cluster can be found, from main sequence fitting for example
- Any extinction to the cluster can be found and corrected for.

The age of clusters can thus be calculated with respect to the zero age main sequence by comparing the observed values of time sensitive quantities to those predicted by evolutionary models. One such method is to fit the upper main sequence turn off point to find the best-fit model isochrone. Since the pre-main sequence life times are much shorter than the main sequence life times, old clusters can be assumed to be effectively coeval, however, for very young clusters a non negligible dispersion in arrival time on the main sequence ($\sim 10^7$ yrs, cf. Larson (1972)) could cause problems with this approach.

When looking in young clusters, an added bonus is that not only will the observed quantities (L and T_{eff}) mean something in terms of mass, but they will also be more easily measured in the optical and near infrared, since BDs are brighter and hotter when young ($T_{\text{eff}} \sim 3000\text{K}$, $\log L/L_{\odot} \sim -4$).

It is clear then, that if cluster membership is established for an object, these advantages are applicable, and can be used to calculate a reliable mass. Cluster membership can be established using a number of techniques. These are:

- Proper motion surveys can be used to find objects with the same apparent motion through the sky as the cluster.
- Photometry and low resolution spectroscopy can be employed to identify objects that are consistent with BDs at the distance of the cluster.
- High resolution spectroscopy can provide radial velocities for candidates that should be consistent with the cluster. – This involves rejecting high velocity objects as being inconsistent with the bulk motion of the cluster.
- For sufficiently young clusters, H_{α} should be present, indicating active chromospheric activity.

The three most popular open clusters are the Pleiades, Praesepe and the Hyades. The Hyades is the closest (~ 48 pc), but has a large depth to distance ratio. Schmidt plate proper motion surveys have been carried out by Leggett & Hawkins (1988 and 1989), Bryja *et al.* (1992 and 1994), and Reid (1992 and 1993). Leggett, Harris & Dahn (1994) has followed up a number of the BD candidates found with V and I photometry, and some of the fainter candidates may or may not be BDs depending on the true age of the cluster ($\sim 0.9 \pm 0.5$ Gyrs).

Praesepe is approximately the same age as the Hyades, but further away, at ~ 175 pc. Recent proper motion surveys include Jones & Cudworth (1983), Jones & Stauffer (1991) and Hambly *et al.* (1995a), none of which get faint enough to find BDs. Williams, Rieke & Stauffer (1995) gets some what deeper ($V \sim 23$) which is close to, but not into the BD regime in Praesepe. Magazzu, Rebolo & Hodgkin (1997) go considerably deeper, covering 800 square arc-minutes down to $I=21.2$, and find 1 candidate. Follow up infrared photometry and low resolution spectroscopy (red – near infrared) shows that this candidate is indeed of late spectral type (M8.5–M9), which makes RPr1 (as it has been named) a very likely BD.

The Pleiades has proved to be a very popular hunting ground for BDs. Its closeness (~ 135 pc), relative youth and richness make it ideal for proper motion and photometric surveys alike. Proper motion surveys have been carried out by Jones (1981) (to $V \sim 17$), Stauffer *et al.* (1991) (to $V \sim 18$) and by Hambly, Hawkins & Jameson (1993) who goes the deepest ($I \sim 17.5$). The object HHJ3 ($I = 17.4$) from the Hambly survey was thought to be a BD (from its faintness) but failed to show the expected lithium line. Small scale CCD surveys have also been carried out, by Jameson & Skillen (1989) (125 square arc-minutes – R and I), and Simons & Becklin (1992) (200 square arc-minutes – I and K), who found several candidates. Stauffer *et al.* (1989) and Stauffer, Hamilton & Probst (1994) surveyed a somewhat larger area (0.4 square degrees) at V and I, finding several late type objects. These could nevertheless simply be background stars. More recent surveys using deep CCD imaging have produced several successes in the Pleiades. PPL15 was the first bona fide BD discovered (in a V and I survey by Stauffer, Hamilton & Probst (1994)), when it was found to have lithium, by Basri, Marcy & Graham (1996). The lithium line at 6708\AA is highly saturated for initial lithium abundances (its equivalent width will not decrease noticeably until the lithium abundance decreases substantially), however PPL15's lithium line was found to have an equivalent width of only $\frac{1}{4}\text{\AA}$ (initial lithium content should give $\sim 1.5\text{\AA}$, see Rebolo *et al.* (1996)), indicating a factor of 100 in depletion. PPL15 is therefore only just a BD, and can be used as a good representative upper limit to the BD regime in the Pleiades. Two other BDs have also been found in the Pleiades (using R and I), namely Teide1 (Rebolo, Osorio & Martin 1995) and Calar3 (Osorio, Rebolo & Martin 1997) which both show lithium at the initial abundance level of the cluster, and are of lower mass than PPL15. The apparent I magnitudes and the theoretical masses of these BDs are shown in Table (2.2). Other BD candidates being reported currently include PIZ 1 (Cossburn *et al.* 1997), and a collection of 10 new candidates presented by Osorio (1997) from a deep near infrared CCD survey of the Pleiades.

Brown Dwarf	I	Mass(M_{\odot})
PPL15	17.8	0.078
Teide1	18.8	0.056
Calar3	18.7	0.060

Table 2.2: Brown dwarfs in the Pleiades

2.7 Conclusions

In this chapter, I have presented a short review of a number of important areas of theoretical understanding in the field of VLM and BDs. Particularly, the interior modeling being carried out by several groups, which is improving all the time, and the relatively new field of model atmospheres which, when coupled to the interior models provide the best agreement with observations currently available. The method by which theoretical quantities are transferred to the observational plane are also discussed, as well as the use and implications of luminosity and mass functions with respect to VLM and BD population sizes. The lithium test is described briefly, providing an excellent test for BD status, and a review of BD searches in the field (as binaries and free floaters) and in open clusters is given, outlining previous attempts, as well as current successes, particularly in the Pleiades. The presence of lithium in the 3 Pleiades BDs mentioned really is compelling evidence for their substellar nature.

Chapter 3

Photometry

3.1 Introduction

This chapter will begin by describing the photometric scale, and then discussing how photometry can be obtained and accurately calibrated from flux measurements. Also, the methods of measuring these fluxes, and the various relevant filters required will be discussed.

3.2 The Photometric scale

The modern photometric magnitude scale is based upon the work of Pogson in 1856. He defined a scale that approximately agreed with the six brightness classes used by Hipparchos in his first astronomical catalogue (2nd century B.C.). The Pogson scale is shown in equation (3.1).

$$m_1 - m_2 = -2.5 \log \frac{I_1}{I_2} \quad (3.1)$$

m_1 and m_2 refer to the magnitudes of stars 1 and 2, and I_1 and I_2 are the fluxes received from these stars. In order to agree with Hipparchos' "by eye" classifications, the scale is logarithmic, (the response of the eye is nearly logarithmic) and the 2.5 comes about arbitrarily from the brightness divisions chosen. The scale is such that brighter stars have lower magnitude values than fainter ones.

3.3 Magnitudes

Photometry is done with the use of filters, which block out all radiation save that in a specified wavelength range. Many different filter systems exist, with both broad band (a few 100 Å) or narrow band (a few 10s of Å) wavelength ranges, some of which will be discussed in more detail later on in this section. The apparent magnitude zero point for all such filters is defined using the star Vega (αLyr). **Vega always has apparent magnitude 0 by definition regardless of the filter that is being used.** (In fact, it is the average of stars like Vega that is used. Vega may actually have $m_\lambda=0.01$ or 0.02). The zero point for an observation of a star depends on the instrumental configuration used to observe it, and can be defined by rearranging equation (3.1), giving

$$m_1 + 2.5 \log I_1 = m_2 + 2.5 \log I_2 = ZP_{1 \text{ or } 2} \quad (3.2)$$

where ZP is the zero point.

If one wants to compare magnitudes of different stars at different distances, it is necessary to normalise the apparent magnitudes to the same distance and extinction. This distance is taken to be 10 parsecs, and the new corrected magnitudes are called absolute magnitudes (written using an upper case M). The correction used to convert to absolute magnitudes is shown in equation (3.3),

$$M_\lambda = m_\lambda - (5 \log d - 5) - A_\lambda \quad (3.3)$$

where d is the distance of the star in parsecs, and A_λ is the interstellar extinction to the star. The value of $m_\lambda - M_\lambda$ is called the “distance modulus” of a star.

There is one other type of magnitude that has not been mentioned yet. This is the bolometric magnitude (M_{bol} or m_{bol} for absolute or apparent), and refers to the total flux from the star (not just that in one filter band). The correction between observed magnitudes (through filters) and bolometric magnitudes is shown in equation (3.4),

$$M_{bol} = M_\lambda + BC_\lambda \quad (3.4)$$

where BC_λ is known as the bolometric correction, and depends on the filter used and the spectral type of the star being observed. The absolute bolometric magnitude

zero point is defined from main sequence stars with a B-V colour of 0.35 (NOT with respect to Vega). The zero point is chosen so that such stars have $BC_V = 0$, and therefore $M_{\text{bol}} = M_V$.

3.4 Photometric calibration

When radiation passes through the earth's atmosphere the intensity decreases as photons are scattered out of the beam. The amount of radiation scattered is proportional to the size of the column of atmosphere that it has passed through, and is also dependent on the wavelength of the radiation. The size of the column of atmosphere is called the "air mass" and its units are such that one airmass corresponds to the height of the atmosphere directly over head. The air mass increases as one looks closer to the horizon, and a good approximation (ignoring the curvature of the earth) is given in equation (3.5),

$$AM = \sec z \quad (3.5)$$

where AM is the air mass, and z is the zenith distance, the angular distance of the star from the zenith (directly over head). If the earth's curvature is taken into account, a more accurate relationship can be found (see for instance Hardy (1962)), but for $\sec z < 2$ the difference is in the third decimal place, and is negligible.

The intensity of light travelling through the absorbing atmosphere (I_λ) is described from "radiative transfer theory" by equation (3.6),

$$I_\lambda = I_\lambda(0)e^{-(AM)\tau_\lambda} \quad (3.6)$$

where $I_\lambda(0)$ is the intensity above the atmosphere, and τ_λ is the optical depth measured perpendicularly through the atmosphere. Therefore for some star observed at two different air masses (1 and 2), equation (3.6) (logged on both sides) gives the following,

$$\tau_\lambda = \frac{\ln I_{\lambda 1} - \ln I_{\lambda 2}}{AM_2 - AM_1}. \quad (3.7)$$

Some rearrangement then gives

$$\tau_\lambda(2.5 \log e) = \frac{2.5 \log I_{\lambda 1} - 2.5 \log I_{\lambda 2}}{AM_2 - AM_1}, \quad (3.8)$$

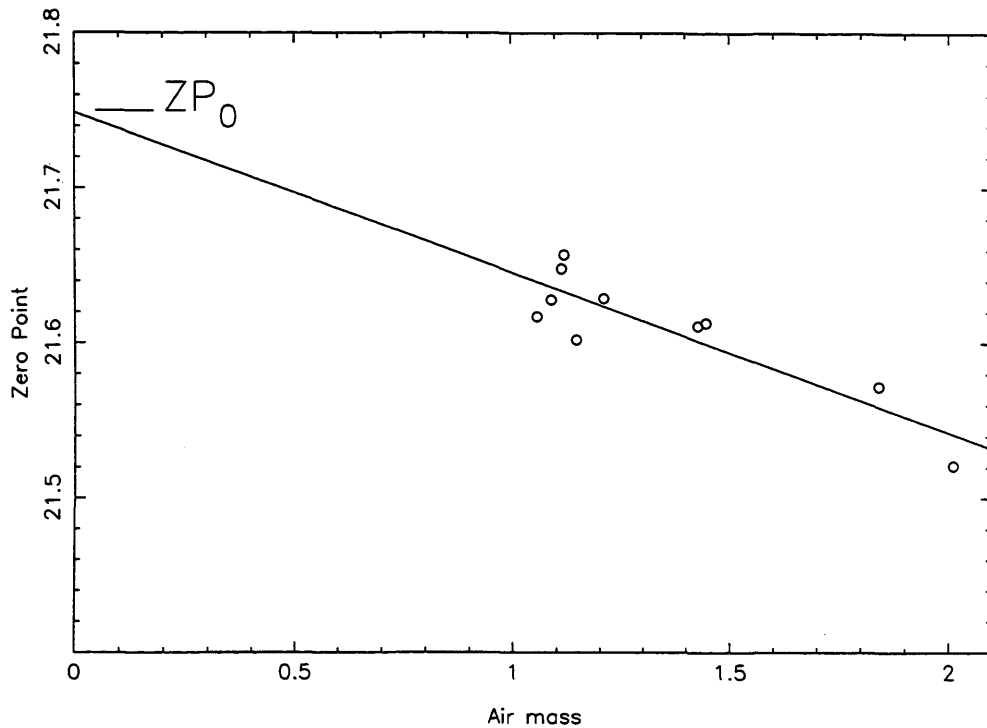


Figure 3.1: An example of an air mass curve. The filter used in this case was the K_s filter at the William Herschel Telescope (La Palma), and the weather was good.

and we can substitute for the zero point from equation (3.2) giving

$$k = \frac{ZP_1 - ZP_2}{AM_2 - AM_1}, \quad (3.9)$$

where k represents the constant $\tau_\lambda(2.5 \log e)$, and is known as the “air mass coefficient”. This then represents a straight line of gradient k on a zero point air mass plot, which is known as an “air mass curve”.

Photometric calibration can thus be achieved by observing a number of standard stars of known magnitude at different air masses on any particular night (when hopefully good weather will prevail, and the atmosphere will be stable), and making such air mass curves for each photometric filter used. When using broad band filters, the different spectral type stars will produce slightly different values of k , since bluer stars will have more flux at the blue-ward side of the filter, and this will of course be scattered more. However, if stars of approximately the same spectral type are used as standards this problem will not arise, and no “colour corrections” will be necessary. An example of an air mass curve is shown in figure (3.1). This

example is from a set of standard stars observed at the William Herschel Telescope on La Palma in 1997, using the K_s filter. The weather was clear all night, and from a least squares fit, k (the gradient) was found to be -0.103 magnitudes per airmass, and ZP_0 (the intercept, or the zero point above the atmosphere) was found to be 21.75^m . The standard error was 0.02^m . Therefore, any non standard star observed on the same night can have a zero point assigned to it from this best fit line at the appropriate airmass position, which will have an error of only 0.02 magnitudes.

3.5 Measuring fluxes

Having discussed the fundamentals of the photometric scale and the method of photometric calibration, I will now describe the way in which stellar fluxes were measured in this work.

3.5.1 Optical Charged Coupled Devices

Optical Charged Coupled Devices (CCDs) are semiconductor (usually silicon) type instruments, cooled to very low temperatures ($\sim 150K$) to reduce thermal charge and its associated noise. The basic detection mechanism uses the photoelectric effect, where the incident light during an exposure creates electron hole pairs. The electrons are then stored using a positively charged electrode (insulated from the semiconductor by a thin oxide layer) as well as a confining “gate” electrode, producing a spatially digitized electric analogue of the optical image. At the end of the exposure, the gate electrode is opened (set positive), and the “buckets” of stored charge are transferred to a read out point (an analogue to digital converter, or ADC) by cycling a series of stepped voltages through a set of electrodes located all along the charge storage points (for a more in-depth description of this process see Kitchen (1997)). The number of electrons represented by one analogue to digital count (ADU) depends on the amplification electronics being used, and is known as the “gain” of the CCD. The important characteristics of CCDs that make them very useful for astronomical observations are summarised below.

- The images created by a CCD are in the form of discrete pixels with digital values associated with them, and are ideal for computer reduction.
- They have high quantum efficiency over relatively large spectral ranges, making them very good for detecting faint sources.
- Detections can be integrated over long exposure times, further improving the ability to detect faint sources.
- They have a large dynamic range, meaning that stars of very different brightnesses can be detected in one exposure.
- They are highly linear detectors over this large dynamic range, so resulting photometry will be very accurate without the need for non linear corrections.
- The large field of view coupled with the large dynamic range means that even if the weather forbids accurate calibration, relative photometry can be done between bright and faint stars on the same image.

3.5.2 Infrared imaging cameras

Modern infrared cameras are also semiconductor devices. For example, IRCAM3 is the infrared camera at The United Kingdom Infrared Telescope on Mauna Kea, Hawaii. The materials used in the array are Indium and Antimony (In and Sb), but the detection process is similar to that for optical CCDs, but for photons of lower energy. The important differences between infrared cameras and CCDs are summarised below.

- Infrared arrays are in general considerably smaller than optical CCDs. For example, IRCAM3 is a 256 x 256 array, compared to a typical optical array of $\sim 1000 \times 1000$. This means that their sky coverage is much less.
- They must be cooled to a somewhat lower temperature ($\sim 35\text{K}$) than optical CCDs.
- Even in these reduced temperatures more dark current is produced.

- The infrared sky is however relatively bright, and this is beneficial because high quality flat fields can be made by median filtering a series of individual exposures together.

3.5.3 Image reduction

Raw CCD images have an instrumental signature that must be removed before any accurate photometry can be obtained. The required procedures are outlined below.

- In order to prevent the ADC receiving a negative signal (due to noise on a low level back ground), an artificially induced electronic off set is added to each pixel charge. This off set is known as the “bias level”, and has an intrinsic noise known as the read-out noise. A “bias frame” can be created by taking images of zero exposure time, or by using strips of light insensitive pixels around the light sensitive portion of the chip to create a 2-dimensional bias frame. The bias frame is then simply subtracted from the raw image in a process known as “de-biasing”. The CCD image is then in a form directly proportional to the number of photons detected in the light sensitive pixels.
- The production of dark current due to thermal noise also needs to be removed. Dark current is actually negligible in modern optical CCDs, but is evident in infrared arrays. A dark frame can be created by taking an exposure for the same length as the image exposure, but with the shutter closed. This dark frame can then be subtracted off the CCD image. The CCD image then consists only of photon detections from the observed sources.
- Although CCD pixels are highly linear, they are not all identical in efficiency, and therefore the amount of charge stored per photon varies slightly from pixel to pixel. This can be corrected for in a process called “flat-fielding”. A flat-field can be made by imaging a uniformly bright source (the twilight sky, or the dome of the telescope), and normalising the resulting image to a mean value of 1.0. An alternative method if the dark sky background is sufficiently high (eg: infrared imaging) is to use median filtering of the actual observations (which removes the individual sources), leaving only the sky, which is of course

uniformly bright, and can be normalised to a mean of 1.0 as before. Each image can then be divided by this flat-field, making each ADU registered in any pixel represent the same flux.

The resulting image is then in a form where useful photometry can be extracted. Examples of computer packages designed to carry out the above stages of image reduction are the STARLINK package CCDPACK, and the IRAF package CCDPROC.

3.5.4 Detection of sources

For small field of view images with only a few objects, each source can be located by eye, but for larger fields of view with hundreds or thousands of sources, they need to be located using computer software. One computational method is to search for local density maxima with certain shape (full width at half maxima, or FWHM) and size (some lower limit to the ADUs in the source, and a saturation limit to the ADUs in any pixel) limitations. The IRAF routine DAOFIND uses this approach. An alternative method (used by STARLINK's PISA) is to locate any source whose flux rises above some defined detection threshold, but this approach is less satisfactory when searching for faint sources, since any small imperfections left over from the flat-fielding process may well be larger than the sources that you want to detect, and the software's algorithm has problems.

3.5.5 Aperture photometry

The next step is to obtain the total number of ADUs in each source. This entails calculating a value for the background (the sky) for each source (which will vary slightly between sources because of scattered light, or imperfections in the flat-fielding process) and then counting up the ADUs above this background to give the contribution of the source alone. The sky is found by taking a median average of pixel values in an annulus around the source. The annulus should have a radius of sufficient size to contain a negligible signal from the source, but correctly represents the near by sky background level. The ADUs in the source are then found by simply adding up the the signal above this background level in a circular aperture

of sufficient size. Using the gain of the CCD the number of ADUs in each source is converted into the number of electrons measured, and hence photons detected, and dividing by the exposure time gives the flux. The magnitude of the source then comes directly from equation (3.2),

$$m = ZP - 2.5 \log I, \quad (3.10)$$

where I is the photon flux, and ZP is the zero point for the air mass of the observation.

3.5.6 Errors

There are several sources of error that need to be considered for photometry.

- The error in the estimation of the sky background.
- The error in the flux from the source.
- The error from the read-out noise.

The quantity required to calculate the photometric errors is the “signal to noise ratio”. If it is assumed that the detections come from a Poissonian distribution, then one can say that

$$\sigma_{sky}^2 = Sky_{pixel} \quad (3.11)$$

where σ_{sky} is the standard deviation of the sky background photon flux per pixel (Sky_{pixel}). The signal to noise ratio (S/N) is then given by

$$S/N = \frac{Flux_{source}}{\sqrt{(Flux_{source}) + (Aperture_{source} \times Sky_{pixel}) + (\text{read-out noise})^2}}, \quad (3.12)$$

where $Aperture_{source}$ is the number of pixels in the aperture. For long exposure images the read-out noise becomes comparatively negligible, and the flux from the sky is far larger than the flux from the source. Therefore using equations (3.11) and (3.12), the signal to noise simplifies to

$$S/N = \frac{Flux_{source}}{\sqrt{Aperture_{source} \times \sigma_{sky}}}. \quad (3.13)$$

The number of pixels in the circular aperture (required to contain the flux from the source) will scale with the “seeing” (the FWHM) squared, and therefore,

$$\begin{aligned} S/N &\propto \frac{1}{\text{seeing}} \\ S/N &\propto \frac{\text{Flux}_{\text{source}}}{\sigma_{\text{sky}}}. \end{aligned} \tag{3.14}$$

3.5.7 Aperture corrections

The choice of aperture size is important when trying to get accurate photometry, as well as for keeping errors to a minimum. When trying to obtain accurate photometry of faint sources in an image, it is likely to be the case that a small aperture is needed if the noise from the sky is to be kept to minimum. However, for the brighter sources in the same image this small aperture will clearly not contain all the flux from the source. Because the point spread functions of bright and faint sources alike are the same in any one image, the fraction of missed flux will actually be the same for all magnitudes, but is only apparent in bright sources, because it rises significantly above the noise of the sky. It will therefore be necessary to correct for this short fall in flux, using an “aperture correction”. An accurate aperture correction can be found for any particular image by selecting fairly bright unsaturated stars, and obtaining a set of magnitudes for each star for the required range of aperture sizes. Obviously the stars will differ in brightness, but by offsetting the sets of magnitudes so that the average values (averaged over aperture size) are the same for each star, the effects of the aperture size on the magnitude can be seen. Figure (3.2) shows an example of such a set of magnitudes for 5 bright stars, taken from observations done from the Burrell Schmidt Telescope on KittPeak in 1996. The magnitudes have been averaged to zero, and are therefore labelled instrumental (uncalibrated). The seeing on the night in question was 4 arc seconds, and the aperture that gave the best results for the faint sources had a radius equal to this seeing. However, the brighter stars in the image, as well as the standard stars used to calibrate the data required an aperture of 10 arc seconds. An aperture correction from 4 to 10 arc seconds was therefore derived from the data in the plot, and was found to be -0.3 ± 0.02 magnitudes. This could then be added to the 4 arc second aperture magnitudes of all the stars in the image.

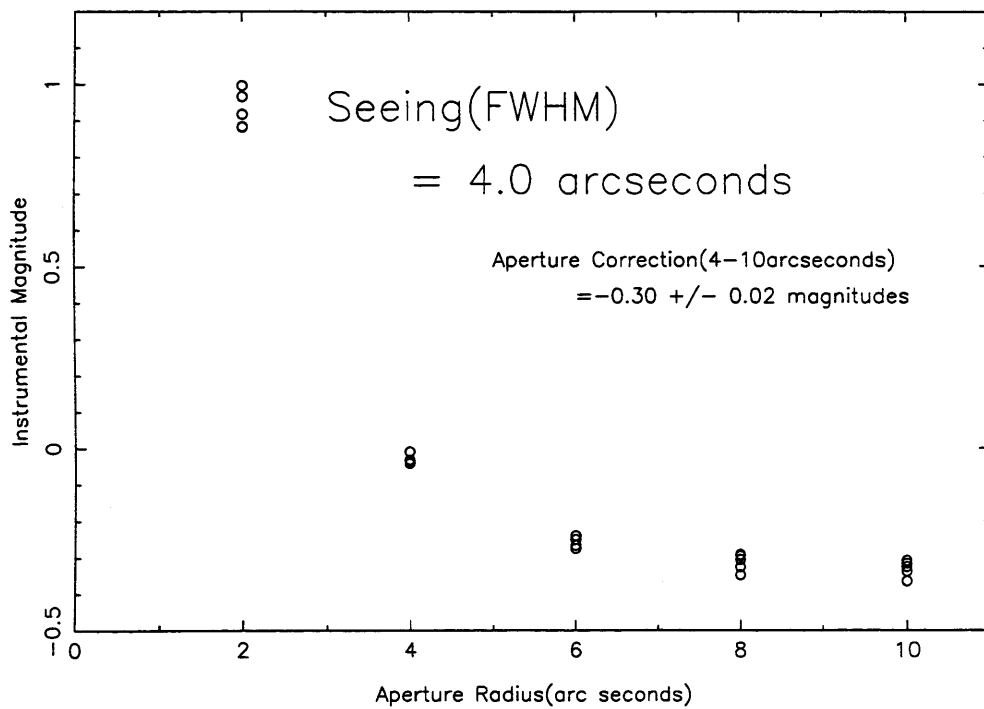


Figure 3.2: An example of an aperture correction, taken from observations done from the Burrell Schmidt Telescope on KittPeak in 1996. The magnitudes have been averaged to zero, and are therefore labelled instrumental (uncalibrated).

3.6 Filter Systems

The standard U ($\sim 3600 \pm 500\text{\AA}$) B ($\sim 4300 \pm 600\text{\AA}$) V ($\sim 5500 \pm 500\text{\AA}$) filter system established by Johnson & Morgan (1953) is the most widely used photometric system, but these filters do not cover the wavelength range best suited for VLM and BDs (where they are brightest). One needs to move into the red and infrared.

3.6.1 Red – near infrared filters

In this range, the definition of a standard filter system is more complicated. There are many different R I filter systems in use. Bessell (1976, 1979, 1983, 1986, 1987, 1990 and 1995) discusses the Kron-Cousins, photographic and Gunn filter systems, as well as a set of interference filters, which he refers to as “CCD” filters. Polynomials are given to convert from the various filter systems into the Kron-Cousins system and vice versa, since Kron-Cousins magnitudes are by convention the standard for reference. Another important filter is the Z filter (see Schneider, Hoessel & Gunn (1983)), which is an open ended infrared filter whose transmission begins at about 0.85 microns (0.1 micron red-ward of the I filter).

The filter systems most relevant to this work are those in use with CCDs. This includes the “CCD” filter set mentioned by Bessell, which is from the “Kitt-Peak Observatory” (KP) as well as a filter set from the “Royal Greenwich Observatory” (RGO), which are glass filters.

The effective band passes of the standard Kron-Cousins (Cou) R and I filters are actually intrinsically convolved with the response of a photo-multiplier tube. However, the RGO and KP filter sets must be convolved with the response of the CCD detector being used, in order to obtain the relevant effective band passes. In order to compare the different filter systems, Figure (3.3) contains two plots. The first shows the actual filter band passes for the R, I and Z filters from the RGO and KP filters sets. The RGO filters are shown as dashed lines and the KP filters as dot-dashed lines. The response function of a typical modern optical CCD chip (a Tektronix chip) is also shown as a solid line. The RGO filters have the characteristic asymmetric profiles associated with glass filters, tailing off at the longer wavelength

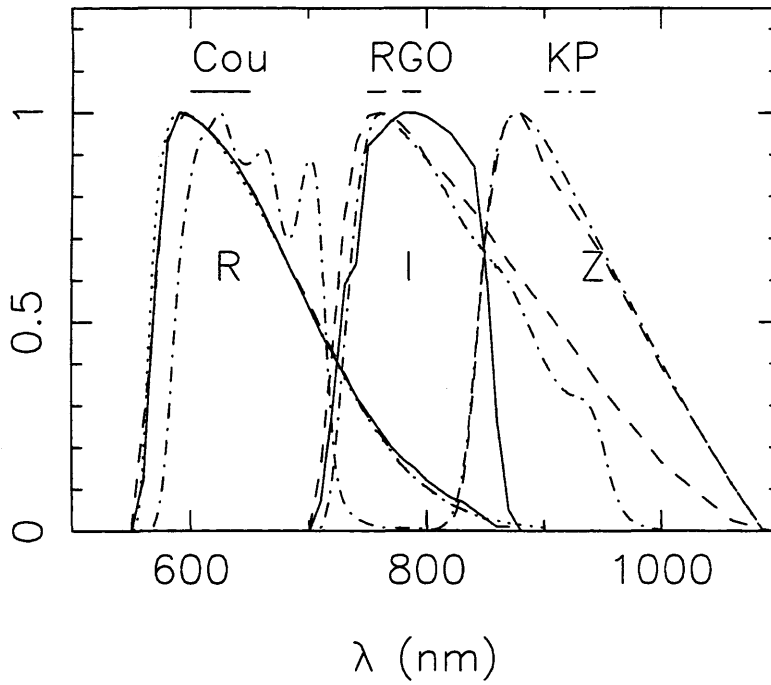
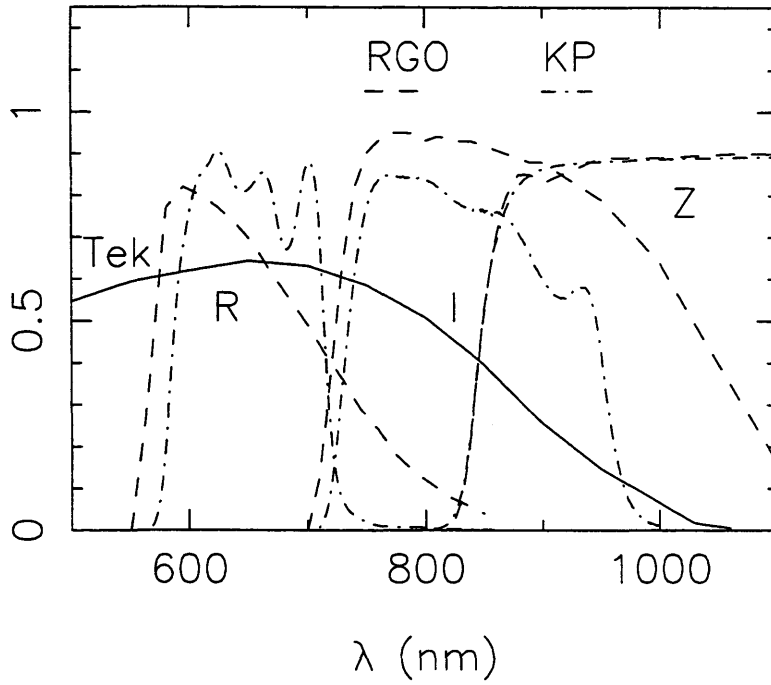


Figure 3.3: Filter pass bands for Cousins (solid line), RGO (dashed line) and KP (dot-dashed line) filters. The top plot shows the actual filter band passes, and the lower plot shows the filter passes convolved with a modern CCD response function.

side. The KP filters have a more “top-hat” type profile with no substantial overlap between R and I. The KP Z filter is a “Gunn” filter, but is almost identical to the RGO Z filter. Both filters rely on the detector to provide the long wavelength cut-off. The second plot in Figure (3.3) shows the pass bands of the filters convolved with the response of the Tektronix chip. The Kron-Cousins R and I pass bands are also shown for comparison. It is clear that R_{RGO} is virtually identical to R_c , but that R_{KP} is considerably different. I_{RGO} and I_{KP} are similar, with I_{RGO} being slightly more efficient at longer wavelength. The effect of the CCD response on the Z filters is clear, making them effectively “long-I” filters.

3.6.2 Infrared filters

The filter pass bands above 1 micron are chosen to exploit the transmission of the earth’s atmosphere. This transmission is shown in Figure (3.4). The dotted line from 0.35 to just below 1 micron represents the U – Z band previously discussed, and is a fairly uniform region of good transmission (data taken from Allen (1973)). After this point, the data comes from the UKIRT world wide web home page. It is clear that the atmospheric transmission is close to 100% in three places. These wavelength ranges have been exploited by the use of the J ($\sim 1.2\mu\text{m}$), H ($\sim 1.6\mu\text{m}$) and K ($\sim 2.2\mu\text{m}$) filters constructed for use in various telescopes. Bessell & Brett (1988) review the different sets of these filters, and gives relationships between the infrared colours they produce.

3.7 Conclusions

In this chapter, the basic photometric methods used in the context of this work have been described, as well as details particularly appropriate to the photometry of faint sources, such as aperture corrections, and the determination of accurate errors which are required to determine the significance of the calculated magnitudes. The filters and different filter systems used have also been described, and it is clear that differences between the effective band passes (which are also detector dependent) of

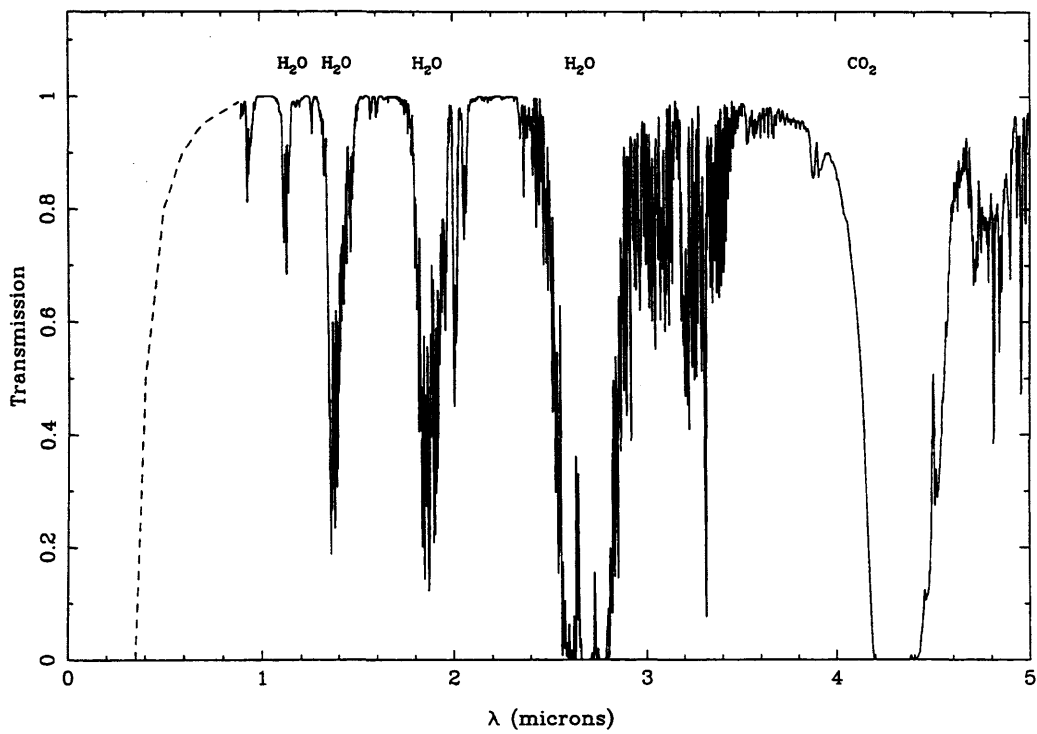


Figure 3.4: The transmission of the earth's atmosphere against wavelength.

these filters means that careful interpretation of the photometry is required when comparing different results, or the predictions of theory.

Chapter 4

Praesepe: RIZ survey

4.1 Introduction

This chapter describes the results of a deep photometric survey of the Praesepe open cluster. The main focus will be on the red to near infrared photometry, but I shall also briefly mention the UBV photometry, which was also reduced as part of this thesis work.

Praesepe is a galactic open cluster in Cancer, and is part of the Hyades moving group (Eggen 1960). Praesepe distance, age, reddening and metallicity have been derived in several sources, and are summarised in Hambly *et al.* (1995b) and references therein. These along with position and proper motion are given in Table (4.1).

Praesepe is considerably younger than the galactic disk, meaning that VLM and BDs will be brighter and hotter than in the field. It's proper motion is sufficiently large to be detectable over a period of about 20-30 years. The cluster is slightly metal rich, and close enough to be able to detect BD members. The next section presents an observational review of the cluster, and the following sections describe the choice of filters when searching for VLM and BDs, the observations, the method used to "flag" galaxies from stars, and the derivation of luminosity and mass functions. At the end I will briefly describe the results of the white dwarf survey.

Praesepe	M44 / NGC 2632
Coordinates (J2000) of cluster centre	R.A. = 8h 40m 12s Dec = +19 42 00 Galactic (II) 205.510, 32.480
Proper motion	$\Delta\alpha=30\text{mas/yr}$ $\Delta\text{dec}=-8\text{mas/yr}$
Distance modulus	6.05
Age	(0.9 ± 0.5) Gyrs
Reddening	none
Metallicity	Fe/H = 0.14

Table 4.1: Praesepe parameters.

4.2 Praesepe: Observational review

Klein Wassink (1927) carried out a proper motion survey to a radius of $\sim 1^\circ$ from the cluster centre, which has been followed up photometrically by several authors (Johnson (1952), Crawford & Barnes (1969), Upgren, Weis & DeLuca (1979), and Weis (1981)). Artjukhina (1966) extends the coverage out to $\sim 4^\circ$, with photometric follow up by Mermilliod *et al.* (1990) in UBVR and I(Kron), who also obtained radial velocities for the candidates. Jones & Cudworth (1983) extended the proper motion depth down to $V \sim 17$, and these members have photometry from Stauffer (1982) in UBVR and I(Kron), and Williams *et al.* (1994) in V and I(Kron). Williams, Rieke & Stauffer (1995) presents VI and K photometry down to $V \sim 23$, and derives a luminosity and mass function. Jones & Stauffer (1991) obtained proper motions down to $V \sim 18$ with $(BV)_{\text{pg}}$ and I_{pg} using the Monet scanning machine at Kitt Peak, as well as deriving a luminosity function. Hambly *et al.* (1995a) used the COSMOS scanning machine to obtain proper motions and R_{59f} , I_{N} photometry down to $I_{\text{N}} \simeq 18.2$, covering an area of 19 square degrees.

Spectral types for high mass ($6.3 < V < 9.1$) Klein-Wassink members have been found by Bidelman (1956), and Abt (1986). Fainter Klein-Wassink members ($V > 9$)

have spectral types from Corbally and Garrison (1983 and 1986), and Williams *et al.* (1994) gives spectral types and H_α equivalent widths for some of the Jones & Cudworth members ($V > 16.5$). Hambly *et al.* (1995b) present spectral types of four HSHJ members ($13 < I_N < 17$), as well as deriving luminosity and mass functions down to $R_{59f} \simeq 20$. The survey presented in this chapter has also been published recently (Pinfield *et al.* 1997) and more recently still, Magazzu, Rebolo & Hodgkin (1997) presented the results of an 800 square arc-minute survey which found one good BD candidate of $I=21.2$, with a spectral type of about M9.

Other observational work includes a radial velocity study of a selection of Klein-Wassink members, to identify binaries, and the photometry of these binaries shows them to lie on a well defined binary sequence down to $V \sim 13$ (Bolte 1991). Also an X-ray survey using ROSAT has been taken (Randich & Schmidt 1995).

4.3 Filters

When searching for very faint red objects such as BDs, there are several factors that need to be taken into consideration.

- The sky coverage provided needs to be as large as possible, so that a survey has a statistically good chance of turning up BDs.
- The detector must be capable of detecting the BDs in a feasibly short exposure time.
- It must be possible to select BDs from the background field star population.

Current infrared arrays cover just over 1 square arc-minute of sky which is about 100 times less than a typical optical CCD setup. Since nearby open clusters are in the order of 10 degrees across, covering a significant fraction of the cluster using an infrared array is not yet feasible. Optical CCDs are clearly better in terms of sky coverage, but how well are they suited to detecting and identifying BDs? In order to answer this question, Figure (4.1) shows the sensitivity of a modern CCD chip (a Tektronix chip) against wavelength, along with typical V, R, I and Z filter pass bands (which have been folded through the chip's quantum efficiency and normalized). Also

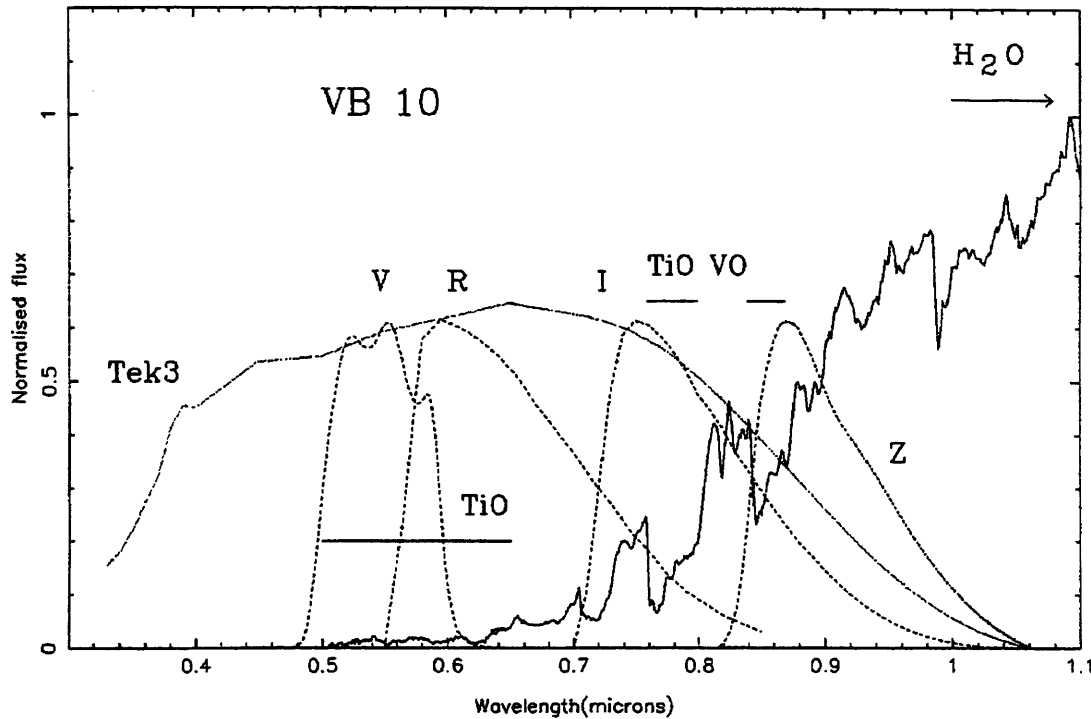


Figure 4.1: The sensitivity of a Tektronix CCD chip: The efficiency is high through the visible but also extends into the near infrared. The V, R, I and Z pass bands are shown as well as the spectrum of the late M dwarf VB10, which has important regions of opacity indicated.

shown is the red to infrared spectra of VB10 (Kirkpatrick private communication), an old disk M8 dwarf star of $T_{\text{eff}} \sim 2506\text{K}$, and $M \sim 0.085M_{\odot}$ (Jones *et al.* 1994). Although VB10 is just above the BD mass limit, objects of this temperature in Praesepe will be less massive (because of Praesepe's younger age) and will therefore be good BD candidates. It is consequently important to appreciate how the features of such a spectrum will affect its observed photometry.

In order to make a detection, one obviously needs to maximize the flux received from the source, and this means making a compromise between looking at the most efficient wavelength region of the CCD, and looking at the brightest wavelength region of the source. The I band is clearly the best in this respect, since the CCDs response is still good, and VB10 is getting much brighter in this filter. The flux in the V band is very low, due mainly to it being in the Wein tail part of the spectrum,

but it is further decreased by the molecular TiO opacities. The R band is a definite improvement on the V band, but is still somewhat lacking in flux. Moving over to the infrared side, the Z band clearly has more flux, even though the response of the CCD is declining. The order of preference in terms of detection ability is then I, Z, R, V.

The final requirement is that the colour information of such objects should act as a sufficiently good temperature indicator, in order to single out cool cluster members from background stars. When using V and I (for example Williams *et al.* (1994)), this will clearly be the case (provided of course that a V magnitude can be obtained for the source), since the two pass bands are separated by some 3000\AA , and the detected brightnesses will differ greatly. The R and I pass bands have a separation of about 2000\AA , and should also provide a good temperature indicator. When using filters as close together as I and Z, the band separation is only about 1000\AA . However, VB10's spectrum rises from about 10% to $\sim 100\%$ of its peak through the I and Z bands, before H_2O becomes the dominant source of opacity. Therefore the short baseline of the photometry will be counteracted by the steeply rising spectrum of such stars, and a good colour temperature relation is the expected result.

The best filter to use for the detection of BDs in Praesepe is I, and for the colour information, one should also obtain Z, and R if it is possible.

There are other advantages to using the I and Z filters. During bright time, these are the pass bands least affected by scattered moon light, since the sky is already bright at these wavelengths due to airglow. Observing time is therefore easier to obtain, since bright time is less popular. Also, because the base line is short, there will be less contamination from red galaxies, where the Balmer discontinuity has been red-shifted to between the two filter passes.

4.4 The survey

4.4.1 Observations

The survey data comprises two sets of observations. The first set was obtained by Ted von Hippel and Derek Jones in 1993 at the 2.5m Isaac Newton Telescope on the

island of La Palma. The aim of their project was two fold. Firstly they planned to obtain U B and V photometry in order to identify Praesepe white dwarfs, as part of a project to calculate the age of the cluster from white dwarf cooling models. Secondly, they wanted to look for Praesepe VLM and BDs using their R and I photometry. My supervisor Richard Jameson met Ted von Hippel at a conference in 1994, and offered to take on board the task of reducing the photometric survey data. Shortly after this I began work on my PhD with Richard, with the Praesepe survey as my first project. The Survey comprised 41 different fields in the cluster centre, with exposure times of 300, 100, 100, 120 and 140 seconds at U, B, V, R(RGO) and I(RGO) respectively. The CCD detector that had been used (at prime focus) was an EEV5 chip which covered 11×10 arc minutes per field. The weather had been reasonably photometric, with seeing of about 2 arc seconds. It should be mentioned that the observers did not image many standards during the run. They took about 5 at the start of one night (in order to get a rough idea of the zero points), but did not do any more after this, or during the other nights. The photometry thus needed to be properly calibrated, and the approach taken is described in section (4.4.2).

The second set of observations were taken once again at the INT, over the new year (1995-96) to complement the first set. This time, the aim was purely to further the search for new VLM and BDs, and to this end Z(KP) exposures of 1000 seconds each were taken of some 24 of the 41 previously surveyed fields. This observing run was during bright time, but as was explained in section (4.3), this is not a problem. The CCD detector used on this occasion was a Tektronix chip which covers slightly less sky than before (10×10 arc minutes at prime focus) and has a similar response function to the EEV5 chip (see Figure (4.1) for the Tektronix response function). However, the weather conditions during this observing run were not photometric, with cirrus present for most of the time, and a seeing of about 2.5 arc-seconds. However relative photometry can still be done under such conditions (see section (3.5)). The method used to calibrate the Z data will be described later in this chapter.

The survey information relevant to the BDs is summarised in Table (4.2).

R I coverage	41 fields $\simeq 1.25$ square degrees
R I seeing	2 arc-seconds
R I photometric ?	Yes
I exposure time	140 seconds
R exposure time	120 seconds
Z coverage	24 field $\simeq 0.67$ square degrees
Z seeing	2.5 arc-seconds
Z photometric ?	No
Z exposure time	1000 seconds

Table 4.2: Survey Criteria.

4.4.2 Image reduction and photometry

The general method of data reduction that was used for this data is described in section (3.5). The particular soft-ware packages that were used for this data are as follows.

The R and I images were reduced using (STARLINK: CCDPACK), and Z images, using (IRAF: CCDPROC). Both software packages produced good results. R I objects were located using (STARLINK: PISA), and Z objects, using (IRAF: DAOFIND), at a 4 sigma detection level. The latter was found to be a more efficient method, but by searching at 1, 2, and 4 sigma levels, PISA was able to locate all the sources. R and I instrumental magnitudes were found with (STARLINK: PHOTOM), and Z instrumental magnitudes, using (IRAF: PHOT). A selection of apertures were used, ranging in size between 3 and 9 pixels, depending on the brightness of the source, but all magnitudes were then corrected to a 9 pixel aperture size, using a derived aperture correction. I objects were matched to R counterparts, taking into account any x-y shift between the images, found from the positions of brighter R and I sources. Since the Z images were taken at a different time, a polar coordinate shift was derived using two pairs of matched I and Z counterparts in

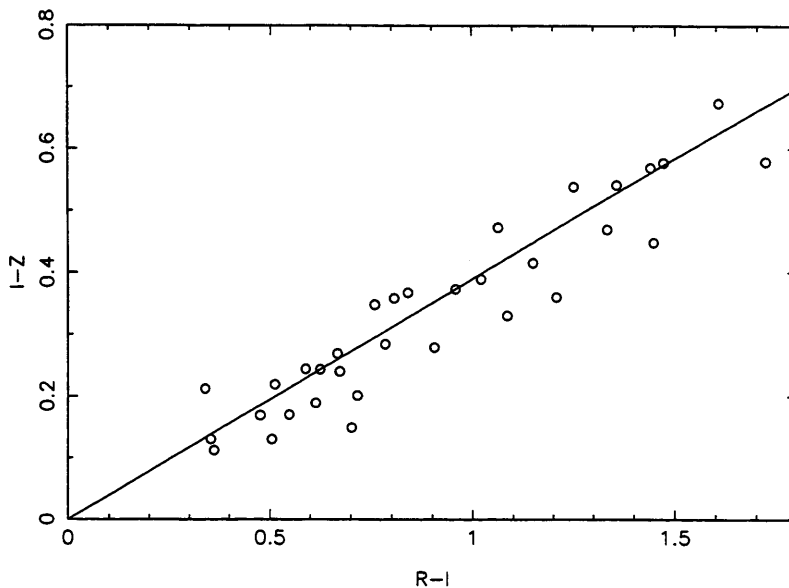


Figure 4.2: Two colour diagram of a selection of bright stars taken from one of the Praesepe fields. The Z photometry has been calibrated such that the best fit to the data (shown as a line) passes through the origin.

opposite corners of each image. Z objects were then matched within a 3 pixel radius of the I objects.

The calibration of the data was achieved using photometric service time. Six overlapping Praesepe fields were imaged at the Jacobus Kapteyn Telescope, La Palma, using R and I RGO filters. Between 5 and 8 calibration stars were used in each image, and a zero point defined so as to give accurate magnitudes for these stars. A typical scatter of ~ 0.1 magnitudes was seen. The Z calibration was done by comparing the resultant I-Z colour to the R-I colour of objects that were found in all three images. Brighter objects were preferentially chosen where possible, and the Z zero point was selected such that the band on the (R-I)-(I-Z) colour-colour plot went through the origin, as it must do by definition for unreddened A0 stars. Figure (4.2) shows an example of such a plot. The instrumental error bars on the bright stars were small (≤ 0.05 magnitudes), and the observed spread of the band

in the colour–colour diagram can be seen to be $\simeq \pm 0.1$ magnitudes. The zero point errors were accordingly set at ± 0.1 .

4.4.3 Shape analysis

There are two potential contaminants of the cluster VLM and BDs. These are red galaxies, and cosmic rays. Galaxies will usually appear as extended sources, and cosmic rays as spiky sources. In order to identify these unwanted elements, some basic shape analysis was carried out.

This shape analysis consisted of extracting the peak counts as well as the total counts in each I source. The local sky background level was then subtracted to give the peak counts resulting from each source alone.

In any one image, the point spread function will be approximately the same. Because the objects' counts are all for the same circular aperture, the total counts in any point source will scale directly with its peak counts, and so unsaturated stars will lie on a “stellar band” with a gradient of 1 in a $\log(\text{Peak counts})$ - $\log(\text{Counts})$ plot. As the seeing varies slightly between images, this band will move up (improved seeing) or down (worse seeing) the plot, but the gradient will not change. For the brighter sources, galaxy contamination is much less, and the stellar band is well defined. The peak counts from stars in any of the images could therefore be normalised to some average seeing, simply by moving the stellar band from each image up or down, so that they all over-lap. This was done for the surveyed fields, averaging the seeing to 2 arc-seconds, and the resulting plot is shown in Figure (4.3).

The stellar band is indicated, and is well defined at the brighter end since stellar sources far outnumber extra galactic ones at this brightness. However, as one moves to the fainter side, galaxy contamination increases and also the stellar band spreads out a little due to reduced signal to noise.

The plot only contains sources that match up in the R image, and so solitary cosmic rays are essentially excluded. However, some of the fainter sources lie above the stellar band, due to the interference of cosmic rays, and will have un-reliable photometry as a result.

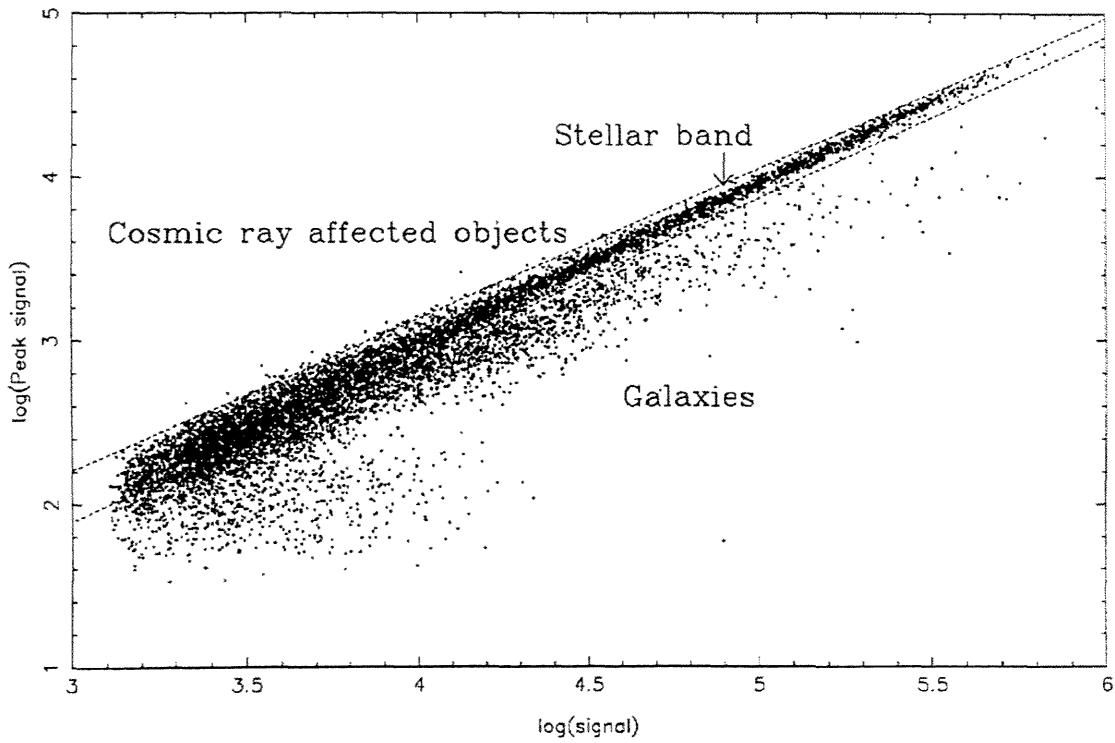


Figure 4.3: Log peak counts against log total counts in I, for objects found in the survey. The stellar band is indicated, and has a gradient of one. Galaxies are flatter, and fall beneath this band. Some objects have been affected by cosmic rays, and appear more spiky as a result. These fall above the band.

Cut off lines (dotted lines in Figure (4.3)) were defined with reference to the brighter sources between which the stellar band lies, with some allowance for the spreading of the stellar band for fainter sources. The extended sources were then flagged as galaxies, and the spiky ones as cosmic ray affected sources.

This method should be very accurate for the brighter sources, but the extension of the star galaxy separation line to fainter sources is clearly not so ideal. There may still be some galaxy contaminants, but to identify these would require some more observations.

4.5 Photometric results

4.5.1 The photometric catalogue

The signal to noise, and photometric errors were found according to the methods described in section (3.5), and the survey achieved the following signal to noise limits.

- $S/N \geq 10$ for $R \leq 21.5$, $I \leq 20$ and $Z \leq 21.5$.
- $S/N \geq 5$ for $R \simeq 23$, $I \simeq 22$ and $Z \simeq 23$.

The resultant photometric catalogue of data contains $\sim 10,000$ objects, all of which have I magnitudes. The Z images go deeper than the I images because of the longer exposure times. Consequently, the faint objects in the I fields that were observed at Z all have Z magnitudes, apart from those that were near bright stars, where the saturating bright star ruins the faint object's Z profile. Further more, some of the brighter I objects were saturated in their own right on the Z images because of the long exposure times. Many objects have R photometry also, however the S/N limit in R means that some faint red objects are undetectable in this filter. The following summarises the three classes of photometric object.

- **RIZ object:** An object with R, I, and Z photometry. It was both detectable, and unsaturated in R, I and Z.
- **RI object:** An object with R and I photometry, but no Z photometry. It was detectable and unsaturated in R and I, but either wasn't covered by the Z

survey, or the Z counterpart was saturated, or spoiled by a nearby bright star or region of poor image quality.

- **IZ object:** An object with I and Z photometry, but no R photometry. It was detectable and unsaturated in I and Z, but its R counterpart was either too faint to be detected, or was spoiled by a nearby bright star or region of poor image quality.

4.5.2 The Praesepe sequence

In order to identify cluster members from background stars on the resulting colour magnitude diagrams, it was necessary to locate the cluster sequence. This was done in two ways.

Field star sequence

Although Praesepe is young compared to the galactic disk, Praesepe stars are sufficiently old to have almost finished their radial contraction stage (see Figure (2.1)). This means that Praesepe VLM or BDs with a certain T_{eff} will have the same luminosity as field stars of the same T_{eff} . Therefore, the Praesepe sequence can be identified by determining the positions that field stars of various spectral type would occupy on the colour magnitude diagrams, if they were at the distance of the cluster.

These expected photometric magnitudes and colours were calculated using a set of spectra of late field M dwarfs, which were provided by Davy Kirkpatrick. The RGO R I, and KP Z filters were convolved with the relevant CCD response function to provide a set of effective band passes for each filter-instrumental set that was used. These effective band passes as well as the Cousins I band pass were multiplied through each M dwarf spectrum to obtain the relative fluxes that would be observed through each filter. These relative fluxes provide an instrumental colour for each M dwarf, which needs to be calibrated with respect to a standard star. The standard star chosen was α Lyrae, which has zero colour by definition. By obtaining instrumental colours for α Lyrae as was done for the M dwarfs, the colour offset required to calibrate the M dwarfs was found. This offset is of course simply the

correction required to give α Lyrae a colour of zero. The required calculation is shown in Equation (4.1), which as an example is done for the I-Z colour.

$$I - Z_{old-disk} = 2.5 \log \left\{ \frac{Z \text{ flux}}{I \text{ flux}} \right\}_{old-disk} - 2.5 \log \left\{ \frac{Z \text{ flux}}{I \text{ flux}} \right\}_{\alpha \text{ Lyrae}} \quad (4.1)$$

The colours obtained for each M dwarf were R-I, I-Z, and $I_{\text{cousins}} - I_{\text{RGO}}$. This last colour could be used in conjunction with the published $M_{I(\text{cousins})}$ magnitudes (Jones *et al.* 1994), as well as Praesepe's distance modulus to produce the I_{RGO} magnitudes that the M dwarfs would have in Praesepe.

Isochrones

The uncertainty in the age of Praesepe (see section (4.1)), as well as problems with the VLM and BD models (see section (2.3)) mean that no one isochrone is going to be totally reliable, in terms of both defining the stellar sequence, or defining the mass of objects. However, by using both a young, and an old isochrone to represent the spread in the possible age of the cluster, an idea of where mass divisions lie can be found. This was done using the models of D'Antona & Mazzitelli (1994). An age of 0.5 Gyrs was chosen to represent a young Praesepe, and an age of 0.9 Gyrs as a more conservative estimate. The luminosities from the model were converted into magnitudes using bolometric corrections, as described in section (2.4). The colours were obtained using a temperature scale calculated from the M dwarfs, using their derived T_{eff} values (Jones *et al.* 1994).

4.5.3 Colour magnitude diagrams

Candidate Praesepe members were selected by their position in the IZ and RI colour-magnitude diagrams. Both diagrams were used where possible, and where an object only appeared in one, it was ensured that it was well separated from the background field stars.

The two colour magnitude diagrams produced are shown in Figure (4.4). The position of the M dwarfs as they would appear in Praesepe are shown by large crossed circles, defining where the VLM BD sequence should lie. Proper motion members from Hambly *et al.* (1995a) covered by this survey are shown as open triangles.

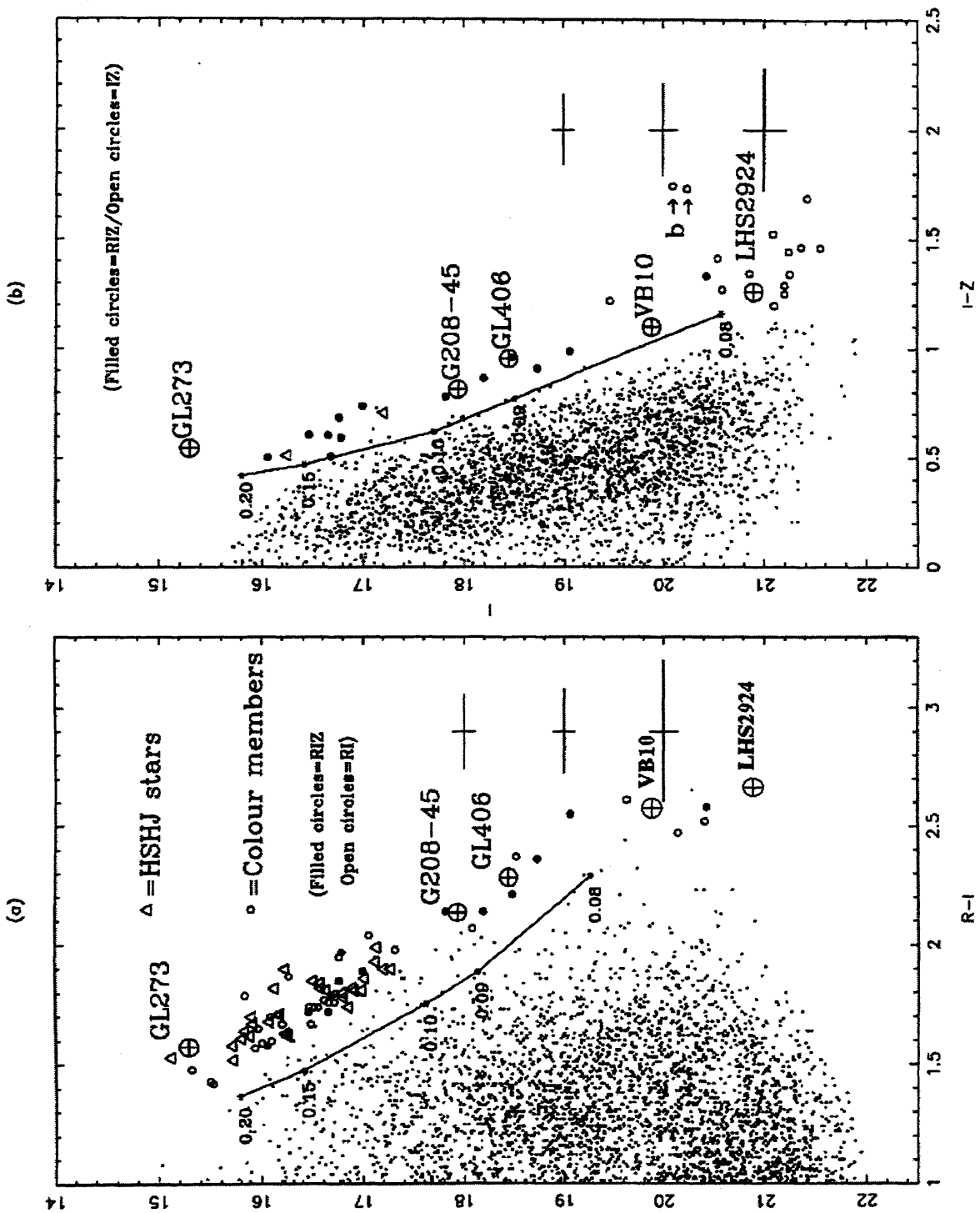


Figure 4.4: The I versus $R-I$, and I versus $I-Z$ colour magnitude diagrams for the survey. The the M dwarfs are shown by large crossed circles. Proper motion members are shown as open triangles. The circles are new photometric candidates, where filled circles indicate RIZ objects, and open circles indicates RI only objects in the first diagram and IZ only objects in the second. The isochrones shown in each diagram are from the models of D'Antona & Mazzitelli (1994), for ages of 0.5 and 0.9 Gyrs, in the first and second diagrams respectively. Two binary candidates are indicated by a 'b', and typical photometric errors are shown down the side of each diagram.

These help define the top of the stellar sequence, and enable the other photometric members brighter than $I_{\text{RGO}} \sim 17.5$ to be rejected as non proper motion members. The smaller circles represent the new photometric candidates found by this survey, where filled circles are RIZ objects in both colour magnitude diagrams, and open circles are RI objects in the first colour magnitude diagram, and IZ objects in the second. The dots are the background field stars, and several one colour photometric members have been classed as this due to their other colour being inconsistent with membership. The two isochrones of D'Antona & Mazzitelli (1994) for ages of 0.5 and 0.9 Gyrs are shown in the first and second diagrams respectively. Representative error bars are shown down the side of both colour magnitude diagrams at their appropriate I position.

Bolte (1991) showed that the majority of stars existing as binaries in Praesepe fall on a binary sequence, located $\simeq 0.75$ magnitudes above the single star sequence. The two stars indicated with 'b' in the second colour magnitude diagram stick out from the rest of the sequence, and have a colour magnitude position consistent with binarity. It is also possible that these objects are foreground stars.

It is clear from a comparison that the two isochrones are similar down to the $0.09M_{\odot}$ point, but that the BD limit of $0.08M_{\odot}$ moves down by $\simeq 1$ magnitude between the two ages. The true age of the cluster then determines how many of these candidates could be BDs.

4.5.4 Summary

The candidates then comprise 87 photometric members. Of these, 30 are known photometric and proper motion members from Hambly *et al.* (1995a), and 31 can be rejected as non proper motion members, because they are bright enough to have been considered in the proper motion survey. Between 15 and 19 are candidate BDs depending on the age of Praesepe. The remaining 7-11 are low mass Praesepe main sequence candidate members. The RIZ photometry and coordinates of the new candidate members form part of the table in Appendix (A.1). The candidates are labelled RIZpr 1-26, where the "RIZ" indicates the filters used in the survey, and "pr" is for Praesepe.

4.6 Luminosity and Mass functions

4.6.1 The mass luminosity relation

To begin with, a mass-luminosity relation $I(m)$ was derived, to convert the luminosity function into a mass function. The evolutionary tracks of D'Antona & Mazzitelli (1994), were used to provide luminosity and temperature as a function of mass for the more conservative age estimate of 0.9 Gyrs. The bolometric corrections described in section (2.4) were used to obtain absolute Cousins I magnitudes for each mass division in the model (from the luminosity), and then by adding the distance modulus of the cluster, the apparent magnitude in Praesepe was found. A polynomial fit to this data was made, giving,

$$M/M_{\odot} = 56.054 - (11.4130)I + (0.8760)I^2 - (2.9989 \times 10^{-2})I^3 + (3.8623 \times 10^{-4})I^4. \quad (4.2)$$

The data and the polynomial fit are shown in Figure (4.5).

4.6.2 Correction factors

The next step in deriving a mass function is to calculate the luminosity function. The Praesepe candidates were binned into I_{RGO} bins one magnitude wide, and mass values were assigned to the upper and lower bin limits, as well as the mid bin magnitude, using the mass luminosity relation. The number of stars in each bin then needed to be corrected by some factor to take into account contamination and incompleteness.

The contamination is from background stars that look like photometric members, and can be estimated by comparing the number of photometric members to the number of proper motion members that are also photometric members. The ratio of brighter proper motion members (open triangles in Figure (4.4)) to photometric members (circles plus triangle), is 50%. A correction factor of 0.5 is then appropriate for the brighter stars in the survey, and was extended to the fainter candidates also.

Because only the cluster centre was imaged, this incompleteness needed to be corrected for as well. This was done by following the procedure used by Hambly

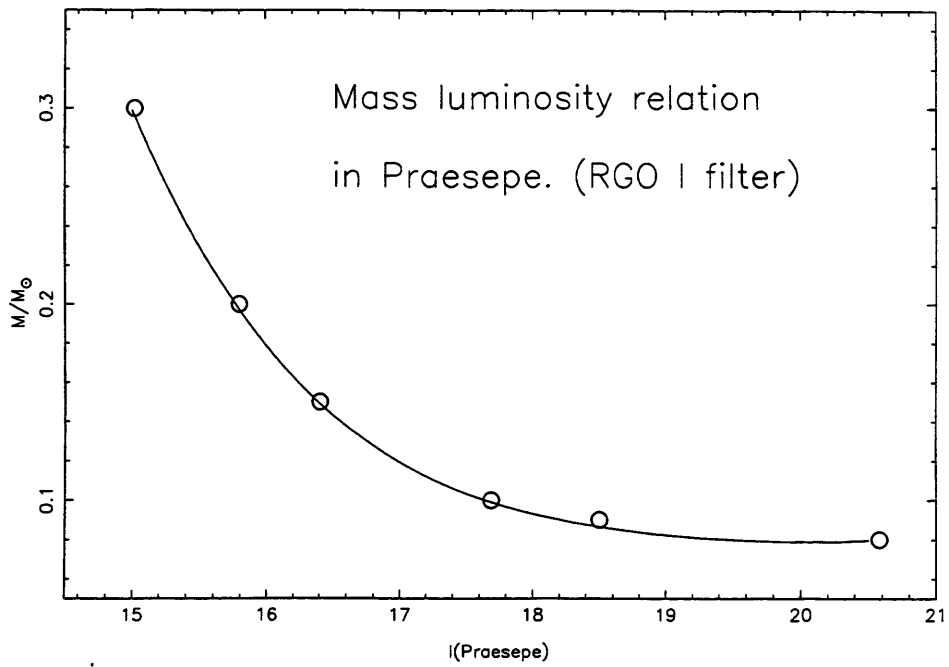


Figure 4.5: Mass luminosity relation in Praesepe for an age of 0.9 Gyrs. The data points from the model of D'Antona & Mazzitelli (1994) are shown as open circles, and a polynomial fit is plotted on top.

et al. (1995a) and Jones & Stauffer (1991). A surface density distribution of the form

$$\rho = \rho_0 e^{-r/r_0} \quad (4.3)$$

is assumed for each given cluster mass range, where ρ_0 is the central surface density of the cluster and r_0 is the characteristic scale length of the surface distribution. By integrating Equation (4.3), the total number of stars in the cluster can be found for the particular mass or luminosity range :

$$\int_0^{\infty} 2\pi(\rho_0 e^{-r/r_0})r dr = 2\pi\rho_0 r_0^2 \quad (4.4)$$

Therefore, the total number of stars in the cluster per I magnitude bin LF_I , follows from ρ_0 and r_0 . Since the highest mass bin used here overlaps with the Hambly survey, the value of r_0 for this bin was found using a linear relation between magnitude and r_0 derived from observed stellar distributions (Hambly *et al.* 1995b). For the fainter magnitude bins, values of r_0 were found using the ‘‘King’’ surface density distribution, which has been shown to fit globular and galactic clusters (more will be said on this in chapter 6). By equating this radial distribution to a Boltzmann distribution in the cluster centre, it can be shown that,

$$r_0 \propto \frac{1}{\sqrt{M}} \quad (4.5)$$

where M is the average mass of the stars in the bin. This derivation will be shown and discussed in Chapter 6.

The remaining values of r_0 were then calculated from equation 4.5, using the highest mass bin r_0 , and the mid-bin mass values. ρ_0 was obtained for each bin by multiplying the weighted numbers of candidates in each field by e^{r/r_0} using the cluster centre coordinates quoted in Table (4.1) to get r for each field, and averaging over all the fields.

4.6.3 The mass function

The mass function $N(m)$ was then found using,

$$N(m) = LF_I \frac{dI}{dm} \quad (4.6)$$

I_{RGO}	$\log M/M_{\odot}$	Candidates	weight	LF_1	$\log N(M, dM=1)$
16-17	-0.837	15	100%	250 ± 65	3.62
17-18	-0.977	8	100%	136 ± 48	3.71
18-19	-1.052	5	50%	54 ± 25	3.71
19-20	-1.085	3	50%	36 ± 21	3.87
20-21	-1.094	8	50%	82 ± 29	4.23
21-22	-1.149	9	50%	118 ± 37	4.39

Table 4.3: Praesepe luminosity and mass function results

and the results are summarised in Table (4.3). The luminosity and mass functions are plotted in figures (4.6) and (4.7), as the filled circles. Also plotted as open squares are the luminosity and mass functions of Hambly *et al.* (1995b). It can be seen that the two sets of results join onto each other closely in the complete region of the Hambly survey, as a result of the correction factor used. Two best fit lines are also plotted on the MF diagram. The steeper line is a fit to all the points below $0.4M_{\odot}$, and has a slope of $\alpha = 1.8 \pm 0.2$. The other line ignores the lowest two mass points, reaching down to the BD limit, and has a slope of $\alpha = 1.4 \pm 0.1$.

4.7 Discussion

The value of α found by Hambly *et al.* (1995b) is ~ 1.5 down to the completeness limit of their survey ($0.1M_{\odot}$), which is in agreement with that of the old M dwarf population near the sun. The new RIZ survey data agrees well with the Hambly survey in the over-lapping mass range, and it continues the slope of $\alpha \sim 1.5$ (to with the error bars of the fit) down to the BD limit. However, when the lowest mass points are included, the slope increases, and it is apparent that the slope of the MF could be steepening to as much as $\alpha = 3.8$ into the BD range. As was discussed in section (2.5), lower mass stars and BDs begin to contribute more in terms of mass per unit mass interval than higher mass stars when α becomes larger than 1.

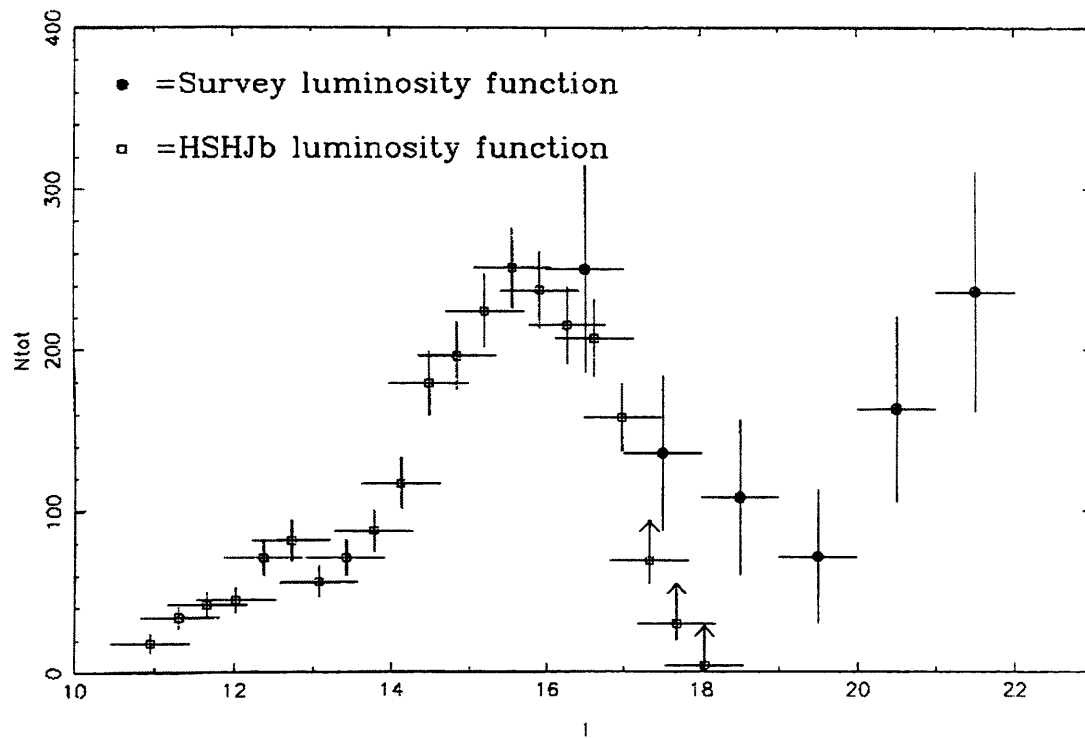


Figure 4.6: The Luminosity function for Praesepe, binned into divisions of 1 magnitude in I . Open squares indicate data found by HSHJb, where arrows indicate lower limits. Filled circles are data from the current survey.

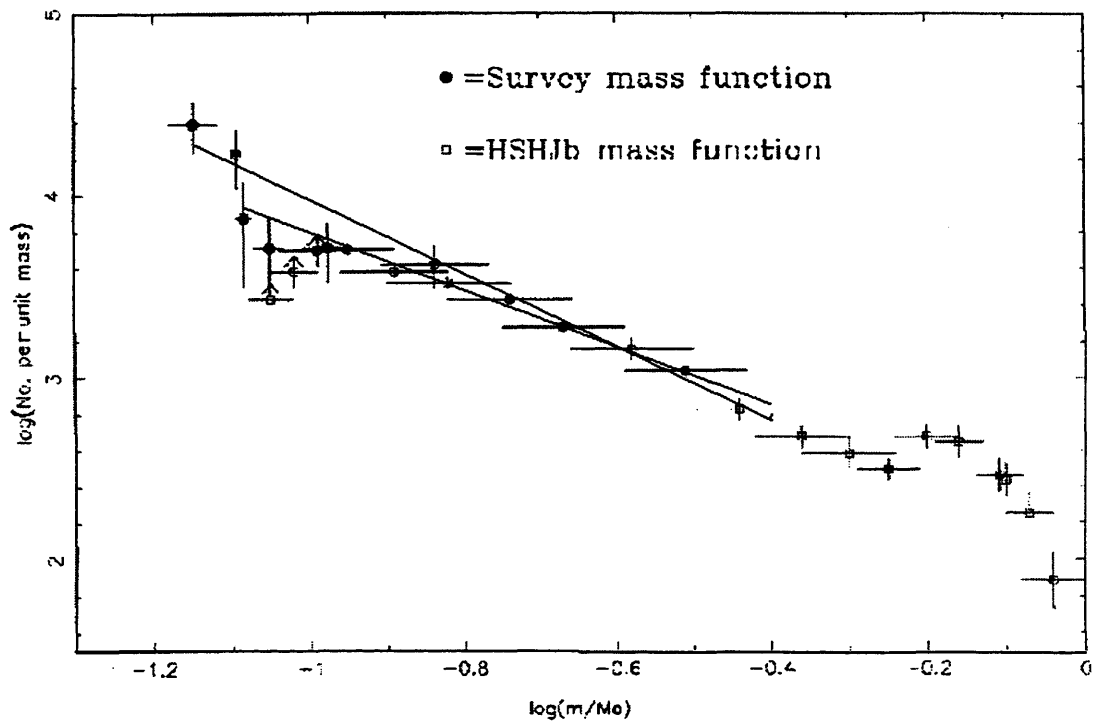


Figure 4.7: The Mass function for Praesepe. The symbols are the same as for Figure 4. Two best fit lines are shown; The steeper one is a fit to all the data below $0.4M_{\odot}$, while the other ignores the two lowest mass bins.

However in order for BDs to dominate the cluster mass, α must be larger than about 2 (because the mass range for BDs is much less than the mass range covering the rest of the cluster stars). This new mass function therefore indicates a possible large population of BDs in Praesepe.

However, there are several sources of error that need to be considered when making this interpretation. The errors in the Z magnitudes of objects that have no R magnitude will be more important, since the colours of these objects are unverified. Since the R cut off occurs in the $I_{\text{RGO}} = 20\text{-}21$ and $21\text{-}22$ magnitude bins, the number of candidates in these bins will therefore be more uncertain than in the brighter bins. These are the points that suggest the possible increase in slope of the mass function, and until follow up observations verify the membership status of these objects, these last two mass function points must be considered as upper limits.

Also, it is worth noting that the main source of error in the mass function is this uncertainty in the membership of the candidates, and any uncertainty in the age of the cluster (and therefore in the mass luminosity relation) is a secondary consideration.

Finally, although the shape analysis will have removed many faint galaxies from the data, the technique is by no means perfect, and some of the candidates may still be red galaxies.

4.8 White dwarfs

The U B and V photometry was plotted in a two colour U-B versus B-V diagram. This diagram is shown in Figure (4.8). Main sequence star can be seen following the standard stellar locus of FitzGerald (1970), dipping down because of the Balmer discontinuity. White dwarfs however, being degenerate helium bodies lie on a straight (black body) line above the main sequence. White dwarf candidates were selected from this region provided they fall in roughly the correct position in the V versus B-V colour magnitude diagram, corresponding to the position of a sample of white dwarfs (Liebert, Dahn & Monet 1988) shifted to the Praesepe distance. The photometry and positions of all the white dwarf candidates is given in Appendix (A.1).

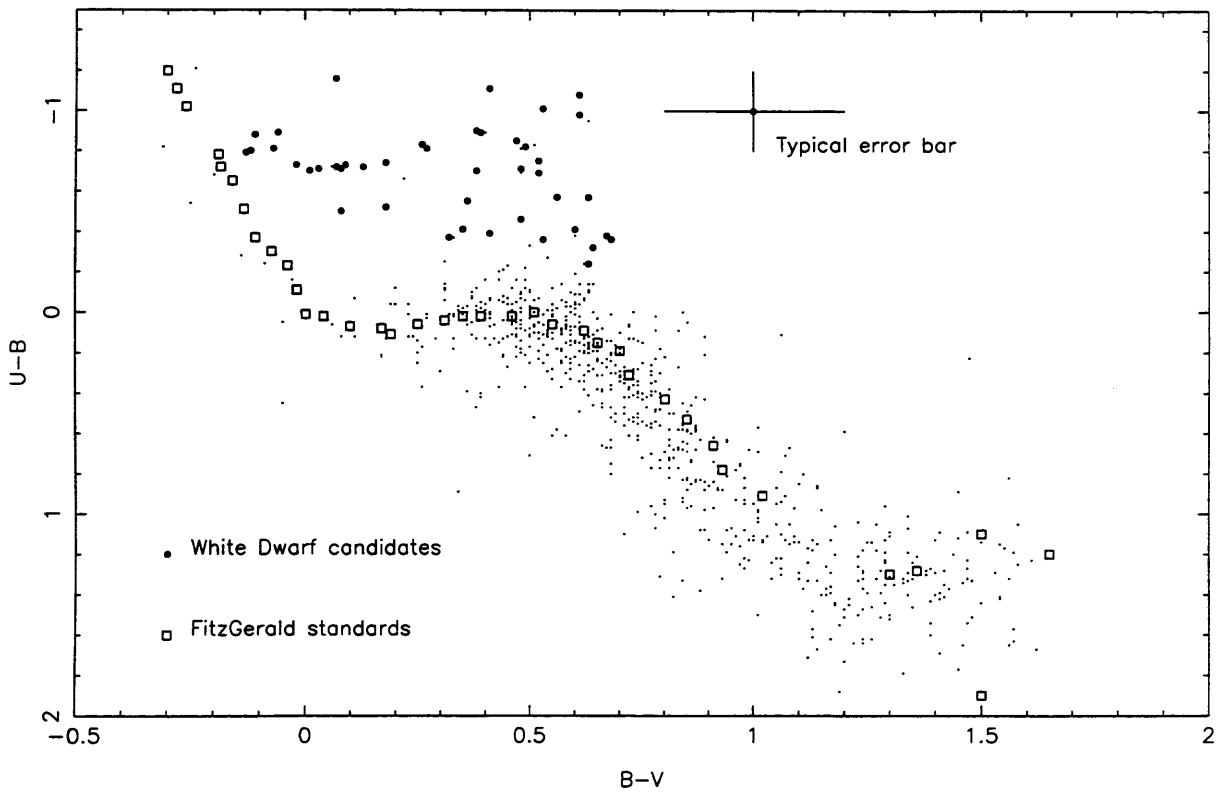


Figure 4.8: The $U-B$ versus $B-V$ two colour diagram for the Praesepe fields. FitzGerald standards are shown by open squares, and the white dwarf candidates are indicated by filled circles.

4.9 Conclusions

Comparing RIZ photometry with theoretical models, I have found 26 new candidate low mass Praesepe members (see Appendix (A.1) and (A.1) for photometry, coordinates and finder charts). These have I magnitudes down to $I=21.5$ and 15 to 19 of them should be BDs if membership is confirmed.

Confirmation of membership requires follow up observations. Proper motions can only be measured after an interval of about 20 years, and radial velocities are difficult to obtain, even with the largest telescopes, because of the faintness of some of the candidates. However, infrared photometry would verify the redness of these candidates very well, since for example the I-K colour is a very strong T_{eff} indicator for late type stars. Also, the smaller pixels scale of infrared detectors would make galaxy identification easier.

Further follow up using low resolution spectroscopy showing a late M spectral type should give a reasonably compelling indication of membership, since the likelihood of finding a sufficiently late field star contaminating the cluster sequence is very small. If one uses the field luminosity function of Kirkpatrick *et al.* (1994), one would expect to find only 1.2 and 0.6 late M field stars per unit magnitude interval in the R I, and I Z survey areas respectively.

This work has been published in Pinfield *et al.* (1997), and a number of the candidates have been followed up with K band infrared photometry, the results being discussed in the next chapter.

Chapter 5

Praesepe: Infrared photometry

5.1 Introduction

This Chapter will focus on Infrared follow up photometry of Praesepe candidate members. The candidates come from two sources. The first is a sample of proper motion members from the survey of Hambly *et al.* (1995a). The second is a collection of my RIZpr photometric candidates which were presented in Chapter (4) and published in (Pinfield *et al.* 1997) (“RIZ” denotes the filters used in the survey, and “pr” is for Praesepe).

The Hambly survey covers 19 square degrees, and covers the magnitude range ($11.0 < I < 17.5$), by employing R (590 nm) and I (715 nm) photographic emulsions (these being more sensitive to redder, low-mass stars than the visual pass band emulsions used previously). The HSHJ catalogue contains 515 probable cluster members, each of which has an associated probability, calculated from Gaussian type distributions fitted to the proper motion vector point diagram of all photometric candidates. Hambly *et al.* (1995b) discusses the distribution and completeness of the catalogue in more detail.

The RIZpr candidates that were chosen consist of 11 of the 26 sources listed in Appendix (A.1). They cover the magnitude range ($17.5 < I < 20.14$), and 5 are two-colour candidates.

The aims of this chapter are firstly, to identify non members in the HSHJ sample (and thus check the effectiveness of the proper motion survey). RIZpr candidates

will undergo the same test to identify non members. I will compare the latest model predictions to the observations, taking into account a binary population, and then identify these binaries and establish how large the binary fraction is. Finally, I will calculate masses for the RIZpr members, and discuss any BD candidates.

The infrared photometry consists of K magnitudes for the sample of 90 HSHJ proper motion members, with J and H magnitudes for 54 of these, as well as K magnitudes for the 11 RIZpr candidates.

5.2 Observations

5.2.1 The HSHJ Proper motion members

Targets were selected from the list of 515 proper motion members in order to give a good spread in magnitude. 54 stars in the magnitude range ($13.2 < I < 17.5$) were observed at J, H and K with IRCAM3 at UKIRT (see section (3.5)) on 12th–13th December 1993. The weather conditions were photometric on both nights, albeit windy. Photometry for stars at the brighter end of the HSHJ survey was obtained by I. A. Steele; He observed 31 stars ($I \leq 13.2$) at K with the SAAO (South African Astronomical Observatory), and 5 stars ($I \leq 13.0$) with the Carlos Sanchez Telescope on Tenerife.

IRCAM3 photometry was reduced with (STARLINK: IRCAMDR), and the J, H, and K magnitudes are on the UKIRT system. The mean photometric errors were found to be $\sim \pm 0.03$ at J and H, and $\sim \pm 0.04$ at K.

SAAO and TCS photometry is single channel photometer data. All the reduction was done at the observatory by the telescope operators. The photometry was converted into the UKIRT system using the transforms of Bessell & Brett (1988).

All of the R and most of the I magnitudes for the Praesepe proper motion stars are the COSMOS magnitudes from the Hambly catalogue converted to the Cousins system using the polynomial conversions given in Bessell (1986). The errors will be essentially the same as those given in Hambly *et al.* (1995a) for the photometric accuracy of the COSMOS magnitudes, which are quoted to be $\sim \pm 0.1$ magnitudes in both wavebands.

Figure (5.1) shows the I, R-I colour magnitude diagram for the total HSHJ sample (shown as dots) with the stars that had K photometry obtained highlighted as filled circles.

The J, H, and K photometry is given in Appendix (A.3), as well as the R and I magnitudes (converted to the Cousins system).

5.2.2 Photometry of RIZpr candidates

The RIZpr targets were chosen in order to extend the HSHJ sequence to fainter magnitudes. In general candidates with an R-I colour were chosen, where the likelihood of contamination is less (due to the longer base line of the filters).

K_{SHORT} photometry for 11 RIZpr candidates was obtained once again by I. A. Steele during international time using WHIRCAM on the William Herschel Telescope, La Palma. K_{SHORT} is a relatively new filter with a band pass intermediate between K and K'. Transforming from K_{SHORT} to K can be done by using half the correction of K' to K, which is well defined by Wainscoat & Cowie (1992). For stars redder than $H-K=0.4$, the correction flattens off to $K_{\text{SHORT}}-K \simeq 0.035$.

The I-K colours found are given in Appendix (A.1), along with the RIZ photometry and coordinates.

5.3 Cluster Membership

Proper motions are not a certain guarantee of membership. To define their sample, Hambly et al. first extracted all stars from the scanned plates having proper motions within 2σ of the known cluster proper motion. This sample of stars will be dominated by cluster members, with relatively few contaminating background stars. Thus, the photometry of these stars could then be used to define the cluster sequence on a colour magnitude diagram. All stars which lay below this cluster sequence were then rejected as non-members. Membership probabilities were computed for the remaining stars, and only stars with membership probabilities greater than 40% were selected for the HSHJ catalogue. The total number of HSHJ candidates is 515.

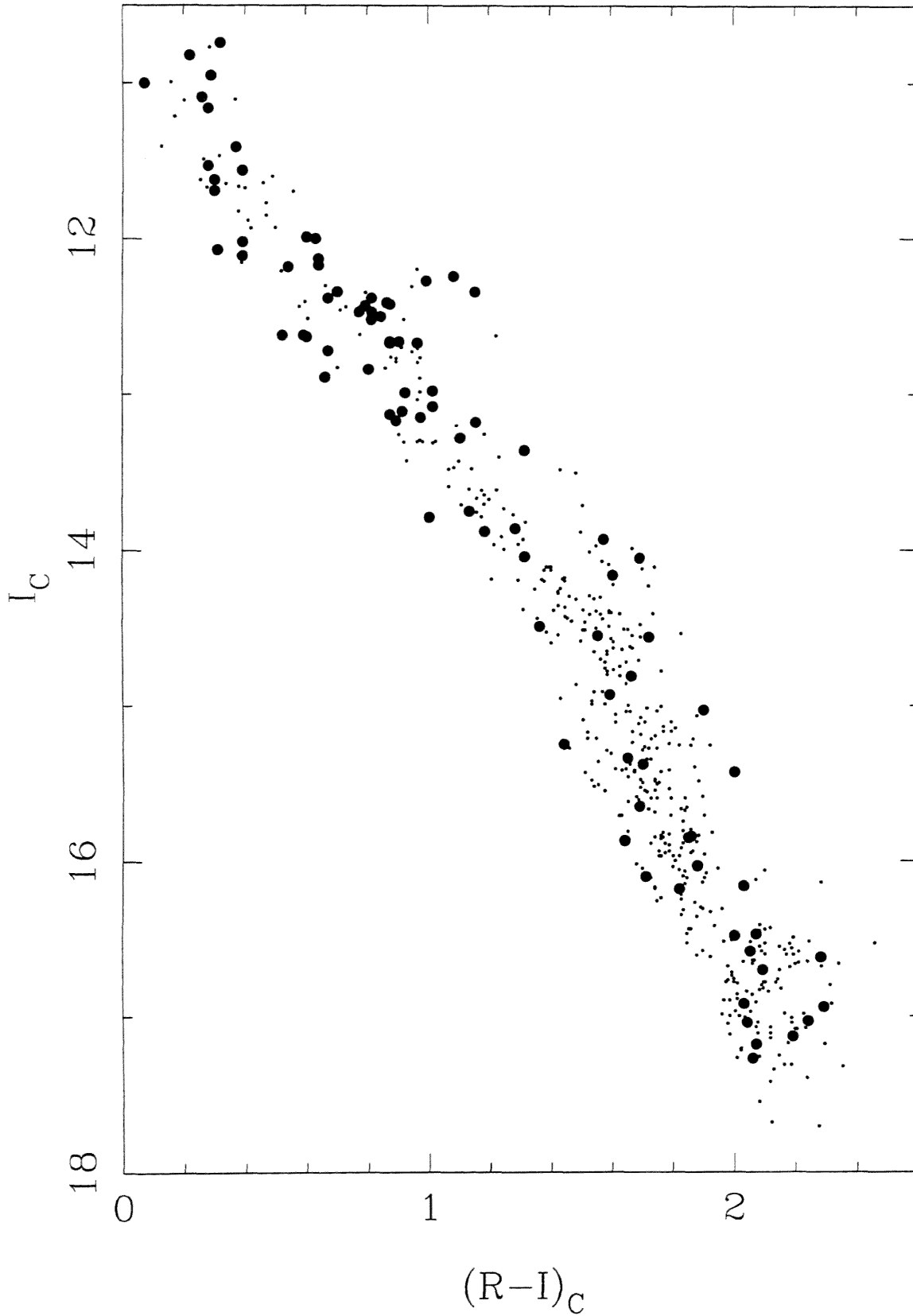


Figure 5.1: The (I_c, R_c-I_c) colour magnitude diagram of the HSHJ proper motion members (shown as dots). The 90 stars selected for infrared photometric follow up are shown as filled circles. This sub-sample covers the magnitude range $(11.0 < I_c < 17.5)$.

The sample of 90 HSHJ target stars selected each has such a membership probability, and one can calculate the number of cluster members expected in the sample, by adding up these probabilities. I calculated the expected number of members to be 80 out of the sample of 90.

In order to see how accurate this prediction is, members can be selected or rejected using the new infrared photometry.

5.3.1 I K selection

Since I-K is a more sensitive T_{eff} indicator than R-I or I-Z, one can verify the redness of a candidate by use of the K photometry. A more T_{eff} sensitive colour magnitude diagram will result, and non members can be identified.

Figure (5.2) shows the (I, I-K) colour-magnitude diagram for the 90 HSHJ stars (shown as filled circles), as well as for the RIZpr candidates (open triangles). Overlaid on the plot are the isochrones of Chabrier & Baraffe (1997) for a distance modulus of 6.05, and ages of 500Myrs and 1Gyr, representing the range of Praesepe ages found by various authors (see Hambly *et al.* (1995b)). Non cluster members were flagged if they fell noticeably to the left of the isochrones. The selected non members have been circled, and comprise 7 of the HSHJ sample, and 3 of the RIZpr candidates. These stars are flagged as non members in Appendices (A.3) and (A.1) respectively.

5.3.2 J H K selection

As a further test of membership we can plot the infrared two-colour (J-H, H-K) diagram (see e.g. Leggett (1992), Leggett, Harris & Dahn (1994), Reid & Gilmore (1984) and Mould (1976)). The most important opacity sources in red dwarf atmospheres are the TiO bands in the optical to red regime, the continuum H^- opacity for both the optical and infrared, and the water bands in the infrared. Mould (1976) and Leggett (1992) show that J-H is metallicity dependent, with metal-poor stars bluer than metal-rich stars.

Figure (5.3) shows the two-colour (J-H, H-K) diagram of the 54 HSHJ stars imaged at UKIRT. Overlaid on the plot is the theoretical isochrone (500Myrs age)

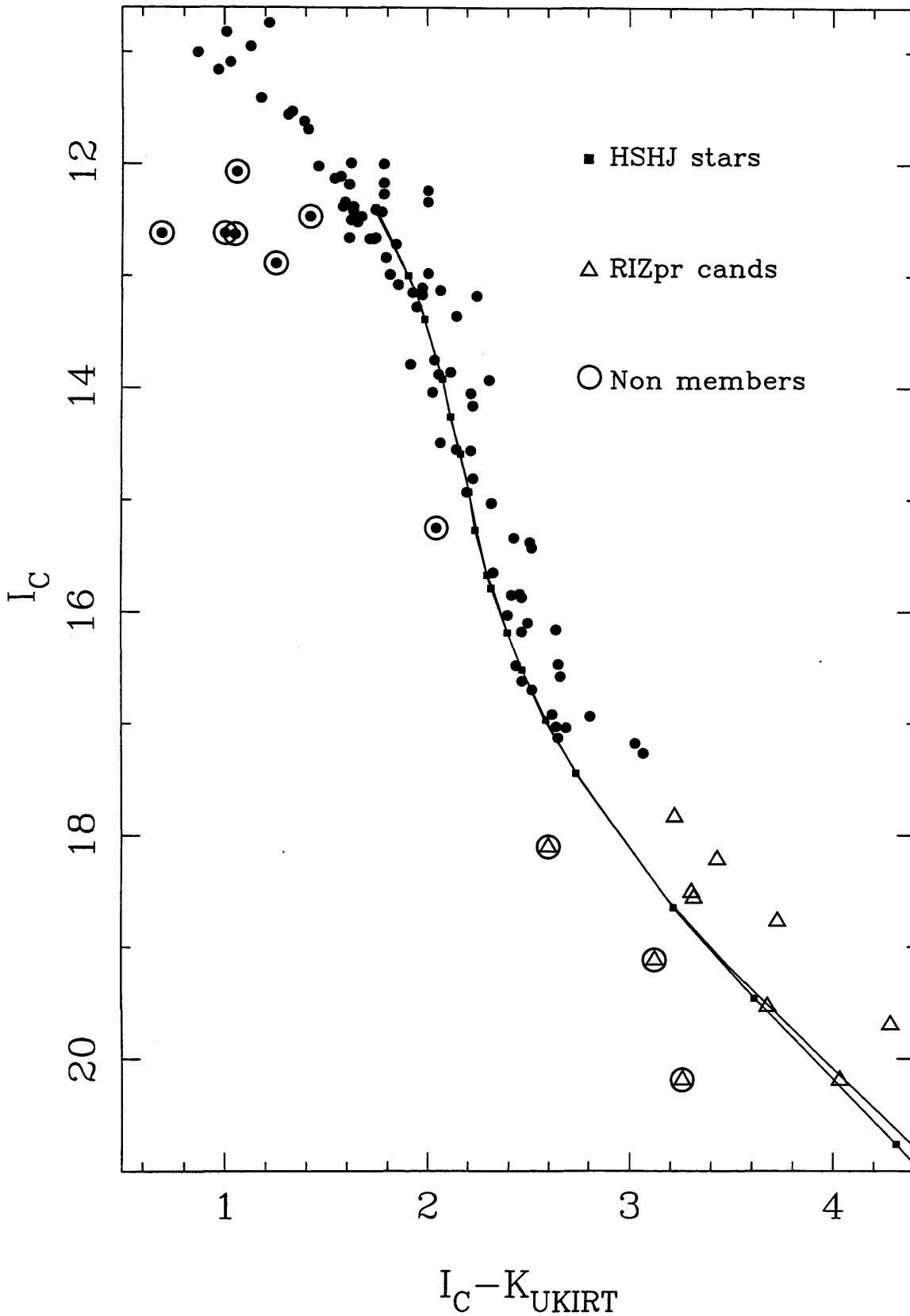


Figure 5.2: The (I, I-K) colour magnitude diagram containing the HSHJ stars (filled circles) as well as the RIZpr candidates (open triangles). Two isochrones are over plotted, from the models of Chabrier & Baraffe (1997) for Praesepe ages of 500 Myrs and 1 Gyr. Non members identified using these isochrones have been circled.

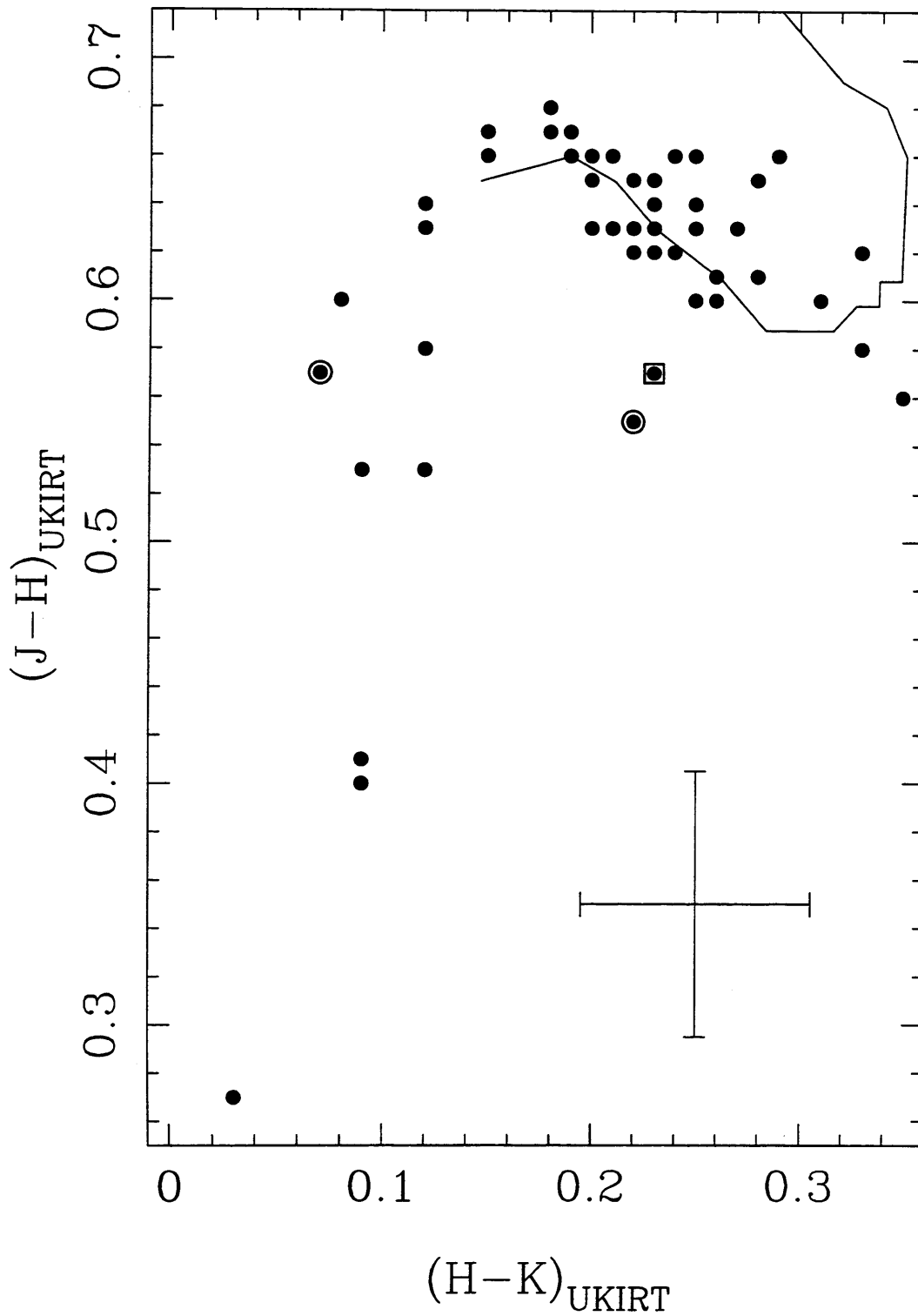


Figure 5.3: The $(J-H, H-K)$ two colour diagram of the 54 HSHJ stars for which J, H and K were obtained. Two of the previously identified non members are circled as before, and one other star has been indicated with a square, as being a possible non member from this diagram.

of Chabrier & Baraffe (1997), and the photometric errors are indicated at the foot of the plot. 2 of the previously identified non members are indicated by circles as in the I, I-K plot. The remainder of the stars follow the isochrone quite closely, with the brighter stars turning downwards at $H-K=0.1$. The 2 circled non members do seem to stand some what away from the majority of the other stars, and there is 1 other star in particular that lies blue-ward of the isochrone (indicating that it is a metal poor field star). This possible non member has been indicated with an open square. Although the photometric errors are potentially large enough to account for the difference, this stars has been flagged with a ? as a possible non member in Appendix (A.3).

Since 54 out of 90 of the HSHJ sample were imaged at J, H and K, and only 1 possible non member identified, it is clear that using (I, I-K) is a very effective way to select cluster members. Making a rough correction to the rest of the sample, I would expect ~ 2 ($90/54$) stars to be rejected by the (J-H, H-K) photometry, to add to the 7 stars rejected from the (I, I-K) photometry. This is 9 non members in total, and leaves 81 members from the sample of 90. This is extremely close to the value of 80 predicted by the probability analysis carried out for the Hambly survey, and I therefore conclude that these probabilities are a very accurate indicator of membership.

5.4 Binaries

It can be shown (see Steele & Jameson (1995)) that the majority of stars systems that are binaries will lie on a “binary sequence” 0.75 magnitudes above the single star sequence, i.e. the line defined by equal mass binaries. Only systems with more extreme mass ratios ($q=0.3$ or less) would lie in the intervening region. Recent Hipparchos results (vanLeeuwen & Hansen Ruiz 1997) demonstrate the binary sequence for higher mass Pleiades stars very nicely, and show little scatter due to variations in chemical abundance between stars.

Figure (5.4) shows the (I, I-K) colour magnitude diagram for the HSHJ sample as well as the RIZpr candidates, with the 500Myrs isochrone of Chabrier & Baraffe

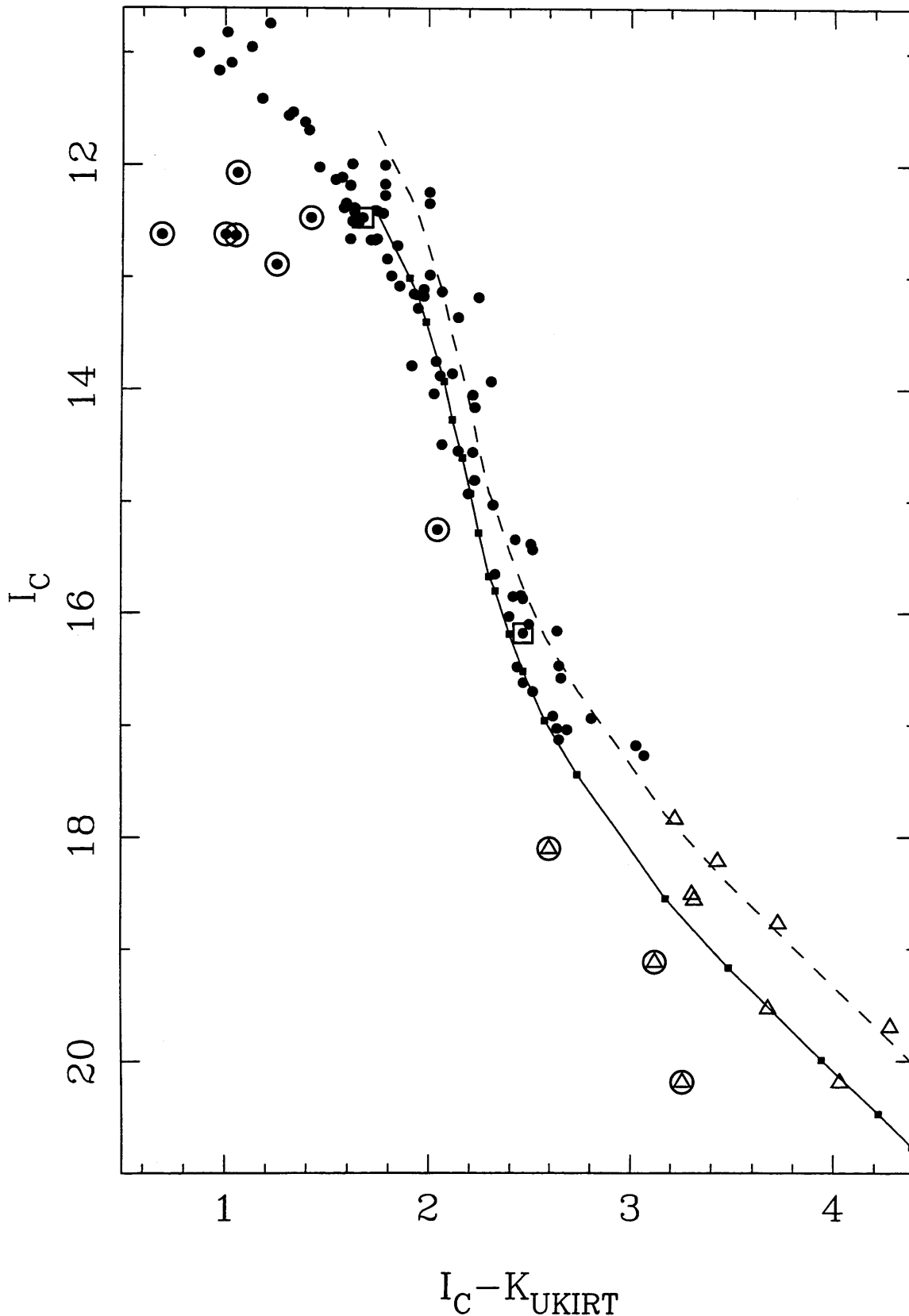


Figure 5.4: The (I, I-K) colour magnitude diagram indicating the binary sequence. Symbols are the same as in Figure (5.2). The 500 Myr isochrone is over plotted as a solid line, and the equal mass binary sequence (0.75 magnitudes above this) as a dashed line. The squares denote masses from 0.70 to 0.072 M_{\odot} in various mass intervals, with the faintest 5 points comprising 0.10, 0.09, 0.08, 0.075 and 0.072 M_{\odot} .

(1997) as well as the equal mass binary sequence (0.75 magnitudes above this) overlaid on the plot. There is significant scatter above the single star isochrone (almost one magnitude), which can not be explained solely in terms of the cluster depth, or photometric errors. The tidal radius of the cluster is some 12 parsecs, corresponding to a depth effect of only 0.3 magnitudes (K. Holland, priv. comm). I therefore ascribe this dispersion to binarity, and it can be seen that the single and double star isochrones encompass the spread in magnitude at any given colour extremely well.

In order to estimate the binary fraction from Figure (5.4), I chose to select binaries as objects which lie above the locus of the midpoints between the binary and single-star sequences. All HSHJ stars flagged in this way are indicated as such in Appendix (A.3). I find that in the region covered by the isochrone, there are 27 HSHJ binary systems, out of a possible 58, which is 47%. This is in very good agreement with the value of 46% found by Steele & Jameson (1995) for the Pleiades, who used the same method.

Of the RIZpr candidates that are members (8 out of 11), 4 lie very close to the binary line. These were accordingly flagged as binary in Appendix (A.1).

5.5 Object masses - Brown Dwarfs

In Figure (5.5) I have plotted the fainter HSHJ stars and the RIZpr candidates using the same symbols as before, as well as RPr1, which is the spectroscopic BD found recently in Praesepe (see section (2.6)). I have over plotted the isochrones of Chabrier & Baraffe (1997) for Praesepe ages of 500Myrs, and 1 Gyr. These lines are identical down to $I=18.75$, after which the 1 Gyr isochrone falls slightly below the 500 Myr one. Incremental mass points have been indicated on these lines, using +'s for the 500 Myr points, and x's for the 1 Gyr points. These points are labelled with their appropriate mass (in Jupiter masses) above, and below the isochrones for the 500 Myr and 1 Gyr points respectively. The equal mass binary sequence is also indicated for each age, with a dashed line.

The two isochrones are very close together, and the RIZpr members as well as

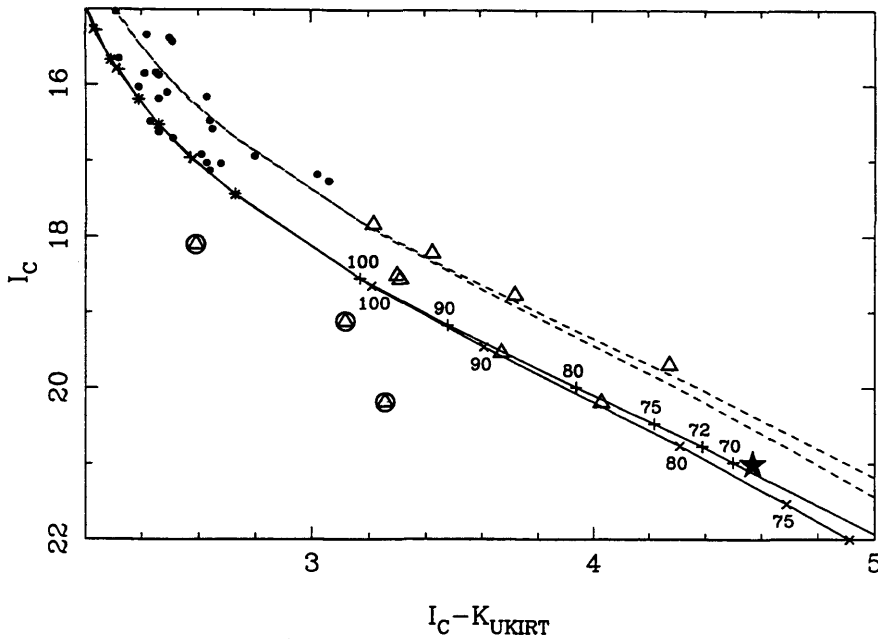


Figure 5.5: The (I, I-K) colour magnitude diagram showing the RIZpr members. The faintest HSHJ stars appear in the top left hand corner. RPr1 (a spectroscopic BD in Praesepe) is shown as a filled star, in the bottom right corner. The 500 Myr and 1 Gyr isochrones are over plotted, with incremental mass points indicated by +’s for the 500 Myr points, and x’s for the 1 Gyr points. These points are labelled with their appropriate masses (M_J) above and below the isochrones for 500 Myrs and 1 Gyr isochrones respectively. The equal mass binary sequence for each age is also shown as a dashed line.

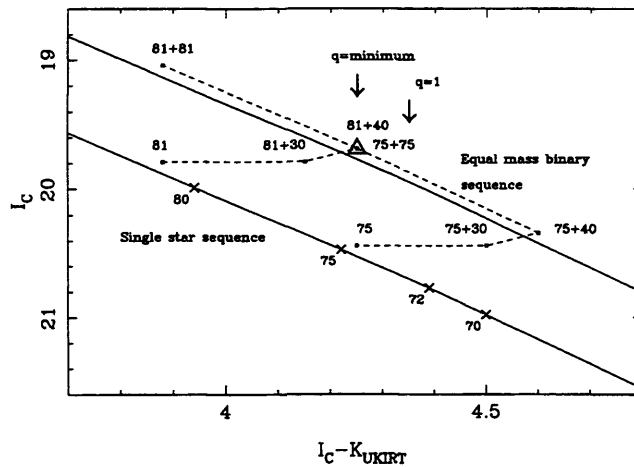


Figure 5.6: The (I, I-K) colour magnitude diagram showing the tracks (as dashed lines) of a VLM and a BD as BD binary companions of various masses are added to the system. The single star sequence for an age of 500Myrs is indicated, with mass divisions shown by x’s, as well as the equal mass binary sequence. The two tracks meet at the open triangle, meaning that this could be a combination of two BDs (75 M_J each) or a VLM (81 M_J) and a BD (40 M_J).

RPr1 all lie very close to either the single star or binary sequences of both ages. The non gray atmosphere models produce results very close to these observations.

In order to calculate the mass of these objects, they need to be divided into two groups; single stars, and binary systems. Calculating the mass for the single stars was done by simply using the model predictions of Chabrier & Baraffe (1997), but for the binaries it is some what more complicated. Steele & Jameson (1995) computed (I, I-K) tracks for VLM and BDs, as companions of varying mass are added to the system. As an example, I have illustrated two such tracks in Figure (5.6). One track is that of a VLM (81 Jupiter masses (M_J)), while the other is for a BD (75 M_J). As the binary companion's mass increases, the system moves redward of the single star, and approaches the equal mass binary sequence, reaching it when the binary mass is 40 M_J . This point is ~ 0.1 magnitudes brighter than the I magnitude of the single star. As the mass of the binary increases, the system moves up, along the equal mass sequence, until the secondary reaches the mass of the primary. This point is 0.75 magnitudes above the original single star position. The open triangle represents the position of RIZpr 18, and it is clear from this example that either the 75+75 M_J (when the mass ratio q equals 1) or the 81+40 M_J ($q = \text{minimum}$) positions are equally valid for this source. These are the two extreme cases, and encompass the possible masses of 75-81 M_J for the primary, and 40-75 M_J for the secondary.

It is clear from this discussion that all the RIZpr members on the equal mass binary sequence are binary systems with mass combinations ranging between these two extremes;

- The binary components could be of equal mass, in which case each star's magnitude would be 0.75 magnitudes fainter than the binary.
- The binary could have only just joined the equal mass binary line, when the higher mass binary member would be ~ 0.1 magnitudes fainter than the binary, and the lower mass member would be $\sim 0.04M_{\odot}$.

I calculated the binary component mass values for these two extreme cases ($q = \text{minimum}$ and $q = 1$ from Figure (5.6)), thus obtaining the range of possible binary combinations. Because of the age uncertainty of Praesepe, I calculated masses using

Age →	500 Myrs		1 Gyr	
RIZpr no.	M (M_J) (q=1)	M (M_J) (Minimum q)	M (M_J) (q=1)	M (M_J) (Minimum q)
2	91+91	104+40	94+94	106+40
8	98+98	115+40	101+101	117+40
18	75+75	81+40	80+80	85+40
21	83+83	93+40	87+87	96+40
RIZpr no.	M (M_J)		M (M_J)	
1	77		82	
4	99		101	
11	84		87	
20	100		102	

Table 5.1: The masses of the RIZpr Praesepe members. The upper portion of the table contains the binaries, and gives the masses of each binary component assuming both a mass ratio (q) of 1, and also a minimum mass ratio (allowing that the binary is on the equal mass binary sequence). The lower portion of the table contains the masses of the single star RIZpr members. Masses were calculated for Praesepe ages of 500 Myrs and 1 Gyr, and are given in Jupiter masses (M_J).

the 500 Myrs and 1 Gyr model isochrones, thus producing two sets of values. These mass values are shown in Table (5.1). The top portion of the table contains the binary members, with equal and minimum mass ratio binary combinations, for both Praesepe ages. The lower portion of the table contains the single stars, with mass values for each Praesepe age. The masses are all given in Jupiter masses.

Of the single stars members, the lowest mass object is RIZpr 1. If Praesepe is 1 Gyr old, this object is $0.082M_\odot$, however if Praesepe is younger (500Myrs), RIZpr 1 will have a mass of $0.077M_\odot$, and will consequently be a BD. The remaining single star members are all VLM.

All of the binary star members potentially contain a BD with a mass as low as $0.04M_\odot$. However, it is likely that the companion is more massive than this, with

an upper mass limit when $q=1$. The faintest binary star member is RIZpr 18, which has an upper limit to the mass of the binary companion of $0.08M_{\odot}$ and $0.075M_{\odot}$ for Praesepe ages of 1 Gyr and 500 Myrs respectively. This binary therefore contains either 2 BDs with masses near the stellar limit, or 1 VLM and 1 BD with a mass in the range ($0.04 < M/M_{\odot} < 0.08$).

5.6 Conclusions

This chapter has achieved several goals.

- Firstly, the infrared photometry of the HSHJ sample has weeded out several non members, and verified the quality of the HSHJ survey, by finding almost exactly the expected number of members (from the probability calculations of Hambly *et al.* (1995a)) from the sample of 90.
- The theoretical models of Chabrier & Baraffe (1997) fit the experimental data very well within the limits of experimental error.
- Using the latest non gray atmosphere models, I have flagged 47% of the HSHJ members as binaries. - A number that agrees very well with 46% for the Pleiades (Steele & Jameson 1995).
- The RIZpr candidates that were followed up at K proved to be mostly cluster members (8 out of 11 lie on or above the single star sequence). Of these, 4 were flagged as binaries, as would be expected if the 47% from the HSHJ stars propagates to the fainter magnitudes of the RIZpr members.
- I calculated mass values for all the RIZpr members, and determined that RIZpr 1 is potentially a free floating BD, and that RIZpr 18 contains at least 1 BD, possibly 2 locked up in a binary system.

Concerning this last point, the identification of VLM and BD binary systems is crucial, especially in coeval samples such as open clusters. Once sufficient numbers of low mass systems with measurable radial velocity curves are found, they will enable direct measurements of the mass-luminosity relationship.

Clearly the RIZ survey discussed in Chapter (4) has been successful in finding potential cluster members, since the success rate of the infrared follow up was 73%. Several of the fainter RIZpr candidates could well be BDs, and obtaining K photometry for these will confirm or reject them as BD Praesepe members. Since the success rate of the RIZpr candidates followed up is higher than the 50% assumed previously, this will increase the values of the mass function for the bins covering $17 \leq I \leq 20$ shown in Chapter (4). The gradient then becomes $\alpha = 1.6 \pm 0.1$, which is once again consistent with the field LF.

Chapter 6

The mass of the Pleiades

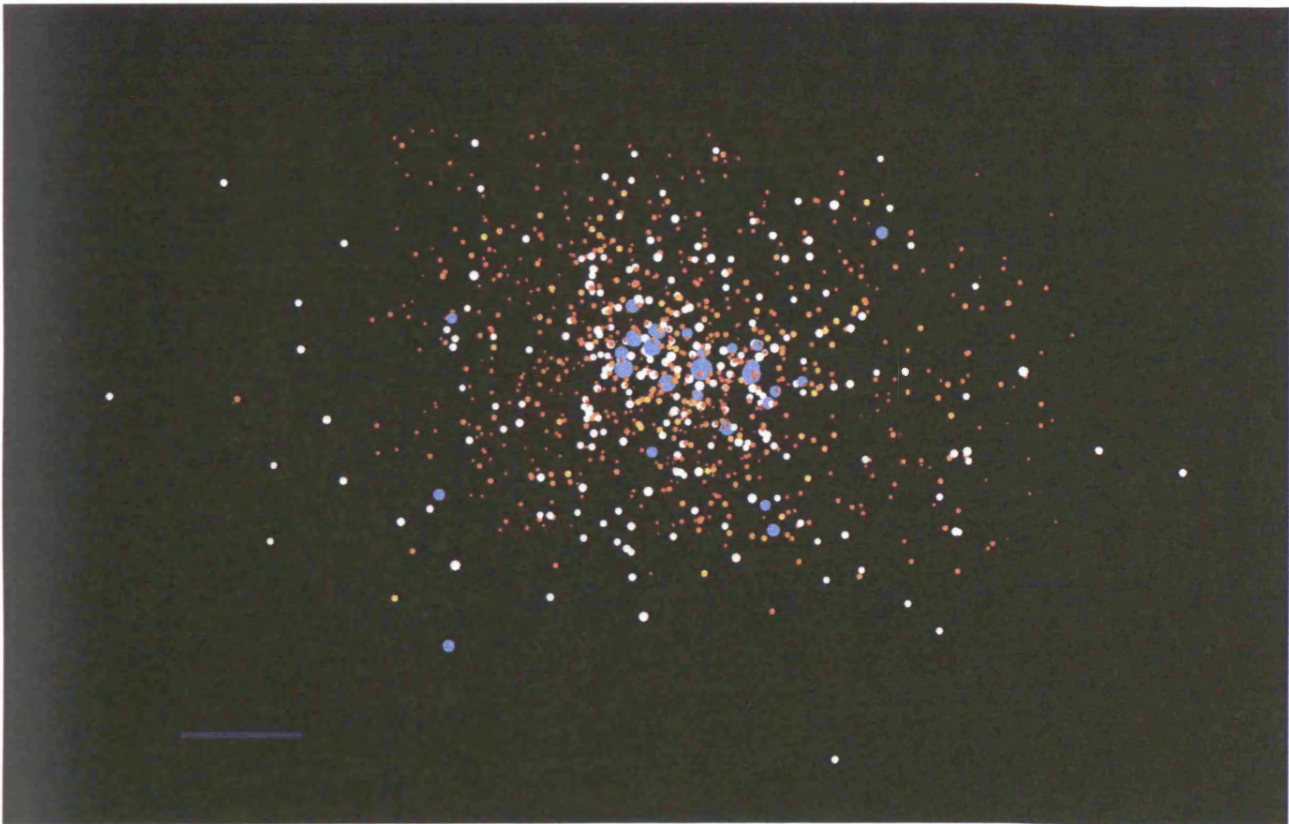


Figure 6.1: The Pleiades.

6.1 Introduction

The work so far described in this thesis has been focussed on the results of deep photometric surveys for BDs in Praesepe. This chapter takes a different approach to the pursuit of BDs. Firstly, the open cluster being considered is the Pleiades, but more importantly, the approach is based on modelling the distribution of cluster stars that have already been identified, and the work described in this chapter has been written up as a paper, and submitted to MNRAS.

The general approach to modelling the Pleiades will be the same as that taken for globular clusters (see for example Da Costa & Freeman (1976)). Although there are of course many important differences between open and globular clusters in general, the approach should be applicable to the Pleiades, the reasons for which will be discussed in the next section.

Having modeled the Pleiades, which in itself yields many useful cluster parameters describing the distribution of stars and potentially the distribution of any BD population, the dynamics of the known Pleiades stellar population will be analysed using the virial theorem to look for evidence of any large as yet undiscovered BD population in the Pleiades.

6.2 The dynamics of star clusters

When a star cluster forms out of a molecular cloud, all its stars will have essentially the same velocity independent of their mass. However, as stars move across the cluster they encounter other stars, and interact gravitationally. The force acting on each of the interacting stars will of course be the same (due to their combined gravitational pull), but the resultant acceleration of each star will be inversely proportional to the mass, and so will be larger for the lower mass stars. As a result, the lower mass stars in the cluster gain kinetic energy from the higher mass stars, until complete equipartition of energy is reached. It will take several mean free times to achieve equipartition, this time being known as the relaxation time (t_{rlx}) (Spitzer (1975) and Inagaki (1985)).

The velocity of stars obviously has a bearing on their distribution, with high

velocity low mass stars being more spread out. If there is enough time for stars to cross the cluster several times (each time takes t_{cr}) between stellar encounters, then there will be an equilibrium between the velocity and density distributions. This is an important requirement if one is to model the cluster. The ratio between t_{cr} and t_{rlx} depends on the number of stars in the cluster (N_c), and is described by equation (6.1) (King 1976).

$$\frac{t_{rlx}}{t_{cr}} = \frac{N_c}{31 \ln \frac{N_c}{2}} \quad (6.1)$$

In globular clusters N_c is very large ($\sim 10^6$), and so $t_{rlx} \gg t_{cr}$. If $N_c = 131$ then $t_{rlx} = t_{cr}$, and so it is not possible to analytically model very small loose star associations. However, large open clusters like the Pleiades contain over 1000 stars, and so an equilibrium should have been established between the velocity and density distributions.

N-body simulations avoid the need for analytical solutions, but are sensitive to the set of initial conditions used. However, a number of such studies have been made: Terlevich (1987) discusses binaries, escape of stars, interactions with interstellar clouds, mass segregation and tidal flattening. Kroupa (1995) concentrates on the effects of various initial binary populations. Fuente Marcos (1995) considers the consequences of various initial mass functions. The point concerning tidal flattening due to the spin up of stars by the tidal force of the galaxy has also been discussed by van Leeuwen (1983), who suggests that it should cause a decrease in the central density of the lower mass stars so that their density peaks at about 1 parsec from the cluster centre. Cluster flattening will be discussed later in this chapter.

The tidal effect of the galaxy also affects the cluster by stripping stars off from the outer regions. This process is called evaporation (Chernoff, Kochanek & Shapiro 1986). It occurs if stars gain enough velocity through encounters to travel out beyond a radius known as the tidal radius r_t (von Hoerner 1957), where the galactic tidal force over powers the clusters own gravity. However, evaporation takes many relaxation times to seriously decrease the number of stars in a cluster.

6.3 Cluster observations

Determining the validity of such dynamical models requires comparison with observations. Surface brightness profiles of star clusters have been obtained in a number of ways.

Globular cluster cores are best studied using star counts or density scans from high resolution photographic or electronographic plates or CCD images (since photometric measurements will be dominated by giants and sub-giants in the core). Such a study, of a over a hundred globular clusters (King (1989), and Djorgovski, Piotto & King (1989)) shows that a King surface density formula (King 1962) fits the core regions of most globular clusters very well.

In the outer regions of globular clusters, integrated surface photometry with concentric apertures, or small aperture scans of the cluster's integrated light are more appropriate (Elson, Hut & Inagaki 1987). The surface photometry for the outer regions of nine globular clusters and three rich open clusters were fitted with the same tidally truncated King density formula, and good agreement was found (King 1966).

Mass segregation has been observed in two globular clusters (Da Costa 1982), in the Pleiades (vanLeeuwen, Alphenaar & Brand 1986), the Hyades (Pels, Oort & Pels-Kluyver 1975) and M11, 35 and 67 (Mathieu 1983 and 1984). This means that clusters should be modeled using a multi mass approach, and a multi mass version of the King model has been used to fit the globular cluster M3 very closely (Da Costa & Freeman 1976).

6.4 The density distribution

6.4.1 Surface density

The previous section described the success of the King surface density distribution. Because of it's proven applicability to open as well as globular clusters, it was the logical choice to use in this work.

The King profile is an empirical function defined by King (1962), which is designed to mimic observed surface density (f_s) distributions in globular and open clusters. These observed distributions follow equations (6.2 a and b) in the inner and outer cluster regions respectively.

$$(a) f_{s(inner)} = \frac{f_o}{1 + (r/r_c)^2} \qquad (b) f_{s(outer)} = f_1 \left\{ \frac{1}{r} - \frac{1}{r_t} \right\}^2 \quad (6.2)$$

Here, r_c is known as the core radius, and is the radius when the surface density falls to half it's central value. r_t is the previously mentioned tidal radius, where f_{outer} falls to zero. f_o and f_1 act as normalisation constants.

King's empirical density function embodies the characteristics of both of these equations, and is shown in equation (6.3).

$$f_s = k \left\{ \frac{1}{\sqrt{1 + (r/r_c)^2}} - \frac{1}{\sqrt{1 + (r_t/r_c)^2}} \right\}^2 \quad (6.3)$$

If $r_t \gg r_c$, it can be seen that equation (6.3) \rightarrow (6.2a) in the cluster central region, since the first term in the brackets dominates. k will then be approximately the central surface density. Also, as $r \rightarrow r_t$, then $\sqrt{1 + (r/r_c)^2} \rightarrow r/r_c$ and $\sqrt{1 + (r_t/r_c)^2} \rightarrow r_t/r_c$, and equation (6.3) \rightarrow equation (6.2b).

Integrating the King profile over a spherical volume between 0 and r_t gives the total number of cluster stars described by the profile (n). The resulting function is given in equation (6.4), and will be used later.

$$n = \pi r_c^2 k \left\{ \ln(1 + x_t) - \frac{(3\sqrt{1+x_t}-1)(\sqrt{1+x_t}-1)}{1+x_t} \right\}, \quad (6.4)$$

where $x_t = (r_t/r_c)^2$.

6.4.2 Space density

Equation (6.3) can also be de-projected to provide a formula for spatial density ($\varphi(r)$) instead of surface density.

$$\begin{aligned} \varphi(r) &= -\frac{1}{\pi} \int_r^{r_t} \left\{ \frac{d}{dx} f(x) \right\} \frac{dx}{\sqrt{x^2 - r^2}} \\ &= \frac{k}{\pi r_c \{1 + (r_t/r_c)^2\}^{\frac{3}{2}}} \frac{1}{z^2} \left\{ \frac{1}{z} \cos^{-1} z - \sqrt{1 - z^2} \right\} \quad (6.5) \\ &\text{where } z = \sqrt{\frac{1 + (r/r_c)^2}{1 + (r_t/r_c)^2}}. \end{aligned}$$

6.4.3 The tidal radius

The value of r_t for the Pleiades depends on a number of quantities; the mass of the Pleiades, the mass of the Milky Way (inside the Pleiades' galactic orbit) and the radius of this orbit. It was assumed that the Pleiades has followed a circular orbit during its lifetime, so the distance between the Pleiades and the galactic centre will have always been the same throughout the life time of the cluster. Therefore, the amount of tidal stripping will depend on the cluster's present distance from the galactic centre (the distance of the solar neighborhood). Treating the cluster and the galaxy as a simple two body system, the forces acting on a star in the cluster's frame of reference will be the differential gravity across the cluster radius (due to the galaxy), and the gravitational pull of the cluster itself. The radius at which these forces are equal is r_t , and at this radius, the forces acting on a star in the cluster's free falling frame are shown in equation (6.6).

$$\frac{GM_g}{(R_g - r_t)^2} - \frac{GM_g}{R_g^2} = \frac{GM_c}{r_t^2} \quad (6.6)$$

M_g is the mass of the galaxy within the cluster's orbital radius R_g , M_c is the cluster mass, and G is the universal gravitational constant. For the case where $R_g \gg r_t$, the equation simplifies somewhat, and r_t can be expressed by equation (6.7) (King 1962).

$$r_t = R_g \left\{ \frac{M_c}{2M_g} \right\}^{1/3} \quad (6.7)$$

The best way to substitute for these values is to use Oort's constants A and B. These constants are found in the equations describing the radial velocity(v) and proper motion(μ) that results from circular motion around the galactic centre as shown in equation (6.8).

$$v = Ar \sin 2l \quad \mu = 0.211(B + A \cos 2l) \quad (6.8)$$

The value of A-B is the angular velocity for the solar neighborhood, and is known to the greatest accuracy ($26.4 \pm 1.9 \text{ km s}^{-1} \text{ kpc}^{-1}$, or $8.56 \times 10^{-16} \text{ s}^{-1}$) (Kerr & Lynden-Bell 1986). Inserting this into equation (6.7) gives,

$$r_t = \left\{ \frac{GM_c}{2(A - B)^2} \right\}^{1/3} = 1.46 M_c^{1/3} \quad (6.9)$$

where r_t and M_c are in units of parsecs and solar masses, and $G = 4.517 \times 10^{-30} \text{ pc}^3 \text{ M}_\odot^{-1} \text{ s}^{-2}$.

6.5 The observed mass of the Pleiades

Having reviewed some theory, and described the cluster model that I am going to use, I will now move on to describing the steps involved in modeling the Pleiades.

6.5.1 The Pleiades catalogue

Membership of the Pleiades can be established in a number of ways, such as proper motion and photometric surveys, as well as spectroscopy. For a more detailed description of this see section (2.6).

The Pleiades catalogue used in this work was painstakingly put together by Charles Prosser and John Stauffer and colleagues, and I am most grateful to them for making the data generally available. It contains members ranging from the most massive of the seven sisters (Alcyone) down to stars just above the stellar limit from the deep proper motion survey of Hambly, Hawkins & Jameson (1993). The catalogue contains some spectroscopic and photometric identification of binaries, but I also added to this the photometry of vanLeeuwen, Alphenaar & Brand (1986) to identify other binaries photometrically. All the sources used to compile the catalogue are shown in Table (6.1).

The amount of available data varies for the stars in the catalogue. However for completeness all “proper motion and photometric” members were selected. For photometry, generally stars within 1 magnitude above and 0.3 magnitudes below the cluster sequence were considered as having acceptable photometry for membership, allowing for binarity and photometric errors. The consistency of the proper motion and photometric measurements vary slightly due to the quality, and the type of data (photographic or CCD) but the most recent values were taken for each star.

6.5.2 Stellar masses

The masses of the catalogue stars were calculated using the V or I photometry. For the brightest members a relation between absolute visual magnitude and mass was derived, using main sequence bolometric corrections, and an empirical mass-luminosity relation (Smith 1983). For the other members, the V magnitudes were

Primary sources for members	
Trumpler, 1921	Proper motion
Hertzsprung, 1947	Proper motion
Ahmad et al., 1965	Proper motion
Artyukhina et al., 1970	Proper motion
Haro et al., 1982	Flare stars
Stauffer, 1984	Photometry
Stauffer et al., 1991	Proper motion and photometry
Hambly et al., 1993	Proper motion and photometry
Other photometry	
Johnson and Mitchell 1958	
Landolt, 1979	
Prosser et al., 1991	
Binary information	
Mermilliod et al., 1992	Spectroscopy
Rosvick et al., 1992	Spectroscopy
Stauffer, 1982	Photometry
van Leeuwen et al., 1986	Photometry

Table 6.1: Pleiades Catalogue Sources

used where available, in conjunction with the empirical mass-luminosity relations of Henry & McCarthy (1993). The relations used cover the range ($10 \leq M/M_{\odot} \leq 0.08$), and are shown in equation (6.10). The distance modulus to the Pleiades of 5.65 can be simply added to M_v to get the m_v in the Pleiades.

$$\begin{aligned}
 \log M &= -(0.1706)M_v + (0.549) \\
 &\text{for } (-3.0 \leq M_v \leq 1.45) \\
 \log M &= (2.456 \times 10^{-3})M_v^2 - (9.711 \times 10^{-2})M_v + (0.4365) \\
 &\text{for } (1.45 \leq M_v \leq 10.25) \\
 \log M &= -(0.1681)M_v + (1.4217) \\
 &\text{for } (10.25 \leq M_v \leq 12.89) \\
 \log M &= (5.257 \times 10^{-3})M_v^2 - (0.2351)M_v + (1.4124) \\
 &\text{for } (12.89 \leq M_v \leq 17.59)
 \end{aligned} \tag{6.10}$$

Finally, the fainter low mass stars typically only had I magnitudes. The theoretical model of D'Antona & Mazzitelli (1994) for an age of 100 Myrs, as well as the I band bolometric corrections given in section (2.4) were used to calculate a theoretical mass-I relation. The relation derived is in terms of apparent magnitudes, and is shown in equation (6.11).

$$\begin{aligned}
 \log(M/M_{\odot}) &= (-11.70) + (2.260)I - (0.1231)I^2 \\
 &\quad + (3.7413 \times 10^{-4})I^3 + (7.21069 \times 10^{-5})I^4 \\
 &\text{for } (12.0 \leq I \leq 19.0)
 \end{aligned} \tag{6.11}$$

6.5.3 Binaries

Binaries were identified firstly, from the sources shown in the third section of Table (6.1). However, this information does not cover the low mass cluster members. Steele & Jameson (1995) found that 46% of low mass stars in the Pleiades are likely to be binaries. Therefore for the low mass members the available photometry could be used to assign binarity. A line was defined parallel to the lower main sequence on the faint member colour magnitude diagram, and was adjusted until the required 46% were on the brighter side. These were then flagged as binaries.

The masses of the binaries were calculated by assuming that each binary comprised two stars of equal mass and T_{eff} . The binary magnitude was increased by 0.75

to obtain the magnitude of each of the two stars making up the binary system. The photometric mass of each of these stars was then found using the mass luminosity relations already described, and the mass of the binary system was obtained simply by doubling this mass.

6.5.4 The cluster centre

The first stage in calculating the distribution of the cluster stars was to locate the centre of the cluster on the sky. This was done by counting the number of stars in strips perpendicular to right ascension and then declination over the cluster region. The strips used were 102×25.5 arc minutes in size, which corresponds to 4×1 parsecs at the distance of The Pleiades (assumed to be 135pc). The strips were centred roughly over the densely populated cluster core, and moved about 1.9° either side in steps of 0.042° , to provide a broad strip counts profile in both right ascension and declination. The resulting profiles are shown in the first plot in Figure (6.2), where angular distance has been converted into parsecs at the distance of the Pleiades. The profiles in the right ascension and declination directions are shown by a dotted line and a dot-dash line respectively.

The strip counts in the central region are somewhat uneven. This is because the bright stars in the centre obscure many fainter stars by saturating regions of photographic plates and CCD images. The centre was therefore located by finding the point from which the wings of the strip counts profile were equidistant. The centre was found to be $R.A.(2000) = 3^h46.6^m \pm 0.2^m$, $Dec(2000) = +24^\circ4' \pm 3'$. This agrees well with van Leeuwen (1983), who finds $7'50''$ north and $6''$ east of Merope (which gives central coordinates of $R.A.(2000) = 3^h46^m26^s$ $Dec(2000) = +24^\circ04'46''$).

Each star could then be assigned circular coordinates (r , and θ) with respect to the cluster centre, where $\theta=0$ corresponds to a vector with increasing R.A. and constant declination.

Having done this, a region of incompleteness (outside the radius in which the centre was defined) in the survey of Hambly, Hawkins & Jameson (1993) (due to different field centres of the first and second epoch plates) was corrected for by

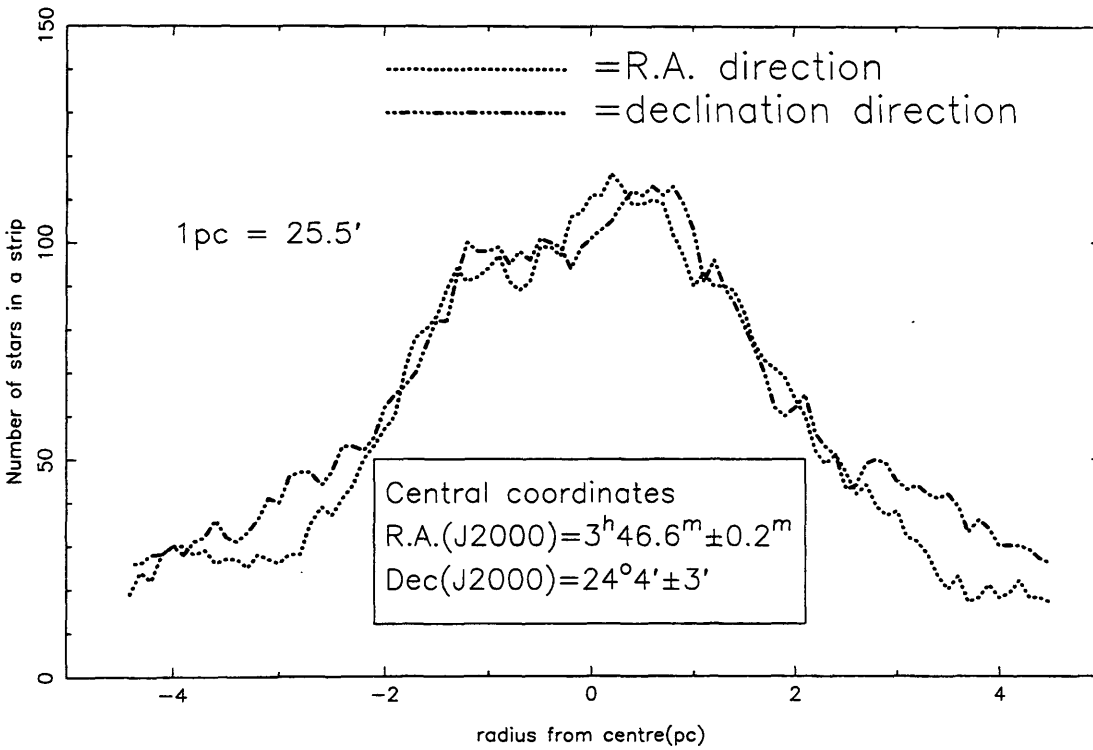


Figure 6.2: The strip counts profiles for the Pleiades, using 4 x 1 parsec strips (at the distance of the cluster) moved through steps of 0.1pc. The strips are moved through right ascension (dotted line), and declination (dot-dash line). The angular scale corresponding to 1pc and the calculated cluster centre are also shown.

assuming symmetry on either side of the cluster centre, and “reflecting” missing stars from a complete region.

6.5.5 Cluster flattening

In order to investigate any galactic induced flattening of the cluster, the coordinates of the members were converted into galactic longitude (l) and latitude (b). This was done using the STARLINK *coco* routine. The same strip counting process as was done before in R.A. and Dec was then repeated in l and b . Figure (6.3) shows the results of these strip count scans, which were done for both high mass ($M > 1M_{\odot}$), and lower mass ($M < 1M_{\odot}$) stars.

Both plots show the cluster to be flattened in the galactic plane direction. However, this effect is, if anything actually more pronounced for the higher mass stars. This is in opposition to the prediction that the galactic gravitational field is the cause of the flattening, because it would cause preferential rotation of the more spread out low mass stars.

Flattening could be caused by the gravitational pull perpendicular to the galactic disk. For a near infinite uniform density thin disc (a rough approximation of the galactic disk), the acceleration induced is independent of distance, but always towards the disk. Because the cluster oscillates above and below the galactic disk, it will flatten while passing through the disk, when the top and bottom of the cluster are pulled closer together. However, this effect should act in the same way for both high and low mass stars, and so once again the evidence suggests otherwise.

It then seems most likely that the flattening is caused by the initial rotation of the molecular cloud that formed the Pleiades, and the collapse process.

This is an interesting result that deserves to be followed up, however it would be very difficult to do in the context of this work, one reason being that the statistics become rather poor if one tries to sample the data azimuthally as well as radially for various masses.

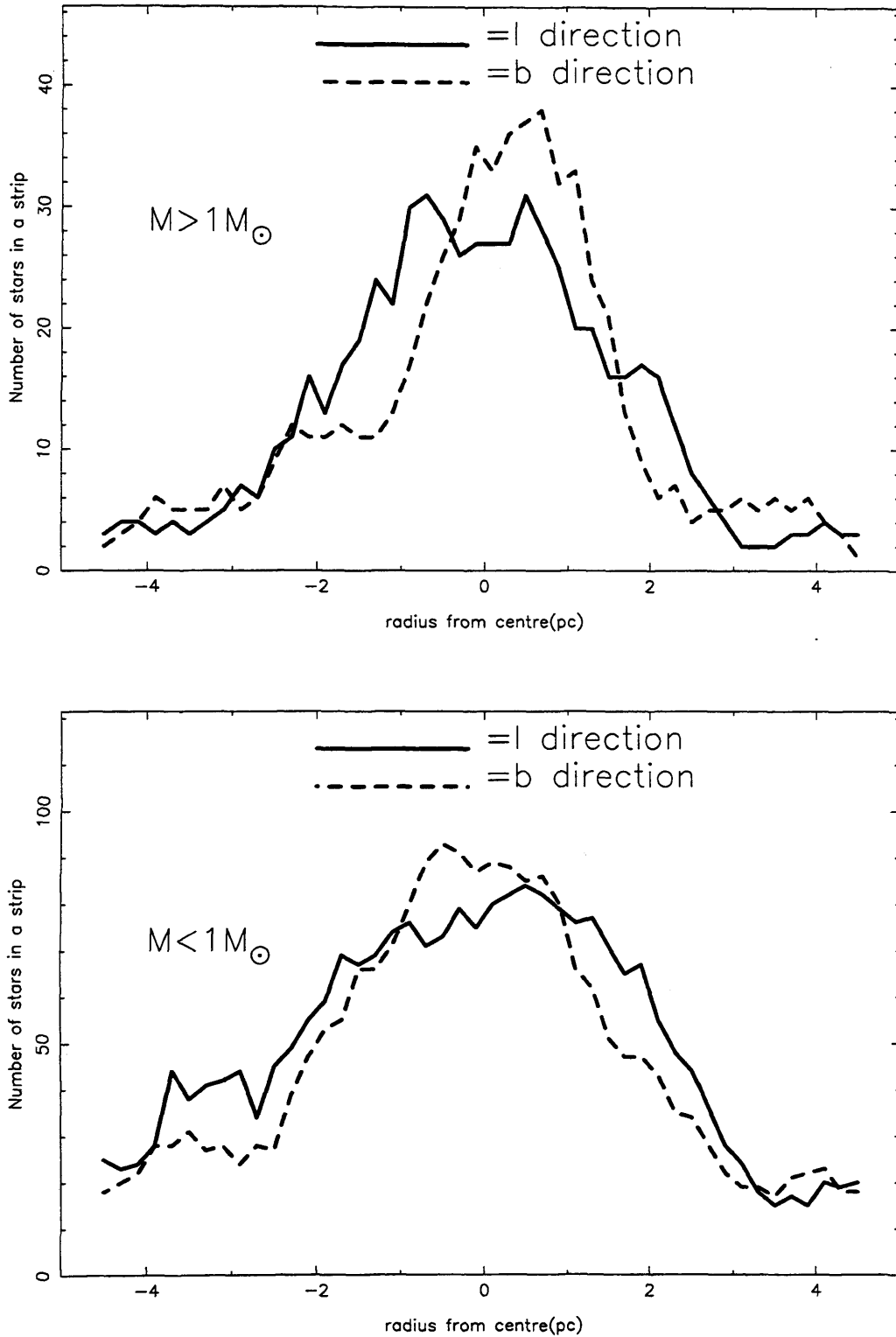


Figure 6.3: The strip counts profiles for higher mass ($> 1M_{\odot}$) and lower mass ($< 1M_{\odot}$) Pleiades stars, constructed by moving the strips through galactic coordinates; longitude(l) and latitude(b).

Bin	Mass range (M_{\odot})	Number of stars	Average mass (M_{\odot})	Completeness
1	12-3	12	5.20	complete
2	3-1.2	118	1.65	\sim complete
3	1.2-0.6	295	0.83	$\rightarrow \simeq 7\text{pc}$
4	0.6-0	642	0.30	$\rightarrow \simeq 6\text{pc}$
$M_{\text{tot}}(\text{catalogue}) = 695M_{\odot}$				

Table 6.2: Mass bins for the Pleiades

6.5.6 The Pleiades distribution

The King profile is for a single mass system, so in order to use it on the large mass range of the Pleiades, the cluster members were binned into four mass bins. The sizes of each bin, along with the number and average mass of stars in each bin are shown in Table (6.2).

Stars were then counted in concentric rings 1 pc wide, at radii steps of 0.5pc from the cluster centre, as far as the completeness of the catalogue allowed. The surface areas of the central region were corrected slightly for the low mass stars, to take into account the regions of saturation from the high mass stars. An estimated value of r_t was assumed to begin with, and best fit values of r_c and k were found for each bin using a routine called `dx_srchmin` (by R. Willingale 1986) which minimised the χ^2 statistic. These best fit parameters along with the average stellar mass in each bin (from Table (6.2)) were then used to calculate the mass of the cluster (M_c) down to the limits of the catalogue using Equation (6.4). Equation (6.9) then gives the expected r_t for this M_c , and the initial estimate of r_t could be compared to this new value, and adjusted accordingly. However, r_c and k vary slightly as r_t changes, so this process was iterated until the input estimate of r_t was within 0.1pc of the output value, producing a self consistent set of cluster dimensions (assuming no extra dark matter in the cluster). This value of r_t was found to be 13.1pc. The results of the χ^2 fitting are summarised in Table (6.3). Also contained in the table are the depth of the cluster in magnitudes as it would manifest itself on a colour magnitude diagram,

Bin	r_c (pc)	r_c limits (68% confidence)	k	k limits (68% confidence)	n	Mass(M_\odot)
1	0.91	[0.50 - 1.51]	1.86	[0.87 - 3.74]	13	66
2	1.38	[1.15 - 1.66]	10.04	[7.86 - 12.69]	115	190
3	2.22	[1.98 - 2.49]	15.90	[14.17 - 17.81]	300	249
4	2.91	[2.63 - 3.23]	32.81	[30.51 - 35.37]	766	230
$r_t = 13.1\text{pc}$, Cluster depth = $\pm 0.2^{\text{mag}}$						
$M_c = 735M_\odot$, $N_c = 1194$, $\bar{m}_c = 0.616M_\odot$						

Table 6.3: Pleiades King fit results

r_t , M_c , N_c (the total number of stars in the cluster) and \bar{m}_c (the average cluster star mass). Values of n have been rounded to the nearest integer.

Figure (6.4) shows the radial surface density plots, and plots of stars out to a given radius for each bin. Overlaid on the density plots are the best fit forms of equation (6.3), and radially integrated versions are overlaid on the plots of star counts out to r , to show how accurately the total number of stars in each bin is being represented.

The errors used for the surface density values were $\pm(100\sqrt{N}/N)\%$. Mass bins 2 and 3 show excellent agreement between the data and the fitted functions. The agreement is slightly worse for the lowest mass bin, but still quite close. The higher mass bin fit is not so good. This is because of the sparsity of stars and the large range in mass, and is shown by the broad 1σ limits of the fitted parameters in Table (6.3). However, the star counts out to r agree well with the radially integrated function at the completeness limit of the bin, which lends some more credence to the fitted values for this bin.

Bin 4 shows marginal evidence for the central density depletion described by van Leeuwen (1983). Alternatively, it could be argued that our correction for obscuration by bright stars for the low mass stars is inadequate.

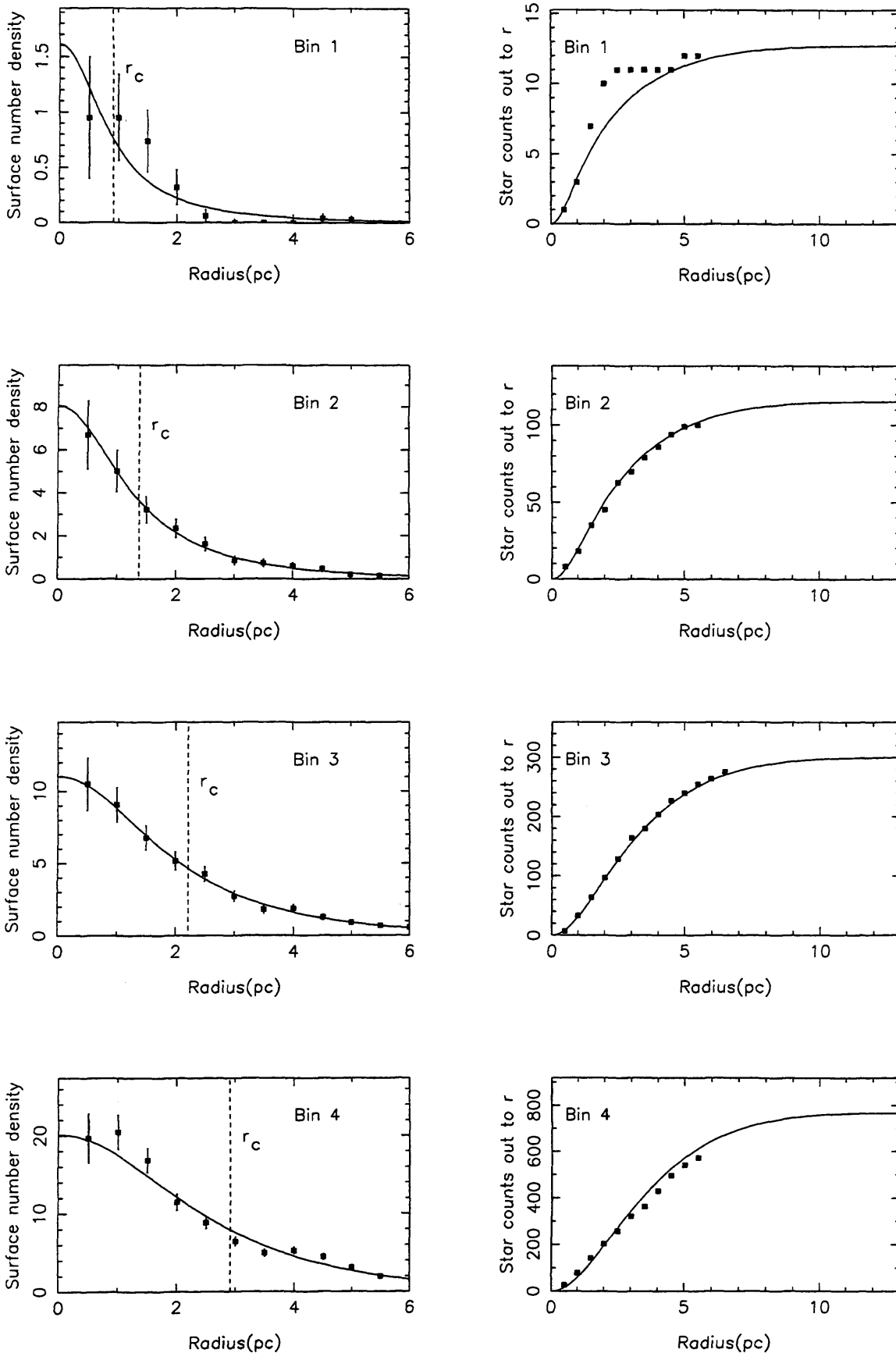


Figure 6.4: The surface density profiles and the star counts out to radius r , for the four mass bins making up the Pleiades. 1σ errors are shown on the surface density data points. Over-laid on the density plots are the best fit forms of equation (6.3), and radially integrated versions are over-laid on the plots of star counts out to r . The best fit values of r_c are also indicated by dashed line on the density plots.

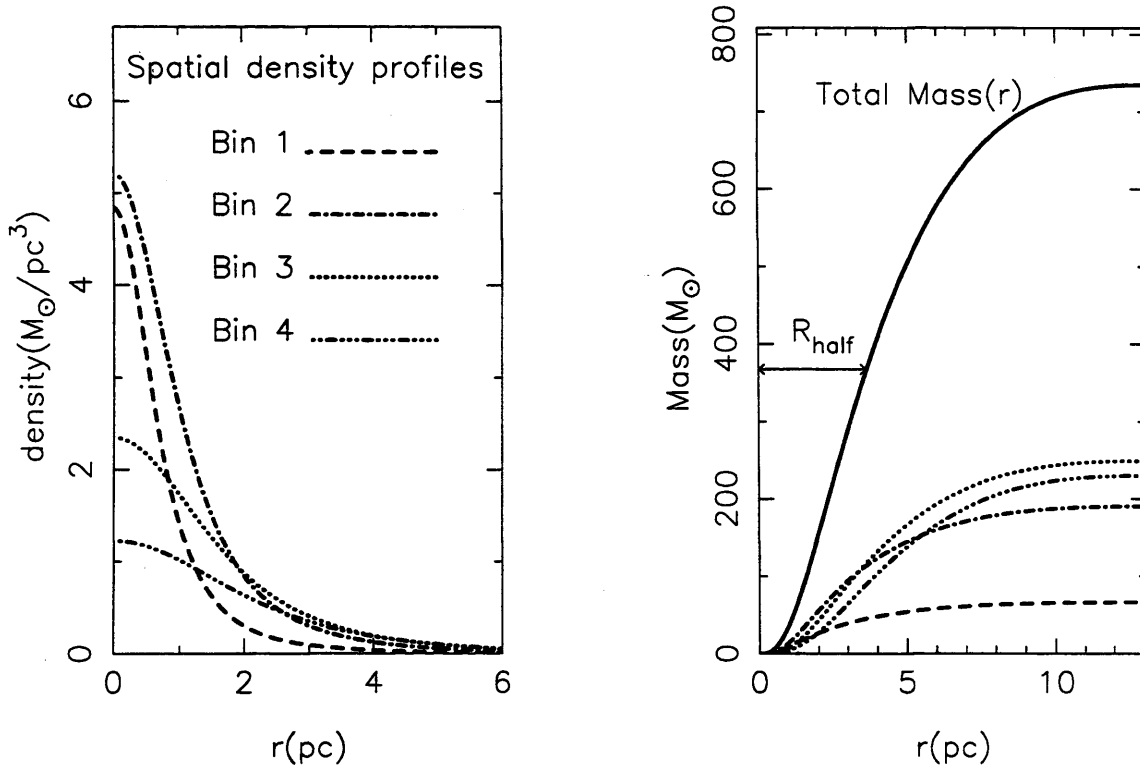


Figure 6.5: The spatial density and mass profiles of the four mass bins constituting the Pleiades. Each bin is represented by a different line type, indicated on the density profiles diagram. The total mass of the Pleiades is also shown on the spatial mass diagram as a solid line, and the radius containing half the cluster mass (R_{half}) is also indicated. The spatial mass diagram covers the full range of the Pleiades out to r_t , showing the total observed mass of the cluster at this point.

6.5.7 Deprojection

Using Equation (6.5) the deprojected density profiles were calculated, and numerically integrated to give the mass of the cluster as a function of spatial radius. The results are shown in Figure (6.5). The four mass bins in each plot are indicated by the different line types shown on the density plot. It can be seen that the two highest mass bins contribute most to the central density, and that the mass bins 2 \rightarrow 4 contribute most to the total mass of the cluster. Also indicated on the mass plot is the radial value R_{half} which is the radius containing half the total cluster mass. R_{half} has a value of 3.66pc.

6.5.8 Pleiades time scales

The accurate value of t_{rlx} was now calculated using equation (6.12), which is also known as Spitzer's reference time (Spitzer 1940),

$$t_{rlx} = 0.8 \frac{\sqrt{N_c} R_{half}^{\frac{3}{2}}}{\sqrt{\bar{m}_c} (\log N_c - 0.5)} Myrs \quad (6.12)$$

where N_c is the total number of stars in the Pleiades. Inserting the values found for the Pleiades gives $t_{rlx} = 96$ Myrs.

Using equation (6.1) a crossing time of 16 Myrs is found. An equilibrium between the density and velocity distributions should thus be a reasonable assumption for the Pleiades.

The evaporation time (the time taken for 1/e of the cluster stars to evaporate) can be calculated by considering the escape velocity of cluster stars (twice the root mean square velocity of the cluster stars). A basic analysis, which ignores the fact that velocity is a function of radius (because of the gravitational potential of the cluster) produces evaporation time scales as a function of mass. The BD evaporation time was thus found to be 560 Myrs ($\sim 6 \times t_{rlx}$). This basic analysis will probably underestimate the evaporation time scale, because if stars travel in ellipses, they will have slowed substantially by the time they reach the edge of the cluster, and so evaporation would take longer. However, it is clear from the approximate calculation that evaporation will not have noticeably depleted Pleiades BDs.

6.6 The dynamical mass of the Pleiades

Having derived a set of self consistent parameters describing the Pleiades, assuming no large amounts of extra dark matter, the next section describes the attempts made to test these criteria, using the virial theorem.

6.6.1 The Virial Theorem

As a cloud of material collapses under gravity it heats up, and gravitational potential energy is converted into two other forms of energy in equal quantities: The kinetic energy of the particles in the cloud, and radiation which is lost from the cloud. Once

equilibrium has been reached, the cloud's gravitational binding energy (Ω) is related to its kinetic energy (T) by the well known virial relation,

$$\Omega = 2T. \quad (6.13)$$

I have shown that there should be an equilibrium between the velocity and density profiles, so one should be able to derive one from the other. This can be done by assuming that a Boltzmann distribution is a good approximation for the stars in each bin for small values of r . Therefore

$$\rho_o e^{\frac{-m\psi(r)}{kT}} = \rho_o \frac{1}{\{1 + (r/r_c)^2\}^{3/2}}, \quad (6.14)$$

where the left hand side of Equation (6.14) is the Boltzmann distribution, and the right hand side is a deprojection of Equation (6.2a) for the cluster centre. ρ_o is the central density of the cluster, m is the mass of the stars being considered (the average mass of stars in a particular bin), $\psi(r)$ is the gravitational field as a function of r , and kT is a typical kinetic energy associated with cluster stars in each bin. In the cluster centre, the density can be assumed to be approximately constant, and therefore, the potential will be $(2/3)\pi\rho_o Gr^2$. Taking natural logs of both sides of Equation (6.14) gives

$$\frac{2m\pi\rho_o Gr^2}{3kT} = \frac{3}{2} \ln \{1 + (r/r_c)^2\} \simeq \frac{3}{2} \left\{ \frac{r}{r_c} \right\}^2, \quad (6.15)$$

since $\ln(1 + x^2) = x^2$ for small values of x . Therefore,

$$kT = \frac{1}{3} m \bar{v}^2 = m \langle \sigma^2 \rangle = \left\{ \frac{4\pi G}{9} \right\} m \rho_o r_c^2, \quad (6.16)$$

where the second and third parts of the equality have been introduced from thermodynamics. \bar{v}^2 is the mean square velocity of cluster stars in a particular bin, and $\langle \sigma^2 \rangle$ is the mean square velocity in any one coordinate. $\langle \sigma^2 \rangle^{1/2}$ is often referred to as the velocity dispersion (Jones 1970). Equation (6.16) has been discussed also by King (1966), and Da Costa & Freeman (1976), and it can be seen that if equipartition of energy has occurred between the cluster stars, and kT is independent of m , then $r_c \propto \langle \sigma^2 \rangle^{1/2}$, and $\langle \sigma^2 \rangle^{1/2} \propto 1/\sqrt{m}$.

Figure (6.6) shows a plot of $\langle \sigma^2 \rangle^{1/2}$ against $1/\sqrt{m}$ for the Pleiades mass bins. The errors used for $\langle \sigma^2 \rangle^{1/2}$ come from the χ^2 1σ limits on r_c , and the errors on

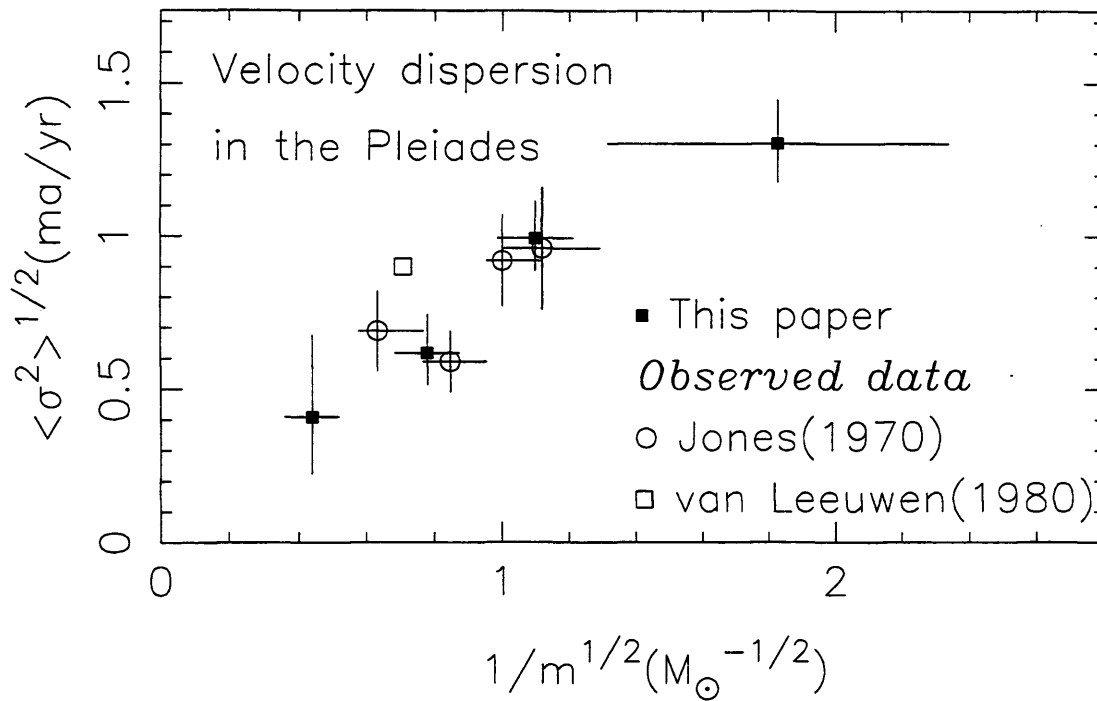


Figure 6.6: A plot showing $\langle \sigma^2 \rangle^{1/2}$ against $1/\sqrt{m}$ for the four mass bins constituting the Pleiades. Observational data from Jones (1970) and van Leeuwen (1979) is shown for comparison. $\langle \sigma^2 \rangle^{1/2}$ is approximately proportional to $1/\sqrt{m}$, indicating near equipartition of energy in the Pleiades.

$1/\sqrt{m}$ are the standard deviation of the stellar masses in each bin. A straight line can be drawn through all the points and the origin taking these errors into consideration, indicating approximate equipartition of energy in the Pleiades. However, the lowest mass bin point falls slightly to the right of this line, indicating that the stars in this bin do not have quite as much kinetic energy as equipartition would imply. This is not surprising, since the age of the Pleiades (~ 115 Myrs, from Basri, Marcy & Graham (1996)) is not much larger than t_{rix} , so the Pleiades has not had quite enough time to reach complete equipartition of energy.

Adding up the individual central densities for each bin gives an overall central density of $13.62 M_{\odot}/\text{pc}^3$, and using the r_c and m values from Tables (6.2) and (6.3), a value of kT for the central region of each bin was calculated. Next, each bin was divided into shells 0.01pc wide, and values of kinetic energy ($(3/2)kT(r)$) were calculated for each shell as a function of r , where it was assumed that $kT(r)$ decreases by an amount equal to $m\psi(r)$, as the stars lose kinetic energy moving through the cluster potential. $kT(r)$ was then numerically integrated in each bin out to r_t , to give the kinetic energy per bin (T_{bin}), where

$$T_{bin} = \int_0^{r_t} \left\{ \frac{3}{2}kT - m\psi(r) \right\} \left\{ \frac{4\pi r^2 \rho(r)}{m} \right\} dr. \quad (6.17)$$

The first part of the integral is the energy per star, and the second part is the number of stars in each shell. The four values of T_{bin} were then summed to give T for the whole cluster.

Next, the binding energy of the cluster (Ω) was calculated from a second numerical integration of the same size where

$$\Omega = \int_{r_t}^0 \left\{ \frac{GM(r)}{r} \right\} \{4\pi r^2 \rho(r)\} dr. \quad (6.18)$$

$M(r)$ is the function shown in the second diagram in Figure (6.5), and $\rho(r)$ is the cluster density function (a summation of the four density plots shown in Figure (6.5)).

Table (6.4) summarises the results of the calculation. The percentage contributions of each mass bin to T and Ω are given for the best-fit cluster parameters, as well as the total values for the whole cluster ($T_{best\ fit}$ and $\Omega_{best\ fit}$). Also shown are the

Bin	T fraction (%)	Ω fraction (%)
1	0.3	7.9
2	3.0	24.7
3	23.9	34.6
4	72.8	32.8
$\Omega_{best\,fit} = 2.8 \times 10^{-10} \text{ M}_{\odot} \text{pc}^2 \text{yr}^{-1}$		$\Omega_{min} = 2.46 \times 10^{-10} \text{ M}_{\odot} \text{pc}^2 \text{yr}^{-1}$
$T_{best\,fit} = 1.6 \times 10^{-10} \text{ M}_{\odot} \text{pc}^2 \text{yr}^{-1}$		$T_{min} = 0.45 \times 10^{-10} \text{ M}_{\odot} \text{pc}^2 \text{yr}^{-1}$

Table 6.4: Virial analysis results for the Pleiades

limiting values, T_{min} and Ω_{min} , found using the 1σ limits of the cluster parameters that give the minimum value of $2T/\Omega$.

The observed values of Ω and T provide information on the quantity of unseen matter in the Pleiades. If there is a substantial amount of dark matter in the form of Brown Dwarfs, then a much larger amount of kinetic energy will be stored in this population than binding energy, since approximate equipartition of energy will ensure that these brown dwarfs have high velocities. However, if the number of Brown Dwarfs is low, then the observed kinetic and binding energies should be well represented by the virial theorem. It can be seen from Table (6.4) that the best-fit cluster parameters give $1.14\Omega_{obs} = 2T_{obs}$, which is very close to the result expected for a cluster containing no extra Brown Dwarfs. In order to obtain a lower limit on the value of $2T_{obs}/\Omega_{obs}$, the 1σ parameter limits that minimize the quantity $(2T_{obs}/\Omega_{obs})$ were used in the virial calculation, the results being shown in Table (6.4), and when this was done the virial calculation yielded $0.37\Omega_{obs} = 2T_{obs}$.

In order to determine an upper limit on the mass of the Pleiades from this result, equipartition was assumed for the cluster. Therefore, $\bar{T} = \bar{T}_{obs}$, where the bars indicate an average value for each cluster star, and so $T/(N_{obs} + N_{bd}) = T_{obs}/N_{obs}$, where N_{obs} and N_{bd} are the observed number of cluster stars, and the number of undetected brown dwarfs. For a simple intuitive calculation, it was assumed that the binding energy of the cluster will be unaffected by additional brown dwarfs, since

they are of relatively low mass, and so $\Omega = \Omega_{obs}$. Therefore we have

$$\frac{2T}{\Omega} = \frac{2T_{obs} N_{obs} + N_{bd}}{\Omega_{obs} N_{obs}} = 1. \quad (6.19)$$

Therefore,

$$N_{bd} = N_{obs} \left\{ \frac{\Omega_{obs}}{2T_{obs}} - 1 \right\} = 2033 \quad (6.20)$$

Assuming a mass of these brown dwarfs of $0.04M_{\odot}$ leads to an extra mass of $\sim 80M_{\odot}$.

A complete solution for the number of extra brown dwarfs was also found, taking into account changes in Ω . This complete solution depends on the average mass of the unseen brown dwarf population, and hence on the form of the sub-stellar mass function. However, by assuming an average mass of $0.04M_{\odot}$ per brown dwarf, we find that $N_{bd} = 3300$, giving an extra $131M_{\odot}$. Using this result, and assuming a form of the MF, a lower limit to the BD mass can be obtained. If the MF has $\alpha = 1.5$, the lower limit is $0.005M_{\odot}$, while if $\alpha = 1.0$, the lower limit is $0.0001M_{\odot}$. Both these limits are lower than predictions of formation theory (see section (2.2)).

Further more, if the equipartition condition is relaxed, then the BDs will have less kinetic energy than predicted by equipartition, and N_{bd} would be larger, increasing Ω , and therefore increasing the mass of the cluster.

6.7 Discussion

I have shown that there is no evidence for a large population of BDs in the Pleiades, however there is potentially a smaller number in existence. The likely distribution of this potential population of brown dwarfs was calculated by assuming some value of r_c , and calculating the required value of k from Equation (6.4). If the mass of these objects is $0.04M_{\odot}$, then $1/\sqrt{m}$ is 5, and the core radius will be larger than any of the observed mass bins. A rough extrapolation of Figure (6.6) gives an r_c of 7pc. The resulting profile is shown in Figure (6.7).

Also shown in the figure is an indication of the resulting upper limit on the Brown Dwarf central surface density. These are shown in units that are applicable to photometric surveys. The size of $10'$ and 1° are also shown with respect to the profile.

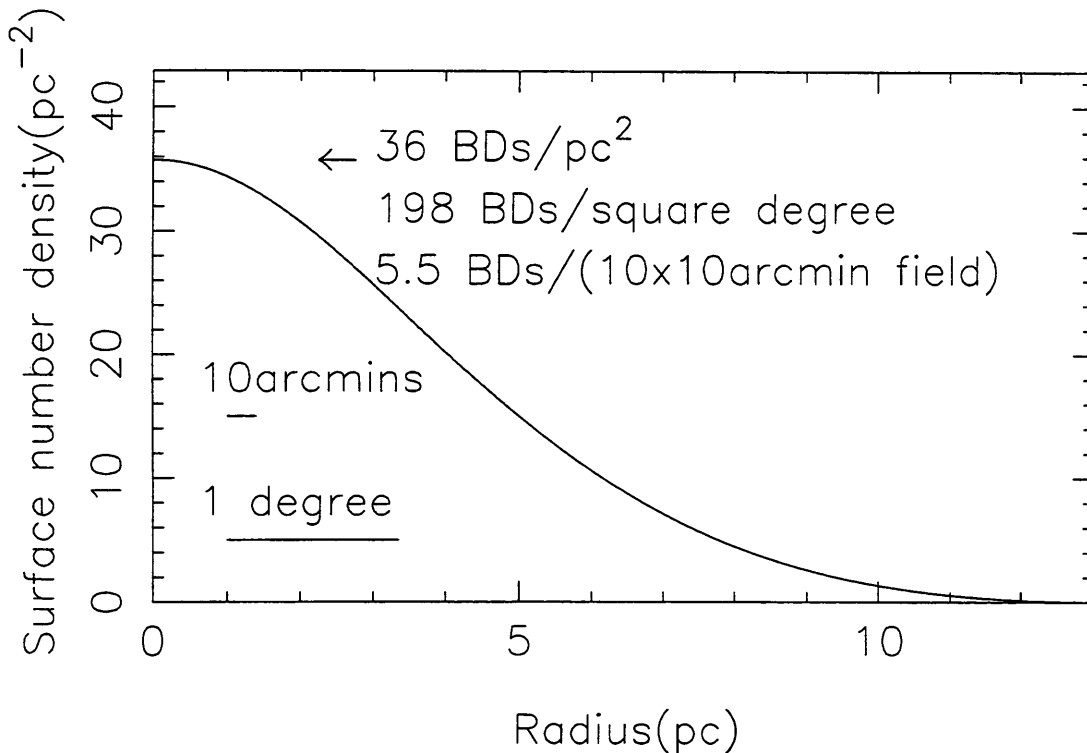


Figure 6.7: The distribution of the largest possible unseen brown dwarf ($m \simeq 0.04M_{\odot}$) population in the Pleiades, from virial analysis of the limiting cluster parameters. The central surface density is indicated using three different units so as to easily relate the profile to photometric surveys. The size of 1° and $10'$ are also shown with respect to the profile.

The latest surveys for BDs (for example that by Osorio (1997)) are turning up about 1 BD candidate per 10' by 10' field down to about $0.035M_{\odot}$. This is therefore consistent with the upper limit shown in Figure (6.7).

I shall briefly mention a very recent result concerning the Pleiades distance. Throughout this paper we have assumed the Pleiades to be at a distance of 135pc (Hambly, Hawkins & Jameson 1991). Very recent results from Hipparchos however suggest a distance of 115pc (vanLeeuwen & Hansen Ruiz 1997). This new distance is in conflict with photometry and matching the main sequence to other clusters and field stars, and vanLeeuwen & Hansen Ruiz (1997) suggest it should not be adopted until this conflict is resolved. Clearly this smaller distance would reduce the core radii but not change the observed cluster mass if one ignores the small decrease in stellar masses as a result of the reduced luminosities (which do not agree with the models). The central density would scale as d^{-3} , the velocity dispersion as $d^{-1/2}$ (see equation(6.16)) and the internal energy as d^{-1} . The gravitational potential energy will also scale as d^{-1} , so the balance of the Virial Theorem is not affected by any change in the distance. Therefore my result that no large population of BDs exists in the Pleiades is unchanged.

6.8 Conclusions

A number of things have been achieved in the work described in this chapter.

- Using a tidally truncated King distribution, the Pleiades stellar distribution has been successfully fitted by splitting the cluster stars into four mass bins, the lowest of which extends down to the stellar limit.
- The tidal radius of the cluster was found to be 13.1pc, which corresponds to a main sequence width of $\pm 0.2^{\text{mag}}$.
- The total mass of the Pleiades (down to the stellar limit) was found to be $735M_{\odot}$. This is in close agreement with the recent result of Raboud & Mermilliod (1997) who uses a smaller Pleiades catalogue containing only 270 brighter members, and uses the virial theorem to calculate a cluster mass of $720M_{\odot}$.

- The relaxation and crossing time were calculated to be 96Myrs and 16Myrs respectively. This indicates that an equilibrium between density and velocity distributions exists in the Pleiades, and that the cluster should be near to a relaxed state at an age of ~ 115 Myrs.
- The total kinetic energy of the cluster was calculated, and compared to the cluster's calculated binding energy, to establish from the virial theorem if an unseen population of brown dwarfs exists in the cluster, containing a substantial fraction of the cluster's kinetic energy. The best fit cluster parameters indicate that no such large population of brown dwarfs exists.
- However, using the 1σ limits on the cluster parameters, an upper limit to the mass of any unseen brown dwarf population of $131M_{\odot}$, was found, assuming that it is comprised of $0.04M_{\odot}$ Brown Dwarfs. Such a population would have a distribution with ≤ 5.5 brown dwarfs per $10' \times 10'$ field in the cluster centre.

Chapter 7

Burrell Schmidt surveys: Pleiades Praesepe & the Hyades

7.1 Introduction

This chapter returns to the subject of deep photometric surveys. The survey work covers three open clusters; The Pleiades, Praesepe and The Hyades. The aim of this project was to cover as much of these clusters as possible, in order to find a large number of VLM and BD candidates, and improve the statistics on the resulting mass functions. In order to achieve this, a telescope with a large field of view was required.

The Burrell Schmidt telescope on Kitt Peak, Arizona (0.61m aperture, $f/3.5$) has a plate scale of 96.6 arcsecs/mm, and is currently fitted out with an S2KA 4.3cm square, 2048x2048 CCD chip. This means that the effective field of view is $\sim 68 \times 68$ arcminutes (slightly over 1 square degree), making it ideal for the project. The relatively small aperture means that exposure times must be considerably longer than previously used (at the 2.5m INT), but an auto-guiding facility is in place on the Burrell Schmidt, which facilitates such long exposures. The pixel scale is also large, at 2 arcseconds per pixel, so shape analysis is not possible.

The response of the S2KA chip is of a slightly different form to the Tektronix chip (see figure (4.1), but shares the characteristic of being sensitive out to 1 micron (see the *“Direct Imaging Manual for Kitt Peak”* - [ftp.noao.edu](ftp://noao.edu), cd `kpno/manuals`,

binary, get direct.ps.Z). The best filters to use are therefore I and Z, as explained in section (4.3). The I filter that was used was I_{KP} .

I will now briefly summarise the characteristics of the three target clusters.

The Pleiades is about 115Myrs old (Basri, Marcy & Graham 1996), and is at a distance of ~ 135 pc ($m - M = 5.65 \pm 0.12$, Hambly, Hawkins & Jameson (1991)), although vanLeeuwen & Hansen Ruiz (1997) finds 115pc in conflict with matching the Pleiades main sequence to field stars and other clusters. The maximum angular diameter is 11° (twice the tidal radius, see Chapter (6)). The Pleiades has essentially solar metallicity, and small reddening ($E(B-V)=0.04$) in general, with only one region of high extinction ($R.A._{2000} = 3^h46^m$, $Dec_{2000} = +23^\circ39.3'$), but this survey avoids this region. For an observational review see sections (6.5) and (2.6).

Praesepe is somewhat older than the Pleiades, at ~ 0.9 Gyrs, and further away at a distance of ~ 162 pc ($m - M = 6.05$, Hambly *et al.* (1995b)). For a detailed description of the cluster, and an observational review see sections (4.1) and (4.2).

The Hyades is approximately the same age as Praesepe, but is considerably closer at a distance of 48pc ($m - M = 3.4$, Reid (1992)). Because of this closeness, the depth to distance ratio is large, and the main sequence is consequently spread out on a colour magnitude diagram, by about $\pm 1^{mag}$. For an observational review of the Hyades see sections (2.5) and (2.6).

7.2 The survey

The observations were taken on the nights of the 13th – 17th December, 1996. We lost half a night as a results of high winds, when the dome had to be closed, but on the whole, the weather was good, and photometric. The effective seeing over the whole exposure times, varied from 4 to about 7 arcseconds. This was not the actual seeing, but the effective seeing for our long exposures, which takes into account the wind, the tracking, and the relatively large angular pixel size.

Field selection was done by avoiding the brightest stars ($M_v < 8$) which would saturate badly during long exposures, but ensuring that there was at least 1 star of about 8th or 9th magnitude in the field, to guide on.

Field	R.A. ₂₀₀₀	Dec ₂₀₀₀	I exp (seconds)	Z exp (seconds)	Seeing (arcseconds)
The Pleiades					
Pl 1	3 54 38	25 00 00	2700	7200	4
Pl 2	3 53 22	23 57 40	3600	7200	4
Pl 3	3 48 52	24 48 00	3300	7200	4
Pl 4	3 47 12	22 32 20	3300	7200	7
Pl 6	3 41 32	24 19 10	3600	6300	6
Praesepe					
Pr 2	8 47 50	18 38 20	3600	7200	4
Pr 3	8 44 27	19 24 00	3600	4500	4
Pr 5	8 38 55	18 36 00	2400	4800	5
Pr 7	8 36 28	21 09 40	3600	7200	4
Pr 9	8 34 48	19 42 00	3600	6300	5
The Hyades					
H 1	4 21 00	16 45 00	1800	3600	5
H 3	4 28 30	15 00 00	1800	3600	5

Table 7.1: The Kitt Peak survey.

The Pleiades was high in the sky during the first half of the night, and Praesepe during the later half. However, on the last night, the moon was quite near to the Pleiades, so we chose to image the Hyades during the first half of that night. The total exposures times aimed for were 1 and 2 hours at I and Z respectively for the Pleiades and Praesepe, and $\frac{1}{2}$ and 1 hour at I and Z for the Hyades. We took several exposures adding up to the required exposure time, in order that the images could be median filtered to get rid of cosmic rays (of which there were ~ 4000 events per hour), and the occasional loss of guiding meant that we did not always achieve the full number of exposures, but the loss of 15 or 20 minutes in a 1 or 2 hour exposure will not have serious consequences to the signal to noise. Median filtering will of course have essentially the same effect on the signal to noise ratio as co-adding, since although the signal will remain the same, the background sky noise of N median filtered images will decrease by \sqrt{N} .

Five Pleiades fields and five Praesepe fields were imaged, as well as two Hyades fields, and the survey information is summarised in Table (7.1).

7.3 Image reduction and photometry

The general method of data reduction that was used is described in section (3.5). The particular software packages used as well as some image manipulation not mentioned before, are described below.

All images were de-biased and flat-fielded (with over-scan bias strips and dome flats) using (IRAF: CCDPROC). A small number of bad pixels were also set to zero at this time. Each set of I and Z exposures for each field then needed to be aligned, since there were small shifts (including slight rotation) between exposures. This was done by selecting one I image, and transforming all the remaining I and Z images onto this, using the packages (IRAF: GEOMAP & GEOTRAN) employing typically 29 reference stars. The transformed images and the reference one were then median filtered using (IRAF: IMCOMBINE), and trimmed so as to contain only regions common to all the component images. The resultant images will therefore have no cosmic ray events in them.

The zero points were found by imaging 3 A0 unreddened standards (lan95-96, lan95-15 and lan100-241 (Landolt 1992)), and employing a 5 pixel aperture. The typical zero point error was 0.03 magnitudes, and it did not change noticeably with airmass. One zero point could thus be used per filter per night. The zero points were also very stable from night to night, with variations of no more than 0.04 magnitudes.

I and Z sources were located using (IRAF: DAOFIND) set at a 7σ detection threshold, and fluxes obtained with (IRAF: PHOT) using an aperture of radius equal to the seeing. All magnitudes were then corrected to a 5 pixel aperture, using a derived aperture correction.

Finally, in order to remove unreliable photometric sources (ones that are contaminated by nearby brighter sources, or ones containing bad pixels), a routine was written in “Q” (R. Willingale 94) to produce an image of all sources that appear to be in or near to where cluster stars should lie. These images could then be checked by eye quite quickly, and rejected if necessary.

7.4 Photometric results

The survey reached $I \simeq 20$, $Z \simeq 21$ in the Pleiades and Praesepe, and $I \simeq 19$, $Z \simeq 20$ in the Hyades, where the exposure times were half as long.

I used (STARLINK: ASTROM) to calibrate the pixel positions of each source, employing about 30 reference guide stars per field. The residuals of the resulting coordinate transforms were of order ± 0.6 arcseconds. The coordinates of the brighter sources will be accurate to this level. There will be an extra source of error for the fainter sources, as they contain less pixels above the background noise, and will therefore centroid less accurately, however the accuracy should still be good to about 1 arcsecond.

In order to define the cluster sequences, I took catalogues of previously identified proper motion and photometric members, as well as all the spectroscopic BDs discovered to date in the Pleiades, and matched them up positionally to my source lists, using (IRAF: TMATCH). These cluster members could be highlighted on the colour magnitude diagrams, to help define where the cluster sequence lies.

Figure (7.1) shows the colour magnitude diagram for the Pleiades fields. Sources are indicated by dots, and filled circles indicate the positionally matched members. The associated photometric errors are shown down the right hand side of the plot. The upper portion

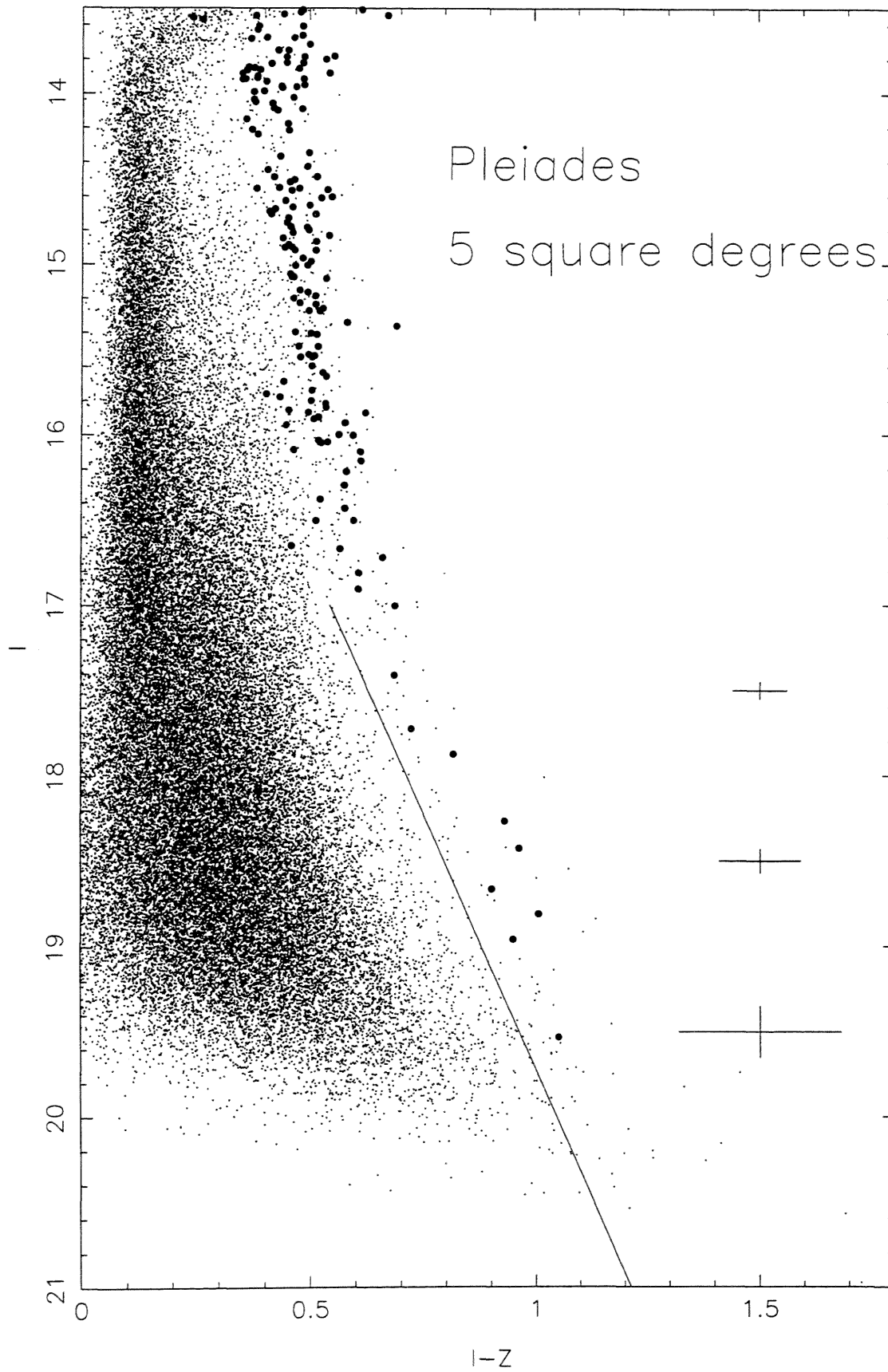


Figure 7.1: Colour magnitude diagram of 5 square degrees of the Pleiades. Previously identified proper motion members (Hambly, Hawkins & Jameson 1993) and spectroscopically verified BDs (Osorio, Rebolo & Martin 1997) are shown as filled circles. The line indicates the candidate selection cutoff, and the photometric error are indicated on the right of the plot.

of the Pleiades sequence is well defined by the large number of proper motion members (mainly from Hambly, Hawkins & Jameson (1991)). This sample stretches down to just over $I=17.4$, ending on the star HHJ3, which is just above the hydrogen burning limit. Below this, 8 spectroscopic BDs were covered by the survey, and show where the sub-stellar sequence lies. This sequence covers the mass range $0.080 - 0.045M_{\odot}$ ($17.75 < I < 19.5$). 3 or possibly 4 of these BDs appear higher than the others, and could therefore possibly be binaries, but the remaining BDs lie on a fairly straight line. I therefore selected BD candidates to the right of the line shown in Figure (7.1), and fainter than $I=17.5$ (just below HHJ3). The photometry and coordinates of the 96 selected Pleiades BD candidates are listed in the table in Appendix (C.1), and finder charts given in Appendix (D.1).

Figure (7.2) shows the colour magnitude diagram for the Praesepe fields. As before, the proper motion members indicate the upper portion of the stellar sequence down to about $I=17.2$. However, since Praesepe is a less popular cluster for deep CCD imaging, the lower portion of the cluster sequence is less well defined. The 2 filled circles are RIZpr 2 and RIZpr 21 from my RIZ survey which were followed up at K (and confirmed as sufficiently red) (Chapters (4) (5)). Both these stars are possible binaries from the I, I-K photometry, and RIZpr 21 in particular looks like a binary in Figure (7.2) as well. In order to define the cluster region, I used the proper motion members to lock down the brighter end of the sequence, and chose a line of similar gradient to that used for the Pleiades making sure that the large number of obvious background stars were excluded from the selection region. This line is shown in Figure (7.2). A lower magnitude limit of $I=17$ was chosen for candidate selection, and the photometry and coordinates of the 141 selected Praesepe VLM candidates are listed in the table in Appendix (A.4), with finder charts given in Appendix (B.2).

Figure (7.3) shows the colour magnitude diagram for the two Hyades fields. The cluster sequence was defined by shifting the Praesepe selection region up the required $5 \log \frac{162}{48}$ magnitudes (2.6^{mag}) and allowing for a cluster depth of ± 1 magnitude. I then defined a candidate selection region that broadened out slightly towards fainter magnitudes, to take into account photometric errors. Since the BD limit in Praesepe could be as bright as $I=19.5$, and the Hyades is approximately the same age as Praesepe, I chose a lower magnitude limit for BD candidate selection of $I=16.5$. The photometry and coordinates of the 33 selected Hyades BD candidates are listed in the table in Appendix (E.1), with finder charts given in Appendix (F.1).

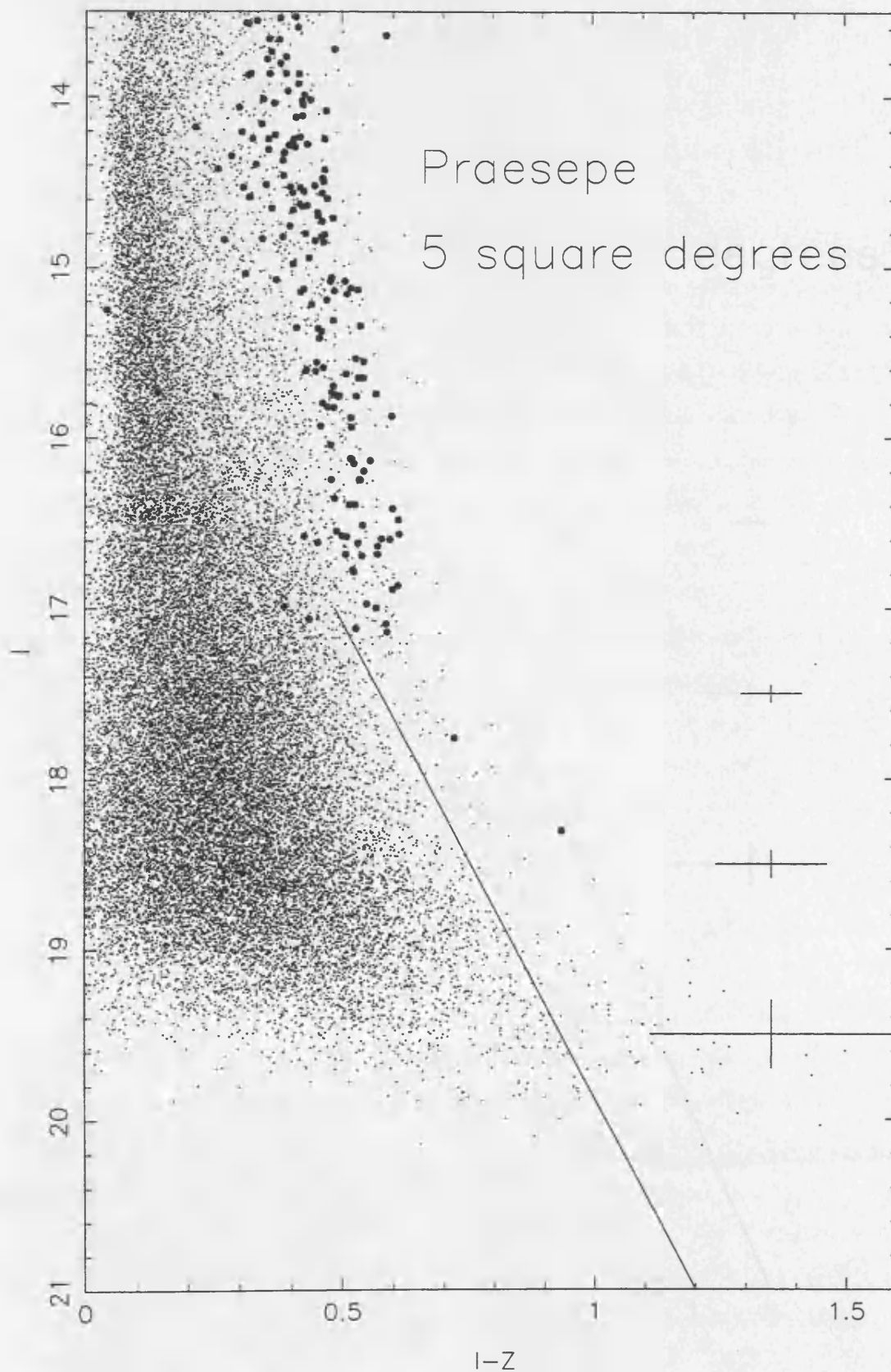


Figure 7.2: Colour magnitude diagram of 5 square degrees of Praesepe. Previously identified proper motion members (Hambly *et al.* 1995a) and two of the candidates from chapter (4) which have been confirmed with K band photometry (chapter (5)) are shown as filled circles. The line indicates the candidate selection cutoff, and the photometric error are indicated on the right of the plot.

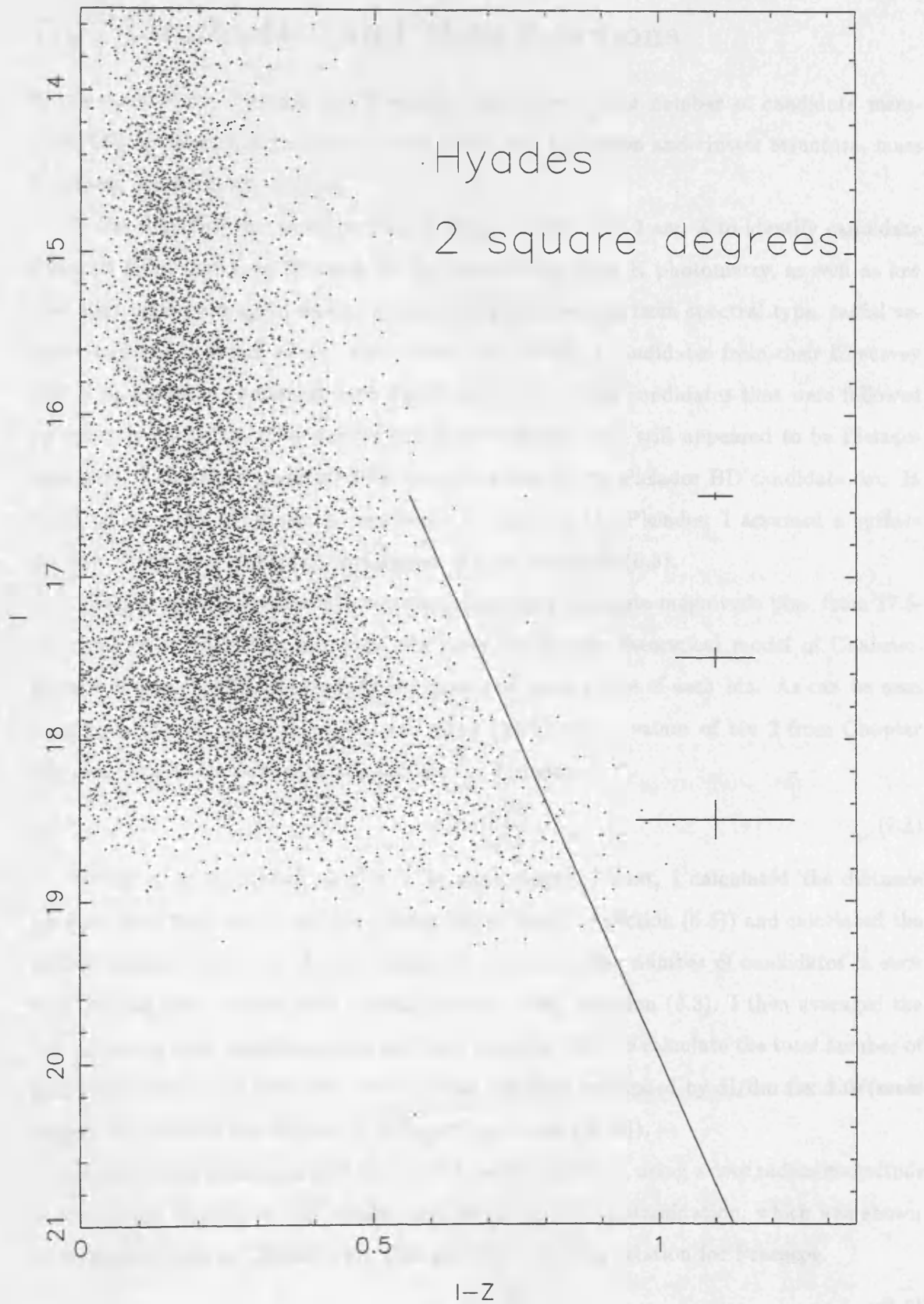


Figure 7.3: Colour magnitude diagram of 2 square degrees of the Hyades. Because of the large depth to distance ratio, and the photometric errors (which are shown on the right of the plot), a generous candidate selection line was chosen, which is shown on the plot.

7.5 Luminosity and Mass functions

In the case of the Pleiades and Praesepe, there are a large number of candidate members, and by making some assumptions about contamination and cluster structure, mass functions can be easily derived.

In the Pleiades, the recent survey of Osorio (1997) used I and Z to identify candidate Pleiades BDs, and then followed up the observations with K photometry, as well as low and high resolution spectroscopy to determine membership from spectral type, radial velocity and the presence of H α . They found that $\sim 70\%$ of candidates from their IZ survey had K magnitudes consistent with membership. All of the candidates that were followed up spectroscopically (after passing the K photometry test) still appeared to be Pleiades members. I therefore assumed 30% contamination for my Pleiades BD candidate list. In order to correct my survey to represent the whole of the Pleiades, I assumed a surface density of the form described in Chapter (6), i.e: equation (6.3).

I divided my candidates into two photometrically complete magnitude bins, from 17.5-18.5 and from 18.5-19.5, and used the most up to date theoretical model of Chabrier, Baraffe & Plez (1996) to calculate the mass and mass range of each bin. As can be seen from equation (6.16), $r_c \propto 1/\sqrt{m}$, and using the m and r_c values of bin 2 from Chapter (6), one obtains the following relation for the Pleiades (7.1).

$$r_c = \frac{1.60}{\sqrt{m}} \quad (7.1)$$

Where r_c is in parsecs, and m is in solar masses. Next, I calculated the distance between each field centre and the cluster center (found in section (6.5)) and calculated the central surface density of the two magnitude bins from the number of candidates in each field (taking into account 30% contamination), using equation (6.3). I then averaged the five values for each magnitude bin, and used equation (6.4) to calculate the total number of BDs in the cluster for each bin. This number was then multiplied by dI/dm (ie: $1.0/(\text{mass range})$) to produce the number of BDs per unit mass ($N(m)$).

I followed the same approach for the Praesepe candidates, using a core radius-magnitude relation from Hambly *et al.* (1995b), and assuming 50% contamination, which was shown to be appropriate in Chapter (4). This gave the following relation for Praesepe.

$$r_c = \frac{1.32}{\sqrt{m}} \quad (7.2)$$

The units are once again parsecs and solar masses. The results of these calculations are summarised in Table (7.2), and the mass functions are plotted in Figures (7.4) and

I range	m(M _⊙)	m range	r _c (pc)	log m	log N(m)
The Pleiades					
17.5-18.5	0.071	0.060-0.080	6.0	-1.149	3.70
18.5-19.5	0.055	0.050-0.060	6.8	-1.260	3.98
Praesepe					
17-18	0.103	0.120-0.092	4.1	-0.987	3.77
18-19	0.087	0.092-0.085	4.5	-1.061	3.78
19-20	0.081	0.085-0.080	4.6	-1.092	4.10

Table 7.2: Cluster mass functions.

(7.5) for the Pleiades and Praesepe respectively. In the Pleiades plot I have also plotted the mass function of Hambly, Hawkins & Jameson (1991), and the dotted line corresponds to $\alpha = 1.3$. In the Praesepe plot I have also plotted the mass functions of Hambly *et al.* (1995b), as well as the mass function that I derived from the RIZ survey in Chapter (4), where the numbers have been increased for mass bins covering ($17 < I < 20$), in line with the 30 percent contamination seen in chapter (5), rather than the 50 percent which was assumed in chapter (4). The dotted line in the Praesepe plot corresponds to $\alpha = 1.5$. The new data do not go quite as deep as the RIZ survey, but the area covered was ~ 5 times greater. The two sets of results agree well with each other, showing that the new method for correcting for the rest of the cluster does not affect the results greatly over the mass range covered. The form of the mass function then appears to be the same as was found in Chapter (4).

7.6 Discussion

The mass functions derived for the Pleiades indicates that α is rising into the BD regime but not sufficiently rapidly for BDs to dominate the cluster mass. In Praesepe, the mass function appears to be steepening at the bottom of the main sequence in both the RIZ data and the Kitt Peak data. This point was discussed in Chapter (4), and it is clear that this effect occurs as a result of the faintest magnitude bins, where contamination will be somewhat more prevalent. It will require infrared photometry and eventually spectroscopy

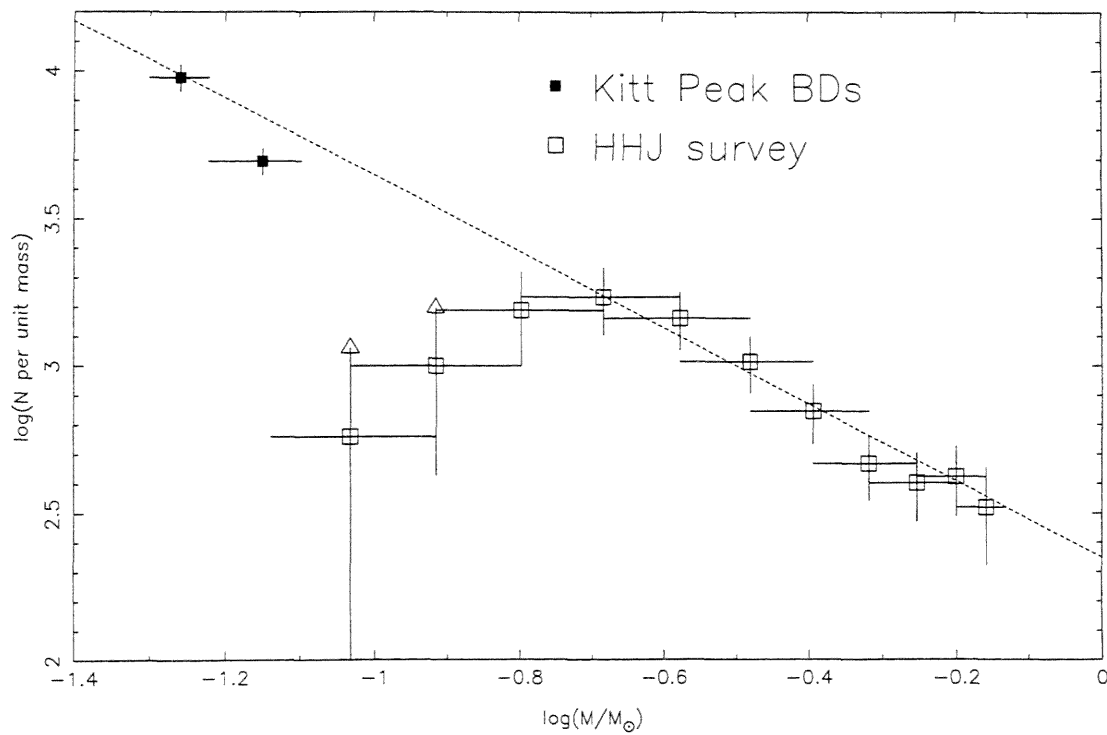


Figure 7.4: The mass function of the Pleiades. The filled squares indicate the values derived from the Kitt Peak IZ survey. The mass function found by (Hambly, Hawkins & Jameson 1991) is shown by open squares. A dashed line of $\alpha = 1.3$ is overlaid on the plot.

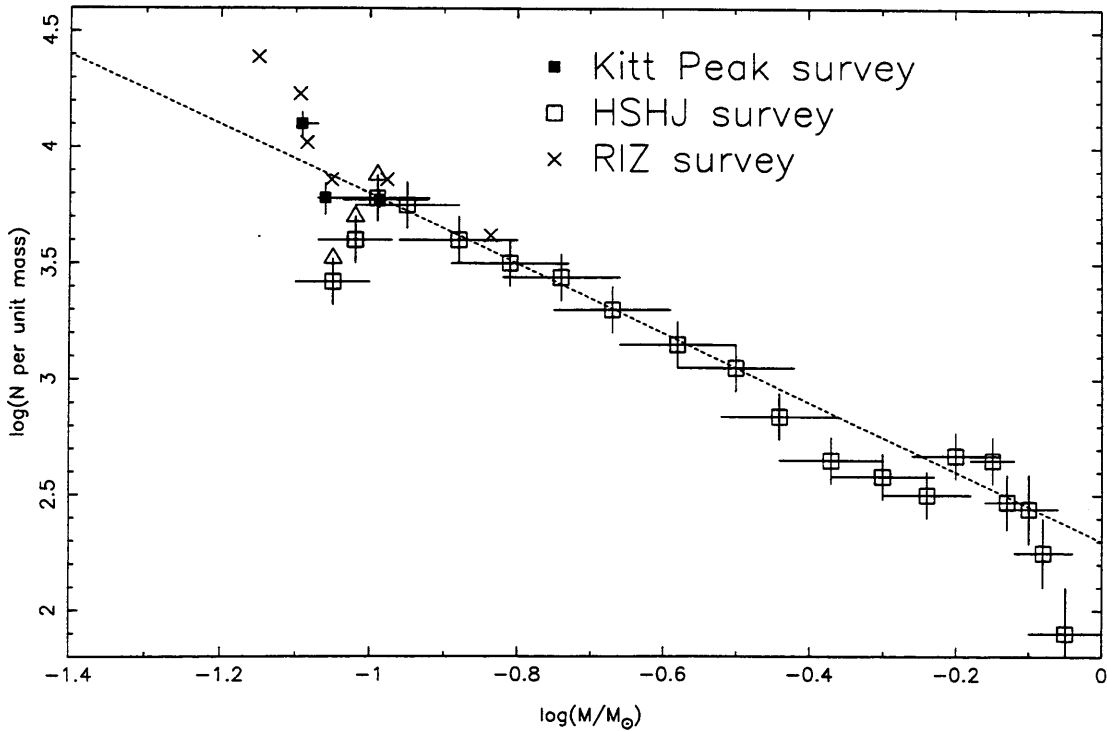


Figure 7.5: The mass function of Praesepe. The filled squares indicate the values derived from the Kitt Peak IZ survey. The mass function found by (Hambly *et al.* 1995b) is shown by open squares, and the mass function derived in Chapter (4) is shown by crosses. The RIZ survey numbers have been increased for mass bins covering ($17 < I < 20$), in line with the 30 percent contamination seen in chapter (5), rather than the 50 percent which was assumed in chapter (4). A dashed line of $\alpha = 1.5$ is overlaid on the plot.

to verify the actual number of cluster members in my candidate lists, and thus lock down the correct form of their mass functions.

In the Hyades, the candidate list will be dominated by contamination from field stars. A mass function is thus out of the question, but the survey easily goes deep enough to detect Hyades BDs, and there are many candidates. In order to decrease the contamination from background field stars, one can of course obtain K magnitudes, but proper motions would be another very useful criteria to reject both background and foreground stars. The proper motion of the Hyades is $(0.070-0.155)$ arcsecs/yr (Reid 1992). That is, a Hyades BD could be expected to have moved about 1 arcsecond in a decade. Since the accuracy of the coordinates of the candidates are somewhat better than 1 arc second, it is feasible to obtain proper motions for them using first epoch measurements from 10-20 years ago. This avenue is currently being investigated, and if successfully combined with infrared photometry and spectroscopic follow up, this could lead to the first bona fide BD discovery in the Hyades.

7.7 Conclusions

By using I and Z filters on the 1 degree square field of view Burrell Schmidt telescope, I have been able to detect 96 BD candidates in the Pleiades. 6 of these candidates are already established as highly likely BDs, and 2 more as certain BDs, since lithium has been detected in them. Therefore, I have found 88 new BD candidates in the mass range $0.080 - 0.045M_{\odot}$. I would expect from other similar small scale surveys that about 70% of these candidates should turn out to be genuine BDs. That is, ~ 60 new BDs in the Pleiades.

The Praesepe candidates, when verified with follow up observations will extend the Praesepe sequence right down to the BD limit, and potentially to beyond it, depending on the true age of Praesepe.

As a preliminary sample, the Hyades candidate list is potentially a source of several BDs, which should become evident when the required follow up photometry is obtained, and proper motions measured.

The Burrell Schmidt telescope has proved to be an excellent instrument to use when trying to cover several square degrees. The tracking was perfectly adequate in general, and saturation was no problem at all.

The candidates discussed in this chapter are all listed in Appendices (C.1), (A.4) and (E.1), and finder charts are given in Appendices (D.1), (B.2) and (F.1).

Chapter 8

Conclusions and Future Work

This chapter will review the thesis as a whole. In Chapter (1) I set out the definitions of very low mass stars and brown dwarfs, defined some nomenclature and described the aims of this thesis work. Chapter (3) describes the principles of photometry and the data reduction that was necessary for much of this work. Chapters (4) - (7) describe the results of the four projects that I have been substantially involved with over the last three years. In the remainder of this chapter, I shall review the results of these 4 chapters.

8.1 Chapter (4) - RIZ Praesepe survey

Chapter (4) describes the results of a deep photometric survey of the Praesepe open cluster. The primary focus of the chapter was the R, I and Z photometry, but the results of a White Dwarf UBV survey that I also reduced were briefly described also. A comprehensive observational review of Praesepe is presented at the beginning of the Chapter.

The choice of filters for BD searches is discussed with reference to this work. This is an important area, since BDs are rather elusive, and only the most effective method of searching will locate large numbers of them. It is clear that optical CCDs are ample for initial photometric surveys when used with the right filters. The filters best suited are then I and Z, with R being some what difficult to obtain, and V substantially worse. Once the candidates have been selected using the resulting photometry, and accurate coordinates calculated, the task of weeding out contaminants using infrared photometry (and eventually spectroscopy) is relatively easy, using for example UKIRT to “point and shoot”.

The resulting Praesepe RIZ photometric catalogue was plotted on two colour magnitude diagrams, and the cluster sequence defined by reference to proper motion members, field M Dwarfs and theoretical isochrones. This resulted in the selection of 26 new candidate VLM and BDs. As a first approximation, the sample was weighted and used in conjunction with a simplified cluster model to construct a mass function for Praesepe down to below the stellar limit. This mass function can be seen to be initially continuing the slope of the proper motion survey of Hambly *et al.* (1995b), and for the faintest magnitudes actually rising into the BD regime. If 50% of the candidates are actual cluster members, then the mass function will be accurate, and about 9 new Praesepe BDs will result.

The results from this chapter need to be followed up with infrared photometry to establish cluster membership with more confidence. This is one of the focuses of Chapter (5). Another point of interest is the cluster model. The one used in this chapter was a simple exponential, and a more refined approach would be an improvement. It may or may not change the general results of the mass function, but could also potentially lead indirectly to information about stellar and sub-stellar populations in open clusters. This will be the focus of Chapter (6).

8.2 Chapter (5) - Infrared photometry

Chapter (5) describes the results of infrared photometric follow up of two sets of candidate cluster samples. 11 of the 26 RIZpr candidates from Chapter (4) were done, as well as 90 proper motion stars from the survey of Hambly *et al.* (1995a).

Firstly, non members were identified using I and K photometry in conjunction with the theoretical isochrones of Chabrier & Baraffe (1997) which were used to indicate the cluster sequence. 7 non members were identified using this approach. Next, J, H and K photometry was employed, and identified 1 possible non member. The resulting number of members agrees almost exactly with the predictions of the proper motion analysis (which assigned each star a membership probability). Binaries were also flagged using an equal mass binary sequence as an indicator, and 47% of the members were found to be multiple. This number agrees very well with 46% which was found for the Pleiades by Steele & Jameson (1995). Several things are clear from these results;

- The theoretical non gray atmosphere model of Chabrier & Baraffe (1997) fit the observations very well to within the photometric errors. This lends credence to the

identification (non members and members) process, as well as suggesting that the physics of VLM and BD interiors and atmospheres is being tackled rather successfully by this group in particular.

- The proper motion survey of Hambly *et al.* (1995a) was very successful at identifying cluster members (90% success), and the probabilities calculated from the proper motion distributions agree with my observations.
- Using an (I, I-K) colour magnitude diagram is an extremely effective method of identifying non cluster members.
- The proportion of binaries in Praesepe appears to be essentially the same as in the Pleiades. Since Praesepe is between 5 and 10 times older than The Pleiades, it seems clear that the binary populations in open clusters do not change in size over time scales of ~ 1 Gyr.

The 11 candidates from Chapter (4) were also plotted with the isochrones, to identify non members. In fact, only 3 of the candidates lay to the left of the isochrone (73% members), but this apparently very successful hit rate will be partly due to a selection effect, since many of the 11 candidates chosen for infrared follow up were two colour candidates, which reduces the likelihood of contamination. However, the success of the RIZ survey is evident. The 4 most massive mass function points derived in Chapter (4) should be accurate (or perhaps even a little low), but the 2 lowest mass points (which is where the slope appears to steepen) are not confirmed or denied by the results of this chapter.

In order to calculate masses for the Praesepe VLM and BD members, one firstly needs to know the age and distance of the cluster. The distance is well known ($m-M=6.05$), but the age is more uncertain. One can of course take lower and upper limits, and thus calculate the limits on the masses. Using upper and lower age limits of 500 Myrs and 1 Gyr for Praesepe, I calculated that the object RIZpr 1 is a free floating BD if Praesepe's age is towards the younger limit. The remaining single star members are all VLM. The RIZpr members flagged as binaries all fall remarkably close to the equal mass binary line. One can thus be fairly confident that these objects are multiple systems, and using the isochrones, I calculated that RIZpr 18 must have a BD secondary. RIZpr 18b would have a mass ranging from $0.04 - 0.08M_{\odot}$, depending on the mass ratio of the system and the age of the cluster. Unless Praesepe is some what older than 1 Gyr (which seems contrary to all

the evidence), then the RIZpr 18 system must contain 1, or possibly 2 BDs (if $q=1$). The remaining 3 binaries all potentially contain a BD, but the likelihood of this is somewhat lower.

Chapters (4) and (5) have thus culminated in a better understanding of the low mass Praesepe sequence and binary population, as well as at least 1, possibly as many as 5 BDs (1 free floater and the rest binary companions), and a possible steepening Praesepe mass function into the BD regime.

We still have a number of the faintest Praesepe BD candidates to follow up with K photometry. We should also obtain optical and even infrared spectroscopy, and eventually proper motions for all the Praesepe BD candidates with the correct positions in the I, I-K diagram if we are to be really thorough.

8.3 Chapter (6) - The Mass of the Pleiades

Chapter (6) aims to understand the dynamics and structure of open clusters from a more theoretical point of view, by focussing on the Pleiades, where much observational work has yielded an extensive membership catalogue. The chapter begins by reviewing previous work, and then describes the cluster model used (a “King” distribution). Binaries were identified where possible from the catalogue, but for the lower mass stars a binary fraction of 46% was assumed ((Steele & Jameson 1995) which agrees with Praesepe also).

The cluster was observed to be flattened in the galactic plane direction, but apparently more so for higher mass stars. This seems to rule out the explanation that the galactic gravitational field is responsible, since this would have the opposite effect. The flattening could then be a result of the cluster oscillating up and down through the galactic disk, or perhaps be caused by the rotation of the cloud that formed the cluster.

The King distribution was fit to the Pleiades surface density with good agreement to the data. Having established the accuracy of the model (at least for the cluster regions that have been observed), one can apply the model in the future when deriving cluster luminosity and mass functions. A tidal radius of 13.1pc was derived, which gave the same tidal mass as the observed distributions, and the observed mass of the cluster was $735M_{\odot}$. The crossing time and relaxation time for the Pleiades were calculated from the model fits, and it was found that $t_{cr}=16$ Myrs, and $t_{rlx}=96$ Myrs. The cluster stars should thus have time to cross the Pleiades several times (during which the velocity distribution “tells” the

density distribution what to be) before a stellar encounter affects this equilibrium. It then seems clear that the Pleiades at an age of 120 Myrs should be essentially relaxed, and that equipartition of energy can have taken place.

Since $t_{\text{cr}} \ll t_{\text{rlx}}$, one can derive velocity distributions from the densities. Plotting these against $1/\sqrt{m}$ produced a straight line, as predicted by equipartition. The lowest mass stars however, do not appear to be moving quite fast enough. However, since lower mass stars will be more spread out, their frequency of interaction will be less than the more centrally condensed higher mass stars, and one would expect them to take longer to speed up through interaction.

This near linear relation means that when one observes small regions of the cluster (to find a local surface density), all you need to do is derive a mass for the members you find, and use this mass to get a core radius for that population. Core radius mass relations for both The Pleiades and Praesepe are given in equations (7.1) and (7.2). The total number of such stars in the cluster then follows from the King function.

Using the derived velocity distributions and the observed mass distributions, the binding energy and kinetic energy of the cluster could be found, and compared, using the Virial Theorem. Any large as yet unseen BD population would show up as a deficit in kinetic energy (since the BDs would have attained high velocities through encounters). Such a deficit was not seen. In fact, the maximum allowed BD population (from the error bars on the model fits) was some $131M_{\odot}$, which is a value consistent with mass function slope continuing into the BD regime at about $\alpha \sim 1.5$.

8.4 Chapter (7) - The Burrell Schmidt surveys

Chapter (7) presented the results of deep photometric surveys of The Pleiades, Praesepe and the Hyades. The telescope used was the Burrell Schmidt on Kitt Peak, with I and Z filters. The Burrell is only 61cm in diameter, but thanks to a 2000 x 2000 pixel CCD, an auto-guider, reasonably good weather, and the advantages of the IZ filter system, we were able to survey the clusters down to $I=20$ (well below the stellar limit in The Pleiades), covering 5 square degrees in The Pleiades and Praesepe, and 2 square degrees in The Hyades.

The advantage of this setup is clearly the large sky coverage, while the disadvantages are the pixel scale which was 2 arcseconds, and the fact that in 1 square degree it is

difficult to get close to the cluster centre without ones field of view containing brighter cluster members that will saturate the CCD and possibly cause disruptive charge bleeding.

By carefully selecting fields that avoid bright stars however (by eye, using the SAO catalogue - $V < 9$), one can avoid the problem of excessive bleeding. It is also worth pointing out that in the field Pl 3 the faintest of the seven sisters was just on the image, and that bleeding was apparent but not sufficiently bad to ruin a substantial portion of the image.

The large pixel scale means that shape analysis will be rather un-fruitful, but the majority (perhaps all) of the contaminating red galaxies can be identified during the process of infrared photometric follow up, which is not particularly time consuming per object (cf: 1-4 minutes for $K=14.3-15.8$ ($S/N=50$), which as an example, is the exposure time range required for the $I=17.5-20$ Pleiades BD candidates). Another minor draw back is the large effective seeing (due partly to the large pixels scale), which means that brighter stars can “swallow up” near line of sight objects. An example of this occurring is in in field Pl 3, where the BD PIZ 1 (see section (2.6)) which is 4.5 arcseconds away from a brighter background star, is swallowed up in the brighter star’s point spread function. If there are $\sim 10,000$ sources per image (2000×2000 pixels), and one assumes that a source will be lost if it is within ~ 3 pixels of another, then $\sim 7\%$ will be affected ($270,000/4,000,000$). The effect is thus fairly small.

The surveys resulted in 96 BD candidates in the Pleiades (6 of which are previously identified BDs), 141 Praesepe VLM (2 of which are RIZpr members), and 33 Hyades BD candidates.

The positions of the 6 previously identified Pleiades BDs in the I, I-Z colour magnitude diagram appear to define the cluster sequence (with some evidence of a binary sequence) very well. This lends confidence to the remainder of the candidates, and if as Osorio (1997) found, about 70% of I, I-Z candidates are really members, then the survey will have turned up 62 new BDs in the Pleiades.

The Praesepe candidates stretch down to just above the stellar limit, or perhaps just below it, if Praesepe is only 500 Myrs old. There may therefore be some BDs in the candidate list. Also, even if all the candidates are above the stellar limit, many may be binaries, and as was described in Chapter (5), identifying binary stars near the BD limit is an important task, where light curve analysis allows BD masses to be measured dynamically.

The Hyades candidates will be mainly contaminants, but it may be possible to obtain

proper motions using a 1st epoch I plate stack. A collaboration with Dr. M. R. S. Hawkins (R. O. E.) has been started to try measuring proper motions. Infrared photometry as well as optical and infrared spectroscopy are also required.

Follow up infrared photometry for all these candidates is an important next step, and will presumably lead to the identification of a large number (>100) of open cluster VLM and BDs.

8.5 Closing remarks and the future

At the start of this PhD. work, previous searches for BDs had produced no direct evidence of bona fide sub-stellar objects. In her summary remarks to the ESO Workshop in Garching, "The Bottom of the Main Sequence And Beyond" (August 1994), Virginia Trimble observed that "It would be interesting to assemble a list of all BD candidates ever proposed, and what became of them... the interval between a star's being added to the list and being removed however *is* getting smaller !", and having listed many candidates that "bit the dust" in Garching, concluded that only "A few stars continue to cling to the ragged (BD) cliff" but that these are all very much borderline cases.

During the three years of my thesis work, the state of affairs has changed substantially. Many previous candidates had been ruled out as a result of failing the Lithium test, but this changed with PPL 15 (first found in 1994), when the lithium doublet was seen in its spectrum (1996). The first bona fide BD had been found, and was followed by Teide 1 (1995) in the Pleiades which showed lithium, and the companion Gl229b (1995), which has a T_{eff} as low as 900 K. These exciting new discoveries were reported at the Ninth Cambridge workshop, "Cool Stars, Stellar Systems and the Sun" in 1995, and several other BDs have been identified since, both in the field and in open clusters.

The work described in this thesis has produced large numbers of BD (as well as VLM) candidates as both free floating objects and in binary systems. Photometric and spectroscopic follow up will indicate the contaminants, and leave the cluster members, at which point the accurate numbers can be used in conjunction with the appropriate cluster model to define the open cluster mass functions right down to, and beyond (in the case of The Pleiades) the stellar limit to a statistical accuracy much better than has been achieved to date.

The field of VLM and BD is advancing rapidly, both observationally and theoretically,

and any pessimism they may have been at the Garching conference can no longer be founded.

It is clear that the 2MASS and DENIS surveys are going to turn up large numbers of local field BDs. However I suspect that clusters will remain as the best places to determine luminosity and mass functions. To reach the lowest masses ($\sim 0.01M_{\odot}$) we will need to change our surveying strategy from using CCDs to using IR arrays. Surveys at J in the Pleiades could quite easily reach a mass of $0.01M_{\odot}$. Large area IR arrays are needed. The Cambridge IR Survey Instrument (CIRSI) should meet just this need. Water and methane filters could be used for BD candidate confirmation.

Appendix A

Praesepe photometry

This appendix contains tables of photometry and coordinates (J2000) of Praesepe candidate VLM and BDs found during this thesis work, as well as new photometry of previously identified candidate members. The coordinates are all accurate to $\sim \pm 0.5$ arcseconds.

Section (A.1) is for the VLM and BD RIZ candidates from Chapter (4), including the K photometry and the non member and binary flags from Chapter (5). The magnitudes are I_{RGO} and R_{RGO} .

Section (A.2) is for the white dwarf candidates from Chapter (4).

Section (A.3) is for the infrared photometry of the HSHJ sample from Chapter (5), including non member and binary flags, as well as Cousins R and I magnitudes.

Section (A.4) is for the VLM Kitt Peak candidates from Chapter (7). Two of these candidates were also found in the RIZ survey (section (A.1)), and these are indicated in brackets. The I magnitudes are I_{KP} .

A.1 R I Z Praesepe VLM and BD candidates

Flag codes: n=non member, b=binary

RIZpr no.	flag	I	R-I	I-Z	I-K	R.A.	Dec
1		20.14 ± 0.12	2.47 ± 0.35	-	3.98 ± 0.14	08 36 54.55	+19 54 15.1
2	b	18.19 ± 0.04	2.14 ± 0.07	0.87 ± 0.04	3.40 ± 0.06	08 37 02.11	+19 52 07.0
3		21.20 ± 0.22	-	1.25 ± 0.26	-	08 37 29.91	+19 50 09.1
4		18.52 ± 0.03	2.37 ± 0.08	-	3.27 ± 0.05	08 38 11.69	+19 59 44.4
5		20.86 ± 0.16	-	1.34 ± 0.25	-	08 38 21.78	+20 05 53.2
6		21.09 ± 0.16	-	1.52 ± 0.21	-	08 38 33.17	+19 49 13.2
7		21.24 ± 0.16	-	1.44 ± 0.23	-	08 39 20.05	+19 42 41.1
8	b	17.81 ± 0.02	2.14 ± 0.04	0.78 ± 0.03	3.19 ± 0.04	08 39 20.43	+20 01 36.9
9		21.25 ± 0.22	-	1.34 ± 0.24	-	08 39 24.09	+19 58 08.3
10		20.54 ± 0.10	-	1.41 ± 0.15	-	08 39 32.54	+20 00 54.4
11		19.47 ± 0.06	-	1.22 ± 0.07	3.61 ± 0.15	08 39 47.72	+19 28 03.6
12	n	20.10 ± 0.12	-	1.74 ± 0.15	3.17 ± 0.24	08 39 48.82	+19 26 07.3
13		20.24 ± 0.07	-	1.73 ± 0.17	-	08 40 27.55	+19 28 48.9
14		20.59 ± 0.08	-	1.27 ± 0.15	-	08 40 46.12	+20 03 25.0
15		21.36 ± 0.16	-	1.46 ± 0.25	-	08 40 47.72	+20 02 41.0
16		21.10 ± 0.13	-	1.20 ± 0.23	-	08 40 59.08	+20 07 57.8
17		20.41 ± 0.10	2.52 ± 0.35	-	-	08 41 08.14	+20 09 01.9
18	b	19.63 ± 0.08	2.61 ± 0.19	-	4.21 ± 0.09	08 41 08.48	+19 54 01.1
19		21.42 ± 0.18	-	1.69 ± 0.26	-	08 41 10.31	+20 07 15.5
20		18.48 ± 0.04	2.21 ± 0.08	0.96 ± 0.04	3.27 ± 0.06	08 41 24.84	+19 57 26.5
21	b	18.73 ± 0.05	2.36 ± 0.11	0.91 ± 0.07	3.68 ± 0.06	08 42 11.46	+19 52 50.0
22		21.55 ± 0.17	-	1.46 ± 0.25	-	08 42 21.72	+20 07 35.9
23	n	19.06 ± 0.03	2.55 ± 0.09	0.99 ± 0.04	3.06 ± 0.16	08 42 54.63	+20 03 35.9
24		20.43 ± 0.16	2.58 ± 0.42	1.33 ± 0.17	-	08 43 01.25	+19 49 59.7
25		21.20 ± 0.13	-	1.29 ± 0.21	-	08 43 49.12	+20 07 30.0
26	n	18.08 ± 0.04	2.07 ± 0.06	-	2.57 ± 0.06	08 43 59.47	+20 07 10.3

A.2 U B V Praesepe white dwarf candidates

UBVpr no.	V	U-B	B-V	R.A.	Dec
1	21.21	-0.74	0.18	08 36 46.39	+20 00 39.2
2	20.72	-0.36	0.68	08 37 44.55	+20 02 36.5
3	21.08	-0.98	0.62	08 38 11.90	+20 00 24.7
4	21.41	-1.16	0.08	08 38 19.52	+19 42 29.9
5	21.82	-0.85	0.47	08 38 20.26	+20 01 00.0
6	21.83	-0.73	-0.02	08 38 31.15	+19 42 42.6
7	20.18	-0.70	0.52	08 38 35.56	+19 29 17.5
8	20.43	-0.71	0.03	08 38 36.79	+19 33 40.7
9	21.42	-0.46	0.48	08 38 38.30	+19 43 56.2
10	18.90	-0.72	0.13	08 38 44.07	+19 59 55.5
11	19.31	-0.70	0.38	08 38 58.00	+19 33 33.2
12	21.16	-0.81	-0.07	08 39 02.63	+20 04 19.8
13	17.61	-0.71	0.07	08 39 07.50	+19 21 53.8
14	19.57	-0.73	0.09	08 39 16.21	+19 42 45.6
15	17.70	-0.78	-0.13	08 39 34.73	+19 30 50.8
16	19.39	-0.57	0.56	08 39 59.00	+20 05 22.0
17	20.47	-0.57	0.62	08 40 25.14	+19 48 18.9
18	19.52	-0.38	0.67	08 40 48.85	+20 07 48.5
19	20.36	-0.89	-0.07	08 41 18.00	+19 50 40.8
20	18.74	-0.55	0.36	08 41 22.89	+20 03 56.4
21	18.64	-0.89	0.40	08 41 28.25	+20 01 57.8
22	20.46	-0.72	0.06	08 41 30.88	+20 00 42.7
23	18.44	-0.90	0.38	08 41 51.25	+19 44 09.9
24	18.43	-0.81	0.27	08 41 52.68	+19 44 25.8
25	20.04	-0.42	0.35	08 41 52.84	+19 31 58.0
26	21.45	-0.75	0.52	08 41 56.13	+19 34 45.5
27	20.53	-0.80	-0.11	08 42 00.33	+19 48 30.5
28	21.23	-0.38	0.41	08 42 11.27	+19 55 15.8
29	19.29	-0.82	0.49	08 42 13.00	+19 56 33.9
30	20.14	-0.24	0.62	08 42 15.48	+20 04 55.7

UBVpr no.	V	U-B	B-V	R.A.	Dec
31	19.43	-0.53	0.18	08 42 16.23	+19 33 12.0
32	20.58	-0.37	0.33	08 42 20.22	+20 01 10.2
33	20.33	-1.10	0.41	08 42 37.74	+19 26 24.7
34	21.03	-0.71	0.48	08 42 40.32	+20 00 44.9
35	19.13	-0.83	0.25	08 42 47.82	+19 47 56.6
36	20.71	-0.40	0.59	08 42 49.63	+20 08 45.1
37	17.83	-0.69	0.01	08 42 52.43	+19 51 11.5
38	19.63	-0.32	0.64	08 43 10.23	+19 38 51.3
39	21.41	-1.08	0.61	08 43 17.93	+19 48 55.0
40	20.31	-0.51	0.08	08 43 47.11	+20 02 14.2
41	21.56	-0.36	0.52	08 44 18.89	+20 01 50.3
42	20.70	-0.88	-0.11	08 44 22.68	+19 56 41.5
43	21.15	-1.01	0.54	08 48 35.51	+19 55 30.4

A.3 HSHJ star photometry

Flag codes: n=non member, ? =possible non member, b=binary.

HSHJ no.	flag	R_c	I_c	J	H	K
30		13.05	12.38	0.00	0.00	10.75
31		13.53	12.66	0.00	0.00	11.05
34	b	17.43	15.43	13.77	13.17	12.92
36		13.39	12.72	0.00	0.00	10.88
42	b	17.70	15.85	14.29	13.69	13.44
69	b	12.81	12.17	11.14	10.51	10.39
83		12.50	12.11	11.16	10.63	10.54
85	b	14.00	13.13	11.88	11.22	11.07
93		12.72	12.18	0.00	0.00	10.57
95		19.27	17.03	15.30	14.64	14.40
98	n	13.14	12.62	0.00	0.00	11.93
101		14.02	13.11	0.00	0.00	11.14
106		18.79	16.70	15.08	14.47	14.19
112		14.88	13.75	12.58	11.91	11.72
114		11.06	10.74	0.00	0.00	9.52
115		16.47	14.81	13.44	12.81	12.59
119		11.99	11.69	0.00	0.00	10.28
122	b	14.67	13.36	12.09	11.43	11.22
129		14.06	13.17	0.00	0.00	11.20
132		12.41	12.02	0.00	0.00	10.56
134	b	13.32	12.24	0.00	0.00	10.24
137		13.34	12.50	0.00	0.00	10.88
141		13.56	12.66	0.00	0.00	10.92
144	b	14.33	13.18	0.00	0.00	10.94
145	b	13.99	12.98	0.00	0.00	10.98
149		13.19	12.38	0.00	0.00	10.80
150		13.63	12.67	0.00	0.00	10.94
152		13.26	12.27	0.00	0.00	10.49

Flag codes: n=non member, ? =possible non member, b=binary.

HSJ no.	flags	R_c	I_c	J	H	K
153		11.04	10.82	0.00	0.00	9.81
160		13.33	12.52	0.00	0.00	10.87
161		14.09	13.08	0.00	0.00	11.23
162		11.24	10.95	0.00	0.00	9.82
166		13.29	12.42	0.00	0.00	10.79
176		12.59	11.99	0.00	0.00	10.37
179		11.95	11.56	0.00	0.00	10.25
180		11.81	11.53	0.00	0.00	10.20
181	b	19.33	17.27	15.16	14.54	14.21
184		15.06	13.88	12.68	12.01	11.83
188		11.35	11.09	0.00	0.00	10.06
191	b	17.08	15.38	13.73	13.11	12.88
199	n	13.23	12.63	0.00	0.00	11.58
200	n	16.69	15.25	13.98	13.43	13.21
202	b	12.63	12.00	0.00	0.00	10.22
204	b	15.14	13.86	12.60	11.95	11.75
207		15.35	14.04	12.87	12.21	12.02
208	n	13.21	12.62	0.00	0.00	11.62
213		13.22	12.43	0.00	0.00	10.66
215	b	18.54	16.47	14.73	14.10	13.83
216	n	12.38	12.07	0.00	0.00	11.01
218		18.48	16.48	15.00	14.34	14.05
219		13.91	12.99	0.00	0.00	11.18
227	b	16.28	14.56	13.21	12.61	12.35
231	n	13.55	12.89	0.00	0.00	11.64
232		13.54	12.67	11.72	11.08	10.96
233		18.95	16.92	15.24	14.59	14.31
238		13.27	12.41	0.00	0.00	10.67
241	n	13.28	12.47	11.69	11.12	11.05
243		11.92	11.62	0.00	0.00	10.23
244		13.64	12.84	11.87	11.20	11.05

Flag codes: n=non member, ? =possible non member, b=binary.

HSHJ no.	flag	R_c	I_c	J	H	K
245	b	15.76	14.16	12.80	12.14	11.94
247		13.24	12.47	11.48	10.88	10.80
254		14.79	13.79	12.71	12.08	11.88
258		18.90	16.62	15.06	14.43	14.16
270		16.52	14.93	13.59	12.96	12.74
278		14.38	13.28	12.20	11.52	11.34
283	b	19.25	17.18	15.07	14.49	14.16
300	b	15.74	14.05	12.71	12.07	11.84
305	b	16.93	15.03	13.59	12.98	12.72
320		16.10	14.55	13.29	12.64	12.41
321		14.12	13.15	12.08	11.41	11.23
323		11.44	11.16	10.69	10.28	10.19
328	b	18.19	16.16	14.43	13.80	13.53
329		15.85	14.49	13.27	12.64	12.43
339		11.78	11.41	10.72	10.32	10.23
340	b	19.23	16.94	15.05	14.45	14.14
357	b	13.49	12.34	11.19	10.52	10.34
366	b	15.50	13.93	12.50	11.85	11.63
376	?	18.00	16.18	14.52	13.95	13.72
383		13.04	12.34	11.45	10.87	10.75
391		11.07	11.00	10.43	10.16	10.13
400		12.77	12.13	11.24	10.71	10.59
404		17.34	15.65	14.19	13.56	13.33
405	b	17.51	15.87	14.27	13.65	13.41
412		19.32	17.13	15.40	14.84	14.49
421		17.91	16.03	14.55	13.89	13.64
428	b	17.70	15.84	14.23	13.61	13.39
446		19.08	17.04	15.25	14.61	14.36
451	b	18.63	16.58	14.81	14.18	13.93
452	b	17.81	16.10	14.46	13.83	13.61
455	b	16.99	15.34	13.76	13.14	12.92

A.4 I Z Kitt Peak Praesepe candidates

IZpr no.	I	I-Z	R.A.	Dec
1	17.74 ± 0.05	0.71 ± 0.06	8 33 37.87	+20 47 3.2
2	17.04 ± 0.03	0.52 ± 0.04	8 33 38.53	+20 54 47.4
3	17.93 ± 0.05	0.80 ± 0.07	8 33 40.84	+21 12 54.3
4	17.97 ± 0.05	0.66 ± 0.06	8 33 45.87	+21 22 15.0
5	18.14 ± 0.08	0.78 ± 0.09	8 34 3.85	+20 34 8.1
6	17.07 ± 0.03	0.56 ± 0.04	8 34 24.87	+21 13 46.2
7	19.60 ± 0.19	1.07 ± 0.23	8 34 32.97	+20 39 19.4
8	17.03 ± 0.05	0.51 ± 0.06	8 34 38.73	+19 21 52.4
9	20.15 ± 0.32	1.21 ± 0.37	8 34 43.32	+20 37 39.1
10	17.97 ± 0.06	0.80 ± 0.07	8 34 44.99	+19 29 49.5
11	17.26 ± 0.04	0.59 ± 0.05	8 34 52.51	+21 10 39.8
12	19.73 ± 0.25	1.22 ± 0.28	8 34 54.09	+20 36 17.8
13	18.88 ± 0.10	0.83 ± 0.12	8 34 54.65	+19 52 29.3
14	17.61 ± 0.06	0.67 ± 0.07	8 35 4.68	+19 54 26.7
15	17.71 ± 0.06	0.66 ± 0.07	8 35 6.27	+19 54 40.2
16	17.02 ± 0.03	0.52 ± 0.04	8 35 8.38	+21 9 57.4
17	17.39 ± 0.06	0.58 ± 0.07	8 35 9.35	+19 51 4.1
18	18.26 ± 0.07	0.79 ± 0.09	8 35 11.01	+20 6 36.6
19	19.66 ± 0.26	1.09 ± 0.29	8 35 21.80	+21 2 2.8
20	17.02 ± 0.05	0.50 ± 0.06	8 35 24.21	+19 25 43.3
21	19.52 ± 0.14	1.07 ± 0.17	8 35 25.57	+21 6 34.5
22	19.34 ± 0.16	1.00 ± 0.19	8 35 25.78	+20 30 35.5
23	18.87 ± 0.13	0.95 ± 0.15	8 35 28.40	+19 12 21.8
24	17.26 ± 0.04	0.61 ± 0.05	8 35 31.92	+21 1 4.5
25	17.69 ± 0.04	0.80 ± 0.05	8 35 36.42	+21 25 3.9
26	17.15 ± 0.03	0.64 ± 0.04	8 35 43.85	+21 20 56.2
27	19.55 ± 0.14	1.11 ± 0.18	8 35 46.90	+20 41 2.8
28	17.67 ± 0.06	0.61 ± 0.07	8 35 51.23	+19 38 52.4
29	19.40 ± 0.13	0.93 ± 0.16	8 35 58.14	+21 32 45.8
30	17.32 ± 0.06	0.62 ± 0.07	8 36 8.81	+19 37 25.6

IZpr no.	I	I-Z	R.A.	Dec
31	17.18 ± 0.05	0.54 ± 0.06	8 36 9.85	+19 17 15.8
32	18.90 ± 0.08	0.93 ± 0.11	8 36 12.45	+20 57 5.4
33	17.08 ± 0.04	0.61 ± 0.05	8 36 18.78	+21 14 32.8
34	19.22 ± 0.13	0.99 ± 0.15	8 36 21.93	+20 54 14.9
35	19.48 ± 0.15	0.98 ± 0.19	8 36 29.60	+20 52 9.6
36	19.07 ± 0.15	1.19 ± 0.17	8 36 32.14	+21 18 45.8
37	19.04 ± 0.10	0.89 ± 0.13	8 36 40.53	+21 15 48.8
38	18.00 ± 0.05	0.73 ± 0.07	8 36 50.79	+21 4 15.2
39	19.20 ± 0.12	0.89 ± 0.15	8 37 0.85	+19 37 39.2
40 (RIZpr 2)	17.76 ± 0.06	0.72 ± 0.07	8 37 2.11	+19 52 6.4
41	17.73 ± 0.05	0.67 ± 0.06	8 37 18.33	+20 50 34.8
42	20.04 ± 0.42	1.45 ± 0.43	8 37 21.82	+19 15 38.5
43	19.17 ± 0.16	0.89 ± 0.19	8 37 23.79	+18 42 49.0
44	17.28 ± 0.05	0.58 ± 0.07	8 37 24.77	+20 5 45.6
45	17.08 ± 0.05	0.50 ± 0.06	8 37 27.92	+19 28 40.7
46	19.72 ± 0.20	1.02 ± 0.26	8 37 37.26	+21 2 50.7
47	17.40 ± 0.04	0.58 ± 0.05	8 37 39.18	+21 5 50.9
48	17.16 ± 0.05	0.52 ± 0.06	8 37 40.32	+20 12 3.3
49	17.10 ± 0.04	0.58 ± 0.05	8 37 41.48	+18 30 46.9
50	18.05 ± 0.05	0.70 ± 0.07	8 38 8.08	+18 3 32.0
51	17.16 ± 0.04	0.58 ± 0.05	8 38 15.30	+18 56 5.0
52	18.96 ± 0.12	0.89 ± 0.14	8 38 18.42	+18 35 7.8
53	19.73 ± 0.24	1.19 ± 0.26	8 38 19.19	+20 58 0.1
54	17.46 ± 0.04	0.65 ± 0.05	8 38 27.42	+17 57 36.3
55	17.24 ± 0.04	0.54 ± 0.05	8 38 29.87	+18 28 27.3
56	17.14 ± 0.04	0.59 ± 0.05	8 38 40.23	+17 55 58.8
57	17.21 ± 0.04	0.61 ± 0.05	8 38 41.64	+18 34 15.6
58	19.74 ± 0.27	1.43 ± 0.28	8 38 43.44	+18 33 25.7
59	18.26 ± 0.06	0.76 ± 0.08	8 38 50.99	+18 5 47.1
60	17.27 ± 0.04	0.59 ± 0.05	8 38 54.87	+18 14 33.7

IZpr no.	I	I-Z	R.A.	Dec
61	17.38 ± 0.04	0.57 ± 0.05	8 38 55.55	+18 18 18.1
62	17.56 ± 0.04	0.60 ± 0.06	8 39 7.23	+18 1 47.3
63	17.17 ± 0.03	0.56 ± 0.05	8 39 19.35	+18 38 21.7
64	17.15 ± 0.04	0.69 ± 0.05	8 39 22.86	+18 4 32.7
65	19.44 ± 0.23	1.10 ± 0.25	8 39 36.35	+18 46 56.3
66	17.05 ± 0.03	0.60 ± 0.05	8 39 57.91	+18 41 7.9
67	19.14 ± 0.13	0.87 ± 0.16	8 40 7.62	+18 50 37.2
68	19.07 ± 0.14	0.95 ± 0.17	8 40 40.33	+19 1 32.9
69	17.07 ± 0.03	0.57 ± 0.05	8 40 52.46	+18 1 0.4
70	17.09 ± 0.04	0.59 ± 0.05	8 40 53.88	+18 22 55.4
71	18.52 ± 0.09	0.77 ± 0.11	8 40 54.61	+18 5 5.9
72	17.04 ± 0.04	0.60 ± 0.05	8 41 3.29	+18 37 14.7
73	19.58 ± 0.33	0.97 ± 0.36	8 41 11.96	+18 16 50.0
74	17.62 ± 0.04	0.65 ± 0.06	8 41 15.83	+18 16 27.3
75	19.60 ± 0.27	1.50 ± 0.29	8 41 21.22	+18 57 55.2
76	18.92 ± 0.11	0.89 ± 0.13	8 41 24.47	+18 44 3.9
77	17.20 ± 0.04	0.53 ± 0.05	8 41 49.53	+18 50 23.5
78	19.20 ± 0.18	1.02 ± 0.23	8 41 53.42	+18 58 38.5
79	19.97 ± 0.29	1.28 ± 0.32	8 41 53.90	+18 2 40.4
80	17.13 ± 0.04	0.53 ± 0.07	8 41 54.70	+19 36 59.6
81	19.62 ± 0.21	1.42 ± 0.23	8 41 57.19	+18 29 44.6
82	19.02 ± 0.13	1.00 ± 0.17	8 42 0.23	+19 50 8.2
83	19.68 ± 0.26	1.25 ± 0.32	8 42 0.32	+19 49 45.6
84	17.75 ± 0.05	0.70 ± 0.09	8 42 4.64	+19 37 59.8
85	18.80 ± 0.19	1.07 ± 0.21	8 42 8.03	+18 16 40.3
86 (RIZpr 21)	18.31 ± 0.10	0.93 ± 0.14	8 42 11.43	+19 52 49.4
87	19.11 ± 0.12	1.09 ± 0.16	8 42 16.60	+18 46 7.2
88	17.75 ± 0.05	0.65 ± 0.08	8 42 21.35	+19 3 11.9
89	19.39 ± 0.17	1.03 ± 0.24	8 42 34.57	+18 49 1.9
90	19.45 ± 0.19	1.12 ± 0.25	8 42 36.30	+19 53 4.6

IZpr no.	I	I-Z	R.A.	Dec
91	17.99 ± 0.06	0.76 ± 0.09	8 42 38.08	+18 59 36.8
92	19.33 ± 0.13	1.00 ± 0.20	8 43 8.06	+19 20 52.1
93	18.97 ± 0.10	1.05 ± 0.14	8 43 14.88	+19 44 9.3
94	17.97 ± 0.05	0.76 ± 0.08	8 43 17.25	+19 32 22.6
95	19.25 ± 0.16	1.26 ± 0.19	8 43 20.33	+19 5 40.4
96	19.70 ± 0.18	1.21 ± 0.23	8 43 34.08	+19 13 2.0
97	19.28 ± 0.22	1.19 ± 0.27	8 43 43.12	+19 51 38.5
98	19.57 ± 0.19	1.27 ± 0.24	8 43 49.89	+19 43 40.0
99	17.62 ± 0.04	0.62 ± 0.07	8 43 53.88	+18 57 1.2
100	17.12 ± 0.04	0.53 ± 0.07	8 43 56.63	+19 16 17.0
101	19.61 ± 0.20	1.14 ± 0.25	8 44 9.69	+19 35 47.4
102	19.44 ± 0.13	1.09 ± 0.19	8 44 18.70	+18 51 14.6
103	17.92 ± 0.05	0.69 ± 0.08	8 44 20.15	+19 40 47.2
104	19.29 ± 0.21	1.11 ± 0.26	8 44 20.44	+19 52 33.3
105	18.59 ± 0.08	1.00 ± 0.12	8 44 23.89	+19 43 45.9
106	19.20 ± 0.13	1.19 ± 0.18	8 44 24.89	+19 23 41.2
107	18.33 ± 0.06	0.83 ± 0.10	8 44 26.28	+18 54 43.5
108	17.09 ± 0.04	0.53 ± 0.07	8 44 36.36	+19 17 16.7
109	19.42 ± 0.16	1.15 ± 0.22	8 44 40.27	+19 43 37.0
110	18.55 ± 0.08	0.83 ± 0.11	8 44 42.81	+18 54 39.3
111	19.59 ± 0.19	1.21 ± 0.24	8 44 44.39	+19 11 25.8
112	17.67 ± 0.04	0.69 ± 0.08	8 45 13.85	+19 7 36.0
113	18.16 ± 0.04	0.75 ± 0.06	8 45 22.16	+18 13 51.0
114	19.02 ± 0.06	0.86 ± 0.08	8 45 28.07	+18 15 2.8
115	19.67 ± 0.12	1.08 ± 0.16	8 45 29.67	+18 52 52.4
116	17.92 ± 0.05	0.65 ± 0.08	8 45 31.19	+19 23 9.4
117	18.79 ± 0.05	0.83 ± 0.08	8 45 31.71	+18 34 7.5
118	19.42 ± 0.17	1.07 ± 0.22	8 45 37.06	+19 33 54.2
119	17.65 ± 0.04	0.70 ± 0.08	8 45 40.24	+19 51 50.8
120	17.26 ± 0.03	0.55 ± 0.05	8 45 51.38	+19 2 7.9

IZpr no.	I	I-Z	R.A.	Dec
121	19.13 ± 0.11	0.96 ± 0.19	8 46 0.41	+19 43 15.4
122	19.36 ± 0.14	1.03 ± 0.18	8 46 1.91	+19 19 37.1
123	19.09 ± 0.15	0.93 ± 0.19	8 46 4.48	+19 51 27.7
124	19.33 ± 0.17	1.03 ± 0.21	8 46 9.04	+19 44 19.4
125	17.31 ± 0.04	0.56 ± 0.07	8 46 15.04	+19 10 19.7
126	18.47 ± 0.07	0.86 ± 0.11	8 46 16.79	+19 52 28.8
127	19.55 ± 0.20	1.24 ± 0.26	8 46 29.14	+19 47 37.0
128	17.26 ± 0.03	0.60 ± 0.05	8 46 31.93	+18 58 25.0
129	19.70 ± 0.10	0.99 ± 0.15	8 46 41.56	+18 8 48.1
130	17.31 ± 0.03	0.55 ± 0.05	8 46 43.83	+18 23 54.7
131	17.43 ± 0.03	0.66 ± 0.05	8 46 55.55	+18 2 0.3
132	17.21 ± 0.03	0.56 ± 0.05	8 46 56.76	+19 2 40.8
133	19.89 ± 0.15	1.18 ± 0.17	8 47 11.27	+18 58 35.0
134	17.01 ± 0.03	0.59 ± 0.05	8 48 16.93	+18 30 26.1
135	17.54 ± 0.04	0.65 ± 0.05	8 48 20.75	+18 34 23.7
136	17.21 ± 0.03	0.63 ± 0.05	8 48 22.79	+18 2 11.4
137	17.06 ± 0.03	0.55 ± 0.05	8 48 30.52	+18 31 53.2
138	17.37 ± 0.03	0.70 ± 0.05	8 48 34.05	+19 1 15.5
139	19.68 ± 0.10	1.01 ± 0.14	8 48 40.55	+18 54 37.3
140	19.92 ± 0.13	1.09 ± 0.16	8 48 50.27	+18 31 32.4
141	17.17 ± 0.03	0.60 ± 0.05	8 49 34.00	+19 6 22.2

Appendix B

Praesepe finder charts

B.1 R I Z Praesepe candidates

This appendix contains finder charts for the RIZpr candidates from the INT R I Z survey. There is a finder for each source from the table in Appendix (A.1). Each finder is 3.3 by 3.3 arcminutes, and the orientation is indicated (North at the top, and East to the left).

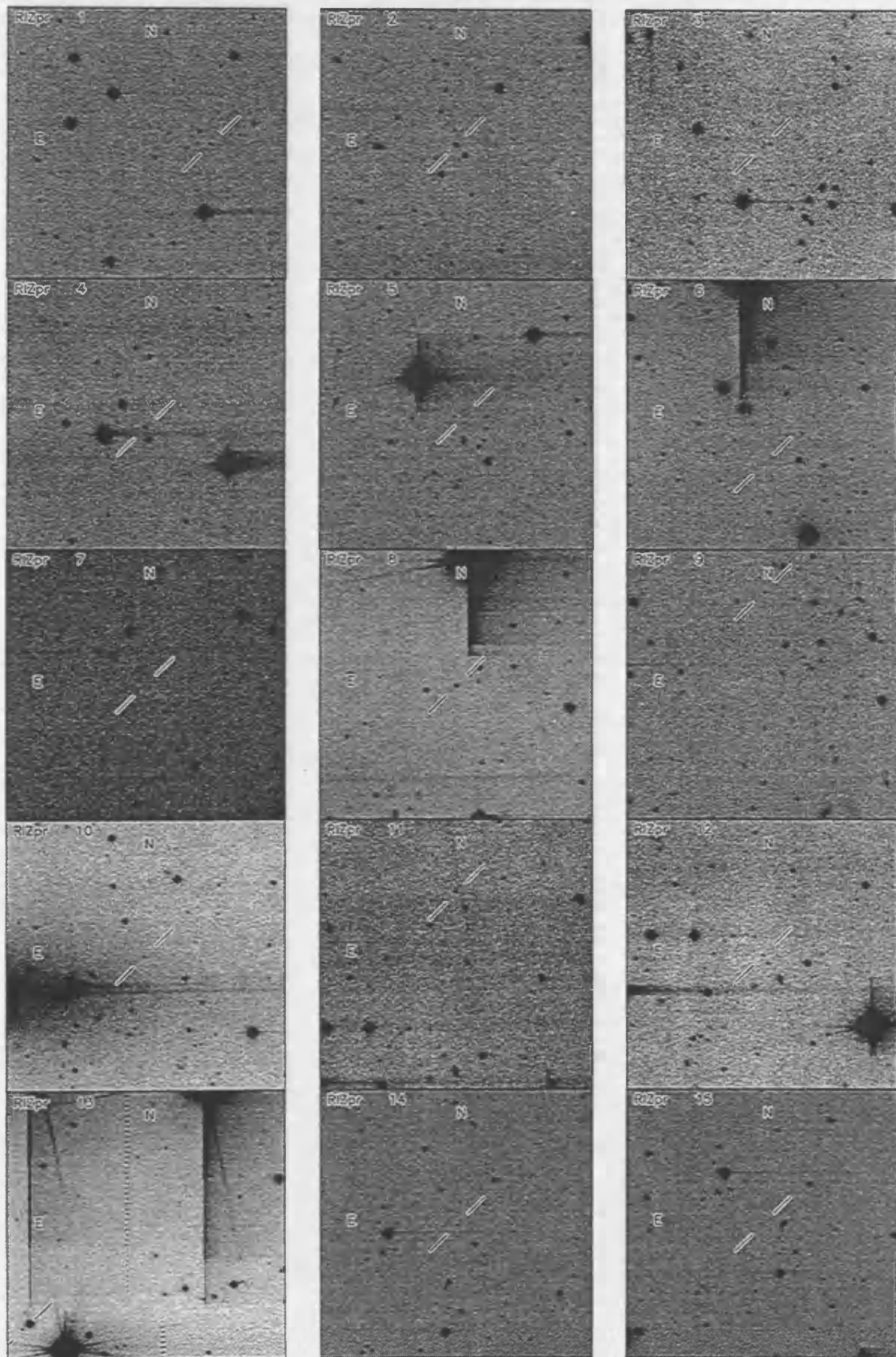


Figure B.1:

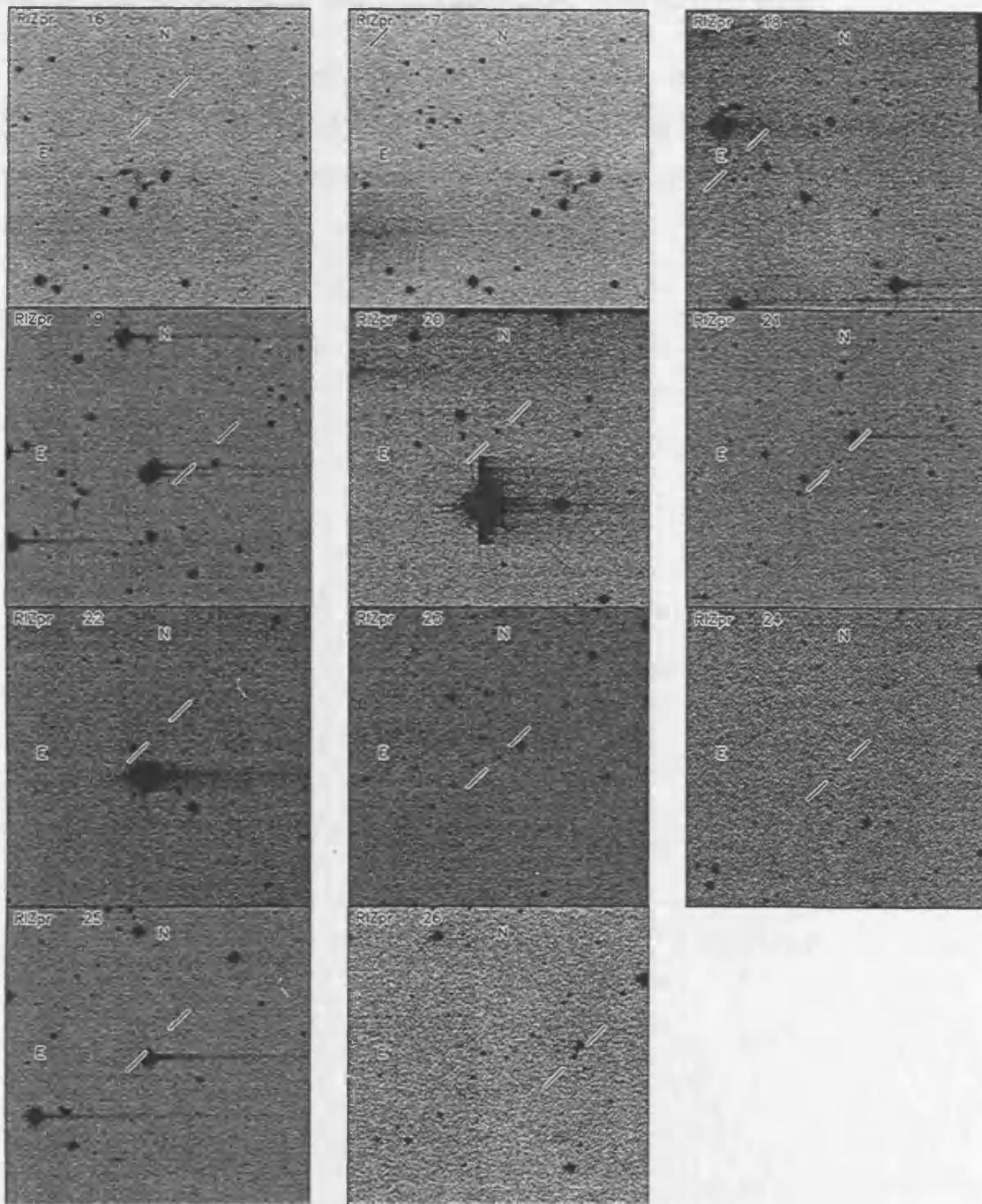


Figure B.2:

B.2 I Z Kitt Peak Praesepe candidates

This appendix contains finder charts for the Praesepe candidates from the Kitt Peak I Z survey. There is a finder for each source from the table in Appendix (A.4). Each finder is 3.3 by 3.3 arcminutes, and the orientation is indicated (North at the top, and East to the left).

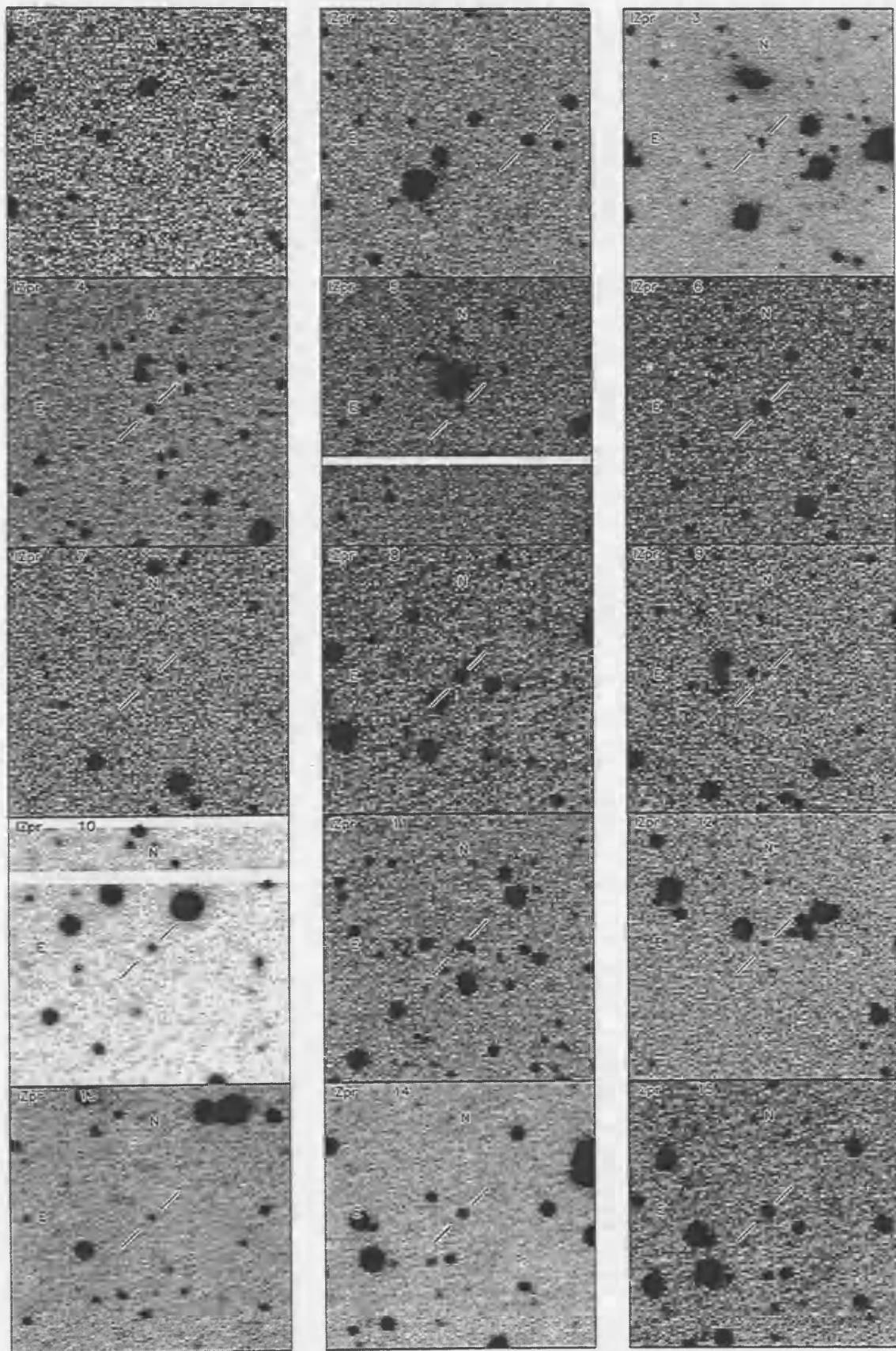


Figure B.3:

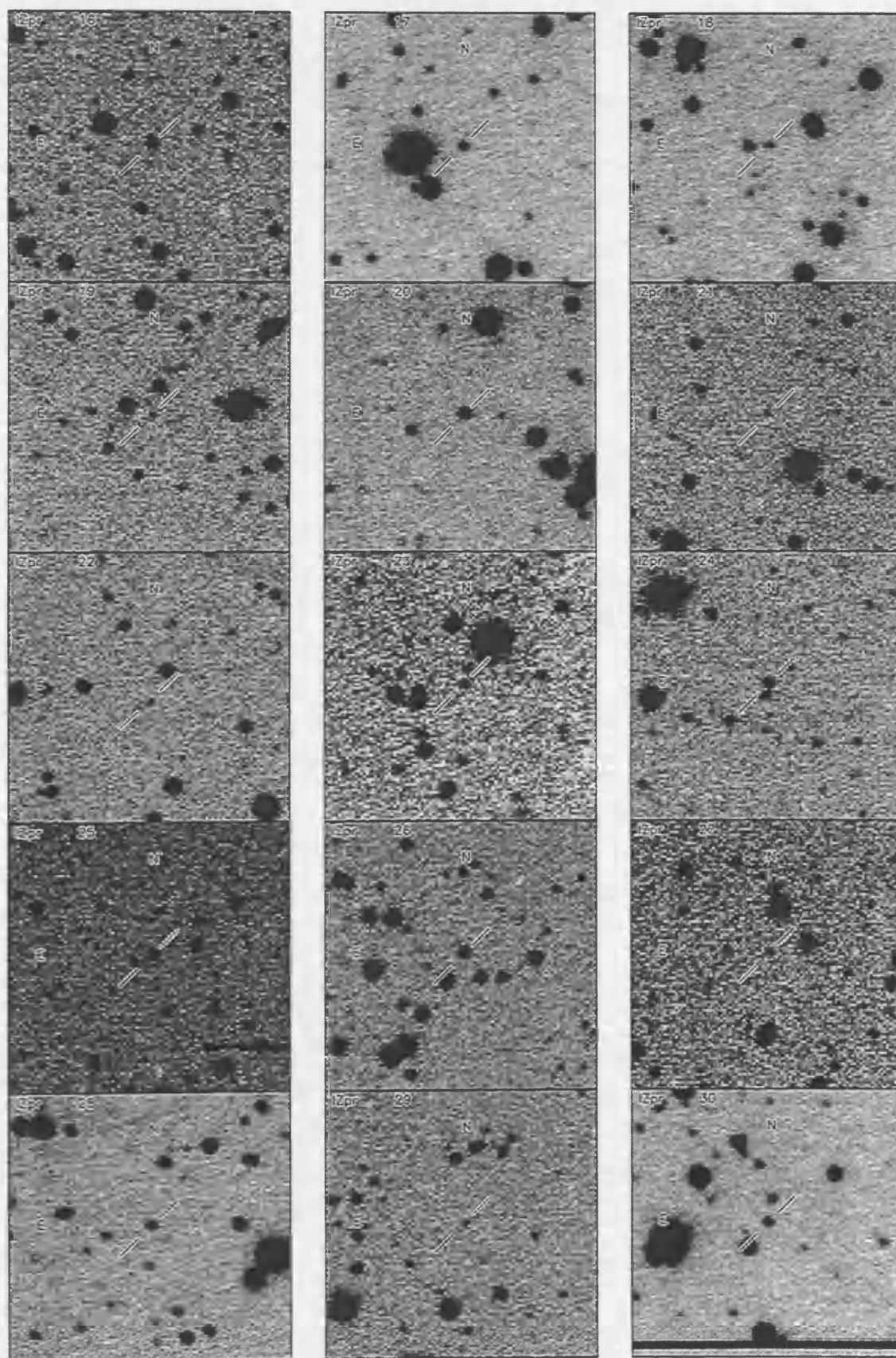


Figure B.4:

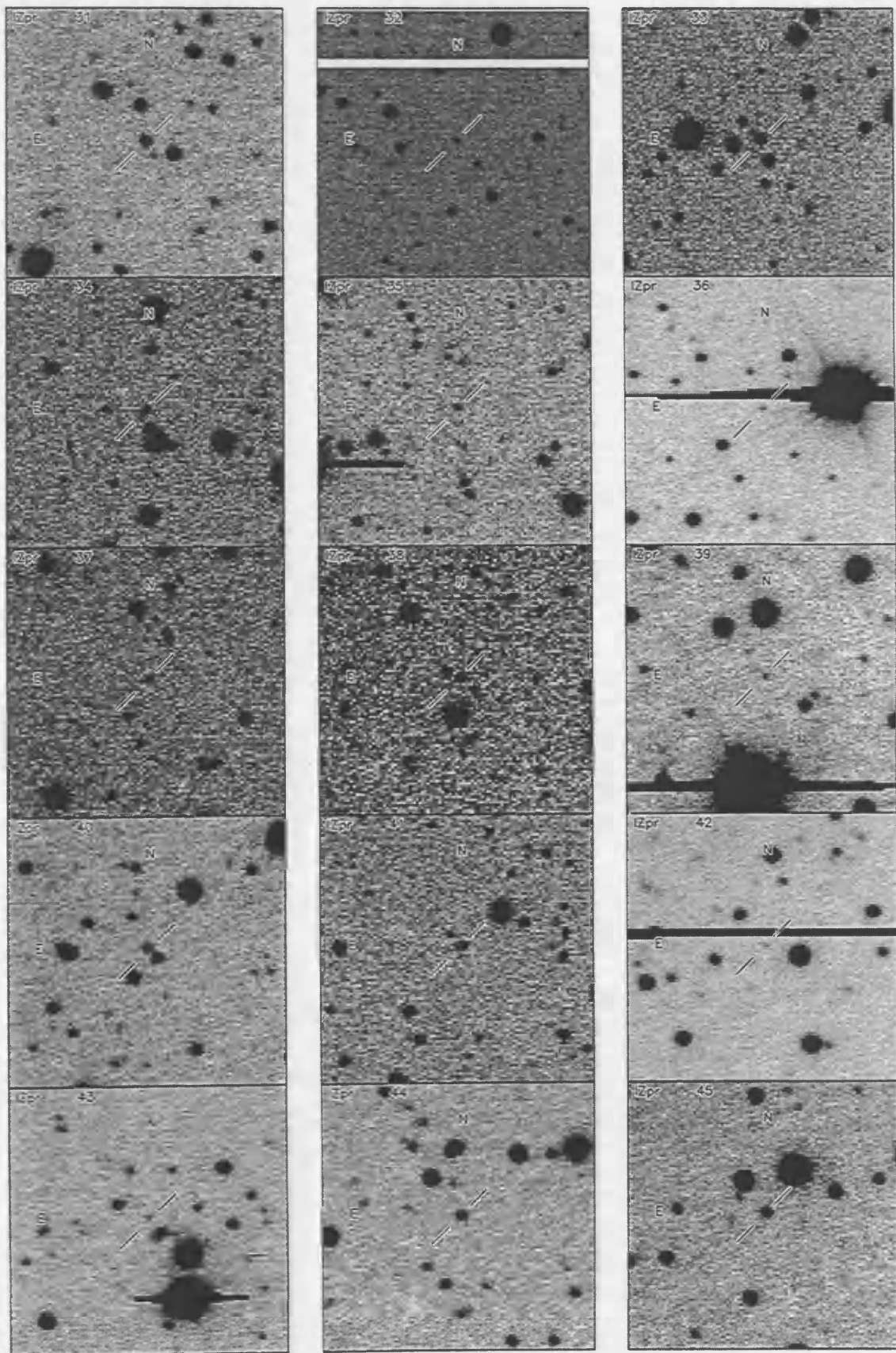


Figure B.5:

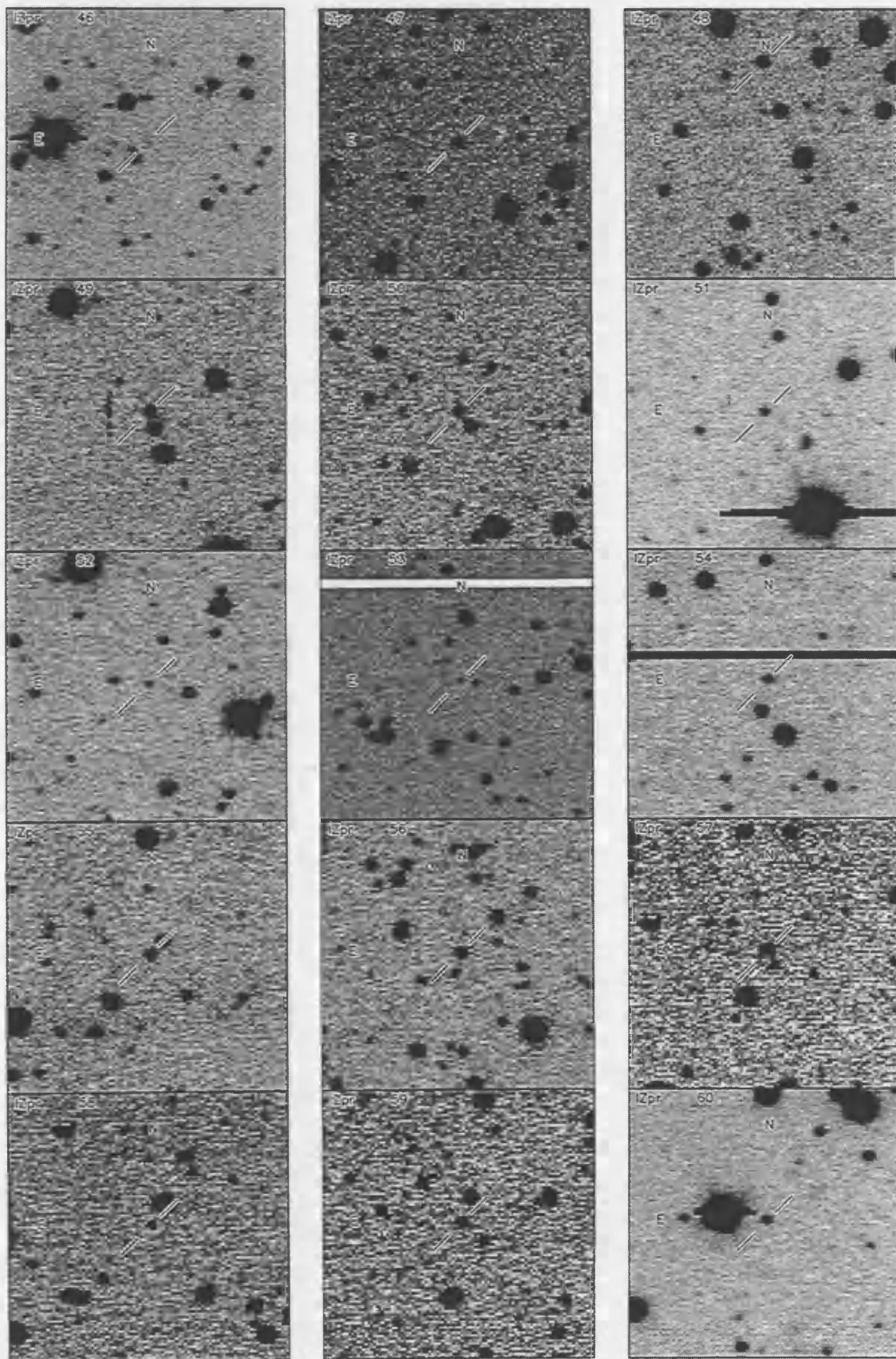


Figure B.6:

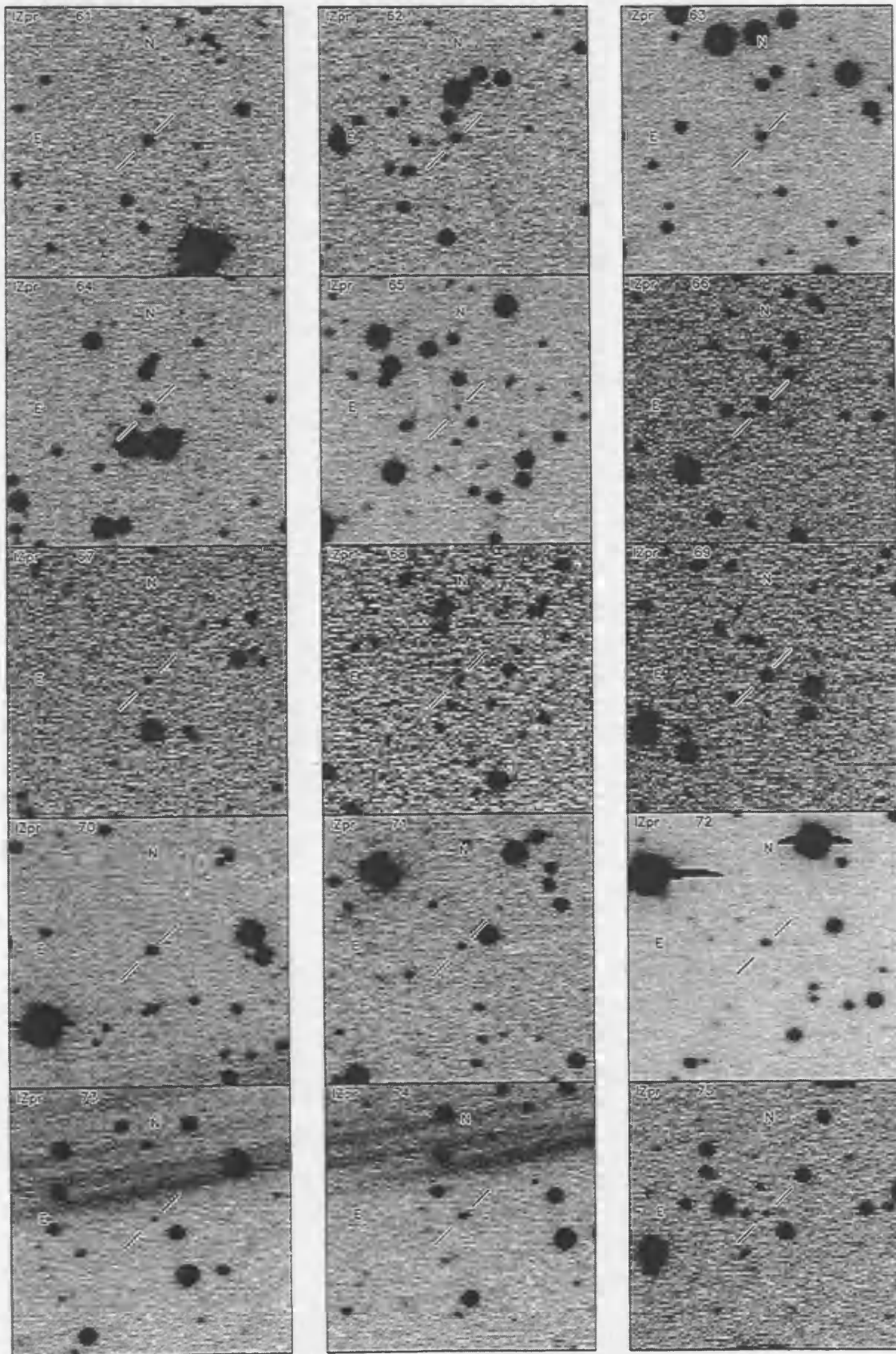


Figure B.7:

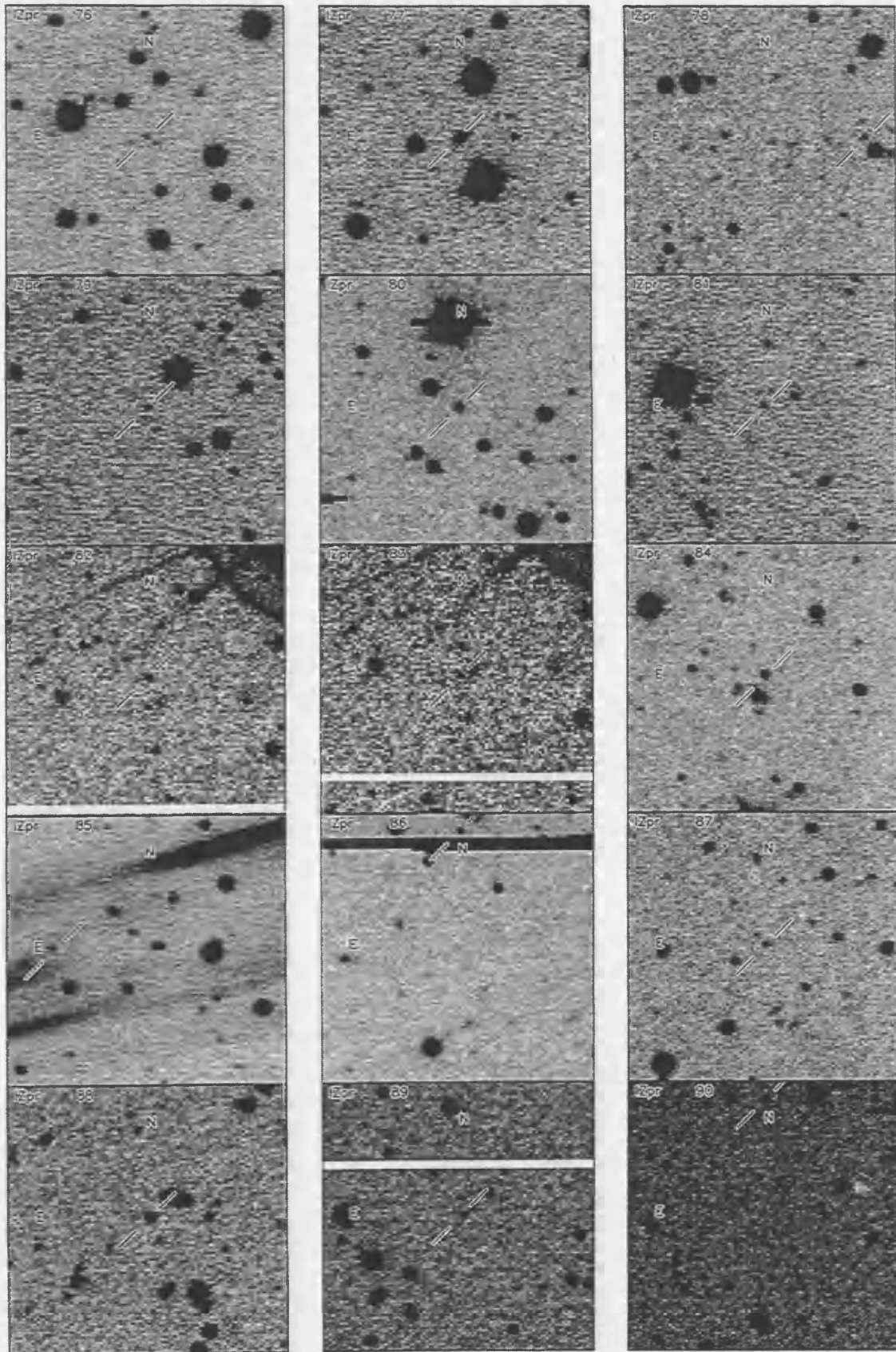


Figure B.8:

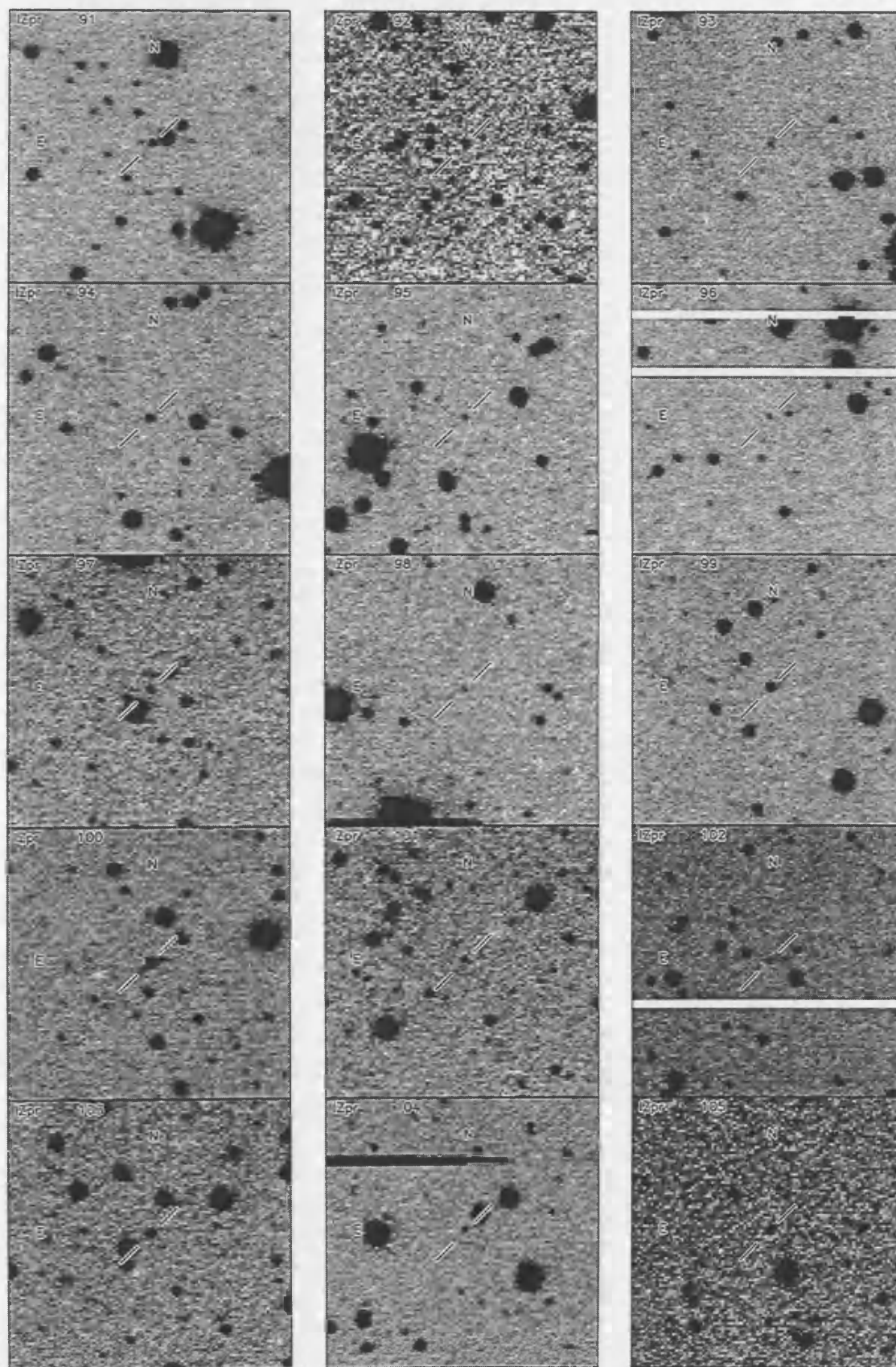


Figure B.9:

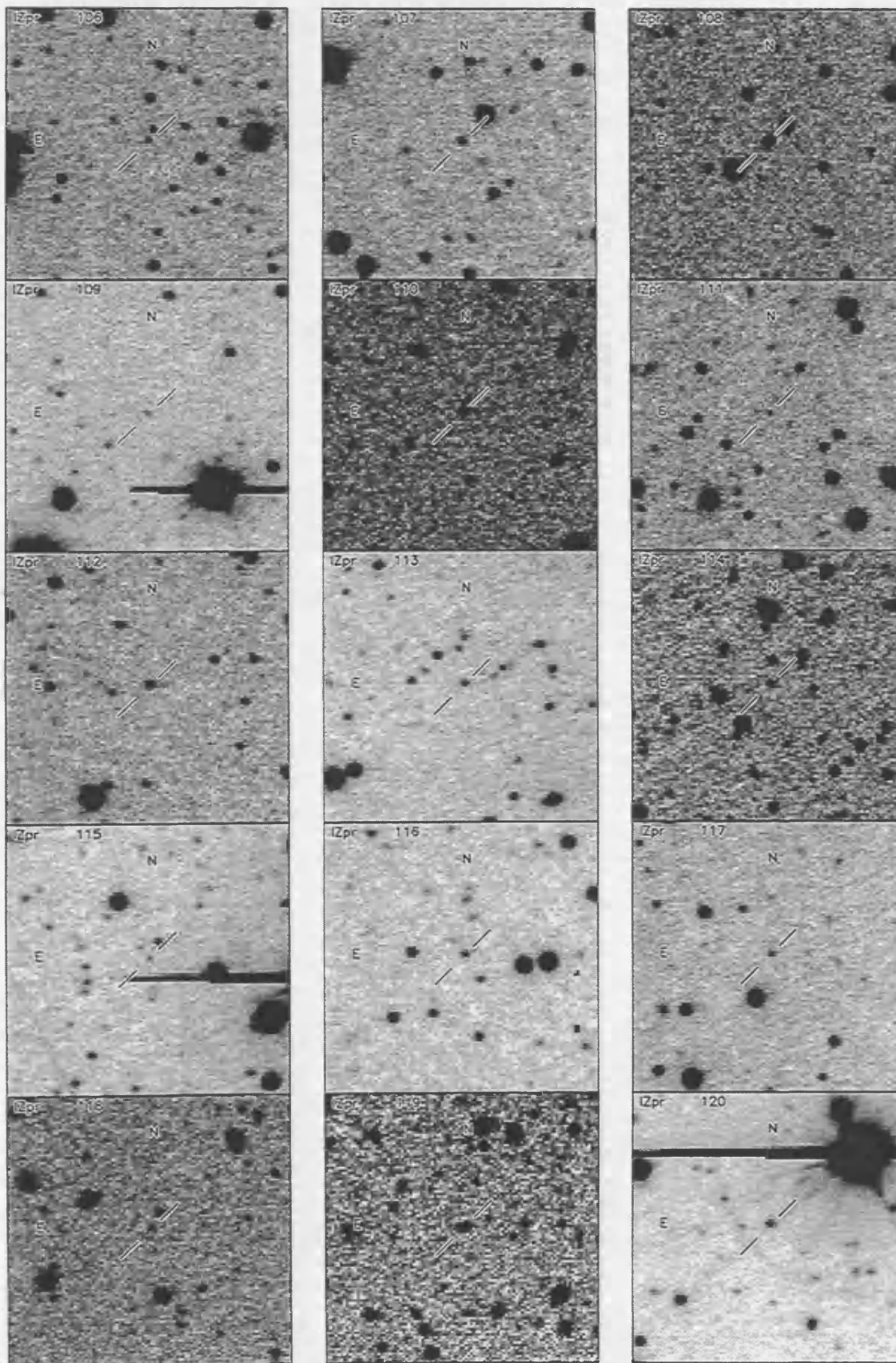


Figure B.10:

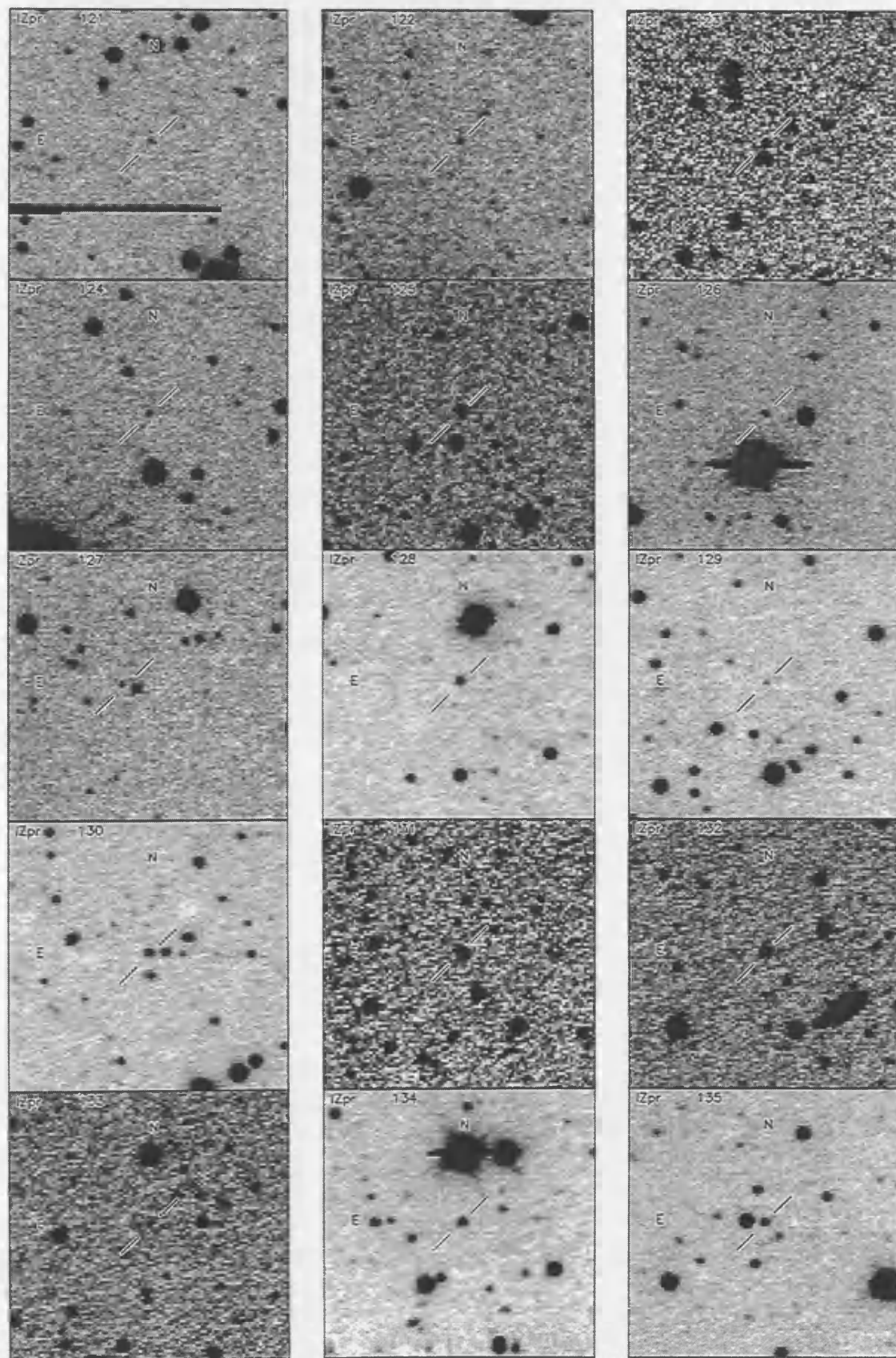


Figure B.11:

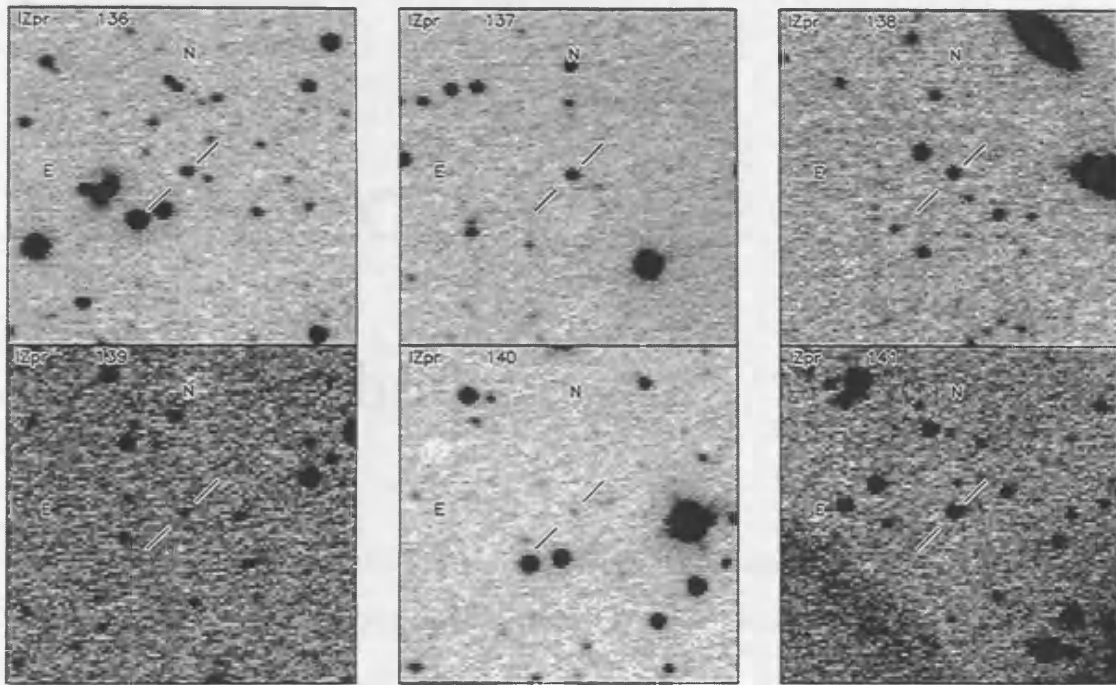


Figure B.12: Six panels (IZpr 136-141) for the HD 63471 Praesepe candidates from Chapter 7. Eight of these candidates are previously discovered spectroscopic BHs and these are indicated by brackets. The I magnitudes are for the stars indicated by brackets.

Figure B.12:

Appendix C

Pleiades photometry

This appendix contains tables of photometry and coordinates (J2000) of the Pleiades candidate BDs found during this thesis work. The coordinates are all accurate to $\sim \pm 0.5$ arcseconds.

Section (C.1) is for the BD Kitt Peak candidates from Chapter (7). Eight of these candidates are previously discovered spectroscopic BDs, and these are indicated in brackets. The I magnitudes are I_{KP} .

C.1 Kitt Peak candidate Pleiades brown dwarfs

IZpl no.	I	I-Z	R.A.	Dec
1	19.89 ± 0.19	1.08 ± 0.21	3 39 16.83	+24 14 23.9
2	17.79 ± 0.04	0.72 ± 0.05	3 40 5.61	+24 36 43.8
3	19.83 ± 0.17	1.33 ± 0.19	3 40 6.21	+23 45 33.3
4	17.99 ± 0.04	0.72 ± 0.05	3 41 8.20	+24 17 36.8
5	18.37 ± 0.05	0.81 ± 0.07	3 42 48.10	+24 4 1.2
6	19.19 ± 0.08	0.92 ± 0.14	3 43 40.20	+24 30 11.3
7	19.26 ± 0.11	1.01 ± 0.16	3 43 45.63	+24 40 41.6
8 (Roque 4)	19.53 ± 0.17	1.05 ± 0.21	3 43 53.46	+24 31 11.3
9	19.47 ± 0.17	0.99 ± 0.19	3 45 5.99	+22 36 4.5
10	19.22 ± 0.15	1.00 ± 0.17	3 45 19.50	+22 3 26.0
11	17.61 ± 0.06	0.69 ± 0.07	3 45 45.11	+22 58 44.8
12	18.73 ± 0.10	0.91 ± 0.11	3 45 50.30	+22 36 6.3
13	18.91 ± 0.08	1.11 ± 0.09	3 45 50.43	+24 13 43.4
14(Roque 13)	18.43 ± 0.05	0.96 ± 0.07	3 45 50.58	+24 9 3.5
15	18.55 ± 0.05	1.07 ± 0.07	3 45 53.18	+25 12 55.9
16	19.54 ± 0.13	1.03 ± 0.16	3 46 8.69	+22 4 48.0
17	20.07 ± 0.18	1.21 ± 0.21	3 46 16.00	+24 27 34.9
18	19.07 ± 0.08	0.96 ± 0.10	3 46 23.05	+24 20 36.1
19	18.18 ± 0.07	0.76 ± 0.09	3 46 23.62	+22 50 16.5
20	18.60 ± 0.05	1.00 ± 0.06	3 46 38.77	+24 14 14.6
21(Roque 14)	18.27 ± 0.04	0.93 ± 0.06	3 46 42.90	+24 24 50.4
22	18.42 ± 0.05	0.93 ± 0.07	3 46 57.33	+24 37 45.4
23	17.56 ± 0.04	0.76 ± 0.05	3 47 5.66	+24 40 3.5
24	18.01 ± 0.04	1.02 ± 0.06	3 47 9.31	+25 13 40.9
25	18.77 ± 0.06	0.85 ± 0.08	3 47 10.88	+24 11 30.6
26(Roque 11)	18.81 ± 0.06	1.00 ± 0.08	3 47 12.02	+24 28 31.5
27 (Teide 1)	18.96 ± 0.07	0.95 ± 0.08	3 47 17.83	+24 22 31.5
28	18.15 ± 0.13	0.78 ± 0.15	3 47 19.67	+22 55 35.3
29(Roque 17)	17.87 ± 0.07	0.82 ± 0.08	3 47 23.90	+22 42 37.0
30	19.32 ± 0.16	1.00 ± 0.18	3 47 34.95	+22 51 4.8

IZpl no.	I	I-Z	R.A.	Dec
31	17.92 ± 0.04	0.74 ± 0.05	3 47 37.82	+24 38 49.0
32(Roque 16)	17.73 ± 0.04	0.72 ± 0.05	3 47 38.97	+24 36 22.1
33	19.60 ± 0.19	0.99 ± 0.22	3 47 41.93	+22 50 36.4
34	18.70 ± 0.11	0.89 ± 0.13	3 47 53.73	+23 1 40.6
35	19.53 ± 0.09	0.97 ± 0.11	3 47 54.74	+24 45 29.1
36	17.61 ± 0.06	0.66 ± 0.07	3 47 57.96	+22 6 51.3
37	19.28 ± 0.08	1.00 ± 0.10	3 48 13.45	+24 15 18.6
38	17.51 ± 0.03	0.67 ± 0.05	3 48 13.88	+24 38 30.1
39	18.30 ± 0.05	0.82 ± 0.06	3 48 18.96	+24 25 12.9
40	18.25 ± 0.07	0.82 ± 0.08	3 48 38.22	+22 33 52.5
41	17.76 ± 0.04	0.70 ± 0.05	3 48 40.82	+24 15 26.5
42	19.34 ± 0.08	1.04 ± 0.10	3 49 12.43	+24 11 12.8
43	17.53 ± 0.03	0.70 ± 0.05	3 49 15.06	+24 36 22.3
44	18.62 ± 0.10	0.82 ± 0.12	3 49 27.08	+22 51 16.1
45	18.64 ± 0.06	0.88 ± 0.07	3 49 35.05	+24 39 16.4
46	19.09 ± 0.12	0.92 ± 0.13	3 49 37.57	+23 0 35.4
47	17.69 ± 0.06	0.66 ± 0.07	3 49 48.97	+23 1 7.5
48	19.23 ± 0.16	0.96 ± 0.19	3 49 50.82	+22 10 32.1
49	19.89 ± 0.22	1.03 ± 0.25	3 50 6.99	+25 9 56.1
50	19.56 ± 0.16	1.02 ± 0.18	3 51 18.47	+23 46 11.5
51	19.57 ± 0.14	1.06 ± 0.19	3 51 24.52	+23 50 38.8
52 (Calar 3)	18.66 ± 0.09	0.90 ± 0.13	3 51 25.52	+23 45 20.8
53	19.08 ± 0.11	0.89 ± 0.14	3 51 36.12	+24 18 44.0
54	19.75 ± 0.20	1.17 ± 0.24	3 51 37.62	+23 48 3.1
55	18.45 ± 0.06	0.85 ± 0.09	3 51 44.85	+23 26 38.7
56	19.14 ± 0.11	1.04 ± 0.14	3 51 49.71	+23 53 15.3
57	19.63 ± 0.11	1.03 ± 0.13	3 52 1.70	+24 49 48.9
58	19.74 ± 0.14	1.45 ± 0.16	3 52 2.00	+23 15 45.9
59	17.59 ± 0.04	0.67 ± 0.07	3 52 6.67	+24 16 0.4
60	18.36 ± 0.06	0.79 ± 0.07	3 52 6.95	+24 20 41.9

IZpl no.	I	I-Z	R.A.	Dec
61	20.23 ± 0.28	1.09 ± 0.30	3 52 11.15	+24 22 41.8
62	20.20 ± 0.31	1.26 ± 0.33	3 52 27.83	+25 24 51.4
63	19.91 ± 0.19	1.09 ± 0.21	3 52 37.74	+25 11 17.8
64	20.16 ± 0.23	1.41 ± 0.27	3 52 52.24	+24 20 20.4
65	17.89 ± 0.05	0.74 ± 0.08	3 52 52.52	+24 11 14.3
66	18.49 ± 0.05	0.80 ± 0.07	3 52 56.69	+24 45 54.5
67	19.72 ± 0.15	1.07 ± 0.16	3 53 6.90	+25 2 11.6
68	18.38 ± 0.07	0.78 ± 0.10	3 53 10.82	+24 18 48.0
69	20.25 ± 0.37	1.14 ± 0.40	3 53 29.53	+25 13 45.5
70	19.47 ± 0.19	0.99 ± 0.22	3 53 34.39	+25 11 30.5
71	20.24 ± 0.25	1.26 ± 0.27	3 53 44.13	+25 21 4.7
72	19.45 ± 0.13	1.17 ± 0.13	3 53 47.98	+24 25 12.7
73	20.26 ± 0.19	1.38 ± 0.21	3 53 48.92	+25 25 48.2
74	17.61 ± 0.04	0.82 ± 0.07	3 53 55.04	+23 23 36.3
75	19.45 ± 0.09	0.99 ± 0.11	3 54 1.07	+24 40 36.6
76	19.72 ± 0.14	1.03 ± 0.16	3 54 3.54	+25 26 1.9
77	19.43 ± 0.11	0.96 ± 0.14	3 54 5.26	+23 33 59.5
78	20.05 ± 0.20	1.11 ± 0.23	3 54 11.06	+24 20 30.3
79	18.84 ± 0.06	1.13 ± 0.07	3 54 15.22	+25 9 51.4
80	18.08 ± 0.04	0.77 ± 0.05	3 54 44.16	+25 15 10.6
81	19.18 ± 0.09	0.99 ± 0.10	3 54 45.78	+25 22 59.2
82	20.57 ± 0.23	1.69 ± 0.25	3 54 52.36	+24 41 50.3
83	19.74 ± 0.12	1.11 ± 0.16	3 55 0.86	+25 14 54.1
84	20.22 ± 0.20	1.20 ± 0.23	3 55 6.96	+24 51 11.2
85	17.72 ± 0.04	0.78 ± 0.04	3 55 22.99	+24 49 4.8
86	19.95 ± 0.19	1.06 ± 0.23	3 55 30.20	+23 51 48.8
87	19.62 ± 0.16	1.05 ± 0.19	3 55 34.82	+23 49 21.2
88	18.44 ± 0.07	0.80 ± 0.10	3 55 44.66	+23 26 33.2
89	17.71 ± 0.04	0.69 ± 0.05	3 55 47.06	+25 14 38.6
90	20.34 ± 0.24	1.17 ± 0.27	3 55 48.25	+25 19 45.6

IZpl no.	I	I-Z	R.A.	Dec
91	20.54 ± 0.31	1.21 ± 0.35	3 55 49.30	+24 56 44.8
92	19.62 ± 0.12	1.03 ± 0.14	3 56 3.21	+24 34 40.6
93	20.97 ± 0.45	1.73 ± 0.47	3 56 7.15	+25 5 46.7
94	20.42 ± 0.24	1.18 ± 0.28	3 56 12.19	+24 55 18.5
95	19.57 ± 0.12	0.98 ± 0.14	3 56 14.76	+24 33 19.7
96	19.71 ± 0.15	1.09 ± 0.18	3 56 22.48	+25 7 50.7

Appendix D

Pleiades finder charts

D.1 I Z Kitt Peak Pleiades BD candidates

This appendix contains finder charts for the Pleiades candidate BDs from the Kitt Peak I Z survey. There is a finder for each source from the table in Appendix (C.1). Each finder is 3.3 by 3.3 arcminutes, and the orientation is indicated (North at the top, and East to the left).

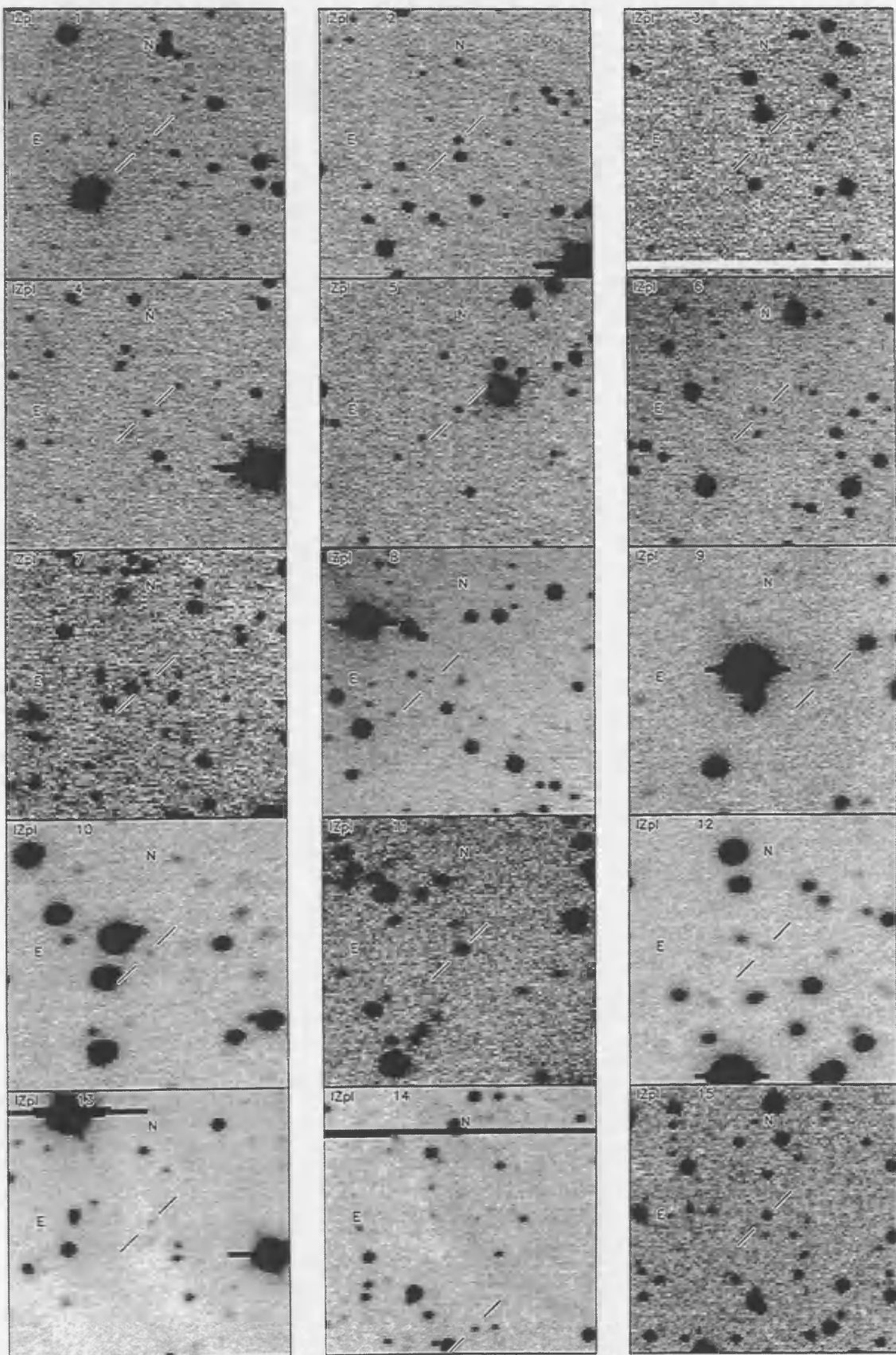


Figure D.1:

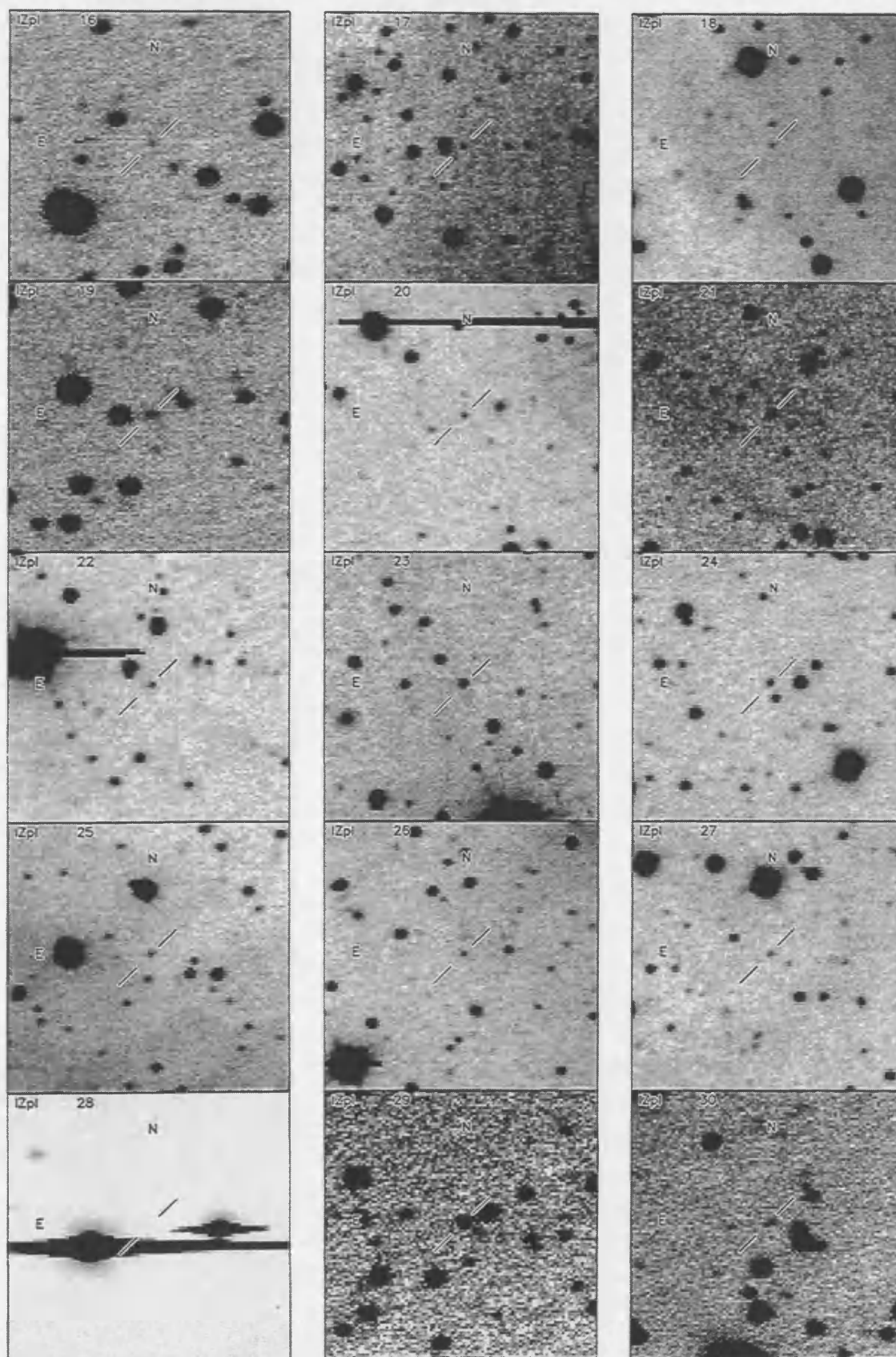


Figure D.2:

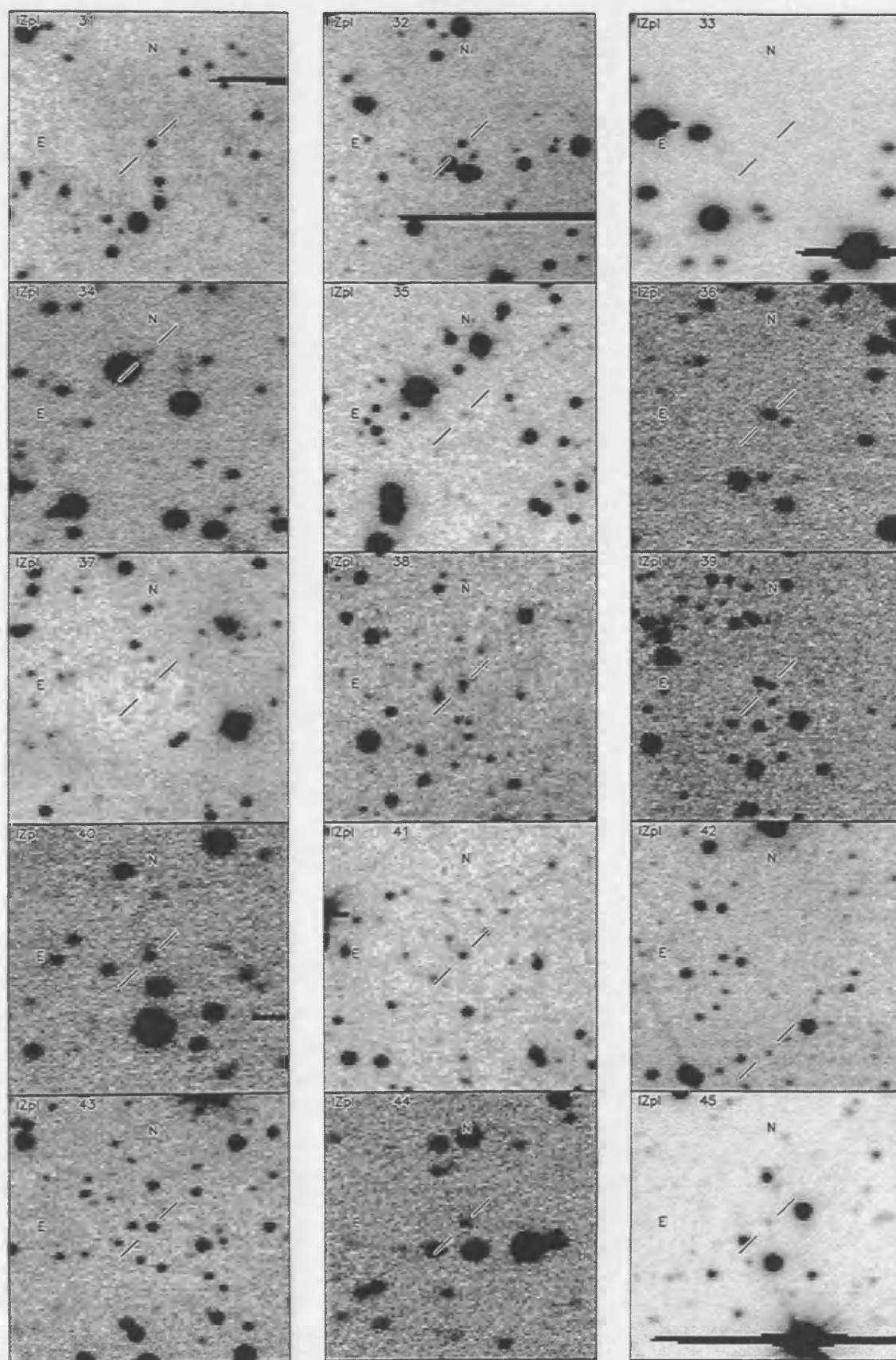


Figure D.3:

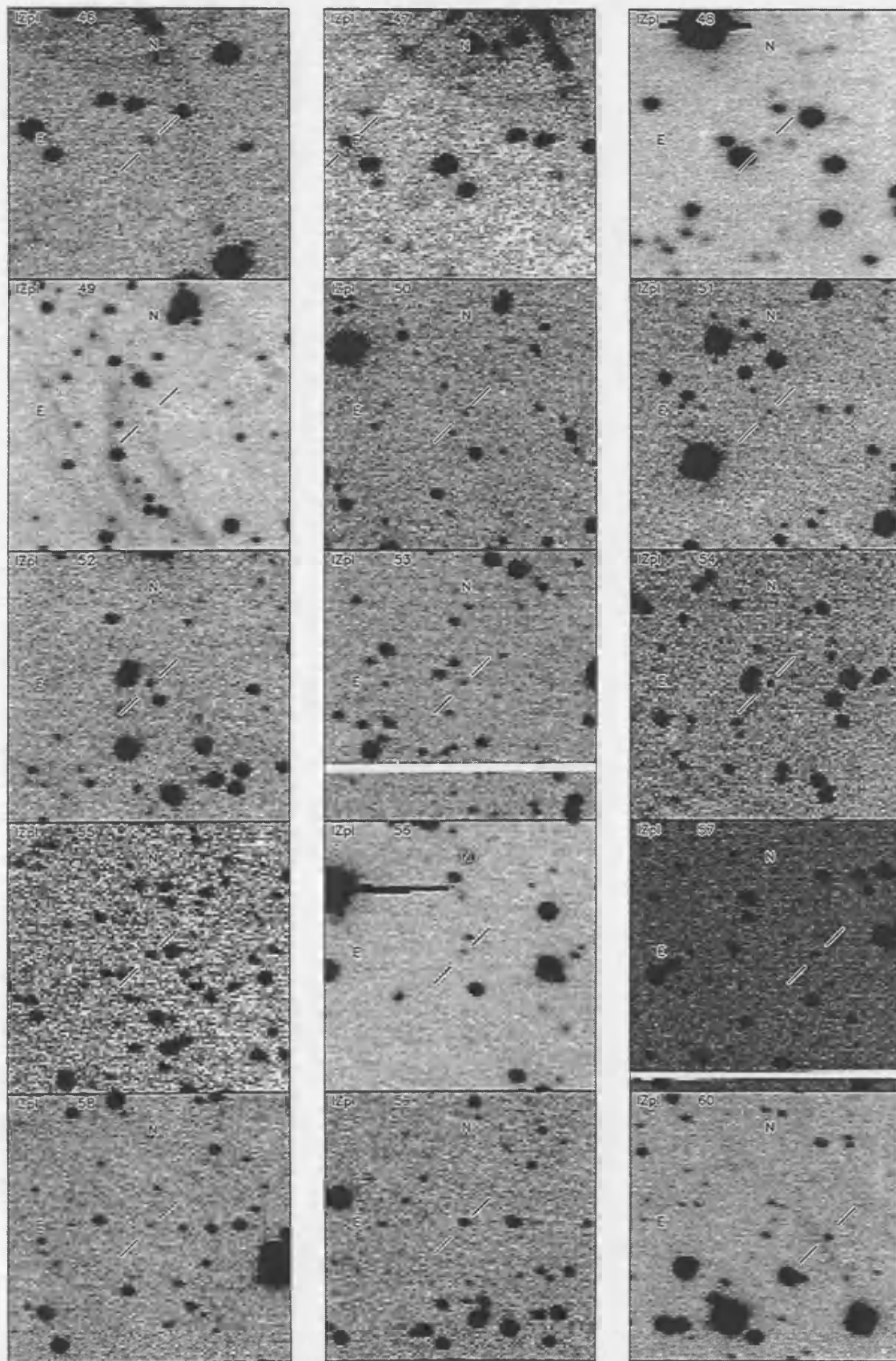


Figure D.4:

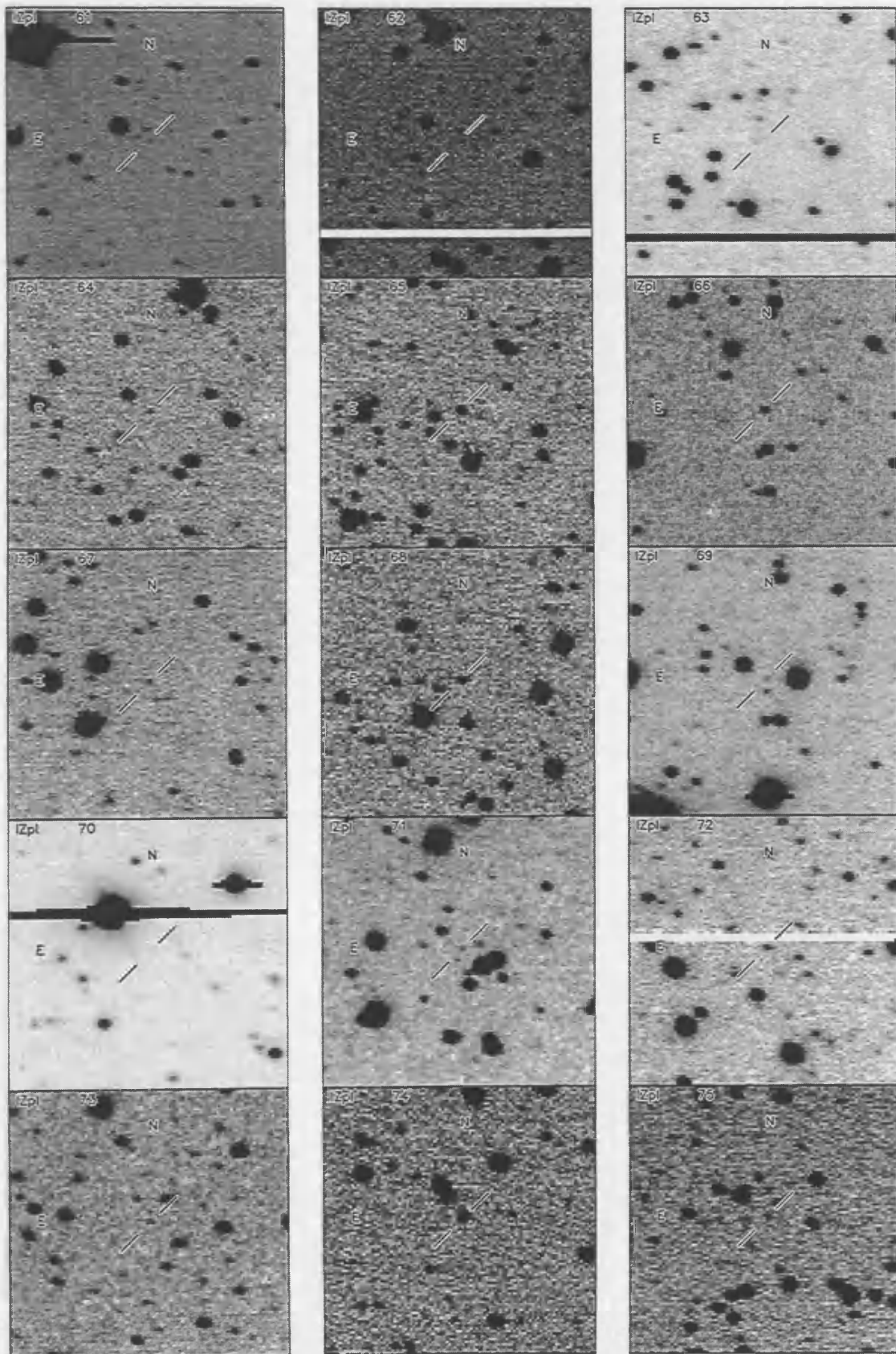


Figure D.5:

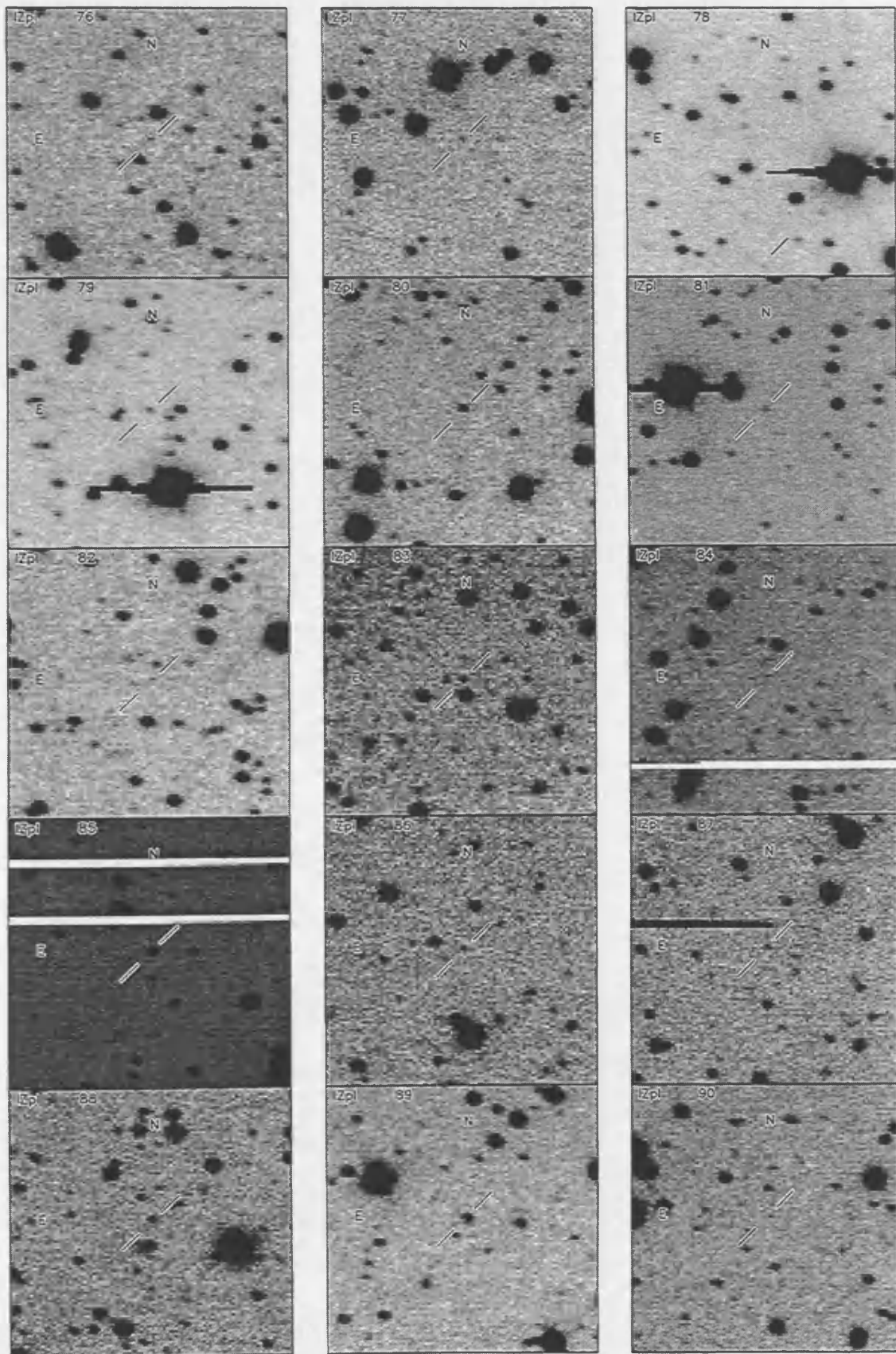


Figure D.6:

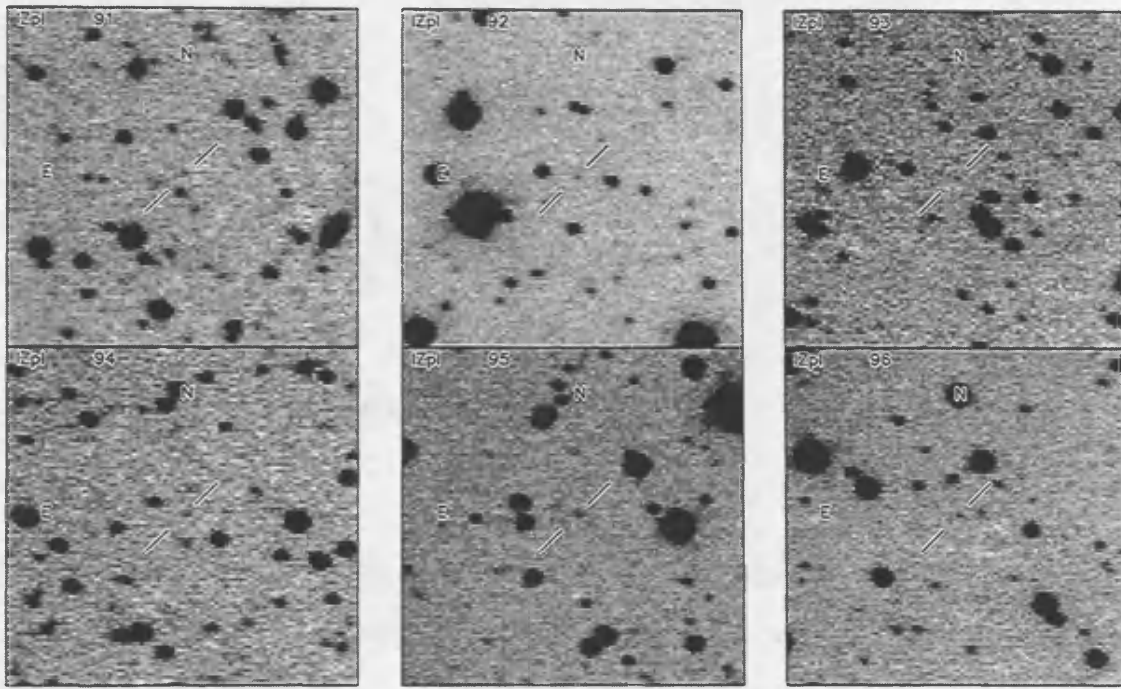


Figure D.7:

Appendix E

Hyades photometry

This appendix contains tables of photometry and coordinates (J2000) of the Hyades candidate BDs found during this thesis work. The coordinates are all accurate to $\sim \pm 0.5$ arcseconds.

Section (E.1) is for the BD Kitt Peak candidates from Chapter (7). The I magnitudes are I_{KP} .

E.1 Kitt Peak candidate Hyades brown dwarfs

IZh no.	I	I-Z	R.A.	Dec
1	18.77 ± 0.18	1.01 ± 0.20	4 21 43.98	+17 3 0.4
2	18.11 ± 0.09	0.86 ± 0.11	4 22 7.51	+16 15 39.9
3	18.53 ± 0.14	1.03 ± 0.16	4 22 36.26	+17 11 24.3
4	18.59 ± 0.15	0.90 ± 0.17	4 23 13.99	+17 7 10.5
5	18.46 ± 0.15	0.83 ± 0.17	4 23 27.44	+16 58 38.5
6	17.65 ± 0.07	0.73 ± 0.08	4 23 32.19	+16 16 9.6
7	18.24 ± 0.09	0.81 ± 0.11	4 23 38.44	+16 20 43.5
8	17.60 ± 0.09	0.74 ± 0.11	4 23 49.69	+16 19 39.9
9	18.44 ± 0.16	0.97 ± 0.18	4 24 2.22	+16 51 6.0
10	18.52 ± 0.13	0.98 ± 0.14	4 24 46.67	+16 37 59.0
11	18.30 ± 0.11	0.80 ± 0.14	4 25 17.44	+16 53 3.4
12	18.72 ± 0.17	0.90 ± 0.21	4 25 29.16	+16 11 51.4
13	18.44 ± 0.13	0.83 ± 0.16	4 25 42.49	+16 42 32.1
14	17.28 ± 0.09	0.77 ± 0.12	4 25 54.69	+16 29 21.9
15	18.93 ± 0.26	0.92 ± 0.29	4 25 57.06	+16 31 9.9
16	18.85 ± 0.10	0.89 ± 0.13	4 29 21.62	+14 36 57.1
17	16.58 ± 0.03	0.64 ± 0.05	4 29 32.26	+15 14 16.0
18	18.82 ± 0.13	0.93 ± 0.16	4 29 57.71	+15 16 50.3
19	19.16 ± 0.16	0.92 ± 0.18	4 30 10.68	+15 3 39.8
20	18.19 ± 0.07	0.83 ± 0.09	4 30 32.81	+14 27 51.3
21	18.16 ± 0.09	0.92 ± 0.11	4 30 45.44	+14 51 23.7
22	18.85 ± 0.11	0.96 ± 0.13	4 31 5.22	+14 50 28.5
23	18.82 ± 0.12	0.94 ± 0.14	4 31 38.59	+14 20 48.4
24	17.86 ± 0.05	0.82 ± 0.07	4 31 50.51	+14 29 23.9
25	17.96 ± 0.06	0.79 ± 0.07	4 31 54.23	+14 32 14.9
26	16.50 ± 0.03	0.77 ± 0.05	4 32 37.91	+15 8 52.3
27	18.61 ± 0.11	0.93 ± 0.13	4 32 45.02	+15 1 9.9
28	17.05 ± 0.04	0.65 ± 0.05	4 33 3.90	+15 8 36.7
29	18.99 ± 0.15	0.90 ± 0.19	4 33 4.08	+14 29 38.4
30	18.59 ± 0.10	0.90 ± 0.12	4 33 7.39	+14 35 38.9

IZh no.	I	I-Z	R.A.	Dec
31	18.40 ± 0.09	0.85 ± 0.12	4 33 11.28	+15 19 41.0
32	18.42 ± 0.09	0.88 ± 0.13	4 33 21.93	+15 19 21.0
33	18.01 ± 0.08	0.78 ± 0.10	4 33 32.25	+15 20 22.8

Appendix F

Hyades finder charts

F.1 I Z Kitt Peak Hyades BD candidates

This appendix contains finder charts for the Hyades BD candidates from the Kitt Peak I Z survey. There is a finder for each source from the table in Appendix (E.1). Each finder is 3.3 by 3.3 arcminutes, and the orientation is indicated (North at the top, and East to the left).

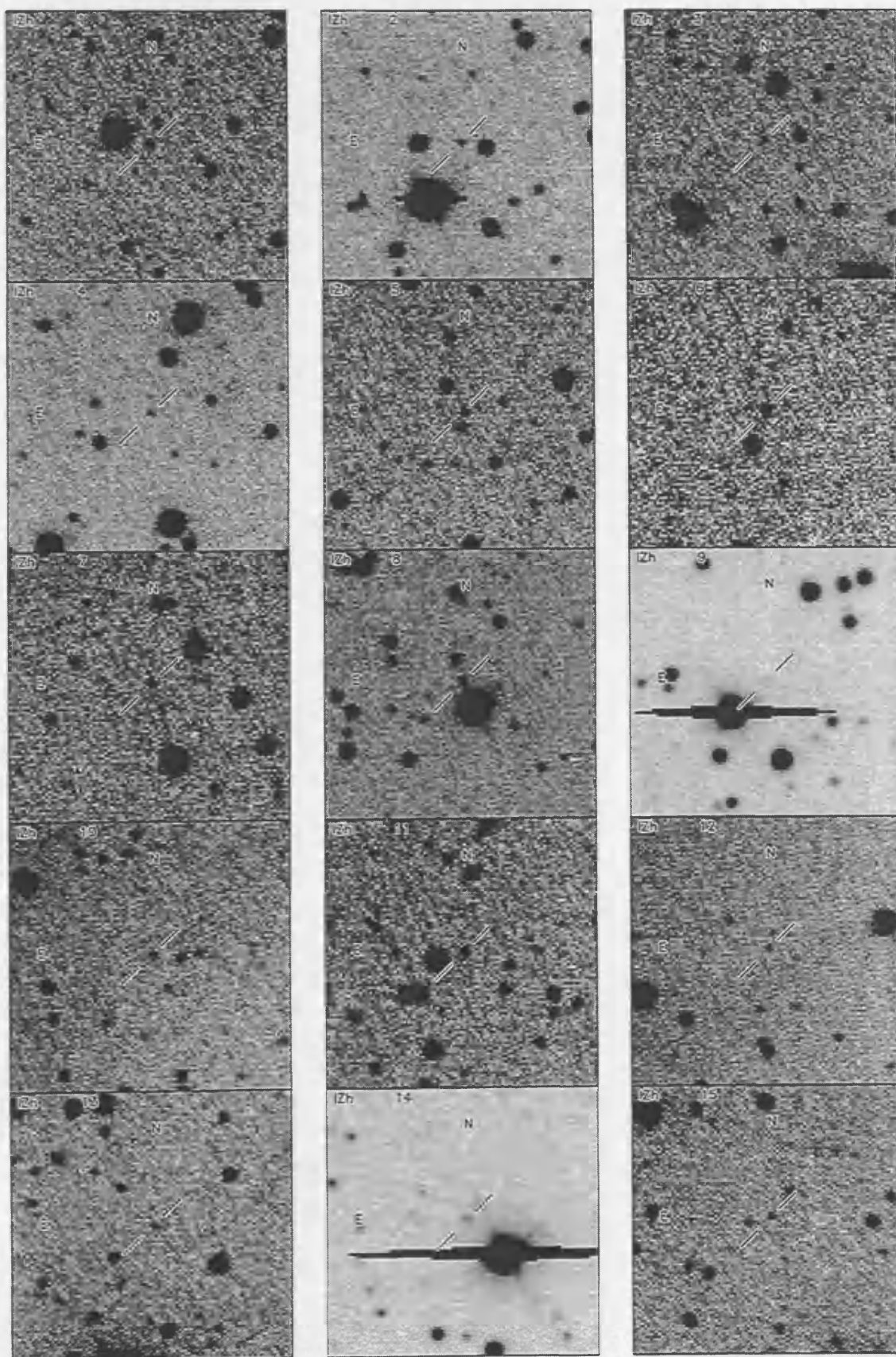


Figure F.1:

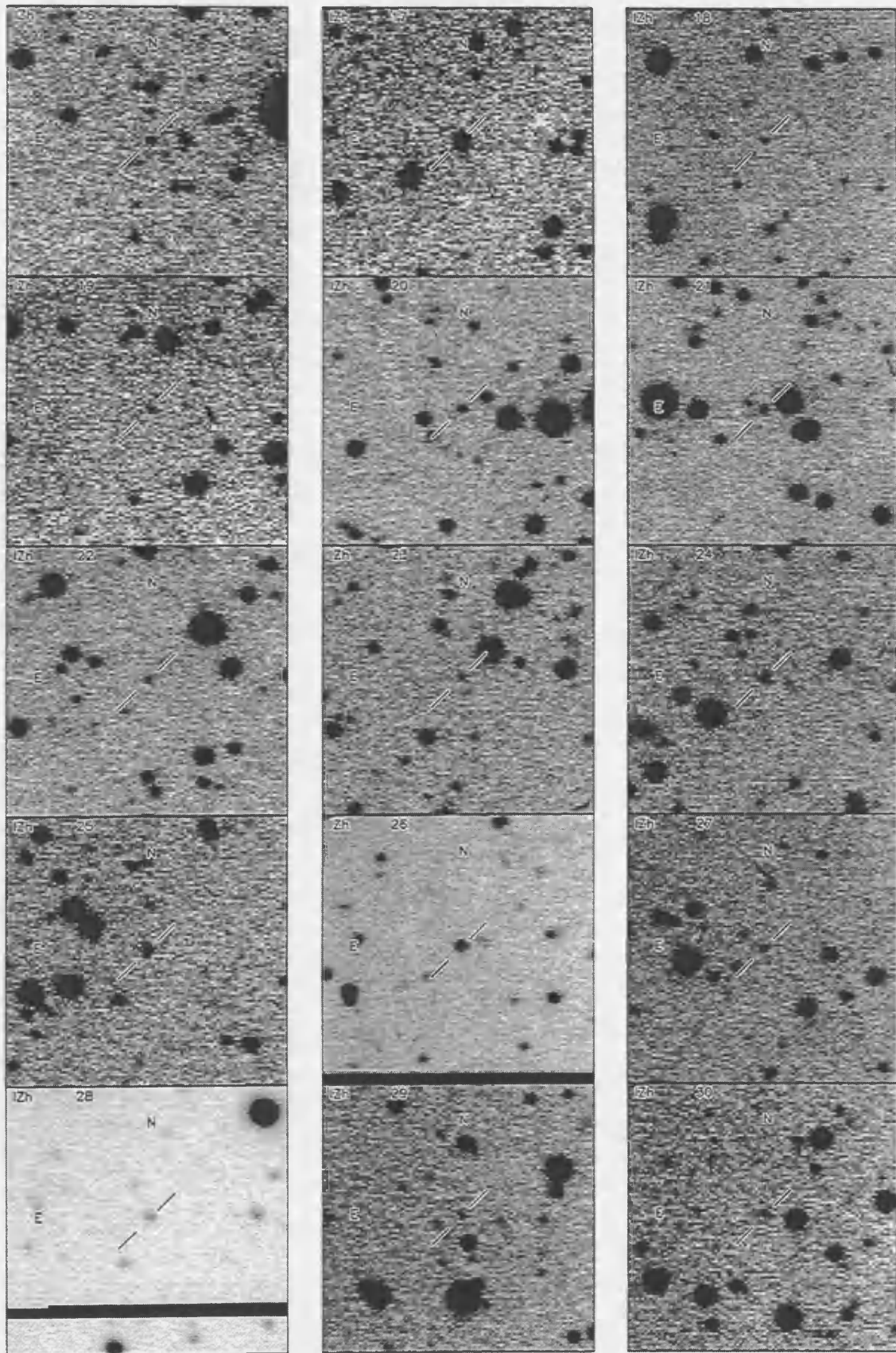
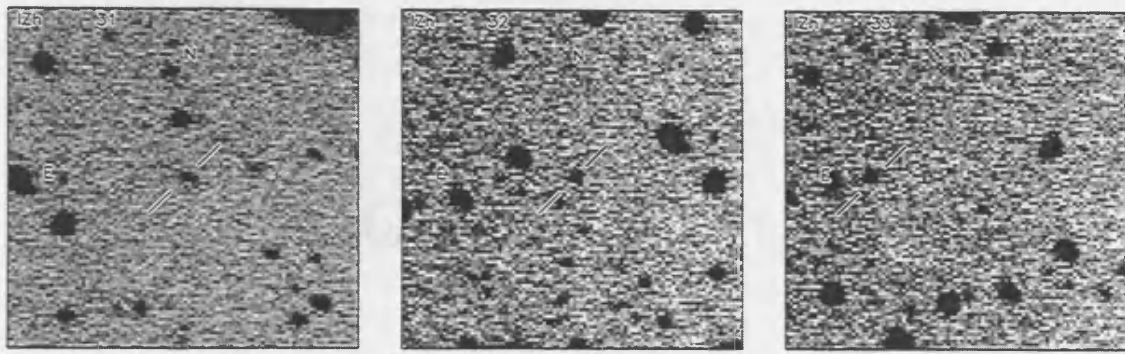


Figure F.2:



Procyon
Alcyon
Collinder 211
Collinder 212
Collinder 213
Collinder 214
Collinder 215
Collinder 216
Collinder 217
Collinder 218
Collinder 219
Collinder 220
Collinder 221
Collinder 222
Collinder 223
Collinder 224
Collinder 225
Collinder 226
Collinder 227
Collinder 228
Collinder 229
Collinder 230
Collinder 231
Collinder 232
Collinder 233
Collinder 234
Collinder 235
Collinder 236
Collinder 237
Collinder 238
Collinder 239
Collinder 240
Collinder 241
Collinder 242
Collinder 243
Collinder 244
Collinder 245
Collinder 246
Collinder 247
Collinder 248
Collinder 249
Collinder 250
Collinder 251
Collinder 252
Collinder 253
Collinder 254
Collinder 255
Collinder 256
Collinder 257
Collinder 258
Collinder 259
Collinder 260
Collinder 261
Collinder 262
Collinder 263
Collinder 264
Collinder 265
Collinder 266
Collinder 267
Collinder 268
Collinder 269
Collinder 270
Collinder 271
Collinder 272
Collinder 273
Collinder 274
Collinder 275
Collinder 276
Collinder 277
Collinder 278
Collinder 279
Collinder 280
Collinder 281
Collinder 282
Collinder 283
Collinder 284
Collinder 285
Collinder 286
Collinder 287
Collinder 288
Collinder 289
Collinder 290
Collinder 291
Collinder 292
Collinder 293
Collinder 294
Collinder 295
Collinder 296
Collinder 297
Collinder 298
Collinder 299
Collinder 300

Figure F.3:

Appendix G

Publication reprints

This appendix contains reproductions of the papers that I was involved with, that were published during the course of this work.

Discovery of the lowest mass Brown Dwarf in the Pleiades.

M.R. Cossburn, S.T. Hodgkin, R.F. Jameson and D.J. Pinfield

Department of Physics and Astronomy, Leicester University, University Road, Leicester LE1 7RH

1997 April 7

ABSTRACT

We have imaged the Pleiades open cluster at I and Z in a search for low-mass stars and brown dwarfs. One very red object, which we have called PIZ 1, at $I=19.64$, $I-Z=1.33$ has been detected within an area of 100 arcmin^2 . Follow up infrared photometry verifies that this object is extremely red with a K magnitude of 15.5. We have also obtained a spectrum which exhibits the spectral features indicative of an extremely cool M dwarf. We estimate the effective temperature and mass of PIZ 1 to be 2300K and $0.048 M_{\odot}$ respectively.

Key words: stars: photometry, low mass, brown dwarfs – open clusters: Pleiades

1 INTRODUCTION

The lowest mass brown dwarf discovered to date is GL229B (Nakajima et al. 1995). This object has an effective temperature less than 1200K and a mass in the range 20 to 50 Jupiter masses. GL229B was discovered as a companion to a nearby star (approximately 5.7 parsecs away) using both optical coronagraphic and direct infrared imaging methods.

To directly detect single brown dwarfs of known age, distance and metallicity, the ideal place to search is within young open clusters. Many brown dwarf surveys have been conducted in the Pleiades open cluster (age 70 to 120 Myr). This is because the Pleiades cluster is near enough so that the lower main sequence is not beyond the limits of detection, but far enough away so that the area of sky covered, (approximately 20 sq deg), is not too large. The cluster is young enough so that any brown dwarfs will be relatively bright. A $0.07 M_{\odot}$ brown dwarf will have $\log(L/L_{\odot}) \sim -2.7$ and $\log(T_{\text{eff}}) \sim 3.495$ (D'Antona and Mazzitelli 1994).

To date, three brown dwarfs have been found in the Pleiades, PPL 15, (Stauffer, Hamilton and Probst 1994), Teide 1, (Rebolo, Zapatero Osorio and Martin 1995), and Calar 3, (Zapatero Osorio, Rebolo and Martin 1997). To confirm the identity of PPL 15 as a brown dwarf Basri, Marcy and Graham (1996) detected the presence of lithium at 670.8 nm. The thick convective atmosphere of a brown dwarf leads to efficient mixing of lithium within the interior so that detection of lithium at 670.8 nm helps to constrain the central temperature. Teide 1 is a proper motion member of the cluster and from spectroscopic measurements, contains lithium. It has a mass of approximately 55 Jupiter masses (Rebolo et al. 1996). The identity of Calar 3 as a brown dwarf member of the Pleiades has been well documented in Martin, Rebolo and Zapatero Osorio (1996). We have obtained a deep CCD image of the Pleiades in the I and Z filters detecting an ex-

tremely faint red object (PIZ 1). In this paper we present follow-up K band photometry and optical spectroscopy.

2 OBSERVATIONS

2.1 Observing Strategy

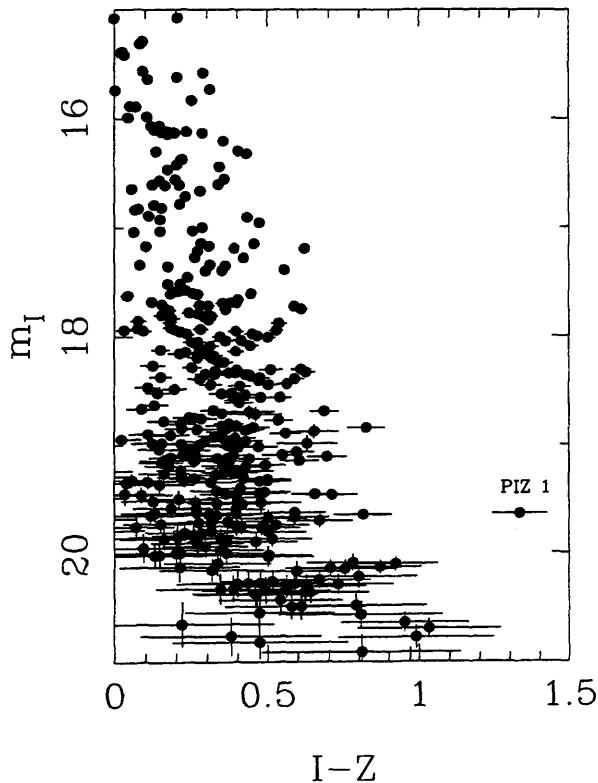
Searches for brown dwarfs at V and I, or R and I rely on the need to observe during dark time. Long exposures are necessary to compensate for the predicted lack of flux from brown dwarf sources at V and R. To be more flexible in the approach to this particular problem, the idea of using the Gunn Z filter (Schneider, Hoessel and Gunn 1983) was proposed. Brown dwarfs should be relatively bright at this wavelength. The I,Z combination suffers little penalty in bright time because the sky background at these wavelengths is dominated by OH emission and not by the lunar continuum. The spectrum of a very low-mass star is very steep in the wavelength region around I and Z and so the I-Z colour should in theory be a good discriminant for low-mass M dwarfs, even though there is a large degree of overlap between the filters (see Pinfield et al. 1997). We also avoid the problems associated with long baseline colour surveys such as I-K, where a large number of red galaxies are found because of the effects of redshifting the Balmer discontinuity (see Jameson, Hodgkin and Pinfield 1996).

2.2 Observations

Observations in I and Z were made in December 1995 using the TEK3 CCD at the prime focus of the Isaac Newton Telescope at the Observatorio del Roque Muchachos on the island of La Palma. The survey covered some 9 fields of 100 arcmin^2 each and yielded 10 candidates. The 5 clearest

Table 1. The coordinates and exposure times for each field

Name	R.A. (2000)	dec (2000)	I Exposure Time (seconds)	Z Exposure Time (seconds)
PL 1	3 49 50.2	24 31 07	240	800
PL 2	3 49 10.2	24 30 40	500	940
PL 3 (PIZ 1 field)	3 48 31.9	24 30 40	500	640
PL 4	3 47 53.0	24 30 39	180	300
PL 27	3 48 38.0	24 00 39	400	600
PL 28	3 47 59.0	24 00 39	240	300
PL 29	3 48 15.0	23 51 00	480	540
PL 53	3 50 30.0	24 03 59	120	520
PL 63	3 49 51.0	24 03 59	120	120

Figure 1. The I versus (I-Z) colour-magnitude diagram for 100 arcmin², showing the position of PIZ 1. Error bars are 1σ .

candidates have been followed up by obtaining infrared photometry at K. PIZ 1 was the only candidate that remained red in I-K. The remaining 5 candidates have not yet been followed up. The 9 field centres and exposure times are listed in Table 1. The images were bias subtracted, flatfielded and trimmed using IRAF routines running on STARLINK. DAOFIND was used to search for point sources and magnitudes derived using the DAOPHOT aperture photometry routines. To differentiate between stellar sources and faint red galaxies, a star galaxy separation procedure was performed, where all the sources were plotted on a $\log_{10}(\text{peak counts})$ versus $\log_{10}(\text{total counts})$ diagram. This form of shape analysis allowed the rejection of cosmic rays and galaxies from the data. The cleaned data for the PIZ 1 field has been presented in a colour-magnitude diagram (Figure 1).

The infrared photometry was obtained in UKIRT ser-

vice time on 22 October 1996 using IRCAM3. The weather was photometric. The infrared photometry was reduced using the STARLINK package IRCAMDR. The infrared data has been used to put PIZ 1 on an I versus I-K diagram (Figure 2) to compare our object with confirmed Pleiades members. Figure 3 shows the finder charts for PIZ 1 at I and K. Coordinates and photometry are given in Table 2.

The spectroscopy was carried out in service time on the 4.2m William Herschel Telescope (WHT) on 31 November 1996. The ISIS double arm spectrograph and R158R grating were used together with the TEK 1124x1124 chip. Five 30 minute integrations were carried out. The spectral coverage is from 6500 to 9500 Å. The spectrum was reduced using IRAF software. This included bias subtraction, flatfielding, optimal extraction and wavelength calibration. The star nearest to PIZ 1 has been identified as spectral type G5 from

its photometry, and was used to remove the instrumental response from the spectrum of PIZ 1. The extracted spectrum of PIZ 1 is presented in Figure 4. We have also plotted the spectra of Teide 1, (Rebolo et al. 1995), BRI 0021-0214, (Kirkpatrick, Henry and Simons 1995), and 2MASP-J0345, (Kirkpatrick, Beichman and Skrutskie 1997), in this figure.

3 DISCUSSION

From an experimental point of view the I-Z colour works as a good discriminate for faint red objects picking out the object PIZ 1 from the background field stars extremely well. This object extends the cluster sequence below Teide 1 well into the brown dwarf regime having an apparent I magnitude of 19.64 and I-Z colour of 1.33.

Photometrically PIZ 1 is a good candidate for membership of the cluster. Both optical and infrared point spread functions are stellar when compared to other objects in the field, indicating that PIZ 1 is not a galaxy, but the conclusive proof is the spectrum, clearly that of a late M dwarf. There is a remote possibility that PIZ 1 is a rare field star that coincides with the cluster main sequence. An old field star of the same effective temperature as PIZ 1 is from theory 0.4 magnitudes fainter than PIZ 1. Thus to mimic a brown dwarf Pleiad it must be in the distance range of approximately 60 to 130 pc. A field of 100 arcmin² then corresponds to a volume of 5.29 pc³. Both Tinney, Reid and Mould (1993) and Kirkpatrick et al. (1994) find $\Phi \approx 10^{-2.3}$ stars per pc³ of $M_I=13.25$ to 14.25. Thus the expected contamination of our sample of stars is of the order of 0.027 field stars per 100 arcmin². The luminosity functions from both Tinney and Kirkpatrick are local to the Sun.

Unfortunately there is no information on the scale height of the luminosity function for very faint field stars. Furthermore the Sun maybe 10 to 40 pc above the plane (Kirkpatrick et al. 1994) and the Pleiades (galactic latitude -24°) therefore 40 to 10 pc below the plane, so it would be difficult to use scale height information even if it were available. Unless the field star luminosity function rises steeply at fainter magnitudes than Teide 1 the contamination would not increase substantially. The likelihood of the field star luminosity function increasing without an increase in the cluster luminosity function is small.

It is useful to compare this object with the low-mass stars and brown dwarfs already identified in the Pleiades cluster. Figure 2 shows the low-mass HHJ stars (Hambly et al. 1993) and the three brown dwarfs, PPL15, Teide 1 and Calar 3. Object PIZ 1 has been plotted and its position indicates that it is significantly redder than Teide 1. PIZ 1 has a K magnitude of 15.5 giving an I-K colour of 4.1. Combining the data from Jones et al. (1994) and the latest models by Chabrier, Baraffe and Plez (1996) we have determined a relationship between the I-K colour and effective temperature. From this we estimate that the effective temperature of PIZ 1 is approximately 2300 K.

To determine the spectral type of PIZ 1, we have used the pseudocontinuum spectral ratios, PC3 and PC4, as defined by Martin et al. (1996). Using both PC3 and PC4 we have classified PIZ 1 as M9. We also note the similarities between PIZ 1 and 2MASP-J0345 in the wavelength region 9300 to 9400 Å. The blueward edge of this feature

is a result of H₂O absorption in the atmosphere of PIZ 1. The redward edge also has a contribution from terrestrial atmospheric absorption by H₂O which we have not removed. TiO absorption at 9208, 9230 and 9248 Å, in the spectrum of 2MASP-J0345 appears considerably stronger than in PIZ 1, indicating that 2MASP-J0345 is cooler. Kirkpatrick et al. (1995) argue that the heights of the pseudocontinuum points at 7550 and 8250 Å decrease moving to objects of later spectral type as a result of increased VO opacity. The VO bands lie on the blueward side of these features, and the effect can be seen in PIZ 1 at 7550 Å. However, at 8250 Å, the effect is less noticeable. H α appears to be present but the errors are large. H α emission is also found in Teide 1, Calar 3 and other low-mass stellar Pleiads.

It is our aim to obtain a better spectrum of PIZ 1 in the near future to determine the object's effective temperature, H α equivalent width and if possible, its radial velocity. Detecting lithium in an object this faint will be extremely difficult, even with the Keck Telescope. Ultimately we should measure the proper motion of this object to further check Pleiades membership.

As a first step towards determining the mass of PIZ 1 we must find the bolometric luminosity (L_{bol}). Jones et al. (1994) derived accurate measurements of M_{bol} and hence bolometric corrections (BC_I , BC_K) for a sequence of cool dwarfs. So we can form a relation between I-K and BC_I or BC_K and convert the I, K photometry of PIZ 1 directly to L_{bol} . We adopt a distance modulus of 5.65 to the Pleiades (Steele et al 1995) and take $M_{bol}=4.75$ for the Sun. We find that BC_I and BC_K give the same results for all the Pleiades brown dwarfs. For PIZ 1 we find $\log(L/L_\odot) = -3.39$. Similarly we find $\log(L/L_\odot) = -2.83$ for PPL 15 (c.f. -2.80, Basri et al. 1996) and $\log(L/L_\odot) = -3.17$ for Teide 1 (c.f. -3.18 Rebolo et al. 1996). Standard procedure would be to locate these objects on the Hertzsprung-Russell diagram and compare with theoretical isochrones (see e.g. Rebolo et al. 1995). However, there is a well known problem with current models in that they overpredict effective temperatures for the coolest objects. To avoid this, Basri et al. (1996) compared the luminosity and lithium abundance of PPL 15 with lithium depletion models from Nelson, Rappaport & Chiang (1993). They find a tight constraint on the age of the Pleiades of 115Myr and derive a mass of 0.078 M_\odot for PPL 15. The age constraint arises because PPL 15 shows partial Lithium depletion ($\sim 99\%$). The time scale for the final stages of Lithium depletion is extremely short for an object of this mass (around 5Myr) and to have found such an object is extremely fortuitous. It should be stressed that this result does not depend solely on one model; a quick look at Figure 17 of D'Antona and Mazzitelli (1994) shows that essentially the same mass and age would be derived for PPL 15 given the same observed quantities. Whether PPL 15 is a 'transition object' or brown dwarf is irrelevant for calculating the masses of the remaining Pleiades brown dwarfs. We may use PPL 15 as a known quantity in mass-luminosity space. For any given model, one can then find that isochrone which best reproduces the mass and luminosity of PPL 15. Using the most recent models of D'Antona and Mazzitelli (private communication) we simply find the mass of PIZ 1 and Teide 1 from their luminosities relative to PPL 15. Using this technique we obtain $M = 0.056M_\odot$ for Teide 1, (in excellent agreement with the mass found by

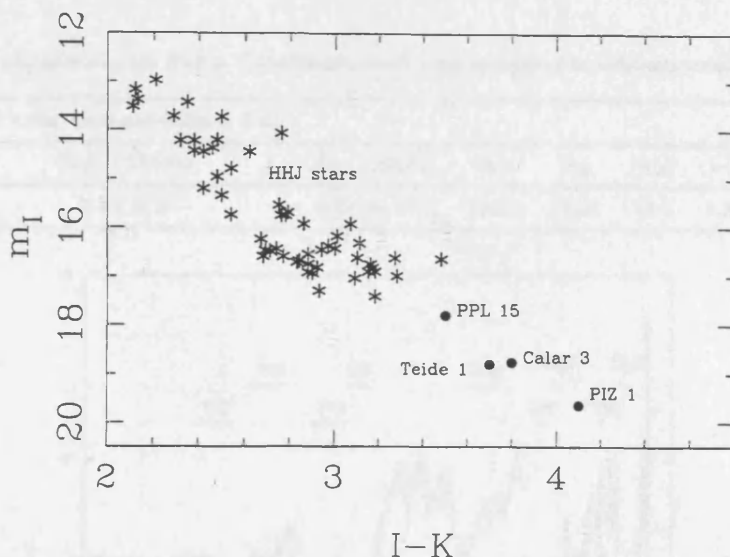


Figure 2. The I versus (I-K) colour-magnitude diagram for the Pleiades showing the low-mass HHJ stars, (Hambly et al. 1993), the brown dwarfs, PPL 15, Teide 1 and Calar 3, and our object PIZ 1.

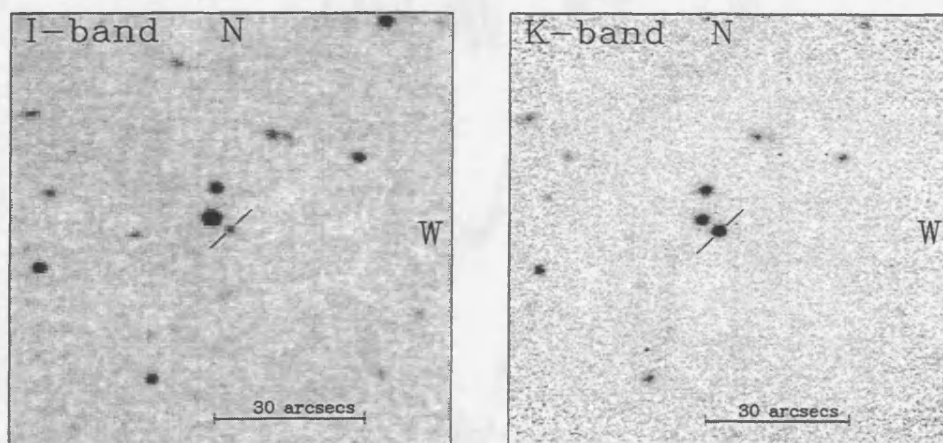


Figure 3. Finder charts for PIZ 1 at I and K. Coordinates and photometry are given in Table 1.

Rebolo et al. 1996), and $M = 0.048M_{\odot}$ for PIZ 1. It is our belief that the same masses would be found using any model (and indeed we find the same values using the model of Nelson, Rapaport and Joss 1986). The only drawback of this method is the heavy reliance on one object - PPL 15. We have assumed that PPL 15 is a single star; its position on the colour-magnitude diagram would actually suggest that it may be a binary. If this is the case all masses discussed above must be reduced and the low-mass Pleiads will have an age greater than 115 Myr.

4 CONCLUSIONS

The brown dwarf PIZ 1 has been detected within an area of 100 arcmin^2 suggesting that the use of the Z filter has been successful. The follow up K-band photometry shows that this object is very red with an effective temperature

in the region of 2300K. This is further supported by the spectrum of PIZ 1. We have determined a mass for PIZ 1 of $0.048 M_{\odot}$. We have also shown that the likely contamination of our sample by field stars should be minimal.

5 ACKNOWLEDGEMENTS

STH is a PPARC supported research associate and MRC and DJP are indebted to the same research council for research studentships. We would also like to thank Don Polacco for obtaining the spectrum of PIZ 1 in November 1996 in service time at the WHT and Sandy Leggett for the K photometry from UKIRT service time. Our thanks also to Davy Kirkpatrick and Maria Rosa Zapatero Osorio for their digitized spectra, and to Francesca D'Antona and Italo Mazzitelli for sending us their latest models.

Table 2. A summary of the photometry for PIZ 1. Coordinates have been measured to sub-arcsecond accuracy.

PIZ 1 distance modulus = 5.65						
R.A. (J2000)	Dec (J2000)	m_I	m_Z	m_K	I-Z	I-K
3 48 31.4	+24 34 37.7	19.64	18.31	15.5	1.33	4.1

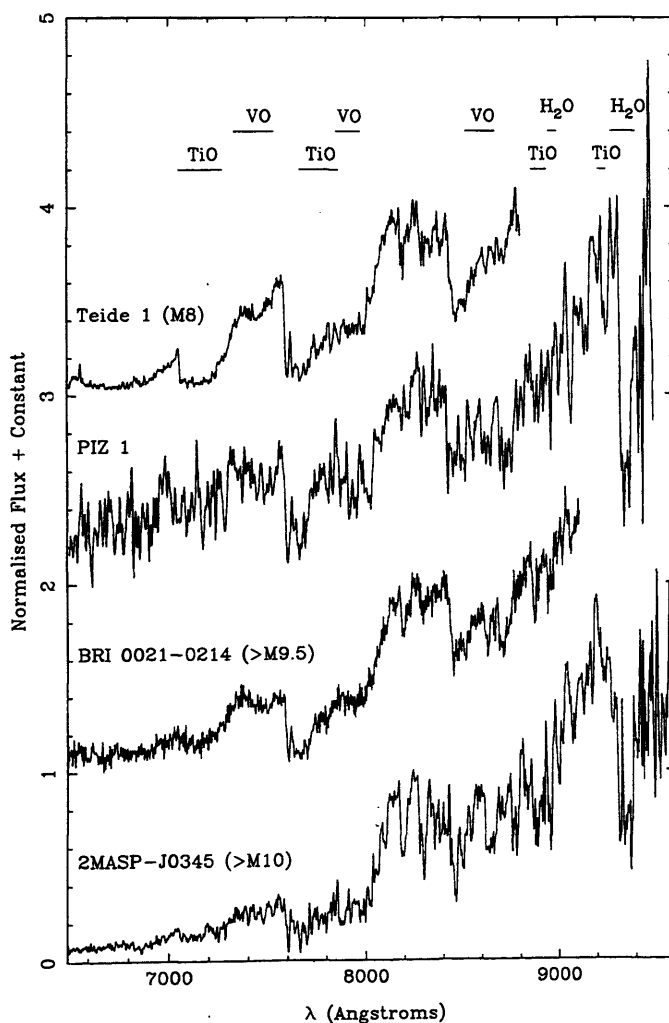


Figure 4. The spectra of Teide 1, PIZ 1, BRI 0021-0214 and 2MASP-J0345 ordered by increasingly late spectral type from top to bottom.

REFERENCES

- Basri, G., Marcy, G.M., Graham, J.R., 1996, ApJ, 458, 600
 Chabrier, G., Baraffe, I., Plez, B., 1996, ApJ, 459, L91
 D'Antona, F., Mazzitelli, I., 1994, ApJS, 90, 467
 Hambly, N.C., Hawkins, M.R.S., Jameson, R.F., 1993, A&AS, 100, 607
 Jameson, R.F., Hodgkin, S.T., Pinfield, D.J., 1996, Cool Stars, Stellar Systems and the Sun, 9th Cambridge Workshop, 109, 363
 Jones, H.R.A., Longmore, A.J., Jameson, R.F., Mountain, C.M., 1994, MNRAS, 267, 413
 Kirkpatrick, J.D., McGraw, J.T., Hess, T.R., Liebert, J., McCarthy, D.W., 1994, ApJS, 94, 749
 Kirkpatrick, J.D., Henry, T.J., Simons, D.A., 1995, ApJ, 109, 797
 Kirkpatrick, J.D., Beichman, C.A., Skrutskie, M.F., 1997, ApJ, in press
 Martin, E.L., Rebolo, R., Zapatero Osorio, M.R., 1996, ApJ, 469, 706
 Nakajima, T., Oppenheimer, B.R., Kulkarni, S.R., Golimowski, D.A., Matthews, K., Durrance, S.T., 1995, Nature, 378, 463
 Nelson, L.A., Rappaport, S., Joss, P., 1986, ApJ, 311, 226
 Nelson, L.A., Rappaport, S., Chiang E., 1993, ApJ, 413, 364
 Pinfield, D.J., Hodgkin, S.T., Jameson, R.F., Cossburn, M.R., von Hippel, T., 1997, MNRAS, in press.
 Rebolo, R., Zapatero Osorio, M.R., Martin, E.L., 1995, Nature, 377, 129
 Rebolo, R., Martin, E.L., Basri, G., Marcy, G.M., Zapatero Osorio, M.R., 1996, ApJ, 469, L53-L56
 Schneider, D.P., Hoessel, J.G., Gunn, J.E., 1983, ApJ, 264, 337S
 Stauffer, J.R., Hamilton, D., Probst, R., 1994, AJ, 108, 155
 Steele, I.A., Jameson, R.F., Hodgkin, S.T., Hambly, N.C., 1995,

6 *M.R. Cossburn, S.T. Hodgkin, R.F. Jameson, D.J. Pinfield.*

MNRAS, 275, 841

Timney, C.G., Reid, I.N., Mould, J.R., 1993, ApJ, 414, 254

Zapatero Osorio, M.R., Rebolo, R., Martin, E.L., 1997, A&AS,
317, 164

Brown dwarf candidates in Praesepe

D. J. Pinfield,¹ S. T. Hodgkin,¹ R. F. Jameson,¹ M. R. Cossburn¹ and T. von Hippel²

¹*Department of Physics and Astronomy, Leicester University, University Road, Leicester LE1 1RH*

²*Department of Astronomy, 475 N. Charter Street, University of Wisconsin, Madison, WI 53706, USA*

Accepted 1996 December 20. Received 1996 December 13; in original form 1996 October 17

ABSTRACT

We present a deep *R*-, *I*- and *Z*-band photometric survey of the open cluster Praesepe. 26 new photometric candidates have been found with $I > 17.8$, extending Praesepe's main sequence down to $I = 21.5$. 19 of the new members are brown dwarf candidates, and two could be binary brown dwarfs. Praesepe's mass function is derived, and found to be rising into the brown dwarf range with $\alpha \geq 1.5$.

Key words: stars: low-mass, brown dwarfs – stars: luminosity function, mass function – open clusters and associations: individual: Praesepe – dark matter.

1 INTRODUCTION

One proposed hypothesis for dark matter in the Galaxy is that it is composed of large numbers of substellar objects with $M \leq 0.08 M_{\odot}$, where the hydrogen-burning core temperature of 3×10^6 K is never reached. These objects are known as brown dwarfs (BDs) (Tarter 1975).

The evolutionary behaviour of BDs has been modelled by various authors (see, e.g., Burrows et al. 1993 and D'Antona & Mazzitelli 1994). It is clear that after $\sim 5 \times 10^8$ yr (when a $0.1 M_{\odot}$ star reaches the main sequence) BDs [$T_{\text{eff}} \leq 2600$ K, $\log(L/L_{\odot}) \leq -3.5$] continue to cool and grow fainter at constant radius, reaching $T \leq 1000$ K and $\log(L/L_{\odot}) \leq -5$ by the age of the Galactic disc. BDs of disc age are therefore very difficult to find, and are in general searched for as companions of brighter nearby field stars. Very little progress has been made in this direction until recently, when Nakajima et al. (1995) found a companion ($0.02 \leq M/M_{\odot} \leq 0.05$) to Gl 229 (a nearby star of age $\sim 10^9$ yr), using a coronagraph to block out much of the light from the primary.

Open star clusters provide an ideal hunting ground for free-floating BDs for several reasons. Their young age means that cluster BDs will be relatively hot and bright, and the cluster's angular extent on the sky leads to the surface density of stars (including BDs) being considerably more than in the field. Furthermore, cluster properties such as distance, age, metallicity and reddening can be found from studies of the brighter members, and inferred for the low-mass population.

Much effort has been devoted to the Pleiades, and two BDs have been found in that cluster: PPL 15 (Marcy, Basri

& Graham 1994) and Teide 1 (Rebolo, Zapatero Osorio & Martin 1995). In this paper, we present observations of Praesepe, which is about 10 times older than the Pleiades.

2 PRAESEPE: OBSERVATIONAL REVIEW

Praesepe is a Galactic open cluster in Cancer, and is part of the Hyades moving group (Eggen 1960). The distance, age, reddening and metallicity of Praesepe have been derived in several sources, and are summarized in Hambly et al. (1995b, hereafter HSHJb, and references therein). These data, along with the position and proper motion of the cluster, are given in Table 1.

Klein-Wassink (1927, hereafter KW) carried out a proper-motion survey to a radius of $\sim 1^{\circ}$ from the cluster

Table 1. Praesepe parameters.

Praesepe	M44 / NGC 2632
Coordinates (J2000) of cluster centre	R.A. = 8h 40m 12s Dec = +19 42 00 Galactic (II) 205.510, 32.480
Proper motion	$\Delta\alpha = 30 \text{ mas/yr}$ $\Delta\text{dec} = -8 \text{ mas/yr}$
Distance modulus	6.05
Age	(0.9 ± 0.5) Gyrs
Reddening	none
Metallicity	Fe/H = 0.14

centre, which has been followed up photometrically by several authors (Johnson 1952; Crawford & Barnes 1969; Uggren, Weis & De Luca 1979; Weis 1981). Artjukina (1966a,b) extends the coverage out to $\sim 4^\circ$, with photometric follow-up by Mermilliod et al. (1990) in $UBVR$ and $I(\text{Kron})$, who also obtained radial velocities for the candidates. Jones & Cudworth (1983, hereafter JC) extended the proper-motion depth down to $V \sim 17$, and JC members have photometry from Stauffer (1982) in $UBVR$ and $I(\text{Kron})$, and from Williams et al. (1994) in V and $I(\text{Kron})$. Williams, Rieke & Stauffer (1995) present V , I and K photometry down to $V \sim 23$, and derive luminosity and mass functions. Jones & Stauffer (1991) obtained proper motions down to $V \sim 18$ with $(BV)_{\text{pg}}$ and I_{pg} using the Monet scanning machine at Kitt Peak, and also derived a luminosity function. Hambly et al. (1995a, hereafter HSHJa) used the COSMOS scanning machine to obtain proper motions and R_{sp} , I_{N} photometry down to $I_{\text{N}} \simeq 18.2$, covering an area of 19 deg^2 .

Spectral types for high-mass ($6.3 < V < 9.1$) KW members have been found by Bidelman (1956) and Abt (1986). Fainter KW members ($V > 9$) have spectral types from Corbally & Garrison (1983, 1986), and Williams et al. (1994) give spectral types and $H\alpha$ equivalent widths for some of the JC members ($V > 16.5$). HSHJb present spectral types of four HSHJ members ($13 < I_{\text{N}} < 17$), and also derive luminosity and mass functions down to $R_{\text{sp}} \simeq 20$.

Other observational work includes a radial velocity study of a selection of members from KW, showing a well-defined binary sequence down to $V \sim 13$ (Bolte 1991). Also, an X-ray survey using *ROSAT* has been taken (Randich & Schmitt 1994).

3 SEARCHING FOR BROWN DWARFS

With the advent of CCDs, observers have been able to probe the sky down to much fainter magnitudes than could be achieved with photographic plates. However, even with the most up-to-date chips, there are various factors that need to be considered when searching for BDs.

First, the sky coverage provided needs to be as large as possible, so that a survey has a statistically good chance of turning up BDs. Current infrared arrays cover just over 1 arcmin^2 of sky (e.g., IRCAM3 at UKIRT). This is about 100 times less than a typical optical CCD set-up. Since nearby open clusters are of the order of 10° across, coverage of a significant fraction of the cluster using an infrared array is not yet feasible.

The newest optical CCD chips have much improved quantum efficiencies which extend down to just over $1 \mu\text{m}$, so their sensitivity is suitable for finding cool, low-mass stars.

Fig. 1 shows the sensitivity of a modern CCD chip (a Tektronix chip) against wavelength, along with typical V , R , I and Z filter passbands. The Z filter is open-ended, beginning at $\sim 0.8 \mu\text{m}$, and is an extension to the Gunn system (see Schneider, Hoessel & Gunn 1983). All the filter responses have been folded through the chip's quantum efficiency and normalized. Also shown is the red-to-infrared spectra of VB 10 (Kirkpatrick, private communication), an old disc M8 dwarf star of $T_{\text{eff}} \sim 2506 \text{ K}$ and $M \sim 0.085 M_\odot$ (Jones et al. 1994). Although VB 10 is just above the BD mass limit, objects of this temperature in Praesepe will be less massive BDs. It is therefore important to appreciate how the features of such a spectrum will affect its photo-

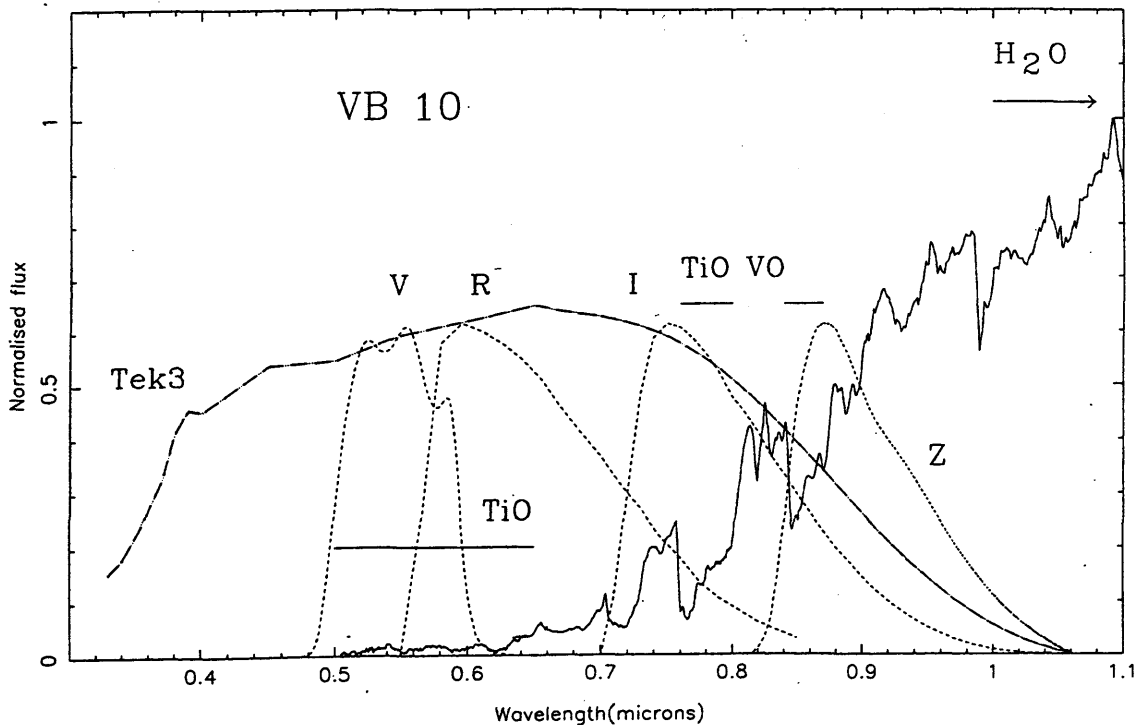


Figure 1. The visible and infrared spectrum of VB 10. The V , R , I and Z passbands are shown, as well as the efficiency of a typical modern CCD chip. Important regions of opacity are also indicated.

metry. In order to maximize the flux received from any BDs observed, it is clear that the best filters to use are *R*, *I* and *Z*, since these occur in the rising part of the spectrum, as far to the red as the CCD sensitivity will allow. The flux in the *V* band is very low, due mainly to it being in the Wein tail part of the spectrum, but it is further decreased by the molecular TiO opacities. A further requirement of photometric results is that the colour information of such objects should act as a sufficiently good temperature indicator, in order to single out cool cluster members from background stars. When using *V* and *I* (e.g. Williams et al. 1994), this will clearly be the case (provided that a *V* magnitude can be obtained for the object), since the two passbands are separated by some 3000 Å. The *R* and *I* passbands have a separation of about 2000 Å, providing a good temperature indicator. When using filters as close together as *I* and *Z*, the band separation is only about 1000 Å. However, the spectrum of cool stars such as VB 10 rises from about 10 to ~100 per cent of its peak through the *I* and *Z* bands, before H₂O becomes the dominant source of opacity. This very steep rise occurs in these bands, for all stars as cool as VB 10. Therefore the short baseline of the photometry is counteracted for such stars, and a good colour–temperature relation is the expected result.

It should also be added that during bright time the passbands least affected by scattered moonlight will be *I* and *Z*, since the sky is already bright at these wavelengths due to airglow; thus observing time is more flexible.

4 THE SURVEY

4.1 Observations

The survey results described in this paper come from data taken during 1993 and 1995–96. The central 1° region of the cluster was imaged in 1993 using the 2.5-m Isaac Newton Telescope, La Palma. An EEV5 CCD (1280 × 1180 pixel) chip was used at prime focus, and images were taken in *R*_{RGO} and *I*_{RGO} glass filters. The pixel scale of the chip was 0.55 arcsec pixel⁻¹, giving an effective image area of ≈ 11 × 10 arcmin. When convolved with the detector response, the *R*_{RGO} filter has an almost identical passband to Cousins *R*, and the *I*_{RGO} filter is fairly similar to Kitt Peak *I*. All fields were exposed for 140 s in *I* and 120 s in *R*, covering ~1 deg². The seeing was about 2 arcsec, and the weather was fairly photometric.

We obtained the second source of data in 1995–96, once again from the Isaac Newton Telescope, but taking 1000-s exposures in Gunn *Z*. The CCD chip used was a Tektronix chip. This chip is slightly smaller than the EEV5 chip, and was mounted at prime focus, covering ≈ 10 × 10 arcmin. Some 24 of the previously observed fields were imaged. The conditions were not photometric, and the observations were made during bright time.

4.2 Image reduction

The *R* and *I* images were debiased and flat-fielded using the Starlink software package CCDPACK. The *Z* images were similarly reduced using IRAF CCDPROC routines. Both software packages produced good results. *R* and *I* objects were located using Starlink's PISA, and *Z* objects using IRAF's

DAOFIND at a 4σ detection level. The latter was a more efficient method but, by searching at 1σ, 2σ and 4σ detection thresholds, PISA was able to locate all the sources. *R* and *I* instrumental magnitudes were found with Starlink's PHOTOM, and *Z* instrumental magnitudes were found using IRAF's DAOPHOT. Apertures ranged in size between 3 and 9 pixel depending on the brightness of the source. All magnitudes were then corrected to the 9-pixel aperture, using a derived aperture correction.

4.3 Object matching

I objects were then matched to *R* counterparts, taking into account any *x*–*y* shift between the images, found from the positions of brighter *R* and *I* sources. Since the *Z* images were taken at a different time, a polar coordinate shift was derived using two matched *I* and *Z* counterparts in opposite corners of each image. *Z* objects were then matched within a 3-pixel radius of the *I* objects.

4.4 Shape analysis

As well as instrumental magnitudes, the peak counts and total counts in each *I* object were extracted, in order to perform a simple shape analysis on the survey. The peak counts for objects in each image were then normalized to an average seeing of ~2 arcsec for all the images, and the total counts also received a correction where appropriate, to normalize them to the 9-pixel aperture size. Fig. 2 shows a log–log plot of normalized peak counts versus total counts in *I*, for each matched object in the survey. In any one image, the point-spread function for all stars will be approximately the same. Since the object counts are for the same circular aperture, the total counts in an object will scale directly with the peak counts. Unsaturated stars will therefore lie on a band with a gradient of 1.0.

Some objects do, however, fall above this band, due to the interference of cosmic rays incident on the CCD during the exposure. Since objects are selected only if they are found in at least two filters, solitary cosmic rays are essentially excluded. However, they can interfere with genuine stars, and cause them to appear more spiky.

Galaxies are extended objects, with a correspondingly larger point-spread function. They will thus have a lower value of peak counts than a star of equivalent brightness, and will fall below the stellar band. Using the divisions indicated in Fig. 2, objects were either flagged as stars, galaxies, or cosmic-ray-affected objects. The stellar band is very clear for large counts, and has been broadened at lower counts to allow for the reduced signal-to-noise ratio. Clearly, star–galaxy separation for faint objects is less than perfect.

4.5 Calibration

Using photometric service time, six overlapping Praesepe fields were imaged at the Jacobus Kapteyn Telescope, La Palma, using *R*_{RGO} and *I*_{RGO}. Between five and eight calibration stars were used in each image, to offset the zero-points accurately. A typical scatter of ~0.1 mag was seen. The *Z* calibration was achieved by comparing the resultant *I*–*Z* colour to the *R*–*I* colour of objects that were found in all

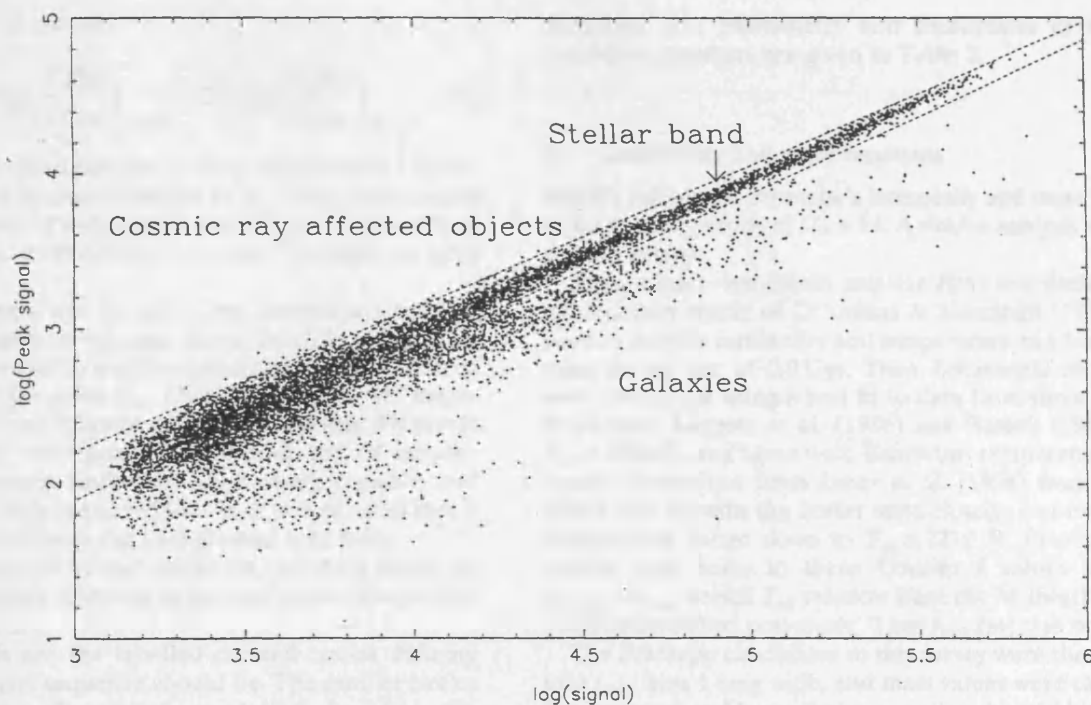


Figure 2. Log peak counts against log total counts in I , for objects found in the survey. The stellar band is indicated, and has a gradient of 1.0. Galaxies are flatter, and fall beneath this band. Some objects have been effected by cosmic rays, and therefore appear more spiky, and fall above the stellar band.

three images. Brighter objects were preferentially chosen where possible, and the Z zero-point was selected such that the band on the $(R-I)$ versus $(I-Z)$ colour-colour plot went through the origin. This is not such a reliable method, since it does not use direct calibration and relies on the instrumental colours of the observed stars. However, the instrumental error bars on the bright stars were small (≤ 0.05 mag), and the observed spread of the band in the colour-colour diagram was ≈ 0.1 mag. The zero-point errors were accordingly set at 0.1 mag, but it should be noted that this source of error is more important for objects that have no R magnitude, since the only colour used to select candidates was $I-Z$.

5 RESULTS AND DISCUSSION

5.1 Photometry

The survey achieved a signal-to-noise ratio ≥ 10 for $R \leq 21.5$, $I \leq 20$ and $Z \leq 21.5$. The 1σ and 2σ detection thresholds found fainter objects also, extending the survey limits to $R \approx 23$, $I \approx 22$ and $Z \approx 23$; however, the signal-to-noise ratio was only 5 for many of these objects.

The resultant photometric catalogue of data contains $\sim 10\,000$ objects, all of which have I magnitudes. The Z images go deeper than the I images because of the long exposure times. Consequently, the faint objects in the I fields that were observed at Z all have Z magnitudes, apart from those that were near bright stars, where the saturating bright star ruins the faint object's Z profile. Furthermore, some of the brighter I objects were saturated in their own

right on the Z images because of the long exposure times. Many objects have R photometry also; however, the R cut-off means that some faint red objects are undetectable in this filter. The following summarizes the three classes of photometric object.

- (1) RIZ object: an object with R , I and Z photometry. It was both detectable and unsaturated in R , I and Z .
- (2) RI object: an object that has R and I photometry, but no Z photometry. It was detectable and unsaturated in R and I , but either was not covered by the Z survey, or the Z counterpart was saturated, or spoiled by a nearby bright star or region of poor image quality.
- (3) IZ object: an object with I and Z photometry, but no R photometry. It was both detectable and unsaturated in Z , but its R counterpart was either too faint to be detected, or was spoiled by poor image quality.

In order to identify cluster members from background stars, it is necessary to locate the cluster sequence. In order to do this, expected photometric magnitudes were calculated from the spectra of a set of old disc stars (provided by D. Kirkpatrick, private communication). The R , I and Z filters were convolved with the CCD chip response to provide the effective bandpasses of each filter for the instrumental set-up that was used. These bandpasses were multiplied through each old disc star spectrum to obtain relative fluxes through each filter for each of the stars. The relative fluxes through each filter were also found for α Lyrae, which could be used as a calibration A0 star with zero colour. Each expected colour for the old disc stars was then calculated as shown in equation (1), which as an example is

done for the $I - Z$ colour:

$$I - Z_{\text{old-disc}} = 2.5 \log \left(\frac{Z \text{ flux}}{I \text{ flux}} \right)_{\text{old-disc}} - 2.5 \log \left(\frac{Z \text{ flux}}{I \text{ flux}} \right)_{\alpha \text{ Lyrae}} \quad (1)$$

Using these derived colours, as well as published I Cousins values for the M dwarfs (Jones et al. 1994), magnitudes (in the RGO system) were found, and using T_{eff} values from the same source, a set of useful colour- T_{eff} relations were derived.

Since Praesepe's age is ≥ 0.4 Gyr, low-mass stars and BDs will have had time to come down their Hayashi tracks, and to settle down on to a stellar sequence similar to that of old disc stars of the same T_{eff} . Cluster members will therefore lie on the same sequence as the old M dwarfs. Members were selected by their position in the IZ and RI colour-magnitude diagrams. Both were used where possible, and where an object only appeared in one, it was ensured that it was well separated from the background field stars.

The photometry of all the candidate members found, as well as the field stars, is shown in the two colour-magnitude diagrams in Fig. 3.

The M dwarfs are the labelled crossed circles defining where the low-mass sequence should lie. The smaller circles represent the new photometric candidates found by this survey, where filled circles represent RIZ objects in both colour-magnitude diagrams, and open circles represent RI objects in the first colour-magnitude diagram, and IZ objects in the second. Open triangles are HSHJa members observed in this survey, which help to define the top of the stellar sequence, and enable the other photometric members brighter than $I_{\text{RGO}} \sim 17.5$ to be rejected as non-proper-motion members. The dots are the background field stars, and several one-colour photometric members have been classed as this due to their other colour being inconsistent with membership.

Bolte (1991) showed that the majority of stars existing as binaries in Praesepe fall on a binary sequence, located ≈ 0.75 mag above the single-star sequence. The two stars indicated with 'b' in the second colour-magnitude diagram stand out from the rest of the sequence, and have a colour-magnitude position consistent with binarity. It is also possible that these objects are foreground stars.

Representative error bars are shown down the side of both colour-magnitude diagrams at their appropriate I position. Also shown are two isochrones, to indicate where mass divisions lie. The isochrones shown in each diagram are from the models of D'Antona & Mazzitelli (1994), for ages of 0.5 and 0.9 Gyr in the first and second diagrams respectively. The two ages used represent a best-guess age for the cluster, and a reasonable lower limit from Table 1. It is clear from a comparison that the isochrones are similar down to the $0.09-M_{\odot}$ point, but that the BD limit of $0.08 M_{\odot}$ moves down by ≈ 1 mag between the two ages.

The candidates then comprise 87 photometric members. Of these, 30 are known photometric and proper-motion members from HSHJa, and 31 can be rejected as non-proper-motion members, because they are bright enough to have been considered in the HSHJa survey. Between 15 and 19 objects are candidate BDs depending on Praesepe's age, of which two are candidate binary BDs, and the remaining 7-11 are low-mass Praesepe main-sequence candidate

members. The photometry and coordinates of the new candidate members are given in Table 2.

5.2 Luminosity and mass functions

HSHJb calculated Praesepe's luminosity and mass function down to a magnitude of $M_R = 14$. A similar analysis was done for this survey.

First, a mass-luminosity relation $I(m)$ was derived. The evolutionary tracks of D'Antona & Mazzitelli (1994) were used to provide luminosity and temperature as a function of mass for an age of 0.9 Gyr. Then, bolometric corrections were calculated using a best fit to data from three sources. Stars from Leggett et al. (1986) and Bessell (1995) have $T_{\text{eff}} > 2800$ K, and agree well. Below this temperature, bolometric corrections from Jones et al. (1994) were chosen, which join up with the hotter stars closely, and extend the temperature range down to $T_{\text{eff}} \approx 2219$ K. Finally, a correction was made to these Cousins I values using an $I_{\text{Cousins}} - I_{\text{RGO}}$ versus T_{eff} relation from the M dwarf spectral analysis described previously. Thus $I_{\text{RGO}}(m)$ was obtained.

The Praesepe candidates of this survey were then binned into I_{RGO} bins 1 mag wide, and mass values were calculated for the upper and lower limits, as well as the mid-bin magnitude. Since only a fraction of the photometric candidate members will be actual members, due to background star contamination, it was necessary to weight the bin numbers to correct for this. HSHJa find 50 per cent proper-motion membership of the photometric members in the faintest magnitude bin ($R_{595} \rightarrow 21$), which agrees well with the fraction of HSHJa stars found in this survey compared to the total number of brighter photometric members. Therefore only the HSHJa stars were used in the brighter two bins, and the fainter bins were weighted by 50 per cent.

This weighted number of stars in each observed mass bin must then be corrected by some factor, in order to represent the whole of the cluster. A surface density distribution of the form

$$\rho = \rho_0 e^{-r/r_0} \quad (2)$$

is assumed for each given cluster mass range, where ρ_0 is the central surface density of the cluster, and r_0 is the characteristic scalelength of the surface distribution. By integrating equation (2), the total number of stars in the cluster can be found for the particular mass or luminosity range:

$$\int_0^{\infty} 2\pi(\rho_0 e^{-r/r_0}) r dr = 2\pi\rho_0 r_0^2 \quad (3)$$

Therefore the total number of stars in the cluster per I magnitude bin, $\Phi(I)$, follows from ρ_0 and r_0 . Since the highest mass bin used here overlaps with the survey of HSHJa, the value of r_0 for this bin was found using a linear relation between magnitude and r_0 derived by HSHJb from observed stellar distributions. As the magnitude increases, and the masses decrease, the mass-luminosity relation turns up, and this linear relation will not be applicable.

King's well-known surface density distribution has been shown to fit globular and galactic clusters (see King 1962). By assuming spherical symmetry, a radial density distribution can be derived. Equating this radial distribution to a

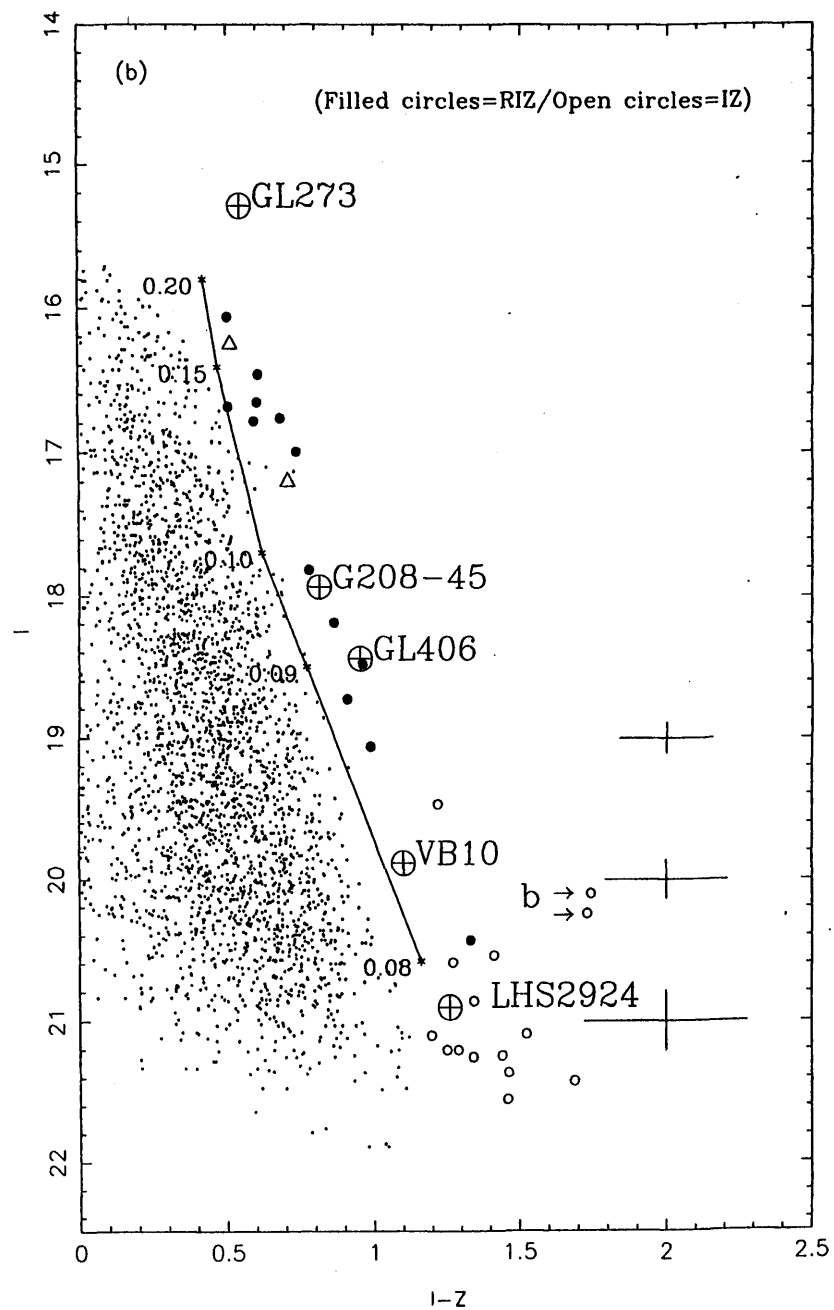
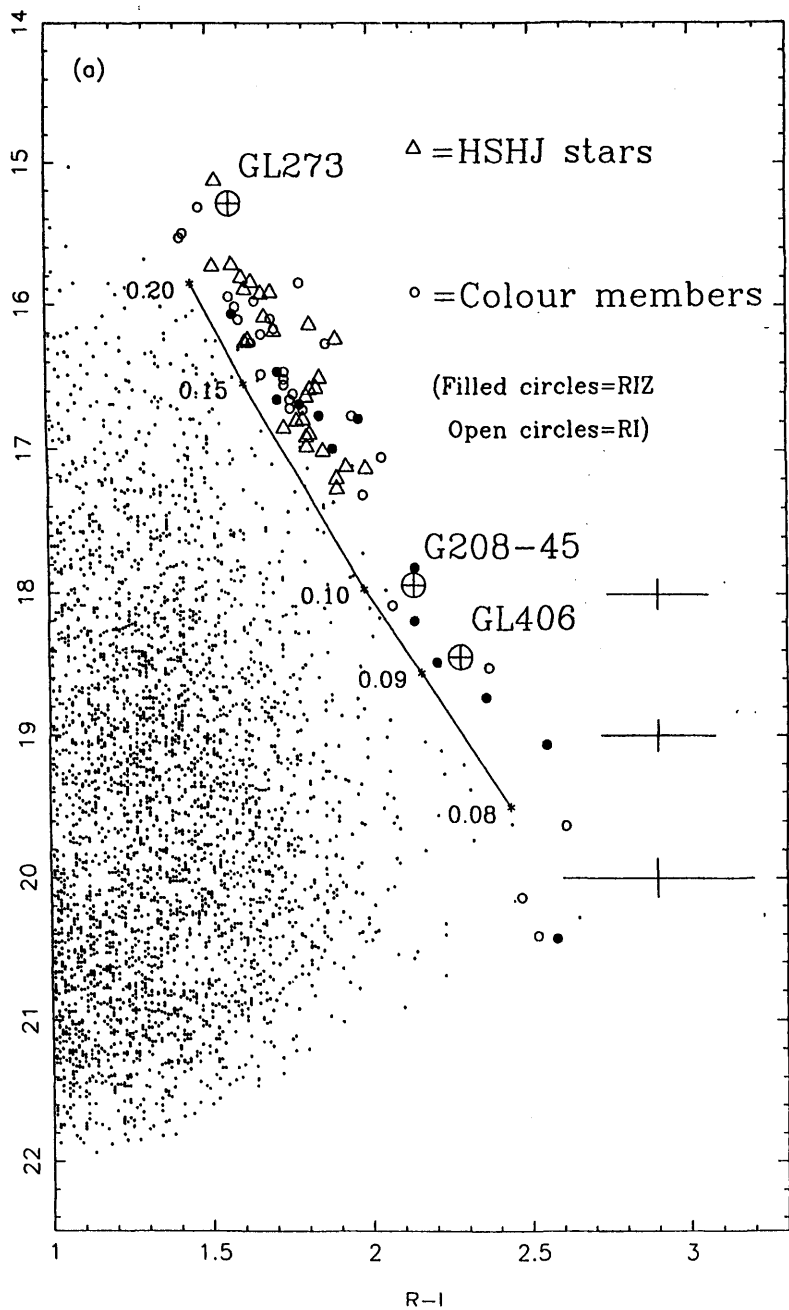


Figure 3. The I versus $R-I$, and I versus $I-Z$ colour-magnitude diagrams for the survey. The position of several old disc M dwarfs, as they would appear in Praesepe, are shown by large crossed circles. HSHJa stars found by the survey are shown as open triangles. The circles are new photometric candidates, where filled circles indicate RIZ objects, and open circles indicate RI -only objects in the first diagram and IZ -only objects in the second. Small dots are non-member field stars, some of which look like photometric members in one colour, but were eliminated as such by the other colour-magnitude position. The isochrones shown in each diagram are from the models of D’Antona & Mazzitelli (1994). The isochrones are for ages of 0.5 and 0.9 Gyr, in the first and second diagrams respectively. In the second diagram two binary candidates are indicated by a ‘b’. Typical photometric errors are shown down the side of each diagram.

Table 2. Photometry and positions of new candidate members.

Name	I	R-I	I-Z	R.A.(J2000)	Dec(J2000)
Object 1	20.14 ± 0.12	2.47 ± 0.35	-	08 36 54.55	+19 54 15.1
Object 2	18.19 ± 0.04	2.14 ± 0.07	0.87 ± 0.04	08 37 02.11	+19 52 07.0
Object 3	21.20 ± 0.22	-	1.25 ± 0.26	08 37 29.91	+19 50 09.1
Object 4	18.52 ± 0.03	2.37 ± 0.08	-	08 38 11.69	+19 59 44.4
Object 5	20.86 ± 0.16	-	1.34 ± 0.25	08 38 21.78	+20 05 53.2
Object 6	21.09 ± 0.16	-	1.52 ± 0.21	08 38 33.17	+19 49 13.2
Object 7	21.24 ± 0.16	-	1.44 ± 0.23	08 39 20.05	+19 42 41.1
Object 8	17.81 ± 0.02	2.14 ± 0.04	0.78 ± 0.03	08 39 20.43	+20 01 36.9
Object 9	21.25 ± 0.22	-	1.34 ± 0.24	08 39 24.09	+19 58 08.3
Object 10	20.54 ± 0.10	-	1.41 ± 0.15	08 39 32.54	+20 00 54.4
Object 11	19.47 ± 0.06	-	1.22 ± 0.07	08 39 47.72	+19 28 03.6
Object 12	20.10 ± 0.12	-	1.74 ± 0.15	08 39 48.82	+19 26 07.3
Object 13	20.24 ± 0.07	-	1.73 ± 0.17	08 40 27.55	+19 28 48.9
Object 14	20.59 ± 0.08	-	1.27 ± 0.15	08 40 46.12	+20 03 25.0
Object 15	21.36 ± 0.16	-	1.46 ± 0.25	08 40 47.72	+20 02 41.0
Object 16	21.10 ± 0.13	-	1.20 ± 0.23	08 40 59.08	+20 07 57.8
Object 17	20.41 ± 0.10	2.52 ± 0.35	-	08 41 08.14	+20 09 01.9
Object 18	19.63 ± 0.08	2.61 ± 0.19	-	08 41 08.48	+19 54 01.1
Object 19	21.42 ± 0.18	-	1.69 ± 0.26	08 41 10.31	+20 07 15.5
Object 20	18.48 ± 0.04	2.21 ± 0.08	0.96 ± 0.04	08 41 24.84	+19 57 26.5
Object 21	18.73 ± 0.05	2.36 ± 0.11	0.91 ± 0.07	08 42 11.46	+19 52 50.0
Object 22	21.55 ± 0.17	-	1.46 ± 0.25	08 42 21.72	+20 07 35.9
Object 23	19.06 ± 0.03	2.55 ± 0.09	0.99 ± 0.04	08 42 54.63	+20 03 35.9
Object 24	20.43 ± 0.16	2.58 ± 0.42	1.33 ± 0.17	08 43 01.25	+19 49 59.7
Object 25	21.20 ± 0.13	-	1.29 ± 0.21	08 43 49.12	+20 07 30.0
Object 26	18.08 ± 0.04	2.07 ± 0.06	-	08 43 59.47	+20 07 10.3

Maxwellian distribution in the cluster centre, we obtain the following:

$$\frac{1}{\left[1 + \left(\frac{r}{r_c}\right)^2\right]^{3/2}} = e^{-M\phi(r)/kT}, \quad (4)$$

where $\phi(r)$ is the gravitational potential, kT is a kinetic energy constant for the cluster, and r_c is the core radius where the radial density has decreased by a factor of $2^{3/2}$ and the surface density by a factor of 2. In the centre of the cluster, where $\phi \propto r^2$, it can be shown that

$$r_c \propto \frac{1}{\sqrt{M}} \quad (5)$$

and, since

$$r_o = \frac{r_c}{\ln 2}, \quad (6)$$

$$r_o \propto \frac{1}{\sqrt{M}}. \quad (7)$$

The remaining values of r_o were then calculated from equation (7), using the highest mass bin r_o , and the mid-bin mass values. ρ_o was obtained for each bin by multiplying the weighted numbers of candidates in each field by e^{r/r_o} , using the cluster centre coordinates quoted in Table 1 to obtain r for each field, and averaging over all fields.

Table 3. Praesepe luminosity and mass function results.

I _{RGO}	logM/M _⊙	Candidates	weight	Φ(M _v)	log N(m)
16-17	-0.837	15	100%	250 ± 65	3.62
17-18	-0.977	8	100%	136 ± 48	3.71
18-19	-1.052	5	50%	54 ± 25	3.71
19-20	-1.085	3	50%	36 ± 21	3.87
20-21	-1.094	8	50%	82 ± 29	4.23
21-22	-1.149	9	50%	118 ± 37	4.39

The mass function $N(m)$ was then found using

$$N(m) = \Phi(I) \frac{dI}{dm}, \quad (8)$$

and the results are summarized in Table 3.

It is worth noting that the main source of error in the new mass and luminosity functions is the uncertainty in the membership of the candidates. This is particularly true for the two faintest magnitude bins, where in many cases only one colour was available. Uncertainties in the age and distance of the cluster are not so important. Also, the faintest magnitude bin is not quite complete down to $I=22$, so there may be slightly more stars in this bin. The luminosity and mass functions are plotted in Figs 4 and 5 as filled circles.

Also plotted as open squares are the results found by HSHJb. It can be seen that the two sets of results join on to each other closely in the complete region of the HSHJa survey. The mass function is conventionally written as a

power law, where $N(m) \propto m^{-\alpha}$. The value of α from HSHJb is 1.5 down to $0.1 M_{\odot}$, which is in agreement with that of the old M dwarf population near the Sun. The new data continue the slope of $\alpha=1.5$ down to and beyond the BD limit. However, the lowest mass points indicate a steeper slope of $\alpha=3.8$. A slope of $\alpha=1.5$ indicates large numbers of BDs,

but no great BD contribution to the cluster mass, and a slope of $\alpha \geq 2$ means low-mass stars dominate the cluster mass. This result indicates that there may be a large population of BDs in Praesepe which, when extrapolated to the field, could contribute significantly to the Galactic missing mass.

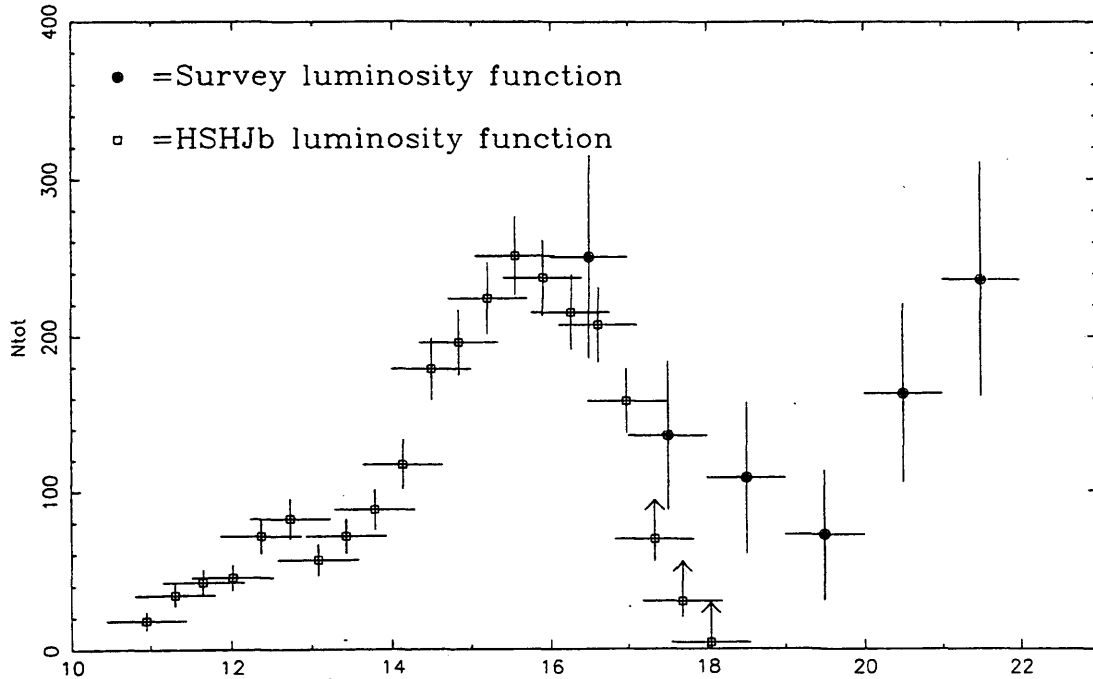


Figure 4. The luminosity function for Praesepe, binned into divisions of 1 mag in I . Open squares indicate data found by HSHJb, where arrows indicate lower limits. Filled circles are data from the current survey.

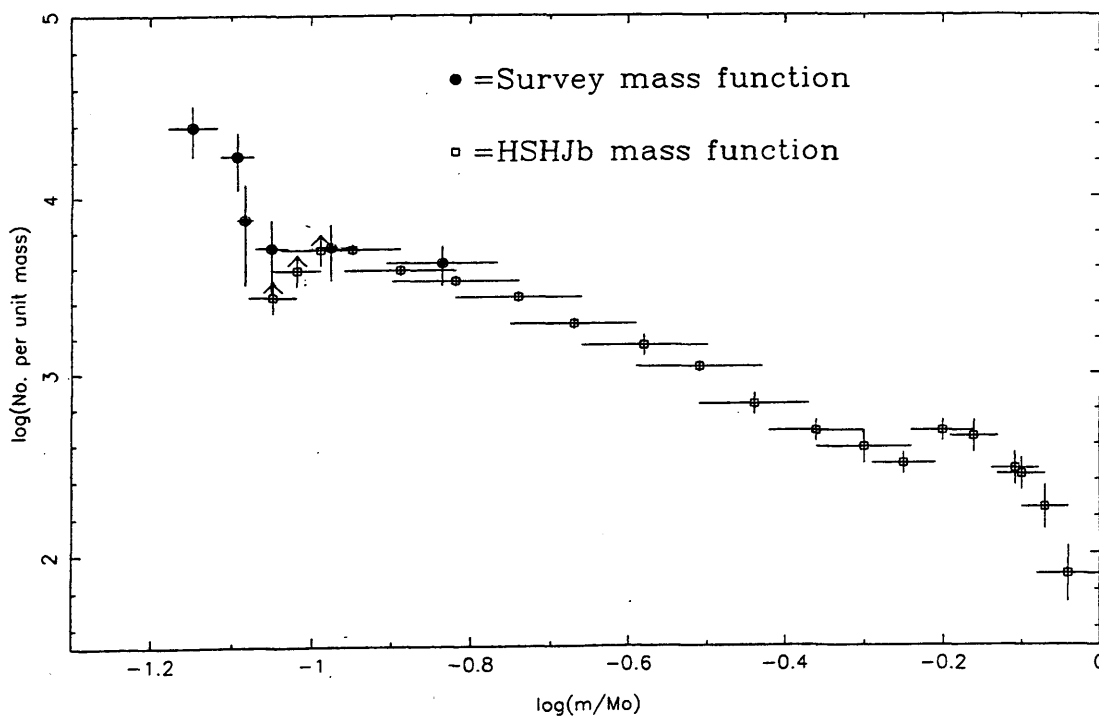


Figure 5. The mass function for Praesepe. Symbols are as for Fig. 4.

6 CONCLUSIONS

Comparing *RIZ* photometry with theoretical models, we have found 26 new candidate low-mass members of Praesepe. These have *I* magnitudes down to $I = 21.5$, and 15 to 19 of them should be BDs if membership is confirmed.

Confirmation of membership ideally requires measuring proper motions, which is straightforward after an interval of about 10 yr, and radial velocities, which will be difficult even with the largest telescopes given the faintness of some of the candidates. However, low-resolution spectroscopy showing a spectral type of late M should give a reasonably compelling indication. Very red low-mass field stars, like Gl 406 and fainter, are very rare. We calculate, using the luminosity function of Kirkpatrick et al. (1994), that we would expect to find 1.2 and 0.6 field stars per unit magnitude interval in the *RI* and *IZ* survey areas respectively. Further photometry in *J*, *H* and *K* bands is also desirable, but would not be as conclusive as spectroscopy, since galaxies can have very red colours and, although hopefully these have been identified by the shape analysis, near the star–galaxy separation line the classification is not so definite. We have calculated the mas function, which extends that found by HSHJb, possibly steepening. However, until more confirmation of the candidates' cluster membership is forthcoming, this can only be regarded as a preliminary result.

ACKNOWLEDGMENTS

We are grateful to Derek Jones for his involvement in obtaining some of the observational data, as a co-investigator, and also to J. Davy Kirkpatrick for making available the M dwarf spectra that were used. We have made extensive use of the Starlink computer facilities at the University of Leicester. Finally, we are grateful to PPARC for time on the Isaac Newton Telescope, and travel funds. DJP and MRC are supported by PPARC research studentships.

REFERENCES

- Abt H. A., 1986, *PASP*, 98, 307
- Artjukhina N. M., 1966a, *Trudy Gos. Astron. Inst. Shternberga* XXXIV
- Artjukhina N. M., 1966b, *Trudy Gos. Astron. Inst. Shternberga* XXXV
- Bessell M. S., 1995, *PASP*, 107, 672
- Bidelman W. P., 1956, *PASP*, 68, 318
- Bolte M., 1991, *ApJ*, 376, 514
- Burrows A., Hubbard W. B., Saumon D., Lunine J. I., 1993, *ApJ*, 406, 158
- Corbally C. J., Garrison R. F., 1983, *J. R. Astron. Soc. Can.*, 77, 28
- Corbally C. J., Garrison R. F., 1986, *AJ*, 92, 90
- Crawford D. L., Barnes J. V., 1969, *AJ*, 74, 818
- D'Antona F., Mazzitelli I., 1994, *ApJS*, 90, 467
- Eggen O. J., 1960, *MNRAS*, 120, 540
- Hambly N. C., Steele I. A., Hawkins M. R. S., Jameson R. F., 1995a, *A&AS*, 109, 29 (HSHJa)
- Hambly N. C., Steele I. A., Hawkins M. R. S., Jameson R. F., 1995b, *MNRAS*, 273, 50 (HSHJb)
- Johnson H. L., 1952, *ApJ*, 116, 640
- Jones B. F., Cudworth K., 1983, *AJ*, 88, 215 (JC)
- Jones H. R. A., Stauffer J. R., 1991, *AJ*, 102, 1080
- Jones H. R. A., Longmore A. J., Jameson R. F., Mountain C. M., 1994, *MNRAS*, 267, 413
- King I., 1962, *AJ*, 67, 471
- Kirkpatrick J. D., McGraw J. T., Thomas R. H., Liebert J., McCarthy D. W., 1994, *ApJS*, 94, 749
- Klein-Wassink W. J., 1927, *Groningen Publ. No. 41 (KW)*
- Leggett S. K., Mountain C. M., Selby M. J., Blackwell D. E., Booth A. J., Haddock D. J., Petford A. D., 1986, *A&A*, 159, 217
- Marcy G. W., Basri G., Graham J. R., 1994, *AJ*, 428, L57
- Mermilliod J. C., Weis E. W., Duquennoy A., Mayor M., 1990, *A&A*, 235, 114
- Nakajima T., Oppenheimer B. R., Kulkarni S. R., Golimowski D. A., Matthews K., Durrance S. T., 1995, *Nat*, 378, 463
- Randich S., Schmitt J. H. M. M., 1995, *A&A*, 298, 115
- Rebolo R., Zapatero Osorio M. R., Martin E. L., 1995, *Nat*, 377, 129
- Schneider D. P., Hoessel J. G., Gunn J. E., 1983, *ApJ*, 264, 337
- Stauffer J. R., 1982, *PASP*, 94, 678
- Tarter J. C., 1975, *PhD thesis, Univ. California, Berkeley*
- Uppgren A., Weis E., DeLuca E., 1979, *AJ*, 84, 1586
- Weis E., 1981, *PASP*, 93, 437
- Williams D. M., Rieke G. H., Stauffer J. R., 1995, *ApJ*, 445, 359
- Williams S. D., Stauffer J. R., Prosser C. F., Herter T., 1994, *PASP*, 106, 817

References

- Abt, H. A., 1986. *PASP*, **98**, 307.
- Adams, F. C. & Fatuzzo, M., 1996. *ApJ*, **464**, 256.
- Ahmad, Lawrence & Reddish, 1965. *Publ. Roy. Obs.*, **1**, 1.
- Alcock, C., 1993. *Nat*, **365**, 621.
- Alexander, D. R., Augason, G. C. & Johnson, H. R., 1989. *ApJ*, **345**, 1014.
- Allard, F. & Hauschildt, P. H., 1995. *ApJ*, **445**, 433.
- Allard, F., Hauschildt, P. H., Baraffe, I. & Chabrier, G., 1996. *Astrophys. J. Letters.*, **465**, 123.
- Allard, F., Hauschildt, P. H., Alexander, D. R. & Starrfield, S., 1997. *Ann. Rev. Astr. Astrophys.*, **35**. in press.
- Allard, F., 1990. *PhD thesis*, Univ. Heidelberg.
- Allen, C. W., 1973. *Astrophysical Quantities*, Athlone Press.
- Artjukhina, N. M., 1966. *Trudy Gos. Astron. Inst. Shternberga XXXIV*, .
- Artyukhina, N. & Kalinina, E., 1970. *Trudy Shternberg Astr. Inst.*, **39**, 111.
- Aubourg, E., 1993. *Nat*, **365**, 623.
- Baraffe, I., Chabrier, G., Allard, F. & Hauschildt, P. H., 1995. *Astrophys. J. Letters.*, **446**, 35.
- Basri, G., Marcy, G. M. & Graham, J. R., 1996. *ApJ*, **458**, 600.
- Becklin, E. E., Macintosh, B. & Zuckerman, B., 1995. *Astrophys. J. Letters.*, **449**, 117.
- Bennett, D., 1997. In: *Brown Dwarfs and Extra Solar Planets*, eds Rebolo, R., Martin, E. & Osorio, M. R. Z. in press.

- Berriman, G., Reid, N. & Leggett, S. K., 1992. *Astrophys. J. Letters.*, **392**, 31. (BRL92).
- Bessell, M. S. & Brett, J. M., 1988. *PASP*, **100**, 1134.
- Bessell, M. S. & Stringfellow, G. S., 1993. *Ann. Rev. Astr. Astrophys.*, **31**, 433.
- Bessell, M. S., 1976. *PASP*, **88**, 557.
- Bessell, M. S., 1979. *PASP*, **91**, 589.
- Bessell, M. S., 1983. *PASP*, **95**, 480.
- Bessell, M. S., 1986. *PASP*, **98**, 1303.
- Bessell, M. S., 1987. *PASP*, **99**, 642.
- Bessell, M. S., 1990. *PASP*, **102**, 1181.
- Bessell, M. S., 1991. *Astron. J.*, **101**, 662. (B91).
- Bessell, M. S., 1995. *PASP*, **107**, 672.
- Bidelman, W. P., 1956. *PASP*, **68**, 318.
- Bolte, M., 1991. *ApJ*, **376**, 514.
- Boss, A. P., 1995. *ApJ*, **439**, 224.
- Bryja, C., Jones, T. J., Humphreys, R. M., Lawrence, G., Pennington, R. L. & Zumach, W., 1992. *Astrophys. J. Letters.*, **388**, 23.
- Bryja, C., Humphreys, R. M. & Jones, T. J., 1994. *Astron. J.*, **107**, 246.
- Burrows, A., Hubbard, W. B., Saumon, D. & Lunine, J. I., 1993. *ApJ*, **406**, 158.
- Butler, R. P. & Marcy, G. W., 1996. *Astrophys. J. Letters.*, **464**, 153.
- Canuto, V. M. & Mazzitelli, I., 1991. *ApJ*, **370**, 295.
- Canuto, V. M. & Mazzitelli, I., 1992. *ApJ*, **389**, 724.
- Chabrier, G. & Baraffe, I., 1997. *A&A*, . in press.

- Chabrier, G., Baraffe, I. & Plez, B., 1996. *Astrophys. J. Letters.*, **459**, 91. (CBP96).
- Chernoff, D. F., Kochanek, C. S. & Shapiro, S. L., 1986. *ApJ*, **309**, 183.
- Corbally, C. J. & Garrison, R. F., 1983. *J. R. Astron. Soc. Can.*, **77**, 28.
- Corbally, C. J. & Garrison, R. F., 1986. *Astron. J.*, **92**, 90.
- Cossburn, M. R., Hodgkin, S. T., Jameson, R. F. & Pinfield, D. J., 1997. *MNRAS Lett.*, **288**, 23.
- Cox, A. N. & Tabor, J. E., 1976. *ApJS*, **31**, 271.
- Crawford, D. L. & Barnes, J. V., 1969. *Astron. J.*, **74**, 818.
- Da Costa, G. S. & Freeman, K. C., 1976. *ApJ*, **206**, 128.
- Da Costa, G. S., 1982. *Astron. J.*, **87**, 990.
- D'Antona, F. & Mazzitelli, I., 1994. *ApJS*, **90**, 467.
- Djorgovski, S., Piotto, G. & King, I. R., 1989. *ddse.work*, **1**, 147.
- Eggen, O. J., 1960. *MNRAS*, **120**, 540.
- Elson, R., Hut, P. & Inagaki, S., 1987. *Ann. Rev. Astr. Astrophys.*, **25**, 565.
- Epchtein, N., 1994. *Ap&SS*, **217**, 3.
- FitzGerald, M. P., 1970. *A&A*, **4**, 234.
- Fuente Marcos, R., 1995. *A&A*, **301**, 407.
- Geballe, T. R., Kulkarni, S. R., Woodward, C. E. & Sloan, G. C., 1996. *Science*, **467**, 101.
- Graham, J. R., Matthews, K., Neugebauer, G. & Soifer, B. T., 1990a. *ApJ*, **357**, 216.
- Graham, J. R., McCarthy, J. K., Reid, I. N. & Rich, R. M., 1990b. *Astrophys. J. Letters.*, **357**, 21.

- Hambly, N. C., Steele, I. A., Hawkins, M. R. S. & Jameson, R. F., 1995a. *A&AS*, **109**, 29.
- Hambly, N. C., Steele, I. A., Hawkins, M. R. S. & Jameson, R. F., 1995b. *MNRAS*, **273**, 50.
- Hambly, N. C., Hawkins, M. R. S. & Jameson, R. F., 1991. *MNRAS*, **253**, 1.
- Hambly, N. C., Hawkins, M. R. S. & Jameson, R. F., 1993. *A&AS*, **100**, 607.
- Hambly, N. C., 1997. In: *Brown Dwarfs and Extra Solar Planets*, eds Rebolo, R., Martin, E. & Osorio, M. R. Z. in press.
- Hardy, A., 1962. *MNRAS*, **911**, 911.
- Haro, G., Chariva, E. & Gonzalez, G., 1982. *Boll. Del Instituto de Tonantzintla*, **3**, 1.
- Hawkins, M. R. S. & Bessell, M. S., 1988. *MNRAS*, **234**, 177.
- Hawkins, M. R. S., 1994. In: *Cool Stars, Stellar Systems and the Sun - 8th Cambridge Workshop*, ed. Caillault, J. P.
- Henry, T. J. & McCarthy, D. W. J., 1993. *Astron. J.*, **106**, 773.
- Henry, L. G., Wilets, L., Bohm, K. H., Levier, R. L. & Levee, R. D., 1959. *ApJ*, **129**, 628.
- Hertzsprung, E., 1947. *Ann. Leiden Obs*, **19**, 1.
- Inagaki, S., 1985. *dsc.symp*, **205**, 1.
- Jameson, R. F. & Skillen, W. J. I., 1989. *MNRAS*, **239**, 247.
- Jameson, R. F., Sherrington, M. R. & Giles, A. B., 1983. *MNRAS Lett.*, **205**, 30.
- Johnson & Mitchel, 1958. *ApJ*, **128**, 31.
- Johnson, H. L. & Morgan, W. W., 1953. *ApJ*, **117**, 313.
- Johnson, H. L., 1952. *ApJ*, **116**, 640.

- Jones, B. F. & Cudworth, K., 1983. *Astron. J.*, **88**, 215.
- Jones, B. F. & Stauffer, J. R., 1991. *Astron. J.*, **102**, 1080.
- Jones, H. R. A., Longmore, A. J., Jameson, R. F. & Mountain, C. M., 1994. *MNRAS*, **267**, 413. (JLJM94).
- Jones, H. R. A., Miller, L. & Glazebrook, K., 1994. *MNRAS Lett.*, **270**, 47.
- Jones, B. F., 1970. *Astron. J.*, **75**, 563.
- Jones, B. F., 1981. *Astron. J.*, **86**, 290.
- Kerr, F. J. & Lynden-Bell, D., 1986. *MNRAS*, **221**, 1023.
- King, I. R., 1962. *Astron. J.*, **67**, 471.
- King, I. R., 1966. *Astron. J.*, **71**, 276.
- King, I. R., 1976. *Star Clusters. I. A. U. symposium.*, **206**, 128.
- King, I. R., 1989. *ddse.work*, **1**, 157.
- Kirkpatrick, J. D., Beichman, C. A. & Skrutskie, M. F., 1997. *ApJ*, **476**, 311.
- Kirkpatrick, J. D., Kelly, D. M., Rieke, G. H., Liebert, J., Allard, F. & Wehrse, R., 1993. *ApJ*, **402**, 643. (KKRLAW93).
- Kirkpatrick, J. D., McGraw, J. T., Hess, T. R., Liebert, J. & Jr., D. W. M., 1994. *ApJS*, **94**, 749.
- Kirkpatrick, J. D., Henry, T. J. & Liebert, J., 1993. *ApJ*, **406**, 701.
- Kirkpatrick, J. D., 1997. In: *Brown Dwarfs and Extra Solar Planets*, eds Rebolo, R., Martin, E. & Osorio, M. R. Z. in press.
- Kitchen, C. R., 1997. *Astrophysical Techniques*, Adam Hilger.
- Klein Wassink, W. J., 1927. *Groningen Publ.*, **41**, 1.
- Kroupa, P. & Tout, C. A., 1997. *MNRAS*, **287**, 402.
- Kroupa, P., Tout, C. A. & Gilmore, G., 1990. *MNRAS*, **244**, 76.

- Kroupa, P., 1995. *MNRAS*, **277**, 1522.
- Kumar, S. S., 1963. *ApJ*, **137**, 1211.
- Kurucz, R. L., 1975. In: *Stellar Atmospheres: Beyond the Classical Models*, 441, eds Crivellari, L., Hubeny, I. & Hummer, D. G.
- Landolt, 1979. *ApJ*, **231**, 468.
- Landolt, A. U., 1992. *Astron. J.*, **104**, 340.
- Larson, R. B., 1972. *MNRAS*, **157**, 121.
- Laughlin, G. & Bodenheimer, P., 1993. *ApJ*, **403**, 303.
- Leggett, S. K. & Hawkins, M. R. S., 1988. *MNRAS*, **234**, 1065.
- Leggett, S. K. & Hawkins, M. R. S., 1989. *MNRAS*, **238**, 145.
- Leggett, S. K., Allard, F., Berriman, G., Dahn, C. C. & Hauschildt, P. H., 1996. *ApJS*, **104**, 117. (LABDH96).
- Leggett, S. K., Harris, H. C. & Dahn, C. C., 1994. *Astron. J.*, **108**, 994.
- Leggett, S. K., 1992. *ApJS*, **82**, 351.
- Liebert, J. & Probst, R. G., 1987. *Ann. Rev. Astr. Astrophys.*, **25**, 473.
- Liebert, J., Dahn, C. C. & Monet, D. G., 1988. *ApJ*, **332**, 891.
- Ludwig, C. B., 1971. *Appl. Opt.*, **10**, 1057.
- Magazzu, A., Rebolo, R. & Hodgkin, S. T., 1997. In: *Brown Dwarfs and Extra Solar Planets*, eds Rebolo, R., Martin, E. & Osorio, M. R. Z. in press.
- Marcy, G. W. & Butler, R. P., 1996. *Astrophys. J. Letters.*, **464**, 147.
- Marcy, G. W., Basri, G. & Graham, J. R., 1994. *Astrophys. J. Letters.*, **428**, 57.
- Mathieu, R. D., 1983. *PhD thesis*, Univ. California. Berkley.
- Mathieu, R. D., 1984. *ApJ*, **284**, 643.

- Mera, D., Chabrier, G. & Baraffe, I., 1996. *Astrophys. J. Letters.*, **459**, 87.
- Mermilliod, J. C., Weis, E. W., Duquennoy, A. & Mayor, M., 1990. *A&A*, **235**, 114.
- Mermilliod, J. C., Rosvick, J. M., Duquennoy, A. & Mayor, M., 1992. *A&A*, **265**, 513.
- Mould, J. R., 1976. *ApJ*, **210**, 402.
- Nakajima, T., Oppenheimer, B. R., Kulkarni, S. R., Golimowski, D. A., Matthews, K. & Durrance, S. T., 1995. *Nat*, **378**, 441.
- Nelson, L. A., Rappaport, S. A. & Joss, P. C., 1986. *ApJ*, **311**, 226.
- Oppenheimer, B. R., Kulkarni, S. R., Matthews, K. & Nakajima, T., 1995. *ApJ*, **270**, 14780.
- Osorio, M. R. Z., Rebolo, R. & Martin, E. L., 1997. *A&AS*, **317**, 164.
- Osorio, M. R. Z., 1997. In: *Brown Dwarfs and Extra Solar Planets*, eds Rebolo, R., Martin, E. & Osorio, M. R. Z. in press.
- Paresce, F., 1997. In: *Brown Dwarfs and Extra Solar Planets*, eds Rebolo, R., Martin, E. & Osorio, M. R. Z. in press.
- Pels, G., Oort, J. H. & Pels-Kluyver, H. A., 1975. *A&A*, **43**, 423.
- Pinfield, D. J., Hodgkin, S. T., Jameson, R. F., Cossburn, M. R. & von Hippel, T., 1997. *MNRAS*, **287**, 180.
- Probst, R. & Liebert, J., 1983. *ApJ*, **274**, 245.
- Prosser, C. F., Stauffer, J. R. & Kraft, R., 1991. *Astron. J.*, **101**, 1361.
- Raboud, D. & Mermilliod, J. C., 1997. *A&A*, **1**, 1. in press.
- Randich, S. & Schmidt, J. H. M. M., 1995. *A&A*, **298**, 115.
- Rebolo, R., Martin, E., Basri, G., Marcy, G. W. & Osorio, M. R. Z., 1996. *Astrophys. J. Letters.*, **469**, 53.
- Rebolo, R., Martin, E. & Magazzu, A., 1992. *Astrophys. J. Letters.*, **389**, 83.

- eds Rebolo, R., Martin, E. & Osorio, M. R. Z. *Brown Dwarfs and Extra Solar Planets*, 1997. in press.
- Rebolo, R., Osorio, M. R. Z. & Martin, E. L., 1995. *Nat*, **377**, 129.
- Reid, I. N. & Gilmore, G., 1984. *MNRAS*, **206**, 19.
- Reid, N., 1987. *MNRAS*, **225**, 873.
- Reid, N., 1992. *MNRAS*, **257**, 257.
- Reid, N., 1993. *MNRAS*, **265**, 785.
- Rieke, G. H. & Rieke, M. J., 1990. *Astrophys. J. Letters.*, **362**, 21.
- Rosvick, J. M., Mermilliod, J. C. & Mayor, M., 1992. *A&A*, **255**, 130.
- RowanRobinson, M., 1979. *ApJ*, **234**, 111.
- Salpeter, E. E., 1955. *ApJ*, **121**, 161.
- Schneider, D. P., Hoessel, J. G. & Gunn, J. E., 1983. *ApJ*, **264**, 337.
- Simons, D. A. & Becklin, E. E., 1992. *ApJ*, **390**, 431.
- Skrutskie, M. F., Forrest, W. J. & Shure, M., 1989. *Astron. J.*, **98**, 1409.
- Skrutskie, N. F. *et al.*, 1995. *BAAS*, **187**, 75.
- Smith, R. C., 1983. *Observatory*, **103**, 29.
- Soloman, P. M., Sanders, D. B. & Scoville, N., 1979. *I.A.U. Symp.*, **84**, 35.
- Spitzer, L., 1940. *MNRAS*, **100**, 396.
- Spitzer, L. J., 1975. *dss.proc*, **3**, 1.
- Stauffer, J. R., Hartmann, Soderblom & Burnham, 1984. *ApJ*, **280**, 202.
- Stauffer, J. R., Hamilton, D., Probst, R., Rieke, G. & Mateo, M., 1989. *Astrophys. J. Letters.*, **344**, 21.
- Stauffer, J., Klemola, A., Prosser, C. & Probst, R., 1991. *Astron. J.*, **101**, 3.

- Stauffer, J. R., Hamilton, D. & Probst, R., 1994. *Astron. J.*, **108**, 155.
- Stauffer, J. R., 1982. *PASP*, **94**, 678.
- Steele, I. A. & Jameson, R. F., 1995. *MNRAS*, **272**, 630.
- Stevenson, D. J., 1991. *Ann. Rev. Astr. Astrophys.*, **29**, 163.
- Tarter, J. C., 1975. *PhD thesis*, Univ. California, Berkley.
- Tarter, J. C., 1986. In: *Astrophysics of Brown Dwarfs*, 121, eds Kafatos, M. C., Harrington, R. S. & Maran, S. P.
- Terlevich, E., 1987. *MNRAS*, **224**, 193.
- Thackrah, A., Jones, H. R. A. & Hawkins, M. R. S., 1997. *MNRAS*, **284**, 507.
- Trumpler, R. J., 1921. *Lick Obs. Bull.*, **10**, 110.
- Uppgren, A., Weis, E. & DeLuca, E., 1979. *Astron. J.*, **84**, 1586.
- van Leeuwen, F., 1979. *stcl.symp*, **1**, 157.
- van Leeuwen, F., 1983. *PhD thesis*, Univ. Leiden.
- van Leeuwen, F. & Hansen Ruiz, C. S., 1997. *R. G. O. pre-print series.*, **272**, 1.
- van Leeuwen, F., Alphenaar, P. & Brand, J., 1986. *A&AS*, **65**, 309.
- von Hoerner, S., 1957. *ApJ*, **125**, 451.
- Wainscoat, R. & Cowie, L., 1992. *Astron. J.*, **103**, 332.
- Weis, E. W., 1981. *PASP*, **93**, 437.
- Williams, S. D., Stauffer, J. R., Prosser, C. F. & Herter, T., 1994. *PASP*, **106**, 817.
- Williams, D. M., Rieke, G. H. & Stauffer, J. R., 1995. *ApJ*, **445**, 359.
- Zuckerman, B. & Becklin, E. E., 1988. *Nat*, **330**, 138.
- Zuckerman, B. & Becklin, E. E., 1992. *ApJ*, **386**, 260.